# Converted wave imaging in anisotropic media using sea-floor seismic data

by

Fabio Mancini


Thesis submitted for the degree of Doctor of Philosophy

School of GeoSciences

University of Edinburgh

2004

I hereby declare that this thesis has been composed by myself and the work described is entirely my own unless explicitly stated in the text.

Fabio Mancini

**LIST OF FIGURES**

# NOTATIONS AND CONVENTIONS

## Abbreviations

| | |
|---|---|
| **4C** | Four component (multicomponent), 3 geophones plus 1 hydrophone |
| **OBC** | Ocean Bottom Cable, containing the multicomponent sensors |
| **P-P** | P-compressional waves |
| **P-SV** or **C** | Converted waves with particle motion in the source-receiver-conversion point plane |
| **P-SH** | Converted waves with particle motion perpendicular to the plane in which SV waves travelSV |
| **NMO** | Normal MoveOut |
| **DMO** | Dip MoveOut |
| **PSTM** | Pre Stack Time Migration |
| **PSDM** | Pre Stack Depth Migration |
| **RMS** | Root Mean Square |
| **CMP** | Common Mid Point |
| **CIP** | Common Image Point (CMP after PSTM) |
| **CRP** | Common Reflection Point (CMP after PSDM) |
| **ACCP** | Asymptotic Common Conversion Point |
| **CCP** | Common Conversion Point |
| **VTI** | Vertical Transverse Isotropy, Polar anisotropy |
| **HTI** | Horizontal Transverse Isotropy |
| **TTI** | Transverse isotropy with a tilted axis |

## Symbols

| Symbol | Meaning | Units |
|---|---|---|
| $v_p$ | P-wave velocity | m/s |
| $v_s$ | S-wave velocity | m/s |
| $v_c$ | C-wave velocity | m/s |
| $v_{pn}$ | NMO P-wave velocity (RMS, stacking) | m/s |
| $v_{sn}$ | NMO S-wave velocity (RMS, stacking) | m/s |
| $v_{cn}$ | NMO C-wave velocity (RMS, stacking) | m/s |
| $v_{p0}$ | P-wave vertical velocity | m/s |
| $v_{s0}$ | S-wave vertical velocity | m/s |
| $v_{c0}$ | C-wave vertical velocity | m/s |
| $x$ | Source-receiver offset | m |
| $x_c$ | Conversion point offset | m |
| $t(x)$ | Travel time at offset x | s |
| $t_0$ | Travel time at zero-offset | s |
| $t_{p0}$ | P-wave time at zero-offset | s |
| $t_{s0}$ | S-wave time at zero-offset | s |
| $t_{c0}$ | C-wave time at zero-offset, defined by the down-going P-wave traveltime, $t_{p0}$, and the up-going S-wave traveltime, $t_{s0}$ | s |
| $\gamma$ | Isotropic velocity ratio, $v_p/v_s$ | |
| $\gamma_0$ | Vertical velocity ratio,$v_{p0}/v_{s0}$ | |
| $\gamma_n$ | NMO velocity ratio, $v_{pn}/v_{sn}$ | |
| $\gamma_{eff}$ | Effective velocity ratio, $\gamma_n^2/\gamma_0$ | |
| $\gamma_{asy}$ | Depth-constant $\gamma_{eff}$ used in binning C-wave data | |
| $C_{ij}$ | Elastic constant | g/(ms$^2$)(GPa) |
| $\delta, \varepsilon, \gamma$ | Thomsen's anisotropic parameter, combinations of elastic constants | |
| $\sigma, \eta, \chi, \zeta$ | Different anisotropic parameters derived from Thomsen's parameters The subscript "*eff*" indicates they are "effective" parameters, the subscript "*i*") indicate interval quantity. | |
| $\rho$ | Density | Kg/m$^3$ |
| $\lambda$ | Fluid incompressibility | N/m$^2$ |
| $\mu$ | Shear modulus | N/m$^2$ |
| $p$ | Ray parameter | s/m |

# Chapter 1: Introduction

## 1.1. Multicomponent technology

In recent years seismic technology has advanced very rapidly trying to answer the new needs of the oil industry. Until recently seismic data were utilised mainly for exploration. 3D seismic data provided an accurate structural image of the subsurface. Acquisition and processing of large 3D seismic surveys was relatively quick and fairly cheap and became soon a commodity in the oil industry. However in the past few years large mergers between the main operators and the effects of the volatile oil price felt in 1999 have produced a steep decline in the exploration activity, shifting the interest toward reservoir characterisation and management. The seismic industry reacted quickly pushing the technology in this direction.

The two main products of this shift were 4D and 4C technologies. 4D (or time-lapse) surveys consist of repeating 3D surveys after an interval of time, i.e. two points in the time axis. When comparing the results of the two surveys the only difference should be due to fluid movements or pressure changes in the reservoir caused by the extraction (or injection) of fluid from (or to) the reservoir. 4D surveys are able to reveal by-passed oil traps, since reservoirs are often divided into compartments, which are not necessarily linked together.

4C (or multicomponent) seismic data allow the joint use of shear waves and compressional waves. The use of shear (S)-waves on its own is not something new; it was used in the past in land survey, but the difficulties of producing and operating a shear-wave source limited its use to few experiments in the late 60s (Garotta, 2000).

The approach of 4C technology is different: it aims to record P-S converted-waves (also called C-waves). These are P-waves converted to S-waves at the reflector; in this way the problem of the shear wave source is avoided. Another advantage of this technique is that is applicable in a marine environment using conventional air-guns as the source while deploying the receiver array directly at the sea-floor.

Converted waves have proved to give better images than P-waves in areas affected by gas clouds or in areas with weak P and strong S acoustic impedance contrasts. Multicomponent data also enable the joint use of S-wave and P-wave information for lithology and fluid prediction. Recently 3D 4C seismic data have been applied to study fractured reservoirs exploiting the shear wave splitting phenomenon. Crampin (1985) showed that when shear waves travel through a fractured body they split in two families, one with motion parallel to the fractures and one with motion perpendicular to it. The first family is faster than the second one. This information can be used to extract information about fracture density and orientation.

4C technology has the clear potential to become one of the most useful tools in reservoir characterisation.

## 1.2. Basics of Ocean Bottom Cable recording

Converted waves are recorded using standard air-gun sources and receiver arrays deployed on the sea-floor, Figure 1.1.

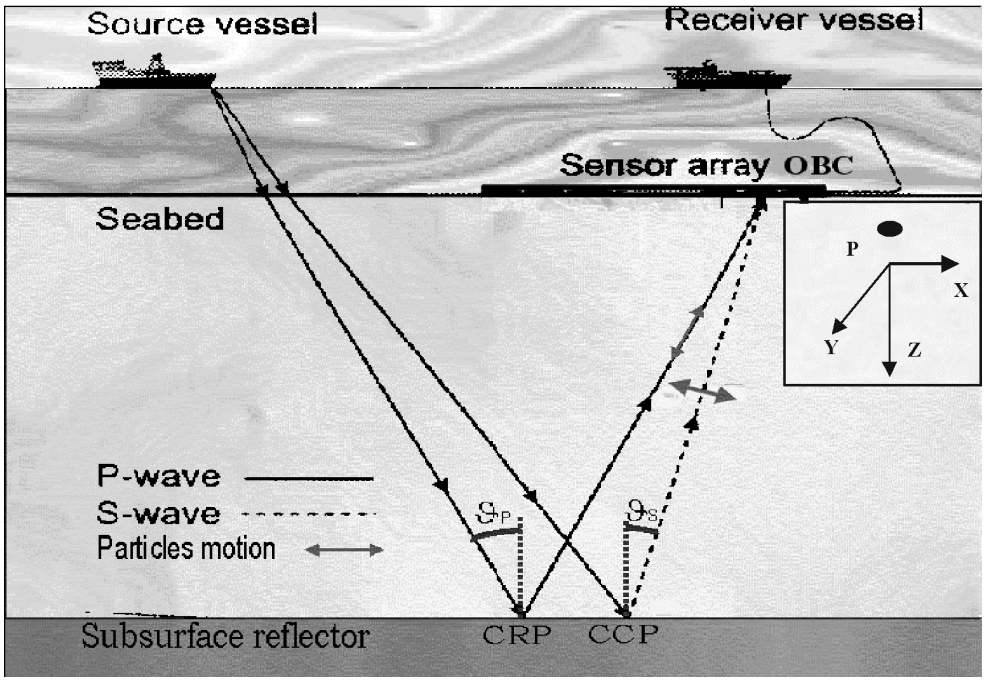


**Figure 1.1:** Schematic view of Ocean Bottom Cable acquisition

The receiver array is composed either of single nodes or, more often nowadays, of receivers contained in a cable, called an Ocean Bottom Cable (OBC), which is easier to move and deploy. Each receiver has four components: a hydrophone to record pressure and a three-component geophone, which records the movement of the sea-floor in three directions perpendicular to one another. The three directions of the geophone are oriented horizontally inline with the source and receiver plane, horizontally crossline to it, and vertically.

The P-P and the P-S converted waves tend to be normally separated. This phenomenon is due to the presence of a low velocity layer just below the water bottom. This layer causes the seismic rays to bend upward, closer to the vertical. This bending is stronger for the S-waves because they are slower, see Figure 1.2. So P-P-waves are recorded on both the hydrophone and, mostly, on the vertical component of the geophone and P-SV-converted waves are recorded in the in line horizontal components. In the presence of cross-dip P-SV waves can be recorded in the horizontal crossline component. If the velocity in the low velocity layer is not very

low, contamination of the different wave types can be found in the three components.

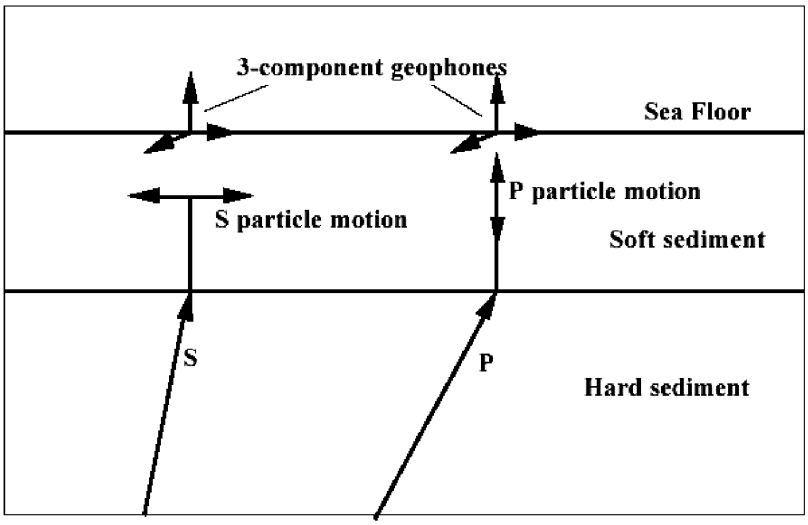


**Figure 1.2:** Effect of the low velocity layer on the P and S-wave raypaths.

In reality recording converted waves is more complicated. Full vector fidelity, in which each sensor inside the three-component package records the incoming wavefield without distortion and consistent with its vectorial nature (Reid and MacBeth, 2000) is rarely achieved, so that often we talk about "vector infidelity" (Dellinger et al., 2001). This infidelity includes problems with geophone orientation, gain and frequency mismatch and wave contamination. These problems can be due to the geophone itself, to the housing, to the coupling between geophone housing and sea-floor, and to the near-sea-floor conditions around the geophones (Dellinger et al., 2001). Different solutions to recover the fidelity have been proposed, among which: a more accurate geophone orientation (Li and Yuan, 1999), fidelity recovery filters (Gaiser, 1998, Dellinger et al., 2001), and deconvolution operators (Bagaini et al., 2000). In this thesis I do not deal with acquisition problems but I focus on processing issues instead.

The acquisition procedure for converted waves requires two vessels: a source vessel and a receiver vessel. The receiver vessel positions the cable and remains stationary while the source vessel shoots either parallel to the OBC or perpendicular

to it. At the end of the line the cable is moved and re-positioned. Clearly the acquisition speed is much lower than in conventional streamer marine acquisition, where the cables move with the boat during the shooting and there are not pauses in the proceedings. The slower speed of acquisition and the technology required for the OBC make converted wave recording more expensive than towed streamer acquisition, and to justify its use there has to be a need for S-wave information.

## 1.3. Use of C-waves, preview of recent work

Traditionally converted waves have been used in imaging zones in which P-wave surveys have not led to satisfactory results. This happens in two typical situations: imaging zones affected by gas clouds or in imaging so-called "transparent" reservoirs. The gas-cloud case was the main motivation for the first 4C surveys in the North Sea. As S-waves do not travel through fluids but only in the matrix of the rock, they are not greatly affected by the fluid-type present in the pore space. Instead when P-waves travel through gas they are distorted and are slowed down, creating the well-known effects of amplitude dimming and “pull-downs”. As gas clouds are often created by gas escaping from the reservoir, they can obscure the main area of exploration interest. Even in their first applications, with some basic processing, converted waves proved to be successful in the task of imaging gas affected areas.

A "pioneer" study was at the Tommeliten Alpha field, carried out by Statoil (Granli et al., 1999). The Tommeliten Alpha field is situated in the Norwegian sector of the North Sea, it has a salt diapiric structure and it is affected by a large gas chimney approximately 2 kilometres wide. The streamer data lack coherence inside the gas chimney. After some unsuccessful tests with P-waves, using long offsets to try to undershoot the chimney, it was decided to use converted waves. The processing applied was a conventional isotropic DMO and post stack migration flow (explained in detail in Chapters 2 and 5). The final converted wave image was of good quality and allowed a more detailed interpretation of the crest of the structure, see Figure 1.3.

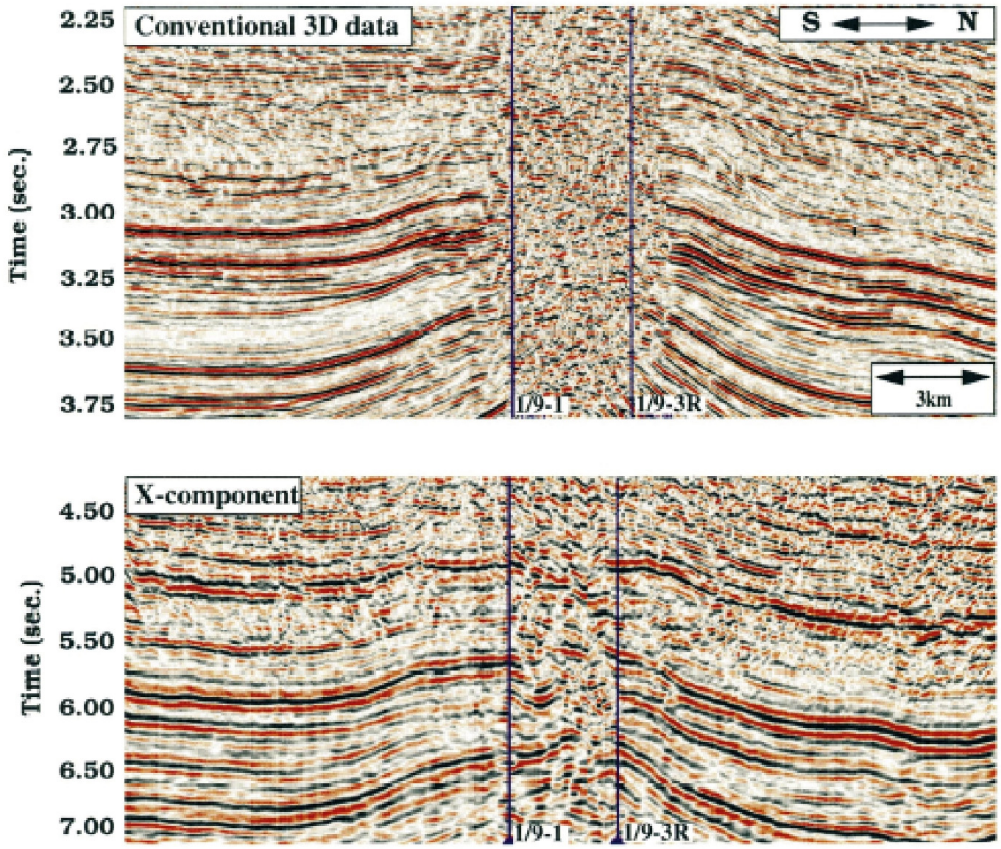


**Figure 1.3**: Tommeliten Alpha results, top: conventional 3D streamer data after migration (P-waves), bottom: inline component data after migration (C-waves). Note the improvement in the definition of the structure in the gas chimneys.

Other well-known successful cases of imaging in gas clouds are the Valhall field (Thomsen et al., 1997, Li et al., 2001), and the Lomond field (Pope et al., 2000).

The second situation in which converted waves proved advantageous is in areas of low P-wave and high S-wave acoustic impedance. Often sand-shale sequences are hard to image with P-wave data since the impedance contrast between them is commonly small. In some cases the S-wave acoustic impedance is much higher, producing a strong reflection. The best example comes from the Alba field (MacLeod at al., 1999). The Alba field is situated in the Central North Sea and the

reservoir consists of unconsolidated turbiditic channel sands sealed by shales. Intra-reservoir shales are sometimes present in the sand, producing high complexity in the reservoir structure. For further development of the field a very accurate map of the top of the reservoir was required. This was very difficult when P-waves were used, due to the low impedance contrast between the unconsolidated sands and the overlying shales. Results from dipole shear logs showed a large velocity contrast between the sands and shales. This information suggested using C-wave data. The final C-wave image showed clear improvements compared with the P-wave one. The improvements included: high amplitude top and base sand reflectors, presence of discontinuities, probably faults, in the sand reflectors and "wing" features in the top sand reflector at the channel edge, interpreted as post depositional deformation (MacLeod at al., 1999), Figure 1.4.

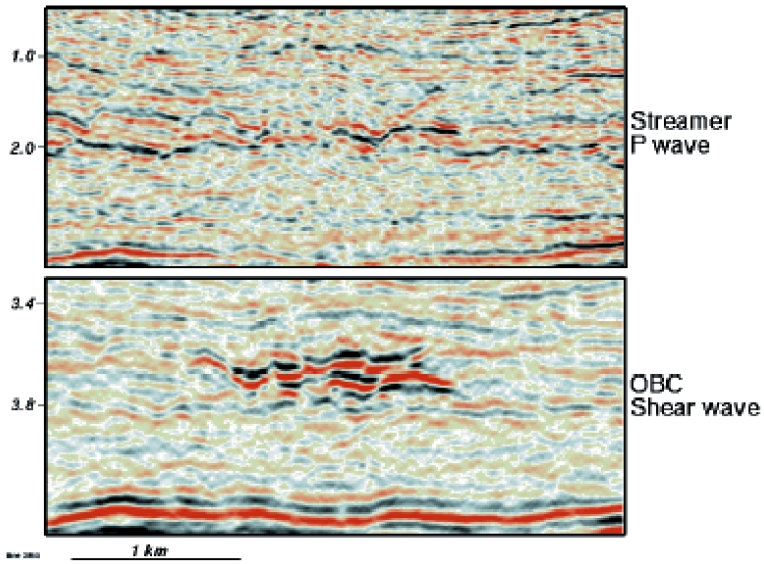


**Figure 1.4**: Alba field results, top: streamer data, bottom, inline component data from the OBC survey. The reservoir shows strong amplitude contrast in the OBC data.

C-waves have also been applied to sub-salt imaging with a good degree of success in the Gulf of Mexico, particularly in the Mahogany field (Kendall et al.,

1998). This result is believed to be due to the fact that the C-wave travel path offers better sub-salt illumination than the P-wave travel path. The authors were able to image accurately the top and bottom salt plus some events, which are potentially sub-salt reflectors.

It is still uncertain whether locally converted waves are able to image underneath the basalt. Hanssen et al. (2000) reached the conclusion that these waves are too weak and too difficult to use, but more recently Van der Baan et al. (2003) show some structures in the sub-basalt using locally converted waves isolated in the far-offset via the use of mutes in the x-t and $\tau$-p domain.

As mentioned before, using 3D 4C seismic data it is possible to extract fracture information. More specifically, analysis of shear wave splitting leads to fracture orientation (from the direction of the fast and the slow shear wave) and fracture density (from the time delay between the fast and the slow shear wave). There are several successful case studies on this topic, but I will not go into details of this practice since my Ph.D. project does not cover this topic. I limit the discussion to the mention of one example of this technique, the Emilio field, and the reason for it is that the results are quite convincing (and also is from my homeland) (Veltri et al., 2002, and Loinger et al., 2002).

The Emilio field is located in the Adriatic Sea, near the east coast of Italy, and the reservoir is composed of fractured carbonates. The purpose of the survey was to ascertain if information about fracture orientation and density from P-S converted waves ma*tc*hed the results from P-P azimuthal anisotropy. The data needed to be initially split to 8 azimuth volumes for the two main fracture trends. These volumes were processed independently and showed strong azimuthal anisotropic effects. When combined together into a single volume oriented as the dominant fracture direction a layer-stripping technique was applied for a final analysis of the fracture at the reservoir. The results showed the presence of two orthogonal fracture trends in good agreement with the well data, above all in the crest of the structure of the Emilio field, Figure 1.5.

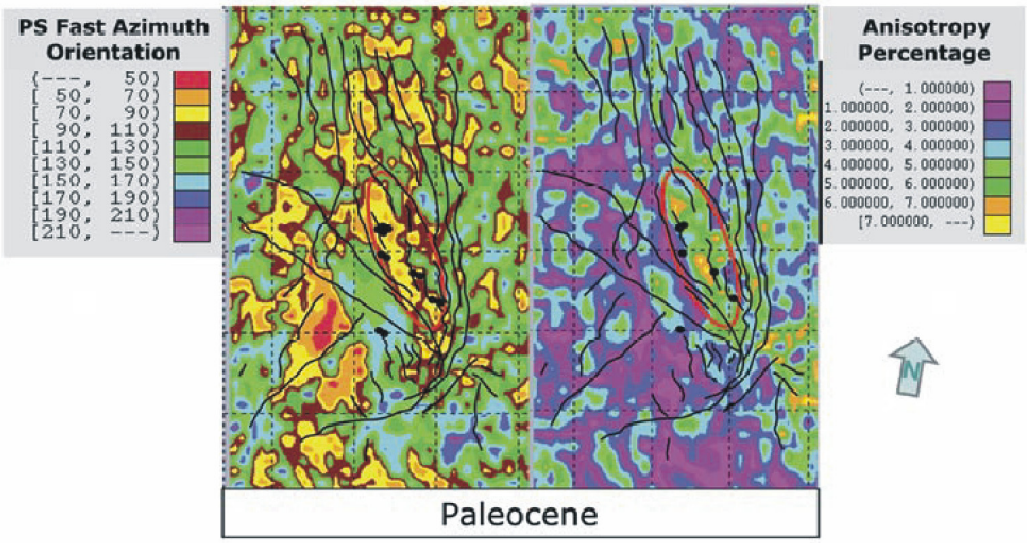


**Figure 1.5**: PS anisotropy maps at the reservoir, on the left the fracture orientation is shown, on the right the fracture density (as anisotropy percentage). The area circled in red is the crest of the Emilio Field, which shows higher anisotropy values and an orientation of N80.

The correlation with P-P azimuthal anisotropy is less convincing, with the presence of occasional discrepancy between seismic data and borehole information. Interestingly, locally well information agrees more with the P-S data than with the P-P data for the estimation of fracture orientation (Veltri et al., 2002). As seen, processing 3D 4C data for fracture detection requires many man-hours and computer power, due to the need to work in multiple azimuth volumes sometimes.

These examples mentioned above show the possible advantages in the use of multicomponent seismic data; nevertheless the technology is not yet widespread in the industry. The reason for that is mainly the high cost of acquisition and the complexity of the processing. Despite that, MacLeod et al. (1999) affirm that the total cost of the acquisition and processing for the 3D 4C Alba dataset was less than the cost of one trouble-free horizontal well. Unfortunately, since 1999, oil companies have limited their budget for exploration and have not invested heavily in this new technology offered by the seismic industry.

There is still high potential in this technique. It is believed that the real strength of multicomponent seismic data lies in the integration of P and S-wave

information. P and S-wave velocity ratios can be used for lithology discrimination and for fluid prediction, as shown, for example, by Garotta et al. (2002). Figure 1.6 shows schematically that shear wave velocities are required to discriminate different lithologies, Berg (1997). P-velocity on its own is not enough for distinguishing lithologies, for example a $v_p$ of 4000 m/s could indicate gas-bearing sandstones, brine-bearing sandstones or shales.

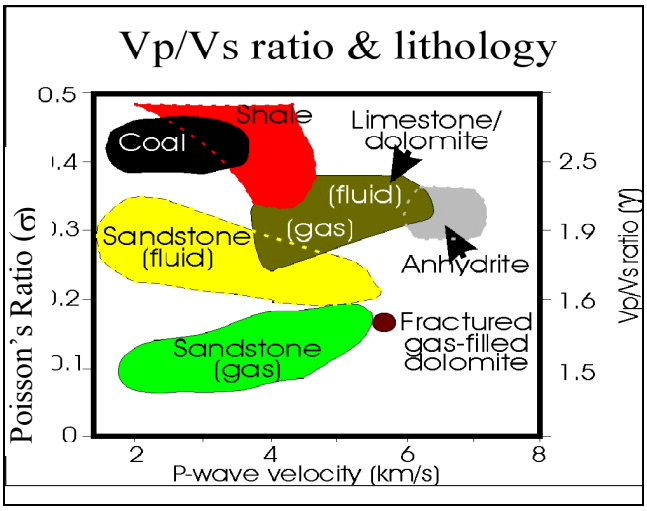


**Figure 1.6:** Schematic link between $v_p/v_s$ ratio and lithology, from Berg (1997).

The difficulty of this integrated data analysis comes from the fact that we do not acquire waves in pure S-mode but in converted mode. In order to extract the S-wave velocity some complex processing is required.

## 1.4. C-wave main processing problems

In the past few years better knowledge of P-SV wave behaviour has improved their acquisition, processing and their imaging capabilities. But still several issues need investigating. I have already mentioned the difficulties related to acquisition vector fidelity; here I focus on the main processing problems, which can be summarised as follow:

- Asymmetry of the ray path of C-waves;
- Event correlation in the P and C-sections;
- Effects of polar anisotropy.

The first issue, the asymmetry of the ray path, leads to the fact that even in horizontal layers the Common Mid Point (CMP) assumption is not valid and we have to sort the data in Common Conversion Point (CCP) order. Whilst the CMP position can be easily found as the mid-point between source and receiver positions, the CCP position is dependent upon both the geometry and the physical parameter $v_p/v_s$, the ratio between P and S-waves velocities, which is an unknown quantity at the beginning of processing.

The second issue is partially linked to the first one. To correlate events in P- and C-stacks it is necessary to have an estimation of the S vertical velocity, which is also required for lithology and fluid prediction. Only if we are certain to be looking at the same layer of rock can all the successive interpretations make sense. Event correlation is not a trivial issue. P-waves and C-waves have different arrival times and different frequency content (see Chapter 4), and sometimes events are imaged differently due to different reflection coefficients for the different wave-types, as in the case of the Alba field. In areas affected by gas, P-wave data often cannot be used with great accuracy. At this point in time I believe event correlation is the main obstacle to the widespread use of multicomponent seismic data for lithology and fluid prediction.

The final issue is the effect of polar anisotropy. The fact that the earth is seismically anisotropic, with different wave speeds for different directions of propagation, has been known for years. For P-wave processing the effects of anisotropy are often ignored; the advantages of the isotropic approximation at the price of some small positioning errors are considered worthwhile, at least when working in areas of limited structural complexity. In converted wave processing anisotropy is more difficult to ignore for two reasons: S-waves are more sensitive to the presence of polar anisotropy (Kristiansen et al., 2003) than P-waves and the effects of anisotropy are generally confined to the middle-to-far offset (distance between source and receiver) data, where the C-wave energy is the highest. In Chapter 2 I will

review the theory on anisotropy and in Chapter 9 I will show how to account for anisotropy in seismic processing.

## 1.5. Thesis objectives

The aim of this project is to improve the current knowledge and practice of converted wave processing in anisotropic media in the time domain. Throughout this thesis I use data from a 2D 4C seismic line acquired over the Lomond Field, in the Central North Sea, made available by BG Group, which is the CASE sponsor for this project. I prove here that this area is seismically anisotropic and that failure to take anisotropy into account during processing leads to poor converted wave imaging. I present a complex model-building scheme to estimate the parameters required in the anisotropic Pre-Stack Time Migration algorithm, which I use as imaging tool.

Apart from anisotropy, the basic parameters required in converted wave processing are the converted-wave stacking velocity based on non-hyperbolic moveout and different velocity ratios, such as the binning velocity ratio and the vertical velocity ratio. These parameters are extracted from analysis on asymptotically binned gathers, that is, gathers binned with a constant value of the velocity ratio $v_p/v_s$. I carried out a detailed sensitivity analysis which shows that, in areas affected by dip, the stacking velocity is sensitive to changes in the initial value of the asymptotic velocity ratio. Small velocity errors are propagated as the square in the re-calculation of the depth-variant velocity ratio and cannot be ignored. Velocity iterations may be necessary. The binning velocity ratio can also be derived using imaging criteria, that is, the symmetry in the positive and negative offset images. I show that this procedure provides a valid and velocity-independent estimate of the binning velocity ratio and should always be used in zones of complex geology.

The vertical velocity ratio is derived conventionally by event ma*tc*hing in the P-wave and converted wave stacks. I present an attempt to use well log derived velocity ratio to avoid this interpretative step. Velocity information from 4C seismic data and well logs shows some discrepancies, the $v_p/v_s$ extracted from the seismic data is around 30% higher. I analysed possible reasons including the effects of gas,

polar anisotropy and frequency-dependent dispersion. In the Lomond Field wells, gas shows little or no effect in the sonic log, probably due to the fact that the sonic tool is reading very close to the borehole wall where there is very little gas. The presence of polar anisotropy in deviated wells has a strong effect: it lowers the velocity ratio by about 15%. The effects of frequency-dependent dispersion are more difficult to quantify with accuracy. Residual errors in the seismic interpretation have also to be considered. Importantly, I prove that the ratio producing the best image is the one derived from seismic data, which suggests that the use of the raw well-log derived velocity ratio in multicomponent processing should be avoided.

I quantify anisotropy using an effective parameter, $\chi_{eff}$, which represents converted-wave anisotropy as a combination of P- and S-wave anisotropy. This parameter can be estimated from converted waves seismic data alone and I show two different ways of extracting it. This parameter is used in an anisotropic processing sequence based on Pre-Stack Time Migration (PSTM). This flow requires careful model building and allows updating in the time-migrated domain.

Comparing the values of the anisotropic parameter and of the binning velocity ratio before and after PSTM highlights the difference between the initial model and the updated model. Both are in fact sensitive to the presence of dip. Before PSTM a direct correlation between the presence of dips and the value of the anisotropic parameter is visible. After PSTM anisotropy is generally lower and the imprint of the geological structure is reduced, suggesting that part of the residual moveout attributed to anisotropy prior to PSTM may have been caused by dip. Similarly, the binning velocity ratio calculated after PSTM does not show areas of minimum present before PSTM and linked to apparent velocities in the dipping parts of the region. This analysis confirms the importance of defining the model in the time-migrated domain.

The PSTM image ma*tc*hes with a high degree of accuracy the geological interpretation carried out by geologists at BG Group. PSTM tests show that the inclusion of anisotropy allows the use of the full range of offsets, which is important to produce the correct image of the target area. I compare this result with the image obtained from a flow based on isotropic Dip Moveout (DMO) and post-stack

migration. Although this image is already an improvements compared with the P-data image in the gas-affected zone, differences in the position of the steep-dipping events and geological misties are evident in the post-stack migrated image. This mis-positioning is due to the isotropic approximation and to the limitation of the DMO and post-stack migration flow.

The necessity to include anisotropy is confirmed by an integrated analysis of local geology, well logs and seismic data. The Lomond Field overburden is mainly composed of finely laminated shales, a lithology believed to be a strong source of polar anisotropy. The image I obtained from the full Pre-Stack Depth Migration (PSDM) on P-P data reveals a depth misma*tc*h with the well markers. Since the events in the Common Reflection Point (CRP) gathers appear well flattened, proving that the velocity used is correct, the depth misma*tc*h has to be attributed to anisotropy. Other clear evidences of the presence of anisotropy come from well logs. P-velocity angular dependency is evident in sonic logs. Similar angular dependency of the velocity can also be observed comparing interval velocities and average velocities from well logs and check shots (assumed to be for vertical propagation) and seismic data (non-vertical propagation). These results leaves little doubt that the Lomond Field is seismically anisotropic.

## 1.6. Thesis structure

Following this introductory chapter, Chapter 2 gives a review of the main theories which have been proposed to deal with the complexity of converted wave analysis. In the same chapter I also discuss the best-known practices on converted wave processing. In Chapter 3 I present the data used throughout the thesis, and I give information on the acquisition techniques used.

In Chapter 4 I present details of the P-S-wave characteristics, such as amplitude behaviour, frequency content and other features that have to be taken into account when working jointly with P-P-wave data. This is followed by the analysis of the processing results, in Chapter 5, obtained using an isotropic sequence, which I label “conventional”, since it is often used by the main seismic contractors. Chapter 5

also contains initial analyses of some of the main parameters required in converted wave processing.

In Chapter 6 I investigate the possibility of using well log information to avoid the need of event correlation in order to extract the vertical velocity ratio, which is one of the required parameters. Chapter 7 deals with sensitivity analysis of the main processing parameters: converted wave stacking velocity, velocity ratios and the anisotropic parameter. I will show that the presence of dip plays a major role in parameter estimation.

In Chapter 8 I prove that the Lomond field is seismically anisotropic. Evidences come from well log information and combined analysis between them and seismic information. I also investigate the geological setting to show that in the Lomond field it is only natural to have seismic anisotropic effects, as the main sediments up to the reservoir level are shaly-mudstones. Chapter 9 is the natural follow up to Chapter 8, as I discuss how to include anisotropy in the processing sequence. I apply two different processing flows to the Lomond data: the more "conventional" DMO + Stack+ Migration and the full Pre Stack Time Migration. Results from each flow are then compared and analysed.

Finally in Chapter 10 I summarise, draw conclusions, and look at the road ahead.

# Chapter 2: Multicomponent processing - an overview

## 2.1. Introduction

This Chapter gives an overview of the main theories and practices in multicomponent processing. In the first part I review the main theories that have been developed to face the processing challenges of P-S converted waves. These are mainly the positioning of the conversion point and the necessity to use far offset traces, therefore needing a more accurate Normal Move Out (NMO) correction, which also takes into account the presence of polar anisotropy.

The first problem arises because P-SV converted wave propagation is not a pure mode. The wave propagates downward as a P-wave and upward as an S-wave. Due to Snell's law the S-leg of the raypath is reflected at a more acute angle than the downgoing P-leg, producing an asymmetric raypath. For processing purposes the consequence is that the Common Mid Point (CMP) approximation is not valid, Figure 2.1, even for horizontal layers. The location of the conversion point is defined by physical parameters as well as by the acquisition geometry.

Since converted energy is mostly contained in the middle-to-far offset traces, see Chapter 4, longer offsets need to be included in converted wave processing. Muting out this part of the data can cause the loss of valuable information. Adequate NMO corrections should be able to correct the medium and long offsets. Anisotropy contributes to causing residual moveout and it should be taken into account.

## 2.2. Theory: Isotropic media

### Conversion point: single layer

Figure 2.1 shows the geometry for a single converted wave raypath in a homogeneous, isotropic and horizontal layer. It is easy to see that the basic approximation used in P-wave processing, the CMP binning, is not valid in this case. The reason is that P-S waves have an asymmetric raypath. Due to the fact that the S-leg is slower than the P leg, the take-off angle of the S-wave is closer to the vertical and the CCP position is shifted towards the receiver. While the CMP position is only related to the acquisition geometry, the CCP position depends on the acquisition geometry and on a physical parameter, the ratio between P and S velocities, $v_p/v_s$, also called $\gamma$. This is one of the main difficulties in converted wave processing, since we do not know this value at the beginning of the processing. Nevertheless, if we want to perform conventional velocity analysis, we need a value for this velocity ratio to sort the data into CCP gathers.

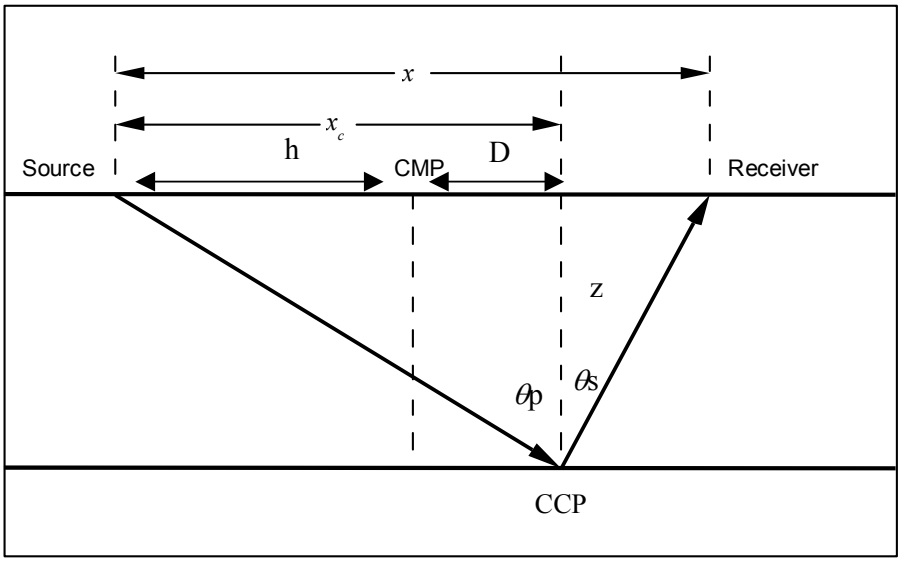


**Figure 2.1**: Geometry of a C-wave raypath for a single horizontal layer.

If we consider the single layer of Figure 2.1, $x_c$ is the CCP offset, $x$ is the source – receiver offset, $\theta_p$ is the P-wave angle of incidence, $t_p$ and $t_s$ are the P and S-wave traveltimes and $v_p$ and $v_s$ are the P and S velocities, then from trigonometry (Thomsen, 1999) we have:

$$x_c = v_p t_p \sin\theta_p \text{, and } x - x_c = v_s t_s \sin\theta_s, \qquad (2.1a), (2.1b)$$

and noting $\sin\theta_s / \sin\theta_p = v_s / v_p = 1/\gamma$ (Snell's law) leads to:

$$\frac{x_c}{x} = \frac{1}{1 + v_s^2 t_s / v_p^2 t_p} = \frac{1}{1 + \dfrac{t_s(x)}{\gamma^2 t_p(x)}}. \qquad (2.2)$$

If we take the limit for the vertical traveltime, zero-offset, then:

$$t_s(0)/t_p(0) = t_{s0}/t_{p0} = v_p/v_s = \gamma, \qquad (2.3)$$

where $t_{s0}$ and $t_{p0}$ are the vertical traveltimes for P and S waves, leaving:

$$x_c = \frac{\gamma}{1+\gamma} x. \qquad (2.4)$$

This is called the Asymptotic Conversion Point Position, ACCP. In practice converted wave data are binned initially with a depth constant value of $\gamma$, assuming that the ACCP position does not change with depth. This initial $v_p/v_s$ is often an educated guess since the ratio is rarely known in advance. Extra information from well logs and/or VSP, regional and (why not?) personal experience are often used.

Looking at the CCP trajectory in a multilayered case, Figure 2.2, we can appreciate the limitation of equation (2.4). In fact, as demonstrated by Figure 2.2, $v_p/v_s$ changes with depth. In a marine environment it is usually higher in the shallow part (sometimes up to 5), where sediments are unconsolidated and the S-waves are slower, and decreases with depth reaching values close to 2.

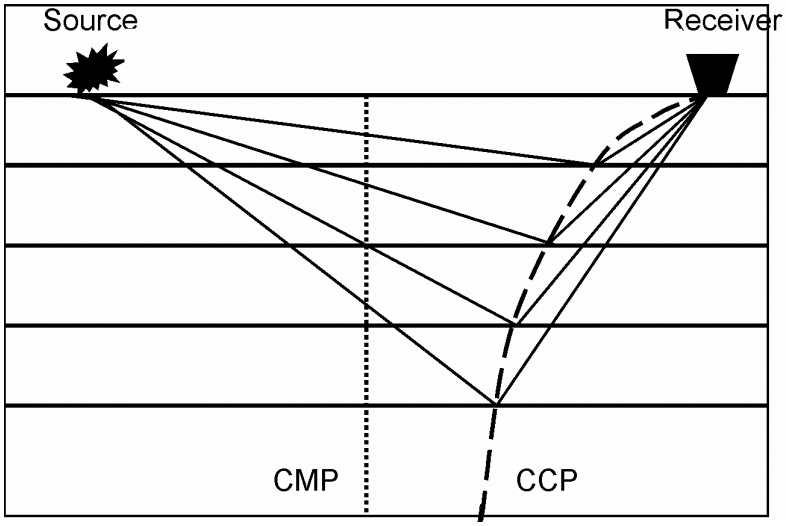


**Figure 2.2**: Geometry of C-wave raypaths for a multi-layer case.

A way of calculating a depth-variant conversion point position was proposed by Zhang (1992). They derived an iteration equation. Looking at Figure 2.1 for a single layer and noting that $\sin\theta_s = \frac{\sin\theta_p}{\gamma}$, and $\sin\theta_p = \frac{x_c}{\sqrt{z^2 + x_c^2}}$, the CCP offset $x_c$, can be derived from:

$$\left(x - x_c\right) = z\,tan\theta_s = \frac{zx_c}{\sqrt{\gamma^2\left(z^2 + x_c^{\,2}\right) - x_c^{\,2}}}. \tag{2.5}$$

so,

$$x = \frac{z x_c}{\sqrt{\gamma^2 \left(z^2 + x_c^{\,2}\right) - x_c^{\,2}}} + x_c, \tag{2.6}$$

which becomes the iteration equation :

$$x_c^{\,new} = \frac{\sqrt{\gamma^2 + \left(\frac{2 x_c^{\,old}}{z}\right)^2 \left(\gamma^2 - 1\right)}}{1 + \sqrt{\gamma^2 + \left(\frac{x_c^{\,old}}{z}\right)^2 \left(\gamma^2 - 1\right)}} x. \tag{2.7}$$

Starting with an initial value of $x_c$ [$x_c = x\gamma/(1+\gamma)$], the correct $x_c$ can be found very quickly with only a few iterations.

A different approach to Zhang is to search for the roots of the exact quartic equation of Tessmer and Behle (1988). For the geometry of Figure2.1 they started with the Snell's law by writing:

$$\frac{\sin^2 \theta_p}{v^2{}_p} = \frac{\sin^2 \theta_s}{v^2{}_s}, \tag{2.8}$$

we can also write Snell's law as :

$$\frac{1}{v^2{}_p} \frac{\left(\frac{x_c}{z}\right)^2}{1 + \left(\frac{x_c}{z}\right)^2} = \frac{1}{v^2{}_s} \frac{\left(\frac{x - x_c}{z}\right)^2}{1 + \left(\frac{x - x_c}{z}\right)^2}, \tag{2.9}$$

we can now substitute :

$$x_c = \frac{x}{2} + D, \tag{2.10}$$

where $D$ is offset of the CCP position from the CMP position.

From the geometry :

$$\sin\theta_p = \frac{h+D}{\sqrt{(h+D)^2+z^2}}, \tag{2.11}$$

$$\sin\theta_s = \frac{h-D}{\sqrt{(h-D)^2+z^2}}, \tag{2.12}$$

where $h$ is the source - midpoint distance.

After few substitutions and manipulations we can write the exact quartic equation, the roots of which give the value of $D$.

$$D^4 + (z^2 - \frac{x^2}{2})D^2 - z^2 x\left(\frac{\gamma^2+1}{\gamma^2-1}\right)D + \frac{x^2}{16}(x^2+4z^2) = 0. \tag{2.13}$$

Equation (2.10) and (2.13) are implemented in ProMAX.

For the same geometry, Thomsen (1999) proposed an approximation for the calculation of $x_c$, using a Taylor expansion of $x_c/z$ in terms of the ratio of the offset, $x$, to the depth of the reflector, $z$:

$$x_c(x,z) \approx x\left[C_0 + C_2(x/z)^2\right]. \tag{2.14}$$

This approximation is valid for small values of offset. The coefficient $C_0$ can be derived in the limit of equation (2.2) as $x \to 0$:

$$C_0 = \frac{\gamma}{1+\gamma}. \tag{2.15}$$

The term linear in $x/z$ is absent since there is no dip.

$C_2$ can be calculated as:

$$C_2 = \lim_{x/z\to 0}\left[\frac{d}{d(x/z)^2}(x_c/x)\right], \tag{2.16}$$
$$= \lim_{x/z\to 0}\left[\left(\frac{dp^2}{d(x/z)^2}\right)\frac{d}{dp^2}(x_c/x)\right],$$
$$= \lim_{x/z\to 0}\left[\frac{p}{x/z^2}\left(\frac{dp}{dx}\right)\frac{d}{dp^2}(x_c/x)\right],$$

where $p$ is the ray parameter, $p = \sin\theta_p / v_p + \sin\theta_s / v_s$, and
$p \to 0$ as $x/z \to 0$.
Knowing that (Snell's law) :

$$x = v_p t_p \sin\theta_p + v_s t_s \sin\theta_s = p v_p{}^2 t_p + p v_s{}^2 t_s, \tag{2.17}$$

then :

$$\lim_{x/z\to 0}\frac{x}{p}\left(\frac{dx}{dp}\right) = \lim_{x/z\to 0}\frac{x}{p}\left(\frac{x}{p} + p\frac{x}{dp}(v_p{}^2 t_p + v_s{}^2 t_s)\right), \tag{2.18}$$
$$= (v_p{}^2 t_{p0} + v_s{}^2 t_{s0})^2,$$
$$= z^2\left(v_p + v_s\right)^2.$$

Recalling equation (2.2) we can write :

$$\lim_{x/z\to 0}\frac{d}{dp^2}\left(x_c/x\right) = \left(\frac{v_p\sqrt{1-p^2 v_s{}^2}}{v_p\sqrt{1-p^2 v_s{}^2} + v_s\sqrt{1-p^2 v_p{}^2}}\right) = \frac{1}{2}\frac{v_p v_s(\gamma-1)}{(\gamma+1)}, \tag{2.19}$$

we can combine equations $(2.16)$ to $(2.19)$ to obtain $C_2$ as :

$$C_2 = \frac{\gamma(\gamma-1)}{2(\gamma+1)^3}. \tag{2.20}$$

To improve the accuracy of this equation for larger offset-to-depth ratio Thomsen (1999) also gave an empirically modified form of equation (2.14):

$$x_c(x,z) \approx x\left[C_0 + C_2 \frac{(x/z)^2}{(1 + C_3(x/z)^2)}\right]. \tag{2.21}$$

The coefficients $C_0, C_2$ stay the same and $C_3$ is given by :

$$C_3 = C_2/(1 - C_0). \tag{2.22}$$

For a single horizontal layer the accuracy of this equation is comparable with Tessmer and Behle (1988) exact equation. The advantage of using this approximation is that it easy to modify for more realistic cases of isotropic and anisotropic multi-layers. It is important to notice that all the equations presented so far require the knowledge of the reflector depth.

**Conversion point: Multilayer**

In a multilayered medium the depth is an unknown quantity at the beginning of the processing. In order to move to more realistic cases we have first to introduce different expressions for the velocity ratio. In fact in a layered medium P and S velocities depend on the direction of propagation and we can no longer use the generic parameter $\gamma$. Instead we have to consider different velocity ratios for the different directions of wave propagation. We define (Thomsen, 1999):

$$\gamma_0 = \frac{\overline{v}_{p0}}{\overline{v}_{s0}}, \tag{2.23}$$

as the ratio of the average vertical P and S velocities (with the subscript "$_0$" I will always indicate vertical directions).

With $\gamma_n$ we indicate the stacking velocity ratio given by:

$$\gamma_n = \frac{v_{pn}}{v_{sn}}, \tag{2.24}$$

$v_{pn}$ and $v_{sn}$ are the short spread (near offset) P and S NMO velocities (with the subscript "$_n$" I will always indicate NMO quantities).

Combining information about $\gamma_n$ and $\gamma_0$ it is possible to calculate a more accurate $\gamma$ for binning purposes, $\gamma_{eff}$. $\gamma_{eff}$ takes into account the layering effects (and therefore the anisotropy induced by the layering) and is given by (Thomsen, 1999):

$$\gamma_{eff} = \frac{\gamma_n^{\,2}}{\gamma_0}, \tag{2.25}$$

Using $\gamma_{eff}$, Thomsen (1999) modified the coefficients $C_0$ and $C_2$, to extend equation (2.21) to multilayered media. In this more realistic case $v_p$ becomes $v_{pn}$. $\gamma_0$ is linked to the vertical arrival times by this relation: $t_{c0}=t_{p0}+t_{s0}=t_{p0}(1+\gamma_0)$, so that:

$$v_{cn}^{\,2} = \frac{v_{pn}^{\,2}}{1+\gamma_0} + \frac{v_{sn}^{\,2}}{1+1/\gamma_0} = \frac{v_{pn}^{\,2}}{1+\gamma_0}\left(1+\frac{1}{\gamma_{eff}}\right). \tag{2.26}$$

This leads to:

$$x_c(x,z) \approx x\left[C_0 + C_2 \frac{\left(\frac{x}{t_{c0}v_{cn}}\right)^2}{\left(1+C_3(x/t_{c0}v_{cn})^2\right)}\right], \tag{2.27}$$

$$C_0 = \frac{\gamma_{eff}}{1+\gamma_{eff}}, \tag{2.28}$$

$$C_2 = \frac{\gamma_{eff}}{2\gamma_0}\frac{\left(\gamma_{eff}\gamma_0 - 1\right)}{(1+\gamma_{eff})^3}(\gamma_0+1), \tag{2.29}$$

$$C_3 = C_2/(1-C_0). \tag{2.30}$$

**Traveltime: single layer**

As for conventional P-wave processing, converted wave traveltime can be described as hyperbolic for small offset-to-depth ratio as a first approximation. Then in a single horizontal layer $t_{c(x)}$ can be found with:

$$t_c^{\,2} \approx t_{c0}^{\,2} + \left(\frac{x}{v_{cn}}\right)^2 , \tag{2.31}$$

with $t_{c0}$ as the vertical C-wave traveltime and $v_{cn}$ as the C-wave RMS velocity. Even for the simple case of a single horizontal layer, Yuan and Li (2001) found that this hyperbolic approximation is accurate only for offset to depth ($x/z$) ratios of less than 0.7.

There is a fundamental difference in amplitude behaviour between P and C-waves. For P-waves the reflected energy is confined mostly in the near offset region and for this reason the rest of the data are generally discarded via the use of a strong mute. In this case the hyperbolic approximation produces fairly accurate results. For C-waves, however, the middle-to-far offset traces are very important, since the converted energy is high in this part of the spread. So if we just mute these traces out, we lose valuable information, but, to be able to include them, more accurate moveout equations are required, as discussed in chapter 4.

If we consider equation (2.31) as a two-term Taylor expansion of $t^2$ versus $x^2$ (Tsvankin and Thomsen, 1994) we can expand it to a third term to improve accuracy:

$$t_c^{\,2}(x) = A_0 + A_2 x^2 + A_4 x^4 , \tag{2.32}$$

with

$$A_0 = t_{c0}^{\,2}, A_2 = \left.\frac{dt_c^{\,2}}{dx^2}\right|_{x=0}, A_4 = \frac{1}{2}\frac{d}{dx^2}\left(\frac{dt_c^{\,2}}{dx^2}\right)\Bigg|_{x=0} . \tag{2.33}$$

$A_4$ is then derived by finding the second derivative of $t_c^2$ with respect to $x^2$. For a single isotropic layer it reduces to (Tsvankin and Thomsen, 1994):

$$A_4 = \frac{-(\gamma - 1)^2}{4(\gamma + 1)^2 t_{c0}^2 v_{cn}^4}. \tag{2.34}$$

This third term however implies that $t_c^2$ depends on $x^4$. Considering that it should depend on $x^2$, Thomsen (1999) gave a modified expression for the C-wave traveltime:

$$t_c^2(x) = t_{c0}^2 + \frac{x^2}{v_{cn}^2} + \frac{A_4 x^4}{1 + A_5 x^2}, \tag{2.35}$$

here $A_4$ remain the same as (2.34). To calculate $A_5$ we consider that at very large offset-to-depth ratios $x_c$ approaches $x$ (see Figure 2.1 and 2.2). This means that the P-wave leg is nearly horizontal while the S-leg is almost vertical so that we can write (Thomsen, 1999):

$$\left(t(x) - t_{s0}\right)^2 = t^2 (1 - t_{s0}/t)^2 \approx const. + x^2 / v_p^2, \tag{2.36}$$

with $v_p$ equal to the P - wave velocity.

Linearizing $t^2$ in the small quantity $t_{s0}/t$, the linear term becomes negligible compared to $x^2$. Then if we set expression (2.36) equal to (2.35) and we get:

$$t^2(x) \to t_0^2 + x^2 / v_{cn}^2 + \frac{A_4 x^2}{A_5} \approx const. + x^2 / v_{ph}^2, \tag{2.37}$$

and, identifying the constant as $t_0^2$,

$$A_5 = \frac{A_4}{\left(\frac{1}{v_{ph}^2} - \frac{1}{v_{cn}^2}\right)}. \tag{2.38}$$

The third term is the one responsible for the medium-to-far offset moveout. Equation (2.35) is strictly valid for a single, horizontal, isotropic layer. One may notice in fact that the velocity ratio in this equation is not the effective velocity ratio.

**Traveltime: multilayer**

The multilayered case will be discussed in the next section, together with the anisotropic case.

## 2.3. Theory: Anisotropic media

Winterstein (1990) defines anisotropy as the "variation of one or more properties of a homogeneous material with direction". In our context we are interested in the variation of seismic velocities with direction.

For pure processing convenience the earth is generally assumed to be isotropic, which, more often than not, is a false assumption. Although this has been known for decades, it was with the advent of converted waves that the topic was given full attention by the oil and gas industry. The reason for this is the high sensitivity of shear waves to polar anisotropy.

Anisotropy needs to be considered during different processing steps: NMO correction, migration and CCP positioning. Ignoring the effects of anisotropy in areas with little structural complexity leads to only small positioning errors. But in complex areas, when the velocity model needs to be extremely accurate, isotropic processing causes considerable errors. (Alkhalifah and Larner, 1994). Anisotropy has also a strong influence on AVO analysis; isotropic processing can in fact create false structures or change the AVO slope (Chen and Castagna, 2000).

Nowadays maximum accuracy is required from seismic processing. More effort has been put into understanding how to be able to process accurately in an anisotropic medium. For its relative simplicity and abundant occurrence in marine sediments, the anisotropic geometry mostly treated is Vertical Transverse Isotropy,

VTI, also called Polar Anisotropy. A VTI medium has a vertical axis of symmetry and in such a medium the velocity does not vary in the horizontal plane. So the horizontal velocity is different from the vertical velocity. The stacking velocity is somewhere in between the horizontal and the vertical velocities.

Even though the exact causes of polar anisotropy are still debated, we can indicate mineral orientation as the main cause of *intrinsic* anisotropy. Fine layering (in which the layer thickness is smaller than the wavelength) is also believed to be a source of anisotropic effects. This is called *extrinsic* anisotropy. For this reason anisotropy is often found to be high in clay-rich sediments such as shales.

Recently more geometries have been studied: Horizontal Transverse Isotropy, HTI, and Tilted Transverse Isotropy, TTI, where the axis of symmetry is tilted. Mathematically VTI and HTI media are easier to treat. A VTI media can be described using a matrix of elastic constants $C_{ij}$:

$$\begin{pmatrix} C_{11} & C_{11}-2C_{66} & C_{13} & & & \\ C_{11}-2C_{66} & C_{11} & C_{13} & & & \\ C_{13} & C_{13} & C_{33} & & & \\ & & & C_{44} & & \\ & & & & C_{44} & \\ & & & & & C_{66} \end{pmatrix}$$

In an isotropic medium we can write the matrix in terms of Lame's constants:

$$\begin{pmatrix} \lambda+2\mu & & & & & \\ & \lambda+2\mu & & & & \\ & & \lambda+2\mu & & & \\ & & & \mu & & \\ & & & & \mu & \\ & & & & & \mu \end{pmatrix}$$

and

$$Vp = \sqrt{\frac{\lambda+2\mu}{\rho}}, \tag{2.39}$$

$$Vs = \sqrt{\frac{\mu}{\rho}}. \tag{2.40}$$

For practical use, it is convenient to express anisotropy using the parameters ε, δ and γ′ (Thomsen, 1986). γ′ is not to be confused with the velocity ratios. The Thomsen's parameters are a combination of elastic moduli $C_{ij}$ as shown in equations (2.41, 2.42, 2.43) and they are dimensionless:

$$\varepsilon = \frac{C_{11} - C_{33}}{2C_{33}} \approx \frac{v_p(90) - v_p(0)}{v_p(0)}, \tag{2.41}$$

$$\gamma' = \frac{C_{66} - C_{44}}{2C_{44}} \approx \frac{v_{sh}(90) - v_{sh}(0)}{v_{sh}(0)}, \tag{2.42}$$

$$\delta = \frac{(C_{13} + C_{44})^2 - (C_{33} - C_{44})^2}{2C_{33}(C_{33} - C_{44})}. \tag{2.43}$$

with $v_p(0)$ P-wave vertical velocity, $v_p(90)$ P-wave horizontal velocity, $v_{sh}(0)$ SH-wave vertical velocity, and $v_{sh}(90)$ SH-wave horizontal velocity.

Figure 2.3 shows snapshots of a wavefront travelling in an isotropic medium, left, and in a non-specified anisotropic medium, right (courtesy of Enru Liu). We can notice that the wavefront in the anisotropic case no longer describes a circle (in 2D), but has a more elliptical shape, with the horizontal direction faster than the vertical. Figure 2.4, from Thomsen (1986), schematically shows a wavefront in two particular cases of seismic anisotropy. The top part is for $\delta = \varepsilon$ and $\delta$ positive, in which the

wavefront is elliptical. The NMO velocity is higher than the vertical velocity. The bottom part shows a more complex wavefront, for $\delta \neq \varepsilon$ and $\delta$ negative. This time the NMO velocity is less than the vertical velocity. These examples are not very common in nature; usually in fact $\varepsilon$ is bigger than $\delta$, and $\delta$ is very often positive (Wang, 2001).

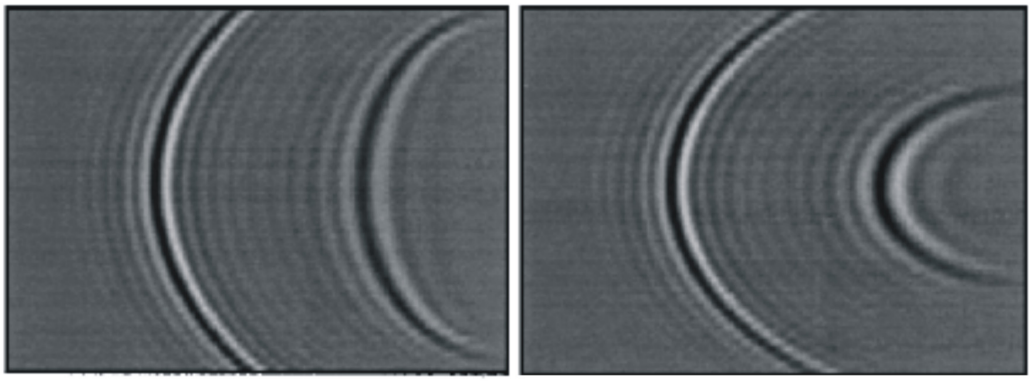

**Figure 2.3:** Snapshots of wavefront travelling in an isotropic medium, left, and in a non-specified anisotropic medium, right. In 2D the wavefront describes a circle in the isotropic case, while it deforms into a more elliptical shape in the anisotropic medium.

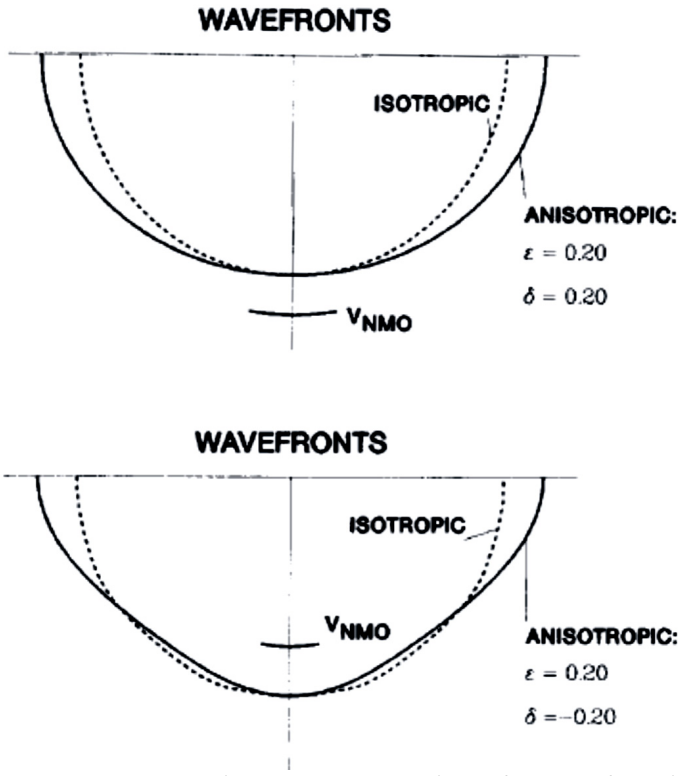


**Figure 2.4**: Top: anisotropy propagation of a wavefront in a polar anisotropic media when $\delta = \varepsilon$ and $\delta$ is positive, elliptical wavefront. Bottom: a more complex wavefront, for $\delta \neq \varepsilon$ and $\delta$ negative.

$\varepsilon$ refers to the degree of P-wave anisotropy, $\gamma'$ to the degree of S-wave anisotropy and $\delta$ relates to the wavefront ellipticity. $\delta$ is also called the P-wave depthing parameter (Audebert et al., 1999), as it is responsible for the correct depth-positioning of P-waves. When $\varepsilon$ and $\delta$ are both less than 0.2 the medium is considered weakly anisotropic (Thomsen, 1986). Most marine sediments show weak anisotropy (Wang, 2001).

For processing convenience a new parameter, σ, was introduced by Tsvankin and Thomsen (1994):

$$\sigma = \left( \frac{v_{p0}}{v_{s0}} \right)^2 (\varepsilon - \delta), \tag{2.44}$$

and used to define NMO velocities. For a single horizontal layer:

$$v_{pn}^{\ 2} = v_{p0}^{\ 2}(1+2\delta), \tag{2.45}$$

$$v_{sn}^{\ 2} = v_{s0}^{\ 2}(1+2\sigma). \tag{2.46}$$

$\sigma$ expresses the difference between the vertical, $v_{s0}$, and the NMO, $v_{sn}$, velocities for shear waves as $\delta$ does for P-waves. As these two parameters are usually positive in marine sediments, the NMO velocity is very often higher than the vertical one.

Going back to the long offset moveout correction problem, Thomsen (1999) modified the coefficients $A_4$ and $A_5$ of equation (2.35) to express the C-wave traveltime in a layered anisotropic media as:

$$t_c^{\ 2}(x) = t_{c0}^{\ 2} + \frac{x^2}{v_{cn}^{\ 2}} + \frac{A_4 x^4}{1+A_5 x^2}, \tag{2.47}$$

$$A_4 = \frac{\dfrac{-1}{(\gamma_{eff}+1)^2}\left[2\eta\dfrac{(\gamma_0^{\ 2}-1)}{\gamma_0}\gamma_{eff}^{\ 2} + \dfrac{(\gamma_n^{\ 2}-1)^2}{4(\gamma_0+1)}\right]}{v_{cn}^{\ 2} t_{c0}^{\ 2}}, \tag{2.48}$$

$$A_5 = \frac{-A_4 v_{cn}^{\ 2}}{1-\dfrac{v_{cn}^{\ 2}}{v_{pn}^{\ 2}(1+2\eta)}}. \tag{2.49}$$

He uses a new parameter here, $\eta$, originally described by Alkhalifah and Tsvankin (1995) as a combination of the two Thomsen's parameters $\varepsilon$ and $\delta$:

$$\eta = \frac{\varepsilon-\delta}{1+2\delta}. \tag{2.50}$$

Although equation (2.47) offers a big improvement over the hyperbolic approximation, recently more studies have tried to improve on its accuracy for larger offset-to-depth ratios (the accuracy analysis for this equation will be presented in the next paragraph). Li and Yuan (2001) decided to use more complex anisotropic

parameters, all derived by combinations of the former parameters. They introduced $\zeta$ and $\chi$, which, for a single VTI layer, are defined as:

$$\zeta = (\gamma_n^{\,2} / \gamma_0^{\,2})\,\eta = \gamma_{eff}^{\,2}\,\eta, \tag{2.51}$$

$$\chi = \gamma_0 \gamma_{eff}^{\,2}\,\eta - \zeta = (\gamma_0 - 1)\,\gamma_{eff}^{\,2}\,\eta, \tag{2.52}$$

where $\zeta$ is to be considered the S-wave anisotropic parameter while $\chi$ is the C-wave anisotropic parameter. To include the effects of layering, they introduced the effective values of $\zeta$, $\chi$ and $\eta$. In the following equations the suffix $i$ indicates interval quantities:

$$\eta_{eff} = \frac{1}{8 t_{p0} v_{pn}^{\,4}} \left( \sum v_{pni}^{\,4} (1 + 8\eta_i) \Delta t_{p0i} - t_{p0} v_{pn}^{\,4}, \right) \tag{2.53}$$

$$\zeta_{eff} = \frac{1}{8 t_{s0} v_{sn}^{\,4}} \left( t_{s0} v_{sn}^{\,4} - \sum v_{sni}^{\,4} (1 + 8\zeta_i) \Delta t_{s0i} \right), \tag{2.54}$$

$$\chi_{ef} f = \eta_{eff} \gamma_0 \gamma_{eff}^{\,2} - \zeta_{eff}. \tag{2.55}$$

where $\Delta t_{p0i}$ and $\Delta t_{s0i}$ are the vertical traveltimes in the $i$-th layer for P and S-waves.

Interestingly these parameters do not vanish in a layered isotropic medium; instead they describe the anisotropic effects induced by layering alone. Using $\chi_{eff}$, Li and Yuan (2001) re-wrote coefficients $A_4$ and $A_5$ for the moveout equation:

$$t_c^{\,2}(x) = t_{c0}^{\,2} + \frac{x^2}{v_{cn}^{\,2}} + \frac{A_4 x^4}{1 + A_5 x^2}, \tag{2.56}$$

$$A_4 = \frac{(\gamma_0 \gamma_{eff} - 1)^2 + 8(1 + \gamma_0)\,\chi_{eff}}{4\, t_{c0}^{\,2} v_{cn}^{\,4} \gamma_0 (1 + \gamma_{eff})^2}, \tag{2.57}$$

$$A_5 = \frac{A_4 v_{cn}^{\,2} (1 + \gamma_0)\,\gamma_{eff} [(\gamma_0 - 1)\,\gamma_{eff}^{\,2} + 2\,\chi_{eff}]}{(\gamma_0 - 1)\,\gamma_{eff}^{\,2} (1 - \gamma_0 \gamma_{eff}) - 2(1 + \gamma_0)\,\gamma_{eff}\,\chi_{eff}}. \tag{2.58}$$

Equation (2.56) is dependent upon four parameters: $v_{cn}$, $\gamma_0$, $\gamma_{eff}$ and $\chi_{eff}$, and these are the new basis used in this thesis for anisotropic processing, see Chapter 9.

Going back to the conversion point computation, using these new anisotropic parameters, Li and Yuan (2001) were able to extend Thomsen's formulation to anisotropic and layered media:

$$x_c(x,t) \approx x\left[C_0 + \frac{C_2 x^2}{(1 + C_3 x^2)}\right], \tag{2.59}$$

$C_0$ and $C_3$ remain as defined in (2.28) and (2.30).
$C_2$, on which $C_3$ depends, takes the value:

$$C_2 = \frac{1}{2t_{c0}^{\ 2} v_{cn}^{\ 2}} \frac{\gamma_{eff}(1+\gamma_0)}{\gamma_0(\gamma_{eff}+1)^3}\left[\left(\gamma_0\gamma_{eff} - 1\right) + 8(\eta_{eff}\gamma_{eff}\gamma_0 + \zeta_{eff})\right] \tag{2.60}$$

## 2.4. Accuracy analysis

It is important to verify the accuracy for the different equations introduced in the previous paragraph. I present here a synthetic study carried out by Li and Yuan (2001) using a model composed of three horizontal layers. The materials used were Dog Creek Shale, Limestone Shale and Taylor Sandstone, in this order, each 500 metres thick. They compare the accuracy of the Thomsen's expression and Li and Yuan's equation, both for the moveout correction and the CCP computation. Table 2.1 summarises the parameters for the three materials.

| **Material** | $v_{p0t}$ | $v_{s0i}$ | $\varepsilon_i$ | $\delta_i$ | $v_{cn}$ | $\eta_{eff}$ | $\zeta_{eff}$ |
|---|---|---|---|---|---|---|---|
| Dog Creek Shale | 1875 | 826 | 0.225 | 0.100 | 1541 | 0.104 | 0.154 |
| Limestone Shale | 3306 | 1819 | 0.134 | 0.000 | 2047 | 0.187 | 0.130 |
| Taylor Sandstone | 3368 | 1829 | 0.110 | -0.035 | 2264 | 0.187 | 0.119 |

**Table 2.1:** Synthetic model used in accuracy test

The residual moveout is calculated as:

$$\Delta t = t_c^{(exact)} - t_c^{(approx)}, \tag{2.59}$$

and the exact traveltime was computed using ray tracing. The results for the traveltime computation, Figure 2.5, show that the Thomsen's expression (2.47) is accurate for offset-to-depth ratios up to 1.0 for the three reflectors while Li and Yuan's equation (2.56) is accurate for offset-to-depth twice as big.

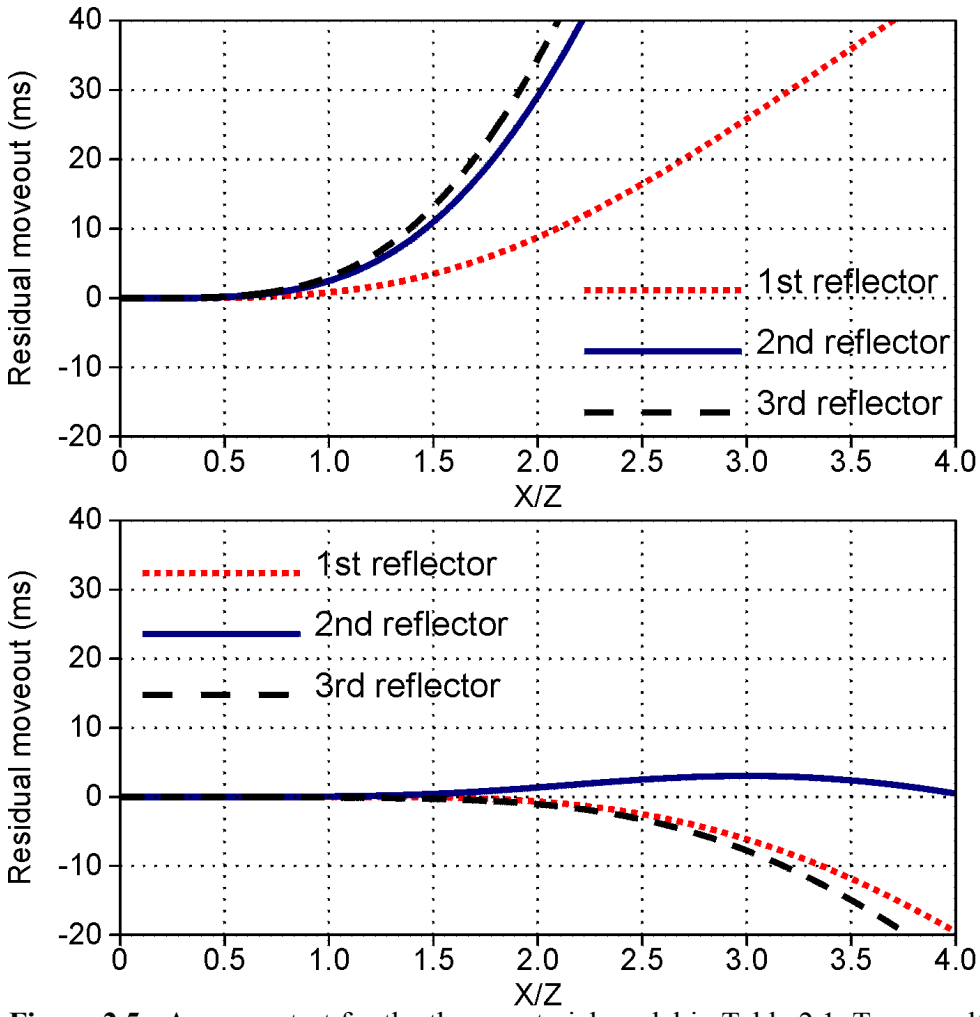


**Figure 2.5**: Accuracy test for the three-material model in Table 2.1. Top: results for equation (2.47). Bottom: for equation (2.56).

Figure 2.6 shows instead the results of their analysis for the CCP position; the relative error is given by:

$$\frac{x_c^{(exact)} - x_c^{(approx)}}{x}. \tag{2.60}$$

Again, the exact CCP position was calculated using ray tracing. The top part of Figure 2.6 shows the accuracy for Thomsen's (1999) expression (2.27), and, at the bottom, the accuracy of Li and Yuan (2001) equation (2.59). The first equation is

accurate for offset-to-depth ratio up to 0.5 only, while the second shows great accuracy for offset-to-depth ratio up to 3.0.

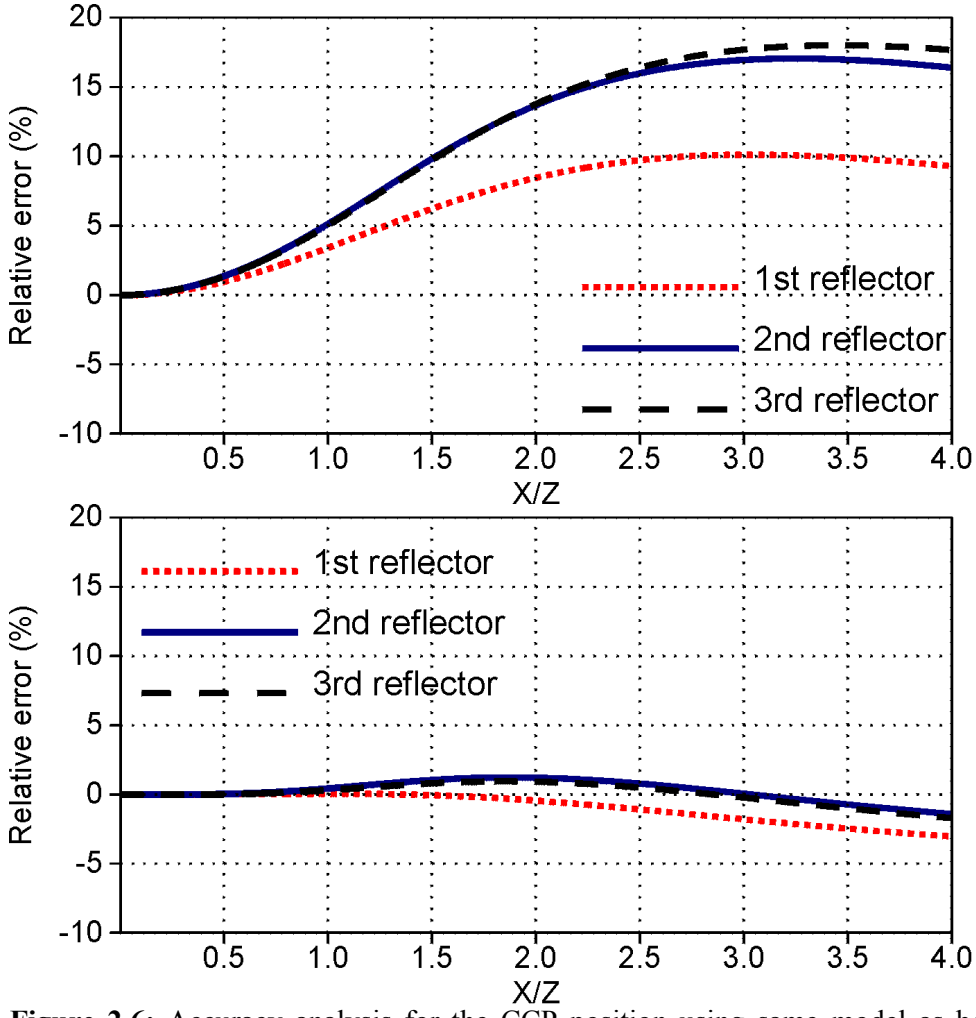


**Figure 2.6:** Accuracy analysis for the CCP position using same model as before. Top: equation from Thomsen (1999). Bottom: equation from Li and Yuan (2001).

## 2.5. Practice

### "Conventional" approach to multicomponent processing

It is not easy to define a "conventional" approach to multicomponent seismic processing. In recent years a lot of effort has been put into this topic. Main geophysical contractors, oil companies and academia are constantly proposing new flows. However, in practice we can narrow it down to three sequences, two in the time domain ((1) DMO+Post Stack Migration and (2) Pre Stack Time Migration, PSTM) and one in the depth domain (Pre Stack Depth Migration, PSDM). These three sequences, in this order, represent an increase in complexity and processing costs, so although PSDM guaranties the highest accuracy (provided the input parameters are correct), it also very time consuming and on this basis it is not always preferred. In this thesis I am interested in time domain imaging so I will not go into details of the PSDM.

When working with converted waves the conventional flows used for P-waves have to be modified accordingly. We have already mentioned the main processing problems that have to be dealt with. The first flow I present here is DMO+Migration, used by some contractors for routine processing, Figure 2.7. The blue boxes represent the processing steps, while in yellow I indicate the necessary parameter inputs. The orange box shows where P-wave information is needed.

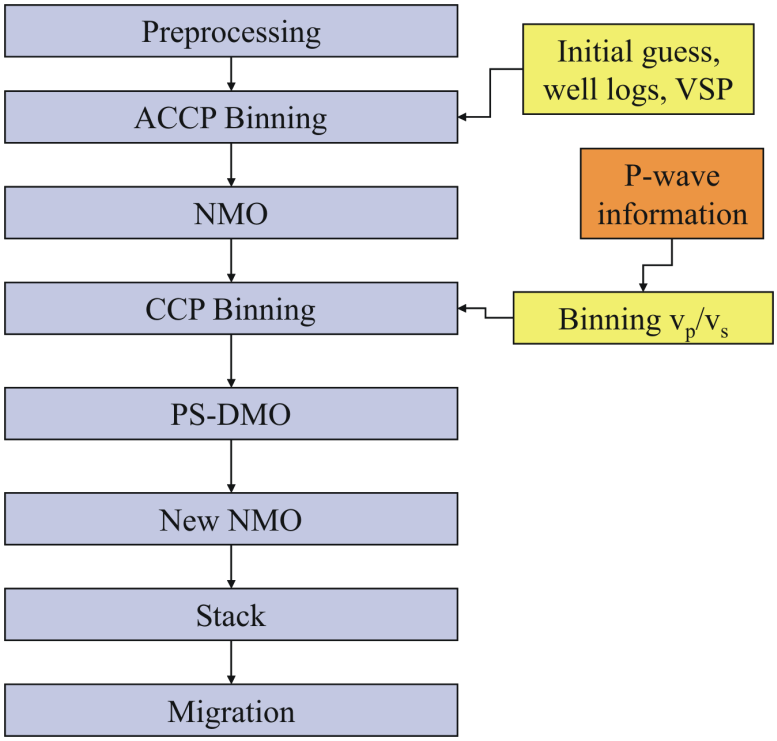


**Figure 2.7:** A generic DMO+Migration processing flow for C-waves. It follows in principle a P-wave processing flow. The difference is in the CCP binning, which requires careful analysis of the velocity ratio $v_p/v_s$. The initial Asymptotic Conversion Point binning (ACCP) is performed using a depth constant $v_p/v_s$.

The preprocessing step is not very different from P-waves, with the exception of the receiver static correction, needed to correct for the presence of statics due to variable low velocity shear wave propagation in a layer at the water bottom. Asymptotic Conversion Point (ACCP) binning is required to use C-wave data for velocity analysis and brute stack and it is based on an educated guess, using well logs and *VS*P information to estimate a depth-constant velocity ratio.

To find the depth-variant binning velocity ratio, different companies use different schemes. Granli et al. (1999) applied $\gamma_0$ from event correlation. I will show in Chapter 5 that this choice is too simplistic for anisotropic layered media. A more accurate way to estimate $v_p/v_s$ for binning purposes is to exploit velocity information (Thomsen et al., 1997). In this case event correlation is still needed, since $\gamma_0$ is required to calculate the effective velocity ratio, $\gamma_{eff}$. Other approaches include: a

correlation-based average $v_p/v_s$ analysis (Van Dok and Gaiser, 2001), working on imaging principles (Audebert et al., 1999), and using borehole information (Leaney et al., 2001). $v_p/v_s$ estimation is one of the most important processing steps.

Dip Moveout (DMO) correction follows CCP binning. For C-waves the DMO operator has to account for the CCP trajectory. The DMO ou*tp*ut data are free of conflicting dip problems (events and diffractions with same arrival time for example) and are more suited for a finer velocity analysis. Inverse NMO is applied, followed by new velocity analysis. The data are then NMO corrected and stacked. The final step is post stack Migration. Yilmaz (2000) states that, for P-waves, the DMO+Migration sequence is equivalent to PSTM. In his Ph.D. thesis Harrison (1992) proves that also for C-waves the same sequence can be considered an equivalent of a PSTM.

Figure 2.8 shows instead a PSTM processing flow. For C-waves PSTM has the advantage of not requiring CCP binning. It is more expensive though, and usually requires a more accurate model building. For C-waves this means not only an accurate migration velocity but also the knowledge of several velocity ratios and anisotropic parameters, if the algorithm can handle anisotropy. This model building is the real complexity of the flow, which, otherwise, looks simpler than the DMO+Migration sequence. Model updating is carried out removing the NMO from the Common Image Points, similarly to the post DMO velocity analysis, see Chapter 5 and 9.

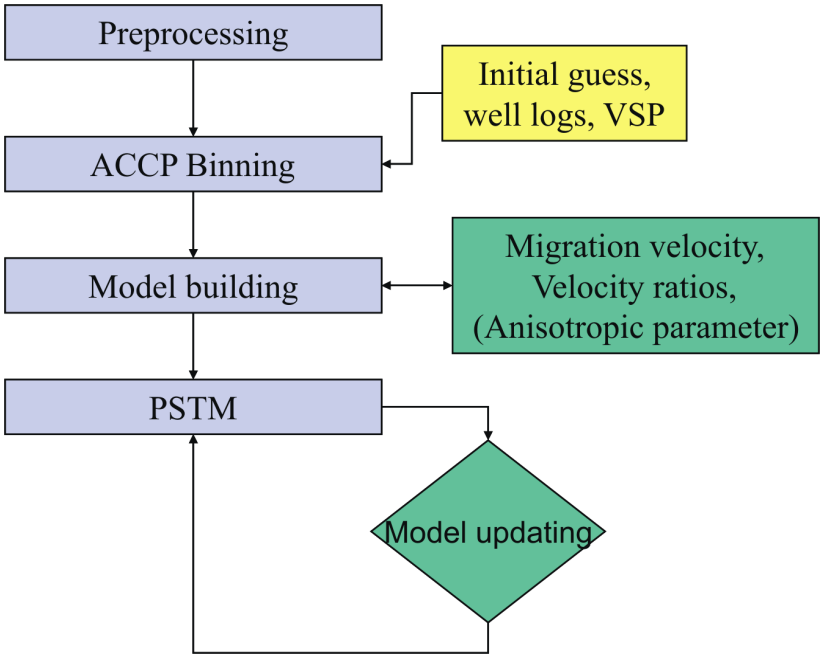


**Figure 2.8:** A generic PSTM processing flow. The difficulty in this kind of flows lies in the model building part.

Using 4C data from the Lomond field I use two versions of the flows shown above. In Chapter 5 I process the data through the DMO+Migration sequence, because it is easy to apply, is fast and requires fewer parameters than the PSTM sequence. At this stage anisotropy is not included in the processing. In Chapter 9 I show the results of the same sequence when anisotropy is accounted for in the NMO stages. Finally, again in Chapter 9, I present the results from an anisotropic PSTM, and I compare them to the two previous results. Details on the parameter estimation are discussed in Chapter 5, 6 and 7.

## 2.6. Conclusions

I presented here the main theories which have been developed in the last ten years or so, to increase the accuracy of converted wave processing. Due to their very nature, C-waves have to be treated differently from P-waves. The fact that they are not a pure propagation mode leads to the issue of the asymmetric raypath. This is a

major complication for seismic processing. The usual CMP assumption cannot be used and we need to search for the CCP position. This position is determined not only by the geometry of the acquisition but also by the velocity ratio $v_p/v_s$.

Converted energy is high in the middle-to-far offset traces. To include them during processing more accurate NMO equations have been developed in recent years. C-waves are also sensitive to the presence of polar anisotropy. The most common anisotropy encountered in seismic processing is VTI. In a VTI medium the horizontal velocity differs from the vertical velocity. This has an effect on the velocity ratio and therefore on CCP binning. Anisotropy is also a cause of residual moveout at far offsets.

Equations to account for the presence of VTI for CCP positioning and NMO correction have been presented. I showed that, for the NMO correction, the accuracy has been greatly improved compared with the hyperbolic approximation used conventionally. In fact while the latter is accurate only for offset-to-depth ratio up to 0.7, Li and Yuan's equation is accurate for offset-to-depth ratio up to 2.0. We are also now able to calculate the CCP position in anisotropic layered media with good accuracy for offset-to-depth ratio up to 3.0

Processing C-waves presents several challenges. Geophysical contractors, oil companies and academic groups have proposed different approaches; I presented here two generic flows in the time domain. They summarise recent practices in C-wave processing. The simpler one is the DMO+Migration sequence, while the more complex is the PSTM flow. I apply both sequences to a 2D 4C line acquired over the Lomond field. The results from the first flow are presented in Chapter 5, while the results from the PSTM are shown in Chapter 9.

# Chapter 3: Study area and data acquisition

## 3.1. Introduction

This Chapter is a brief introduction to the study area and to the datasets used throughout this thesis. The study area is the Lomond Field, in the Central North Sea, a gas condensate field with interesting geological structure and challenging imaging problems, which are the motivation for the use of multicomponent technology. Clearly the main dataset analysed is the 4 Component 2D seismic line, but well logs and check shots are also used, as described Chapter 6 and Chapter 8.

I give here a detailed overview of the multicomponent data acquisition technique, focusing on the Lomond acquisition carried out by WesternGeco in 1998. I also introduce the principles of well log acquisition, focusing on the velocity logs, both for compressional and shear velocity.

## 3.2. Lomond Field

The Lomond field is a gas-condensate field situated at 233 kilometres east of Aberdeen, in the Central North Sea, Block 23/21. It is close to the border between the UK and the Norwegian sectors on the east flank of the Central Graben, as seen in the red rectangle in Figure 3.1.

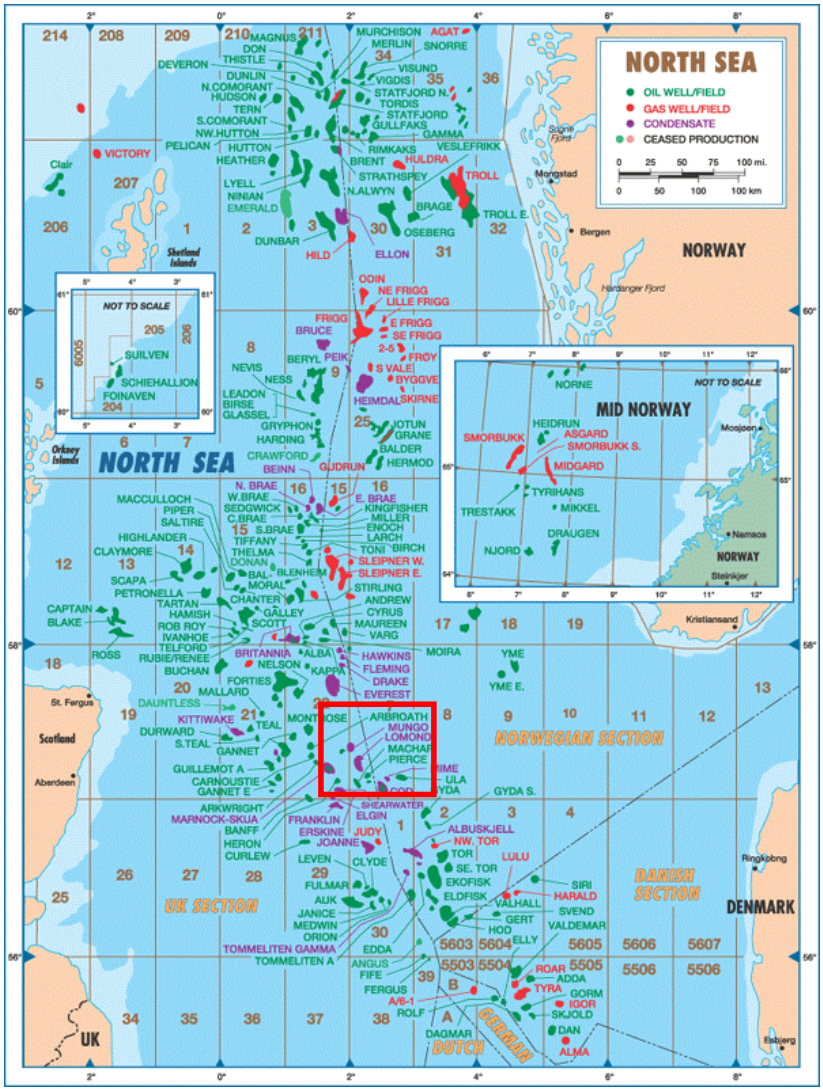


**Figure 3.1**: Lomond field geographical location (courtesy of Acorn Petroleum Services).

The exploration in this area started after some discoveries in the Norwegian sector nearby. The first discovery well, in 1972, tested gas and condensate. Two years later the first appraisal well was suspended and only after ten years was a second one drilled. In 1987 the presence of gas/condensate was confirmed. Production did not start until July 1993.

The Lomond field is operated by BP Amoco (22.22%) on behalf of BG Group (61.11%) and Amerada Hess (16.67%). The development is via a single

platform and the production is in conjunction with the nearby Everest gas/condensate field to which the gas is conveyed before transporting it ashore. The field size is defined as medium: its estimated reserves are: 620 bcf (Billion Cubic Feet) of gas, 10 million barrels of condensate and 3 million barrels of natural gasified liquid. The current production, estimated by BP in 1999, is of 160 mmscf/d (Millions of Standard Cubic Feet Per Day) of gas and 500 bpd (Barrels Per Day) of condensate.

The reservoir is the Palaeocene sandstones of the Forties formation, its thickness is about 200 metres and it is at a depth of 2590 metres. The Forties formation is a submarine fan, deposited during the Palaeocene thermal doming which caused the up-lift of the Caledonian highland. The Caledonian highland provided the source material for the turbidities, which filled the Moray Firth and the East of Shetland platform. Differential displacement of the sea floor due to the up-coming salt diapirs probably triggered the deposition of these alluvial fans (Hodgson et al., 1992). The trapping mechanism is a salt-induced anticline, Figure 3.2. The seal is provided by mudstones from the Rogaland Group, deposited during a period of subsidence at a similar rate to the surrounding sediments. The source rocks are the clay from the Upper Jurassic Kimmeridge Clay formation; migration took place from the late Cretaceous (Hodgson et al., 1992)

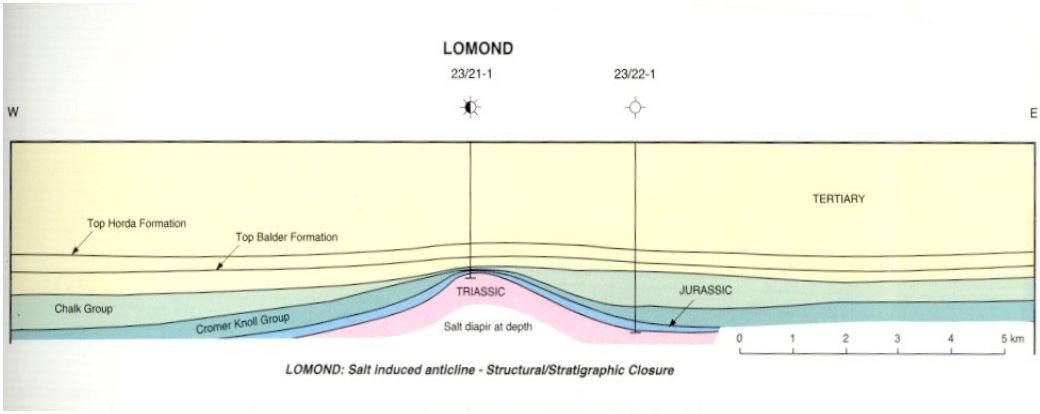


**Figure 3.2**: Lomond field geological profile (courtesy of PESGB).

## 3.3. Motivation for the use of 4C seismic data

The top of the salt induced anticline is heavily faulted and gas leaks through these fractures to the above formations forming a vast zone of gas-saturated rocks. The presence of gas causes two known effects on P-wave imaging: amplitude dimming, due to P-wave energy being attenuated and pull-downs due to a slow-down in P-wave velocity. Figure 3.3 shows the P-wave final migration image I obtained from processing the vertical component data using DMO and PostSTM (a detailed description of the processing results is presented in Chapter 5 and Appendix E).

. The above mentioned gas effects are clearly visible in the central part of the section, at around 2. 4 seconds, black circle.

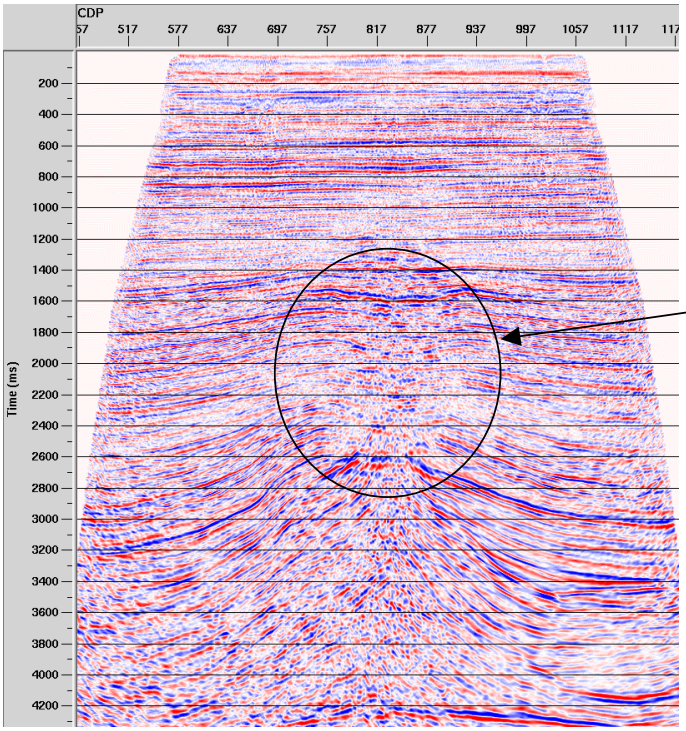


**Figure 3.3**: P-wave final time migration; circled in black is the large area affected by the gas cloud.

The gas pocket is right above the top of the crest, which is also the area of main exploration interest. As PS converted waves image gas filled areas much better than P-P waves (Granli et al., 1999, Caldwell et al., 1999), they are the natural choice in such location.

According to BG Group the use of converted waves in the Lomond field was motivated by the need to optimise the development drilling program, to reduce both risks and costs, and by the possibility of increasing the confidence in defining reservoir limits and assessing volumes (Tim Pointer, personal communication). Figure 3.4 shows BP interpretations of the crest of the Lomond field before and after the 3D 4C data were available (Pope et al., 2000). The use of the C-wave volume allowed the interpreters to map a new set of faults orthogonal to the known north-south trend. The knowledge of the fracture trend is fundamental for well planning.

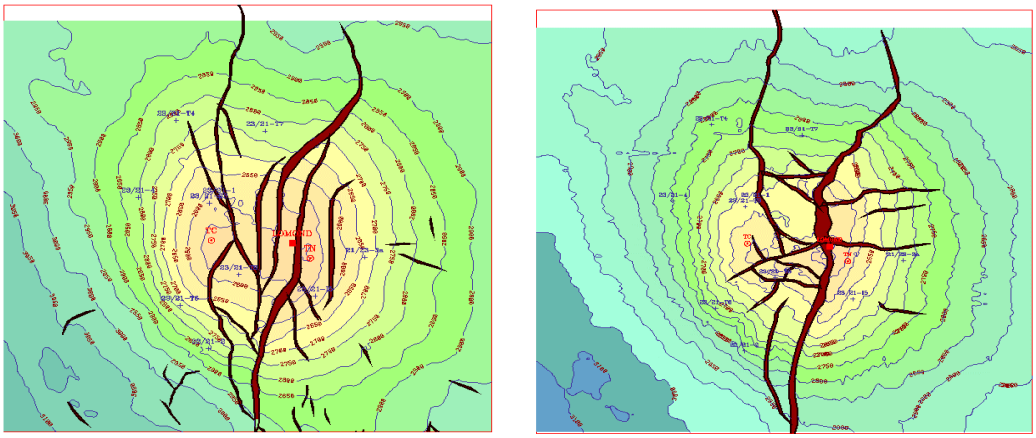

**Figure 3.4:** Lomond field interpretation at the reservoir level, left: from streamer data only, right, from the 4C cube.

## 3.4. Acquisition: Vessels and instruments

4C acquisition requires two seismic vessels, one operating the source, the other deploying the receiver cables. For the Lomond field acquisition, the receiver vessel was equipped with two multicomponent streamers, each 6000 metres long and

with 240 4C groups (hydrophone plus geophones). The group interval was 25 metres. The source vessel used a single source, which was composed of three Bolt airgun arrays, forming a tuned array of 3397 cubic inches. Shot interval was 25 metres and the shooting direction was parallel to the cable.

The recording instruments were contained in a cable similar to a normal streamer, with a polyurethane skin, filled with kerosene. Some extra ballast weight was incorporated to allow faster sinking when deployed, see Figures 3.5 and 3.6.

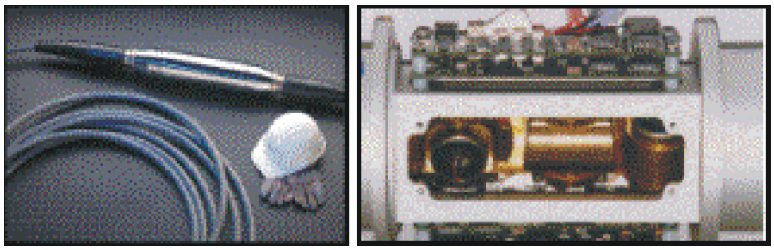

**Figure 3.5**: An example of OBC on the left, 3C geophone on the right, courtesy of PGS.

**Figure 3.6**: OBC being deployed in the receiver vessel, courtesy of PGS.

Simrad USBL transponders were installed at the head and the tail of the cable and used for initial positioning and successive monitoring. The recording vessel handled all the data concerned with the seismic sensors and the position of the cable, while either vessel can control the source firing and source position. For a final and

more accurate cable positioning, Sonardyne acoustic transponders were used. They were positioned at regular interval of 100 metres on the cable, in order to obtain information on the general shape of the cable and on its position. The two vessels were linked via radio telemetry, so that information was passed between the two. The system timing was synchronised. Table 3.1 is a summary of the main information for the acquisition.

**Acquisition parameters**

| | |
|---|---|
| Recording vessel | : Polar Queen |
| Recording system | : Triacq Nessie 4C |
| Number of channels | : 1920 (2 x 960) |
| Record Length | : 10.5 s. |
| Sample interval | : 2 ms. |
| Low cut filter | : 3Hz 127 dB/Oct |
| High cut filter | : 125 Hz 127 dB/Oct |
| | |
| Source vessel | : Akademik Shatskiy |
| Energy source type | : Single Source – Bolt air gun array |
| Total capacity | : 1 x 3397 cu ins |
| Total number of guns | : 24 |
| Number of sub arrays | : 3 strings |
| Sub array separation | : 8 m. |
| Capacity of sub-arrays | : 2 x 1029 and 1 x 1339 cu ins |
| Pressure | : 2000 psi |
| Depth | : 7.5 (+/- 0.5 m.) |
| Shot interval | : 25 m. |
| | |
| Streamer type | : Geco's NESSIE 4C |
| Active length | : 2 x 6000 m. (only 1 in 2D) |
| Separation of streamers | : 600 m. |
| Number of groups | : 2 x 960 (PXYZ) |
| Group interval | : 25 m. |

**Table 3.1**

## 3.5. Acquisition technique

The common practice in acquiring 3D 4C seismic data using Ocean Bottom Cables is to lay the two receiver cables on the seabed and to shoot in pa*tc*hes with direction perpendicular to the cables. This acquisition geometry offers good azimuthal coverage. When acquiring 2D 4C seismic lines often a shooting direction parallel to the cable is chosen instead, as shown in Figure 3.7. WesternGeco acquired the Lomond field 3D data in the conventional orthogonal geometry. They used swaths of 2 cables each with east-west orientation and separated by 600 metres. A total of 25 lines, 8.6 kilometres long, with a 600 metres cable separation and with 4.0 kilometres of run-in and run-out were shot for each swath. At the end of each shooting sequence the recording vessel moved back, retrieved the cables and set up the new swath.

WesternGeco also acquired three 2D lines, with shooting parallel to the cable. Each 2D line was 14.4 kilometres long, with 4.2 kilometres of run-in/run-out and 6.0 kilometres of cable length. The record length was 10500 milliseconds with a sample interval of 2 milliseconds. A band pass filter was applied during acquisition, with a 3 Hz low cut and a 125 Hz high cut. The source was positioned at a depth of 7.5 metres; the cable was at a depth of 87 metres.

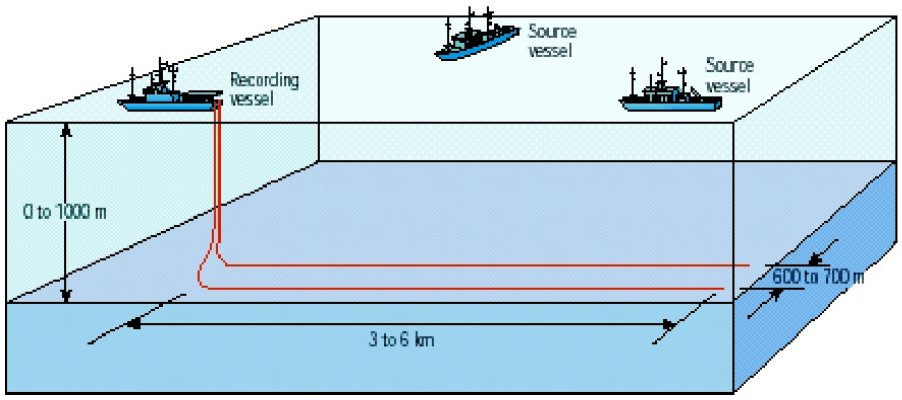


**Figure 3.7**: Schematic display of a generic 3D acquisition set-up (courtesy of Schlumberger).

Figure 3.8 shows a typical shot record from the 2D 4C line. From left to the right the display shows the records from the hydrophone, the inline component, the crossline component and the vertical component. The data quality is generally very good although few spikes and some noise are present on some of the geophone records. The hydrophone and the vertical component records show mostly P-wave arrivals, while the energy in the inline component is due to C-wave arrivals. The crossline record has very little coherent energy. This is confirmed by the stacking results shown in Figure 3.9. On the left part we have the inline component brutestack, with no pre-processing applied (see Chapter 5). On the right part I show the crossline component brutestack, in which is very hard to see any coherent event. P-SV wave energy is focused only on the source-receiver line. This indicates that there is not geological cross dip and that there is little or no conversion of P-waves into P-SH waves.

There is some energy leakage between inline and vertical component, estimated at around 5% (Li et al., 2000), which is quite low.

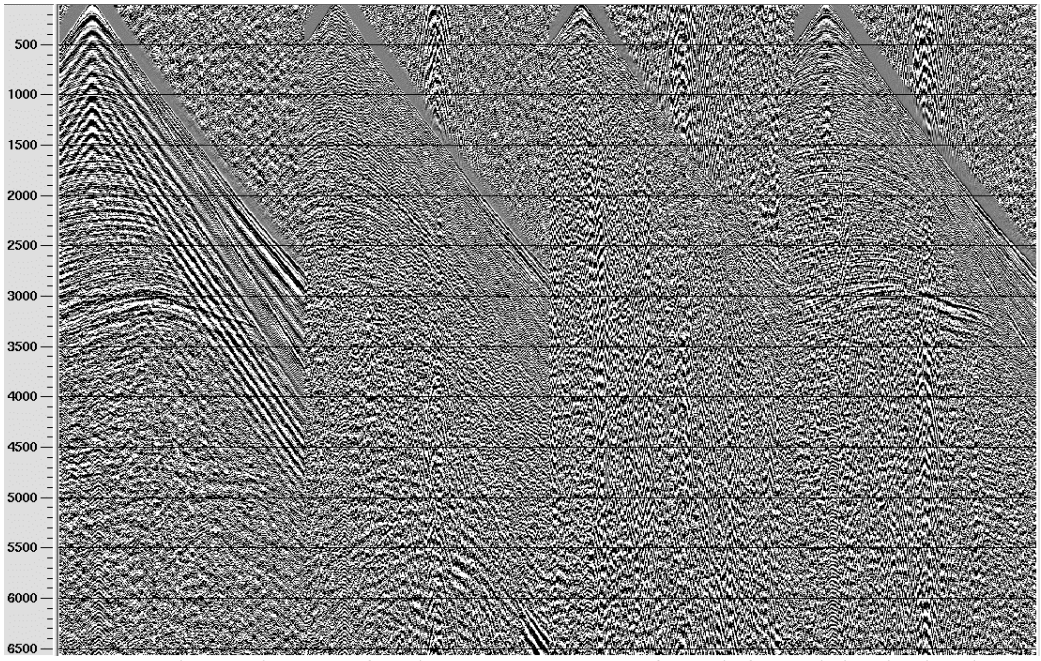


**Figure 3.8**: Shot Point 300 for the 4 components, from left to right: hydrophone, inline component, crossline component and vertical component.

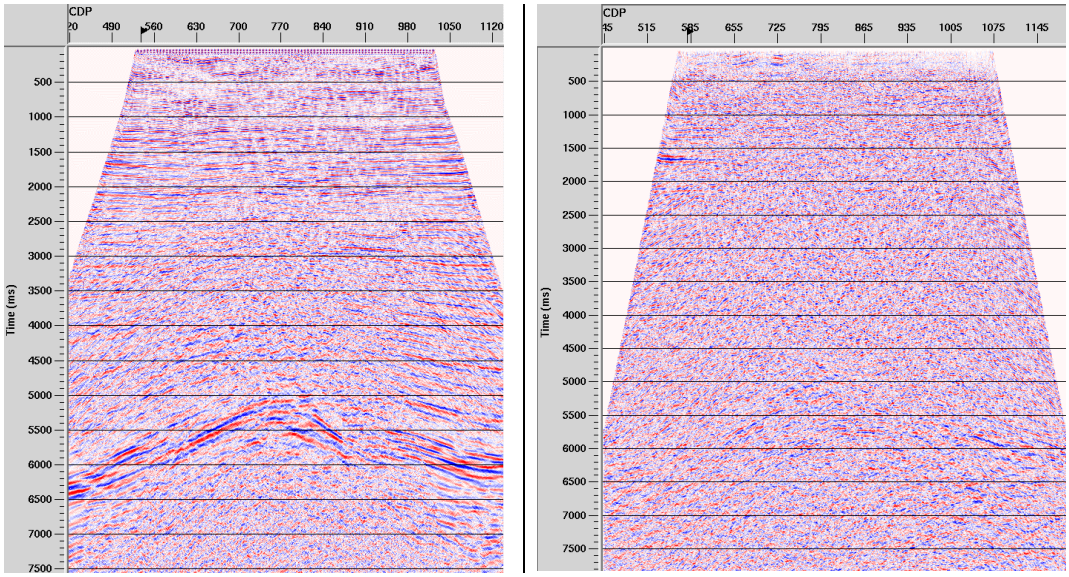


**Figure 3.9:** Left: Inline component brutestack. Right: Crossline component brutestack. On the crossline component there is hardly any coherent signal.

## 3.6. Well logs

Well logs are often used in connection with seismic data. They provide extra information useful in velocity modelling and depth control. Integrating data from seismic surveys and well logs is a fundamental task in reservoir characterisation. In the Lomond field there are numerous production wells which have been logged. These production wells are mostly deviated as they all start at the Lomond platform and then deviate by as much as 50 degrees, as shown in Figure 3.10.

Most of the wells in the Lomond area were drilled in the first phase, before 1993, two of them are part of the new in-fill program, well 23/21-T9 and T10, drilled after 1999 (i.e. after the new interpretation on the 3D 4C data volume). All wells were logged only in the reservoir interval.

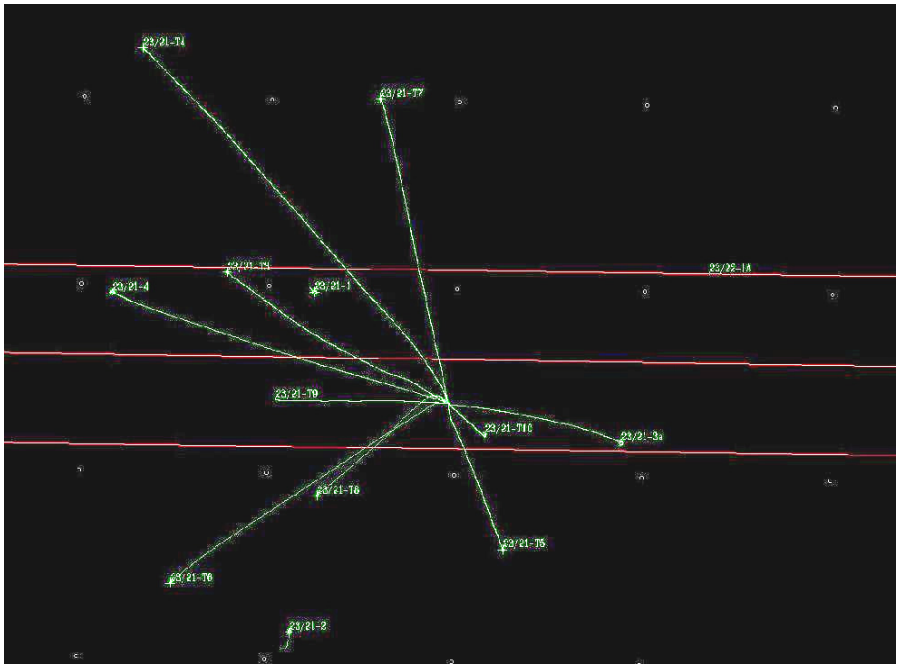


**Figure 3.10**: Well positions in the Lomond Field; in green are indicated the well trajectories, the three 2D 4C seismic lines are indicated in red. Line 381 is the one in the middle.

The pre-1999 wells were acquired with a conventional monopole sonic tool. The monopole tool uses an omnidirectional pressure source which creates a wave propagating in the borehole fluid and then out into the formation. The energy arriving at the formation at a critical angle is refracted, travels in the formation parallel to the borehole and it is refracted back towards the receivers, see Figure 3.11 (a). S-waves are generated in the formation due to P-energy conversion, but can only be recorded in "fast or hard formations". A "fast formation" is a formation in which the shear wave velocity is higher than the compressional velocity in the borehole fluid, see Figure 3.11 (b). In "slow or soft formations" shear waves cannot be distinguished, as shown in Figure 3.11 (c). Shear logs were not acquired in the older wells.

In the two new wells velocity logs were acquired using a new tool (developed by Schlumberger), the Dipole Sonic Imager. It consists of a directional source and directional receivers. The source works like a small piston, creating differential pressure on the borehole walls, see left part of Figure 3.12. This pressure causes

flexing on the walls, with direct generation of both P and S-waves. The source works at frequencies of about 4kHz. The two wave types propagate straight into the formation, but they produce also a shear/flexural wave which propagates in the borehole creating a pressure disturbance in the borehole fluid called "dipole-type" pressure, see Figure 3.11 (c). The receivers record this disturbance. The flexural mode is dispersive: at lower frequencies its phase speed is the same as the shear wave in the formation, but at higher frequencies is lower. The dipole tool allows shear wave recording in slow formations unlike the monopole source, as the flexural wave in these formations is short in duration and concentrated at lower frequencies. Some differences in shear waves speed have been recorded when using both monopole and dipole source. The differences have been attributed to either different depth of investigation of the two tools or different vertical resolution or presence of anisotropy or monopole dispersion (Esmersoy et al., 1990).

The tool itself is a sonde of 9 centimetres in diameter, 15 metres long, containing both monopole and dipole sources, right part of Figure 3.12. The receiver section is located 3.5 metres above the transmitter section and is composed by 8 receiver stations each containing two hydrophone pairs, one oriented with the higher dipole transmitter, the second with the lower. The entire receiver section is about 1 metre long and the receiver stations are spaced 15 centimetres apart.

The velocity ratio, $v_p/v_s$, extracted from the logs, can be used as input to multicomponent processing. In Chapter 6 I discuss the results from an integrated analysis of well and seismic velocities over the Lomond area.

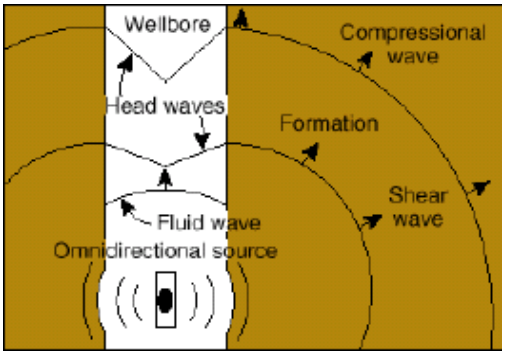


**Figure 3.11 (a):** Waves produced by a monopole source in a "hard formation"

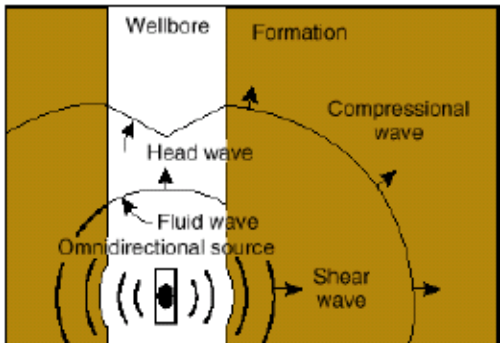


**Figure 3.11 (b):** Waves produced by a monopole source in a "soft formation"

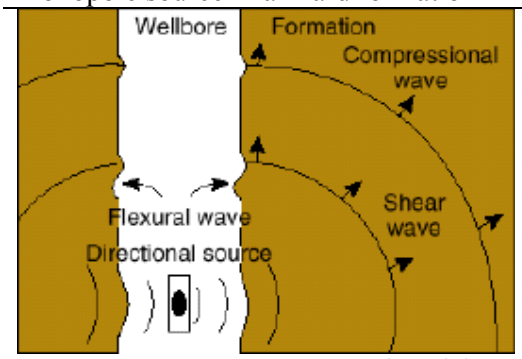


**Figure 3.11 (c):** Waves produced by a dipole source in a "soft formation". All Figures courtesy of Schlumberger.

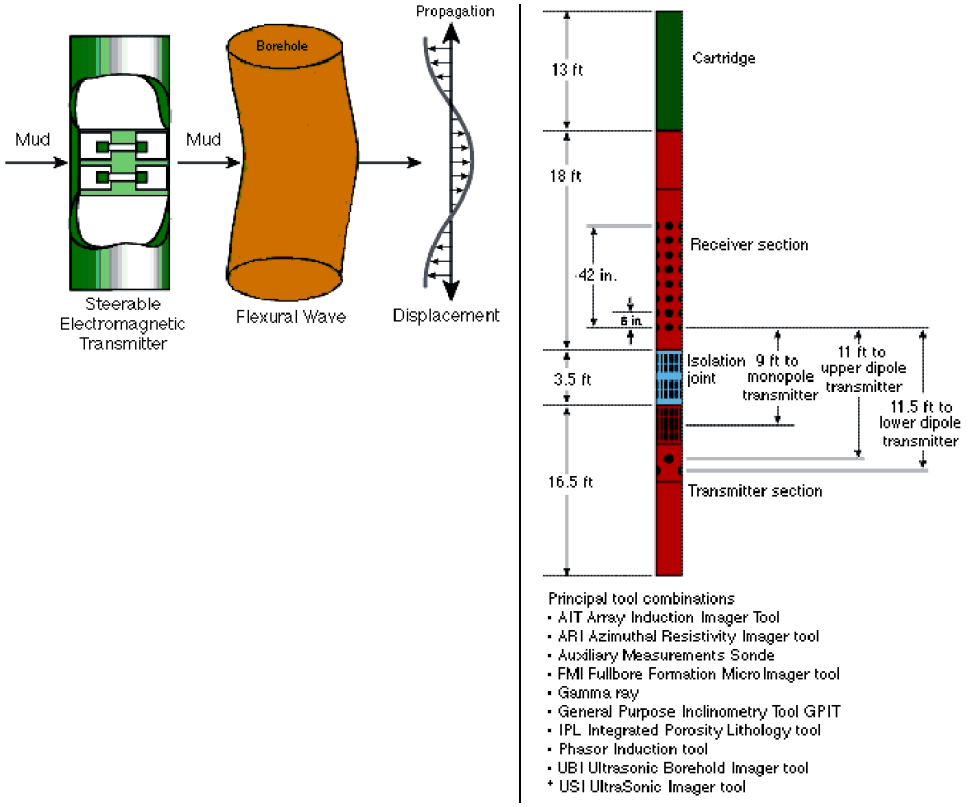


**Figure 3.12:** Left, the Dipole Sonic tool developed by Schlumberger. The small pistons generate directly a flexural wave. Right, well logging tool section. See text for details, (courtesy of Schlumberger).

## 3.7. Check Shots and well markers

Check shots were acquired in all wells. The choice of check level interval varied from well to well, going from a 15 metre interval (50 feet) to 30 metres (100 feet). In some wells the interval chosen was something in between, 23 metres (75feet). Extra levels were always recorded at formation tops. The source was a 3 x 140 cubic inches airgun array, towed by a boat so that it was placed almost vertically above the geophone for every shot since the wells are deviated. The formation tops recorded were: the Top Balder, the Sele formation, the Forties silt and the Forties sandstone formations, Slump, May Maureen, Danian and finally the Ekofisk formation, Figure 3.13.

These kind of information are quite useful; for example in Chapter 8 I use the depth mismatch between well and seismic data and the velocity information provided by the check shot to analyse the presence of polar anisotropy in the Lomond field.

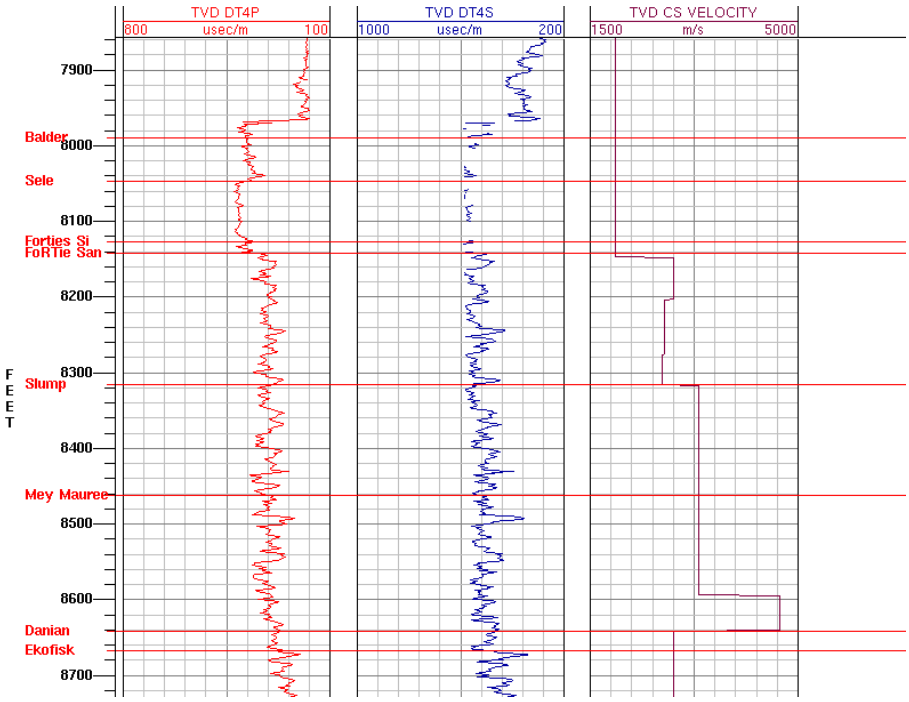


**Figure 3.13:** Sonic log, shear log and check shot velocity curve for well 23/21-T9. The horizontal red lines indicate the well markers.

# Chapter 4: Converted wave characteristics – Examples from the Lomond data

## 4.1. Introduction

In Chapter 2 I reviewed the main theories and processing techniques required to deal with converted waves. Here I highlight some particular characteristics of this mode of propagation, which are important for imaging and joint interpretation with P-waves. In particular from a processing point of view we have to consider that positive and reverse shooting in a split spread acquisition do no lead to the same image, due to the fact that, for PS converted waves, interchanging source and receiver positions does not lead to the same traveltimes in generic cases. So, in tectonically complex areas and in the presence of heterogeneities, the apparent velocities in the two offsets differ.

Also the energy distribution on the offset spread is very dissimilar between P and converted waves. For P-waves the highest energy is confined at near zero-offsets, while for converted waves the highest energy is in the middle-to-far offset traces. This part of the spread, often muted out during processing of P-waves (in the hyperbolic approximation) may contain valuable information.

On the interpretation side we have to be aware of the different frequency content due to different P-wave and S-wave attenuation, above all after about 2.0 seconds traveltime; these differences greatly complicate the visual correlation of events in the in the P and C-wave stacks.

## 4.2. Reciprocity, apparent velocities and diodic velocity effects

For pure mode propagation, either P-P or S-S, the reciprocity principle states that if we interchange the source and receiver locations the arrival times will be the same. This is one of the basic principles in seismology. In the case of P-SV converted waves what happens if we interchange source and receiver positions? Since P-wave velocity differs from S-wave velocity the traveltimes are the same only in a horizontal and laterally homogeneous medium (Nedlin, 1986), see Figure 4.1. In this case in fact, although the raypaths are not coincident, they are a mirror image of each other. But in a generic case of dipping and/or laterally inhomogeneous medium the reciprocity principle, stated as I did above, would not hold. For the principle to hold we have to interchange the nature of the source as well, i.e. the receiver becomes a shear source (polarised as SV), so that, in Figure 4.1, S1 is both the up-coming converted S-wave and the down-going source-generated S-wave. But since in multicomponent acquisition we can not do that, positive and reverse shootings lead to two different seismograms.

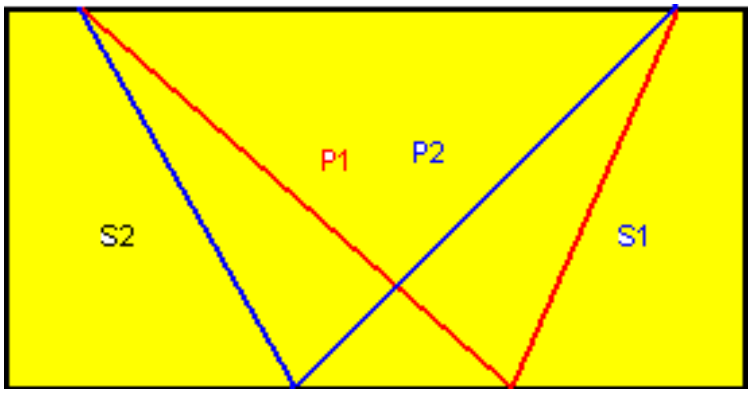


**Figure 4.1:** Reciprocity issues in PS arrival times. The traveltimes for P1S1 and P2S2 will only be identical in a horizontal and laterally homogeneous medium.

This characteristic is of great importance. The presence of dip produces different apparent velocities for the positive and negative offsets. Even the CCP dispersal is different when data are shot up-dip or down-dip (Harrison, 1992). Figure 4.2 shows the asymmetry in an ACCP gather during velocity analysis for the dipping events at 5.5 seconds, yellow dotted line, while the shallow flat events remain symmetric.

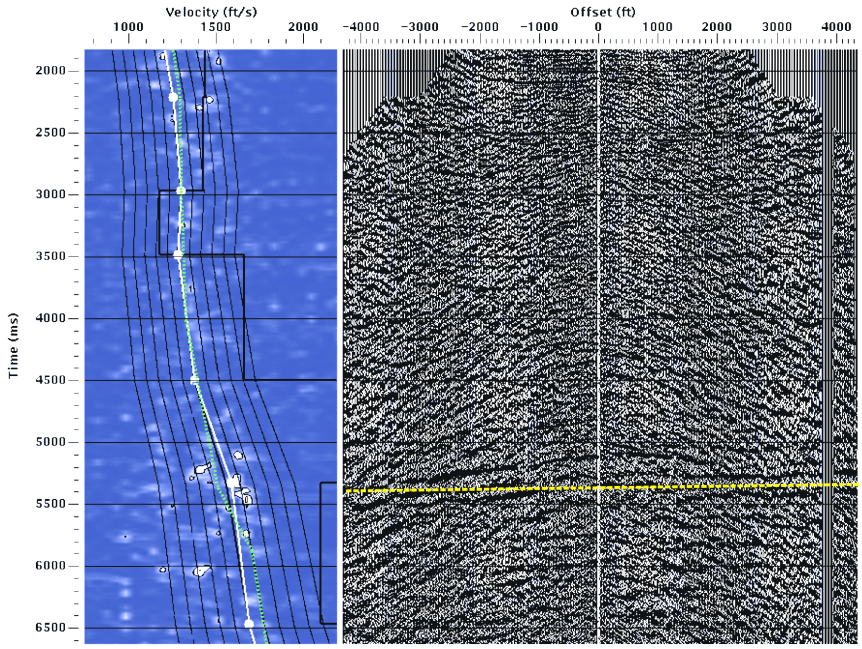


**Figure 4.2**: CCP gather asymmetry for dipping layers, indicated by the yellow dotted line. The presence of dip produces different apparent velocities for the positive and negative offset. The shallow events are, instead, symmetric.

Heterogeneities also produce different effects in the two offsets. Granli et al. (1999), Thomsen (1999) and Li et al. (2001) noticed that the effects of a gas cloud on converted wave traveltime (and imaging) depend on which leg of the ray path travels through the gas. For example, if only the S-leg of the raypath encounters the gas there are no effects, but if it is the P-leg that travels through the gas then C-wave velocities are slowed down, Figure 4.3. This phenomenon is called *diodic velocity*

*effect* (Thomsen, 1999). Figure 4.4 shows these effects on the positive and negative stacks in the Lomond field. The negative offset stack, right, appears disturbed by the gas on the top of the anticline, while the positive offset image, left, is practically unaffected: notice the differences in the two black circles.

In the presence of complex geology and/or heterogeneities in the sub surface, it is no longer feasible to work simultaneously with the two offsets. Instead it is advantageous to split them and process them independently.

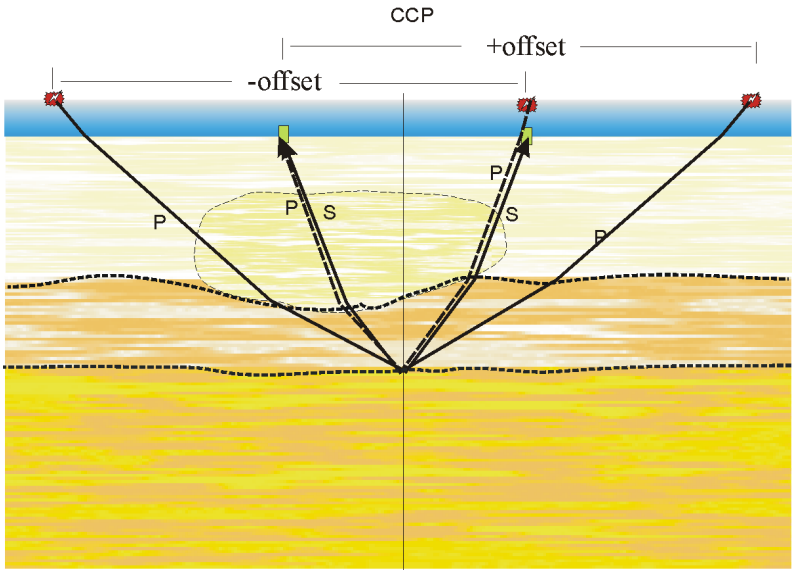


**Figure 4.3**: Diodic velocity effects, from Li et al. (2001). A gas cloud can be encountered either by the P-leg only, or by the S-leg only, or by both. If only the S-wave leg travels through it, the C-wave traveltime is unaffected by the presence of gas.

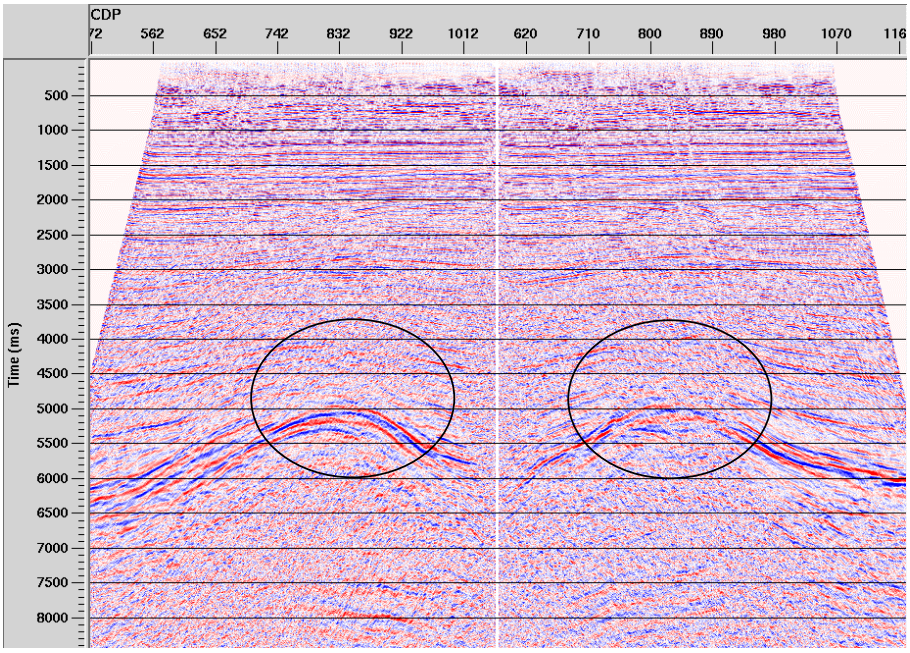


**Figure 4.4**: Effects of the gas cloud on the positive and negative offset images. The negative offset stack is more affected by the gas in the apex of the anticline, black circles.

## 4.3. Amplitude

It is interesting to look at the different amplitude behaviour of P-waves and C-waves. We can look at the amplitude of reflected waves calculated for a single horizontal interface. I built a very simple two-layer model composed of two fictitious materials described in Table 4.1. I then calculated the reflected and the converted amplitude associated with a downgoing P-wave for different angles of incidence. The program I used (*akicomphas*, created by Peter Hanssen and modified by Baerbel Traub, EAP) calculates the effective reflection coefficients for a specified interface using Aki and Richards (1980) exact formula for isotropic horizontal layers. Amplitudes are calculated from the reflection coefficients.

Figure 4.5 shows the results. Our interest is for the angle range from 0 to 40 degrees. For P-waves the amplitude has a maximum at zero-offset and decreases to a minimum at about 25 degrees. For higher angles of incidence it increases until it reaches the critical angle. For P-S converted waves instead the amplitude is zero for

vertical propagation, it increases and reaches its maximum for angles around 25 degrees, then decreases again. For angles above 40 degrees a phase reversal occurs. From a processing point of view this is quite important: in conventional P-wave processing we are used to working mostly with near offset data, low incidence angles, where most of the energy is confined. A strong mute is usually applied to limit the data range. For C-waves the highest energy is confined to higher angles, so the middle-to-far offset traces contain valuable information and should not be discarded.

| $v_p$ (m/s) | $v_s$ (m/s) | $\rho$ (g/cm$^3$) |
|---|---|---|
| 2000 | 1000 | 2.0 |
| 3000 | 1500 | 2.0 |

**Table 4.1:** Simple fictitious model for calculation of PP and P-SV reflectivity

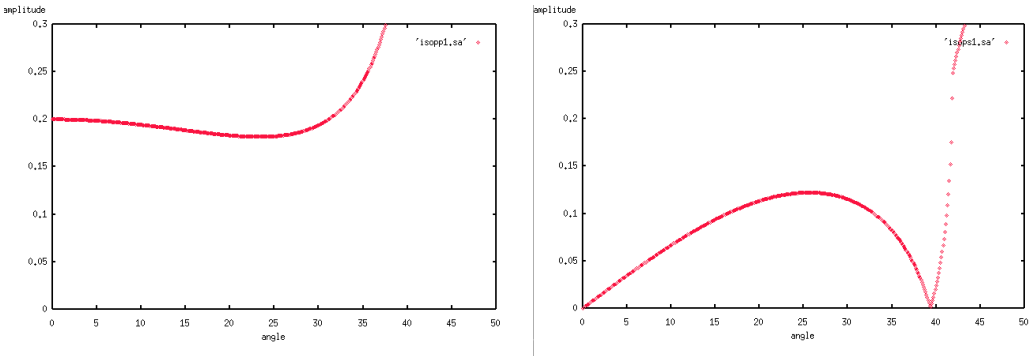


**Figure 4.5**: Reflected amplitude for P and SV waves for a single horizontal interface; model parameters are shown in Table 4.1.

This energy distribution can be observed in the CDP and ACCP gathers shown in Figure 4.6. The CDP gather, on the left, shows maximum energy in the near offset region, probably a mute at about 2500 metres of offset for the main event, at 2.7 seconds, can be applied. The ACCP gather, on the right, shows high energy from 2000 metres offset onwards, while in nearer traces the energy is very low.

Figure 4.6 also highlights another difference often observed in multicomponent data between P-waves and C-waves: the lower signal-to-noise ratio in the inline component.

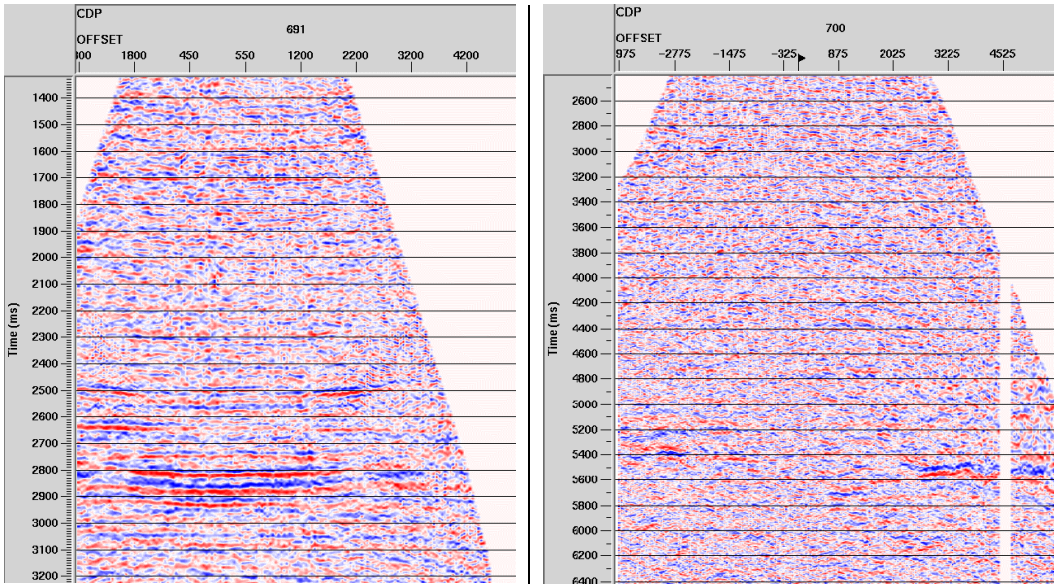


**Figure 4.6:** Example of amplitude behaviour in the Lomond area. A P-wave CDP gather on the left showing maximum energy at near offset, on the right, a ACCP gather in the same location, showing the highest energy in the middle-to-far offset part of the data. NMO is applied on both gathers.

Figure 4.7 shows a C-wave shot gather. We can notice that we have actually energy at zero-offset or, more correctly, at very near offsets, although, above all at 3.0 seconds, the amplitude is still higher in the middle offsets. Why do we see amplitude at such near offsets? Nedlin (1986) showed that in a medium with lateral velocity gradient, or a medium with a dipping reflector and vertical velocity gradients, see Figure 4.8, the normal incident angle does not correspond with the zero-offset P-SV reflection. In fact since the $v_p$ and $v_s$ gradients are different, the normal rays deflect and arrive at the surface at two different locations. This means that the SV-leg arriving at the receiver coincident with the source (zero-offset) is not the one converted at zero-angle and, therefore, it has non-zero amplitude. Still this

consideration does not change the main point I want to make in this paragraph: the need to include longer offsets in C-wave processing.

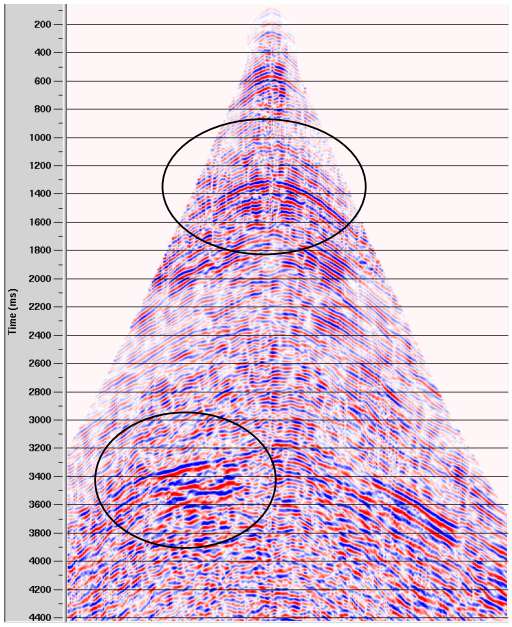


**Figure 4.7:** Shot gather showing amplitude at the nearest offset traces, see upper circle, although deeper events show highest amplitude in the middle-offsets, bottom circle.

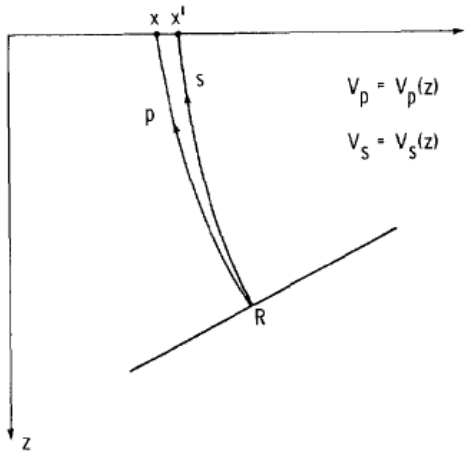


**Figure 4.8:** In a medium with vertical velocity gradients and a dipping reflector, normal-rays for P and S-waves originated in R do not emerge at the same location (zero-offset) in the surface. This implies that the zero-offset P-SV reflection has non-zero amplitude (From Nedlin, 1986).

## 4.4. Frequency

Frequency content differs from P-waves to C-waves with the latter usually exhibiting lower frequency. In Figures 4.9 and 4.10 the spectra for the P-wave and C-wave stacks are compared. The displays show the full stack on the left, the zoom-in of the window used in the analysis in the top-middle part, the frequency-space (F-X) power spectrum in the bottom-middle part and the average power spectrum (in percentage of power) in the right part. On the power spectrum display we have the noise, in black, overlaid to the signal, in red. The noise is the difference between the amplitude spectrum (Fourier transform on a raw trace) and the signal spectrum (amplitude spectrum cross-correlated with a number of adjacent traces). The time window chosen for the analysis is in the central area of the section, which includes the reservoir. There is about 10Hz of difference in the peaks of the spectra between the two wave types, the peak in the P-wave stack is at about 20 Hz while in the C-wave stack it is at 10 Hz.

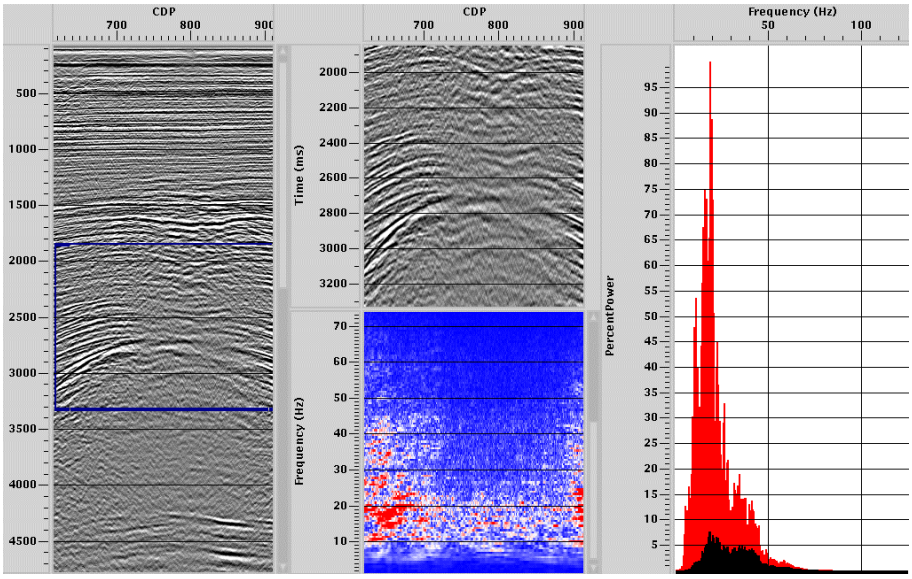


**Figure 4.9**: Amplitude spectrum of the P-wave stack for the target area. The stack is on the left, with a blue rectangle indicating the selected area. On the top part of the central display is the zoom-in of the selected area, the bottom part is the F-X power spectrum, and finally on the left the display shows the average power spectrum. The blue square on the stack indicates the data selection.

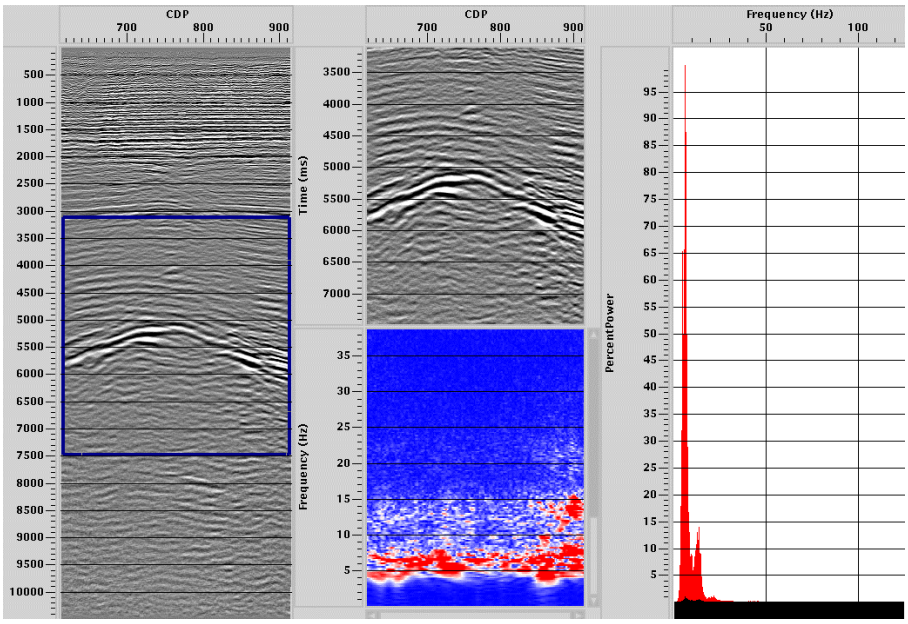


**Figure 4.10**: Amplitude spectrum of the C-wave stack for the target area. The display lay out is the same as Figure 4.7.

We now analyse a shallower time window (first 1.5 seconds, Figures 4.11, 4.12). The results show higher frequency content also in the C-wave spectrum. The two spectra are more comparable, in fact now the frequency peak in the C-wave spectrum is between 15 and 20 Hz.

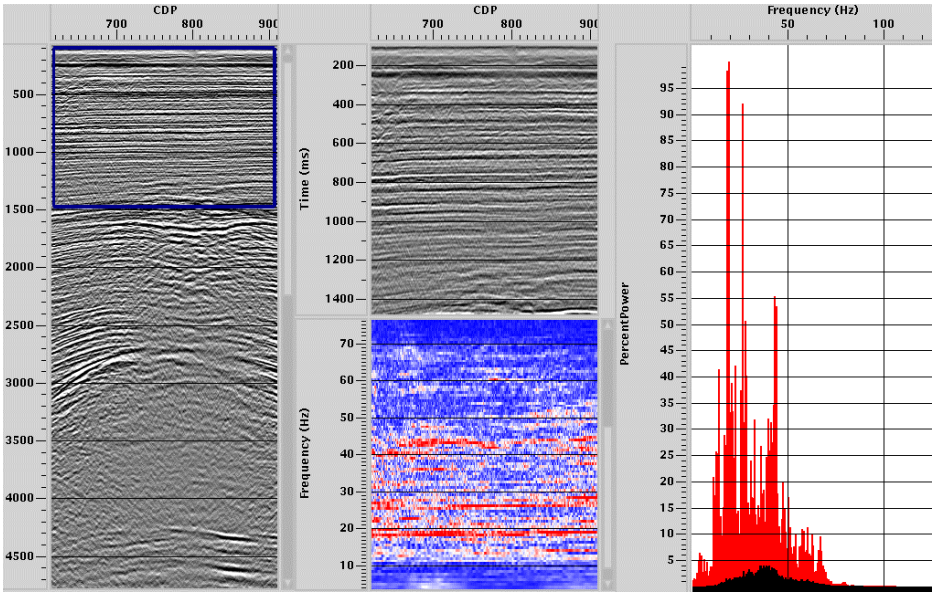


**Figure 4.11**: Amplitude spectrum of the P-wave stack in the shallow. The display lay out is the same as Figure 4.9.

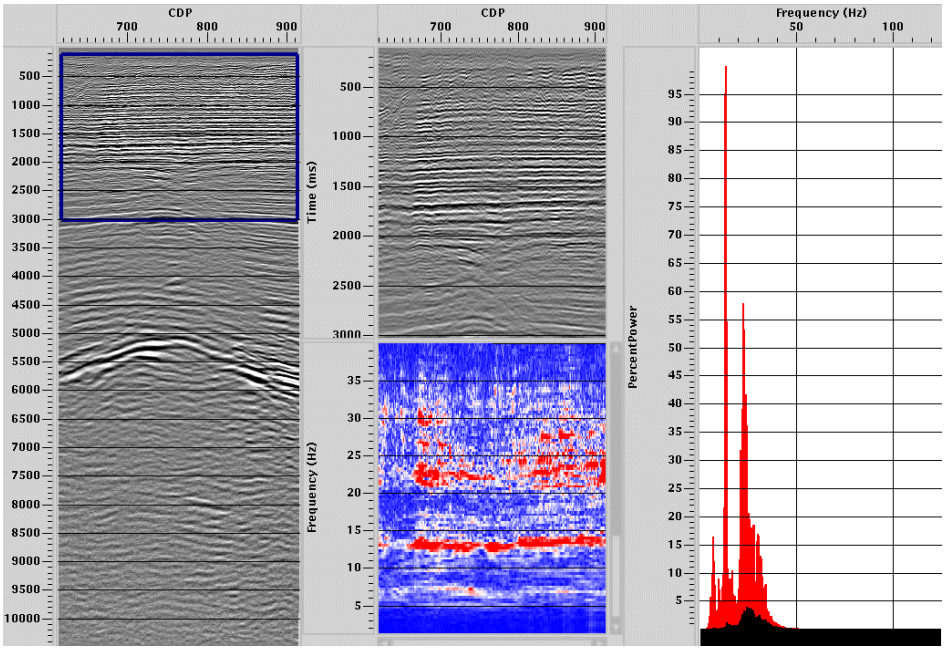


**Figure 4.12:** Amplitude spectrum of the C-wave stack in the shallow. The display windows are the same as Figure 4.9.

These results show that C-waves have greater attenuation than P-waves. Garotta et al. (2003) proposed using the slope of the amplitude spectra towards high frequencies, which is linked to quality factors (Qpp and Qps), to derive a new parameter called *I*'s and defined as Qpp/Qps see Figure 4.13. This parameter can potentially be used for lithology discrimination but has still to be tested.

The difference in frequency content is one obstacle to joint PP and PS interpretation, as it makes it difficult to recognise the same event in the two sections. A greater problem in event correlation is when we have differences in the P- and C-wave reflection coefficients.

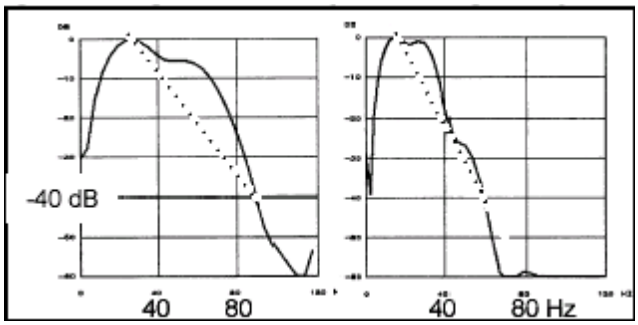


**Figure 4.13:** Frequency spectra slope for P-P and P-SV waves.

## 4.5. Conclusions

Converted waves have characteristics that strongly differentiate them from P-waves, both from a processing and an interpretative point of view. Interchanging source and receiver position leads to different images in zones with complex geology and heterogeneities. Since C-waves are acquired with a split-spread geometry, it is opportune to process the data independently for the positive and negative offsets.

Another important point for processing purposes is to consider the different amplitude behaviour of reflected and converted waves. While reflected waves have highest energy for angles of incidence near zero, converted wave energy reaches its peak for angles of incidence around $25^{o}$. This translates into the need to include the middle-to-far offset traces during processing, since valuable information is contained in this section of the spread.

The frequency content of P and C-wave differs. While in the shallow part the frequency content is not dissimilar, in depth C-waves show greater attenuation than P-waves. This difference, linked to the difference in quality factors, could be used as a lithological attribute. This difference in frequency content makes it harder to recognize the same event in the P-section and the C-section and has to be carefully considered when joint interpretation of P and C-waves is carried out.

# Chapter 5: Result of "conventional", isotropic processing

## 5.1. Introduction

In Chapter 2 I gave an overview of so-called "conventional" multicomponent processing, here I show the results from a similar flow applied to the Lomond field 2D 4C data. These results are important for two reasons. First, because even with this simple processing sequence, achieved almost completely using commercial packages such ProMAX, I can show that converted waves have greater imaging potential in areas affected by gas clouds compared with P-waves. Second, because we consider these results as the basis against which further processing results (i.e. anisotropic Pre Stack Time Migration, see Chapter 9) will be measured. The processing carried out in this chapter does not include anisotropy and for this reason is limited to near offset data (offset-to-depth ratio of less than 0.7). The main software used in this Chapter and in next two are ProMAX, for seismic processing, Nucleus (from PGS) for wavelet modelling, and GMAplus (from Geographix) for well log analysis. Some parameter analyses required new programs written in C.

## 5.2. Processing flow

Figure 5.1 shows a conventional DMO plus Post Stack Migration flow, which includes a detailed velocity ratio analysis for binning purposes. Since layered shales

compose the main lithology of the overburden, we expect anisotropic and layering effects to be present. For this reason, even if we ignore anisotropy during NMO, DMO and migration, we include the effects of layering in the velocity ratio calculation. Results confirm that there is a large difference between the vertical and the effective velocity ratios.

The processing flow described in Figure 5.1 is a joint processing of the vertical and the inline components. Since converted wave processing requires velocity information from P-waves for the $\gamma_{eff}$ estimation, the vertical component is processed first. The flow also has the merits of trying to keep P and C-wave processing as similar as physically possible and it is relatively simple to apply. The key part is the velocity ratios estimation, which has, as I show later, a huge effect on the imaging quality. Details of the processing are presented in the next sections.

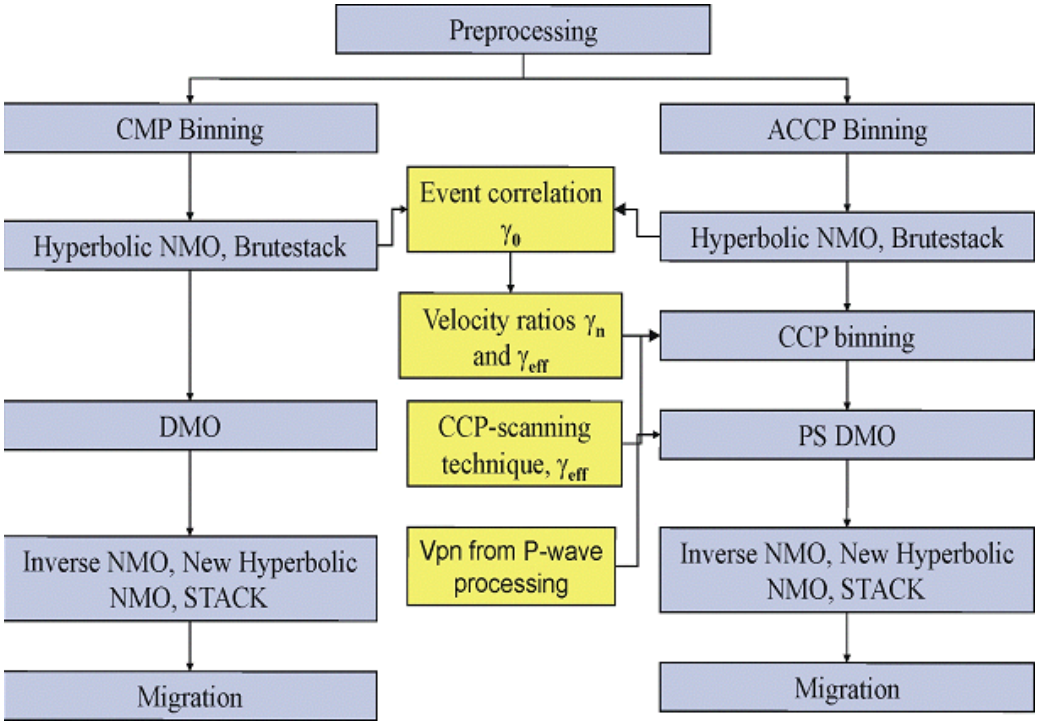


**Figure 5.1:** "Conventional" processing flow for 4C seismic data applied to the Lomond 2D data.

## 5.3. Preprocessing

Preprocessing is common to both vertical and inline components. Often for 4C data the hydrophone and the vertical component are summed. This procedure reduces receiver side multiples (ghost) exploiting the fact that ghosts have opposite polarity in the hydrophone and in the vertical component of the geophone (Barr and Sanders, 1986, see Appendix C). This summation can also improve the overall signal to noise ratio. However, in the Lomond field the vertical component data did not show strong water-column reverberations and had a good signal-to-noise ratio, so this step was judged unnecessary. Preprocessing includes the following steps for both vertical and inline component:

- Geometry application,
- Gain recovery,
- Receiver static correction, (only for C-waves),
    - Signature deconvolution,
- Random Noise and Spikes editing,
- Linear noise removal, F-K filter,
- Deconvolution,

Details on the preprocessing are in the Appendix A, while the ProMAX flows used to apply it are presented in Appendix B.

Figure 5.2 shows the P-wave brutestack after the preprocessing; the image quality is generally good with high signal-to-noise ratio. The salt dome structure is well imaged. The top of the reservoir, Top Balder, indicated by the arrow, shows good continuity except inside the gas cloud, as already highlighted in Chapter 3. Some resolution is lost in the steepest flanks of the salt dome, but this is expected at this stage of processing.

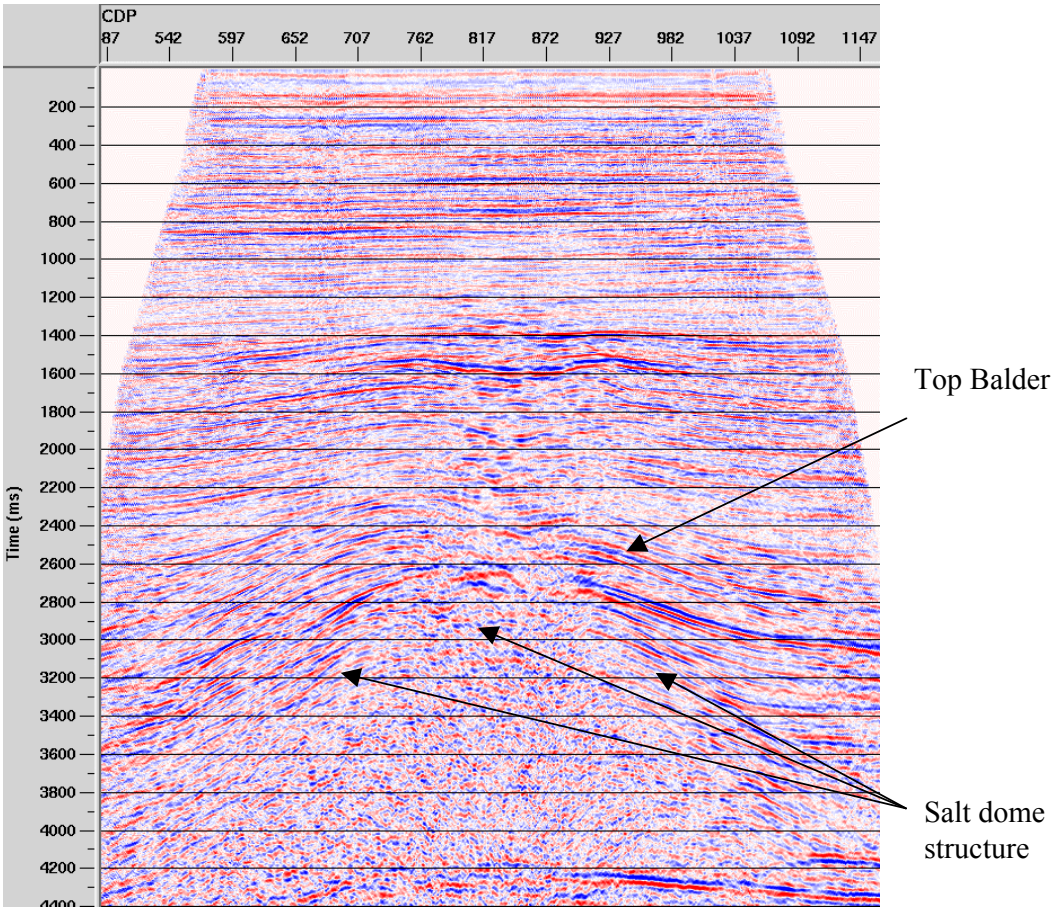


**Figure 5.2**: P-wave brutestack after preprocessing. The arrows indicate the Top Balder and the flanks of the salt dome. The data quality is very good except in the gas-affected area.

Figure 5.3 shows the C-wave brutestack after preprocessing (including receiver static corrections). The reservoir area, again indicated by the arrow, has good continuity, but the overall section shows low signal-to-noise ratio. The noise is particularly high between 2.5 and 5 seconds and mainly composed by high frequencies. No band pass filter was applied at this stage. Apart from the noise, it is worth mentioning that the main event, at 5 seconds, shows good continuity without pull down effects due to the presence of gas.

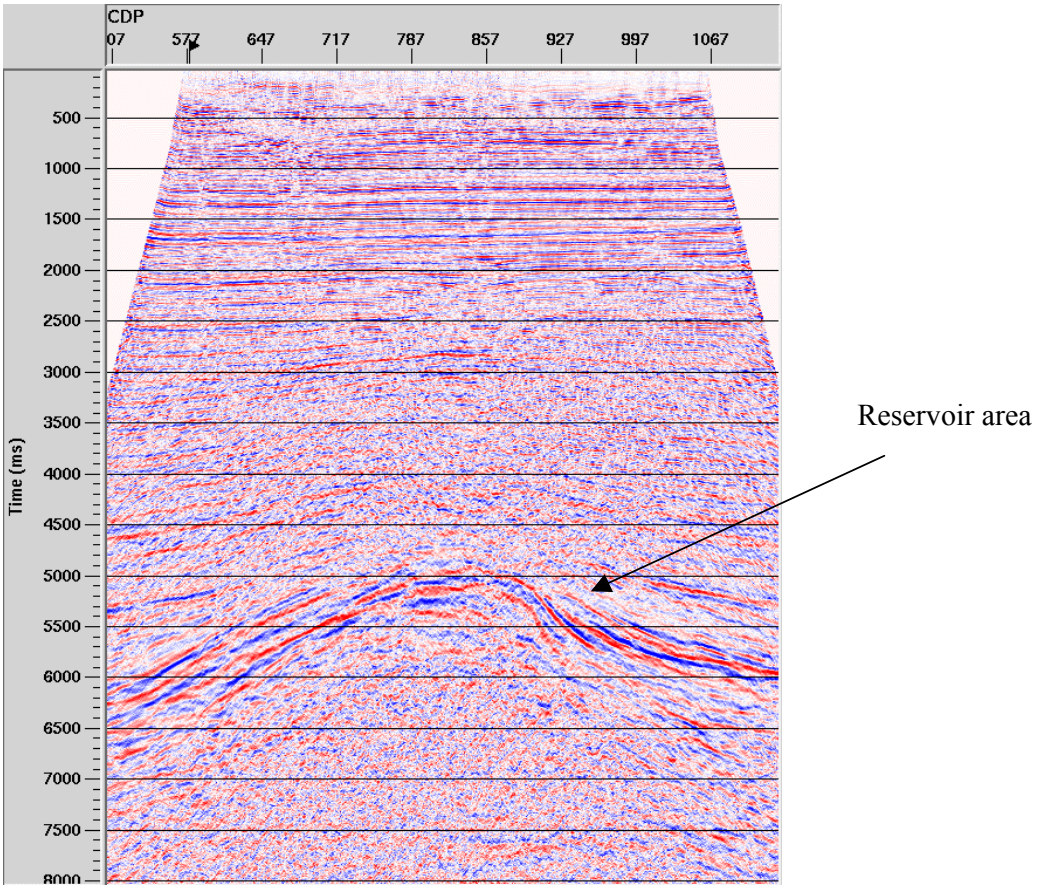


**Figure 5.3:** C-wave brutestack after preprocessing. Notice the low signal-to-noise ratio compared to the P-wave brutestack. The main event, at around 5 seconds, shows good continuity. No pull-down effects are noticeable.

## 5.4. P-wave imaging

In the selected flow velocity analysis, DMO and migration are the key imaging processes. The imaging task is achieved using the following sequence:

1) CMP sorting,
2) Initial velocity analysis at a coarse interval of 80 Common Mid Points (CMPs), (1000 metres interval),
3) Apply NMO correction,
4) DMO,
5) Remove NMO,

6) Second velocity analysis at finer interval of 40 CMPs (500 metres),
7) Stack,
8) Post-Stack Kirchhoff Migration.

A general explanation on this flow was given in Chapter 2. Here I add a few practical details: DMO runs in common-offset planes and requires good fold in each plane. That is, every plane has to be fully populated by seismic traces. Careful testing is required to ensure full coverage. For the Lomond data the optimum bin size was 50 metres, i.e. two traces per bin giving a trace interval of 25 metres.

NMO + DMO-corrected gathers present flat primary reflections and (maybe) still dipping multiples and noise. At this stage it is important to define the optimum mute before stack. Since the NMO correction used is based on the hyperbolic approximation valid for the near offset only, the mute has to be severe. Figure 5.4 shows two CDP gathers after DMO and new velocity analysis with the selected mute applied after step 6. The main events are well flattened proving that the NMO velocity applied in the NMO correction is correct.

The top half of Figure 5.5 shows the DMO velocity field, warm colours indicate high velocities, cold colours are for low velocities; the colour scale is shown in bottom left. This colour scheme is followed throughout this chapter. A small minimum associated with the gas cloud in the central area can be seen.

Before migration, velocities need to be smoothed, as most migration algorithms do not handle rapid changes in velocities in the horizontal direction. It is appropriate to test the optimum velocity performing migrations with velocity variations in percent of the smoothed stacking velocity. The optimum migration velocities are in fact often slightly slower than the stacking ones. This is a well-established rule of thumb in the industry. A possible explanation for it is that this correction compensates for the theoretical and systematic difference between RMS and stacking velocities (Cordier, 1985). Although we use the terms RMS and stacking velocities as synonyms the two are slightly different. In fact, stacking velocities are offset-dependent by definition (the velocity producing the best stacking response in the CMP gather). When the maximum offset tends to zero, the stacking

velocity tends to the RMS velocity (Hubral and Krey, 1980). This is the velocity used in post-stack migration (zero-offset). Since in a stratified, horizontal, either isotropic or anisotropic medium the stacking velocities increase as function of the maximum offset used (Robein 2003), we need to lower them prior to migration. This difference becomes higher in the presence of VTI. After several tests, 95% of the smoothed stacking velocity proved to be the best. The migration algorithm chosen was the Kirchhoff summation, since it is able to handle gentle lateral velocity variations and steep dips. The migration velocity field is shown in the bottom half of Figure 5.5.

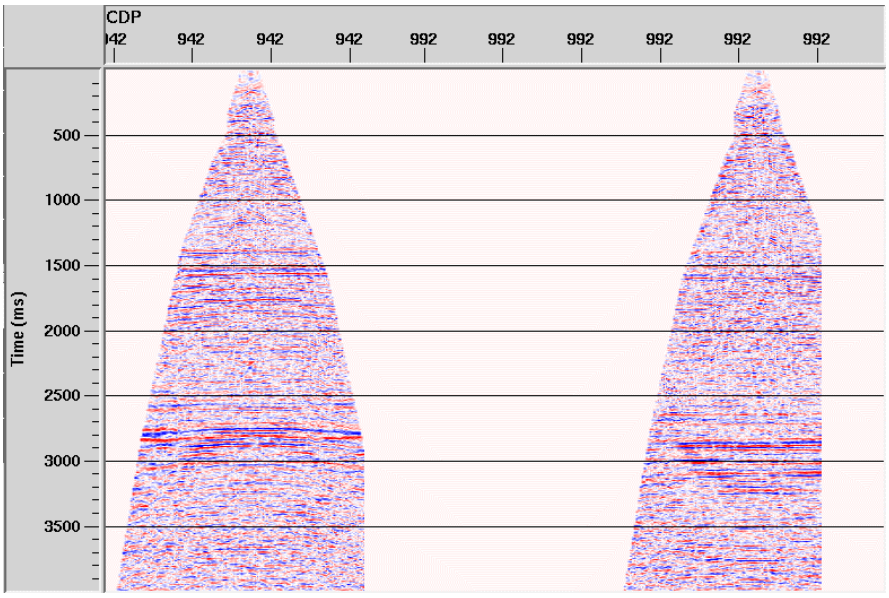


**Figure 5.4**: CDP gathers after DMO and the second velocity analysis. The events are well flattened, the mute shown is the same as that applied during the final stack.

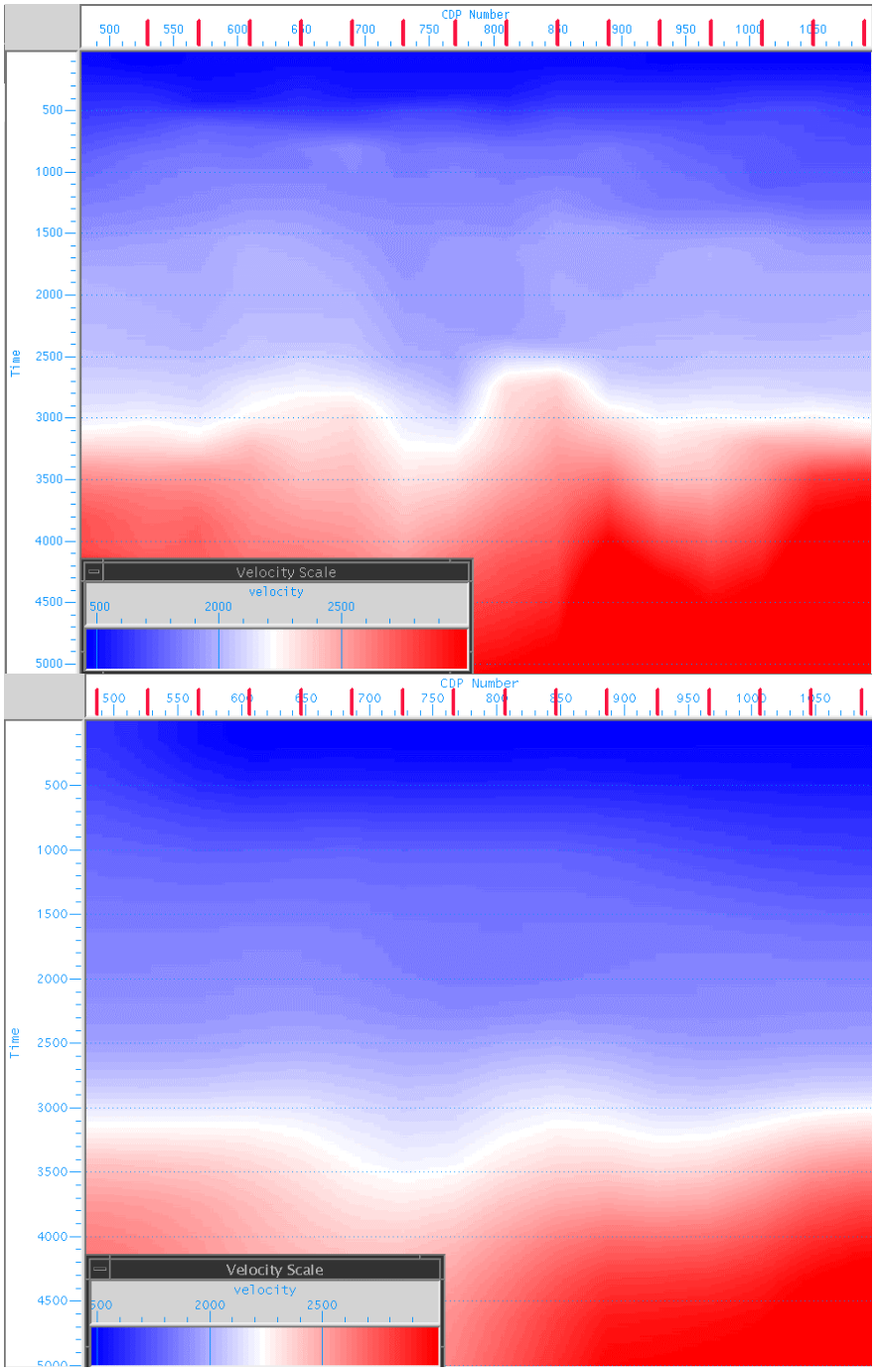


**Figure 5.5**: Top: DMO velocity field after the second velocity analysis. The small decrease in the RMS velocity in the central part of the section is due to the presence of gas. Bottom: Migration velocity field obtained smoothing the DMO velocity field and reducing its value by 5%.

The P-wave final stack after DMO is shown in Figure 5.6. There are not huge differences compared with the brutestack, the main improvements, indicated by the three arrows, can be found for the reflector at 2.7 seconds, in the middle of the section, and at around CDP 940, where it is now possible to see clearly an unconformity trap. Greater continuity can also be observed on the left flank of the dome structure

Figure 5.7 shows the Kirchhoff post-stack migration, the effect of the gas cloud in the central part of the section appears to be very strong. The gas cloud obscures the top of the reservoir, making any attempt at interpretation reliant on guesswork. Apart from this central area the rest of the section is well imaged even in areas of steep dip.

This final result highlights the main problem in the Lomond field as far as imaging is concerned, and fully justifies the extra costs required for multicomponent acquisition. In Appendix E, for completion, I show the imaging results from the PSTM, which, in substance, do not alter the main considerations on the quality of P-wave imaging in this area.

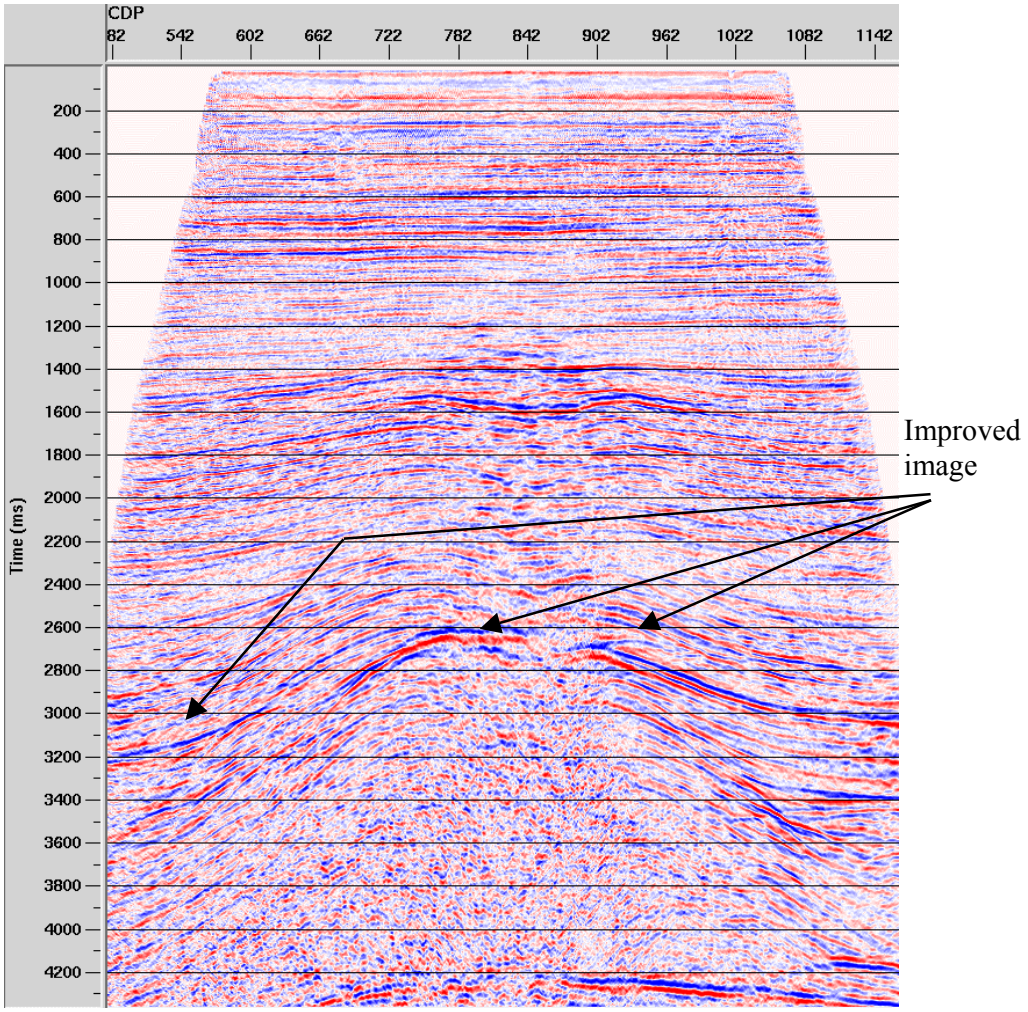


**Figure 5.6**: P-wave DMO final stack, The arrows show where the bigger improvements in image quality compared to the brutestack took place: greater continuity can be observed in the middle of the section, and at around CDP 940, at a depth of 2.7 seconds, and on the left flank of the dome structure.

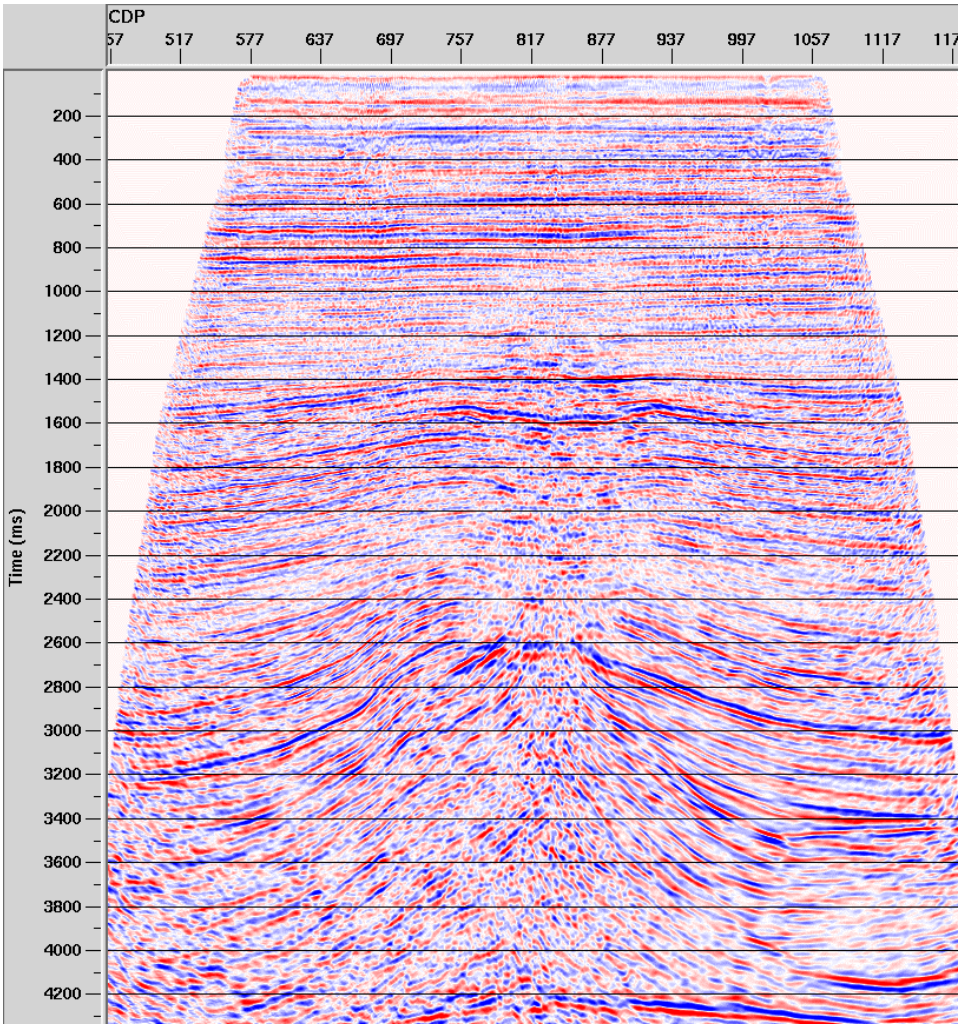


**Figure 5.7**: P-wave final migration. The result outside the gas-affected area is excellent. The steepest events are now well imaged. The gas cloud still obliterates the main events making interpretation impossible.

## 5.5. Converted wave processing, pre-DMO

The DMO+Migration flow for C-waves is very close to the P-wave one:

1) ACCP sorting,
2) Initial velocity analysis (pre-DMO) at a coarse interval of 80 ACCPs (around 1000 meters),
3) Apply NMO correction,
4) ACCP stack,

As explained in Chapter 2, C-wave binning requires information about the velocity ratio, $\gamma$. Since this value is not known in advance, an initial guess has to be made. For convenience a good approximation is to assume this initial $\gamma$ invariant in depth. To avoid nomenclature confusion I call it $\gamma_{asy}$. $\gamma_{asy}$ enables us to sort the data into ACCP gathers. In Chapter 7 I analyse in detail the effects that this initial choice has on the velocity analysis and on the calculation of the NMO and effective velocity ratios. Looking at results from geologically similar fields, for example the Tommeliten Alpha, I choose $\gamma_{asy}$ equal to 1.60.

Velocity analysis is carried out on ACCP gathers with the same velocity tool used for P-waves. We saw in Chapter 4 how the energy for converted waves is at its maximum in the medium and long offset. But at the same time, since the NMO equation applied follows the hyperbolic approximation, the events in this offset range are not properly corrected. High sensitivity to polar anisotropy and complex geology induce strong residual moveout on ACCP gathers. The left part of Figure 5.8 shows an ACCP gather (800) after hyperbolic NMO in which the residual moveout and far traces stretch are evident. The same gather with a severe mute applied is shown in the right part of Figure 5.8. The residual moveout is eliminated at the expenses of ignoring large quantity of data.

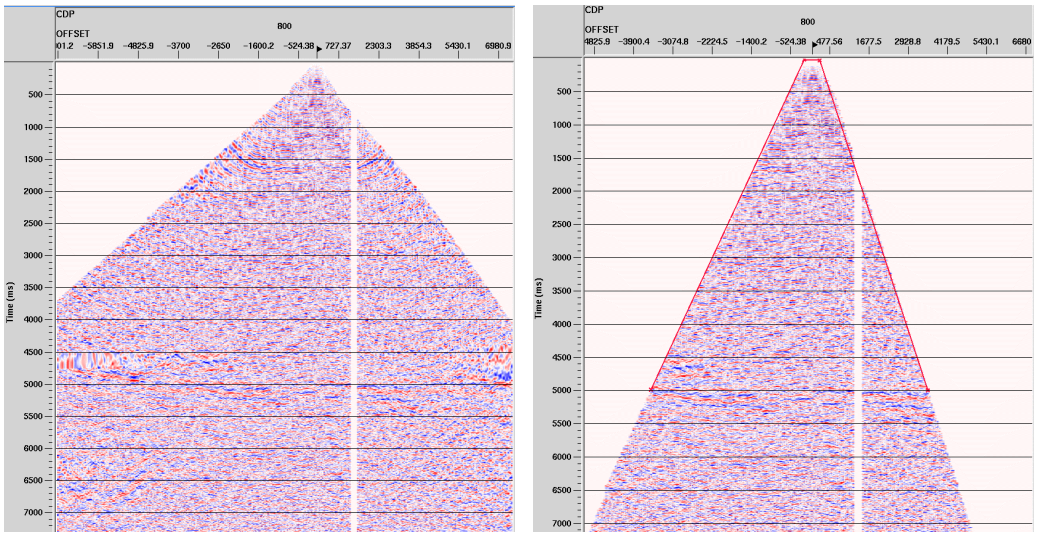


**Figure 5.8:** ACCP gather 800 before and after the mute. To eliminate the strong residual moveout and far offset trace stretch a severe mute is needed and large quantity of data is discarded.

There are two important factors to consider when processing C-waves acquired in areas with heterogeneities with a split-spread acquisition: the presence of diodic velocities and the effects of dip. In Chapter 4 I showed that the negative and positive offsets, in areas affected by gas and dip, have different apparent velocities. The solution in this case is to process the two offset volumes independently. The advantages of this approach can be appreciated in Figure 5.9, which shows two C-wave brutestacks: on the left the image is obtained with velocity analysis on the full gathers, while the image on the right is obtained by splitting the offsets during velocity analysis and NMO and merging them during stack. The image obtained by splitting the offsets shows improved continuity of the events at around 5.4 seconds, circle in black. This stack is the same as that shown in Figure 5.3.

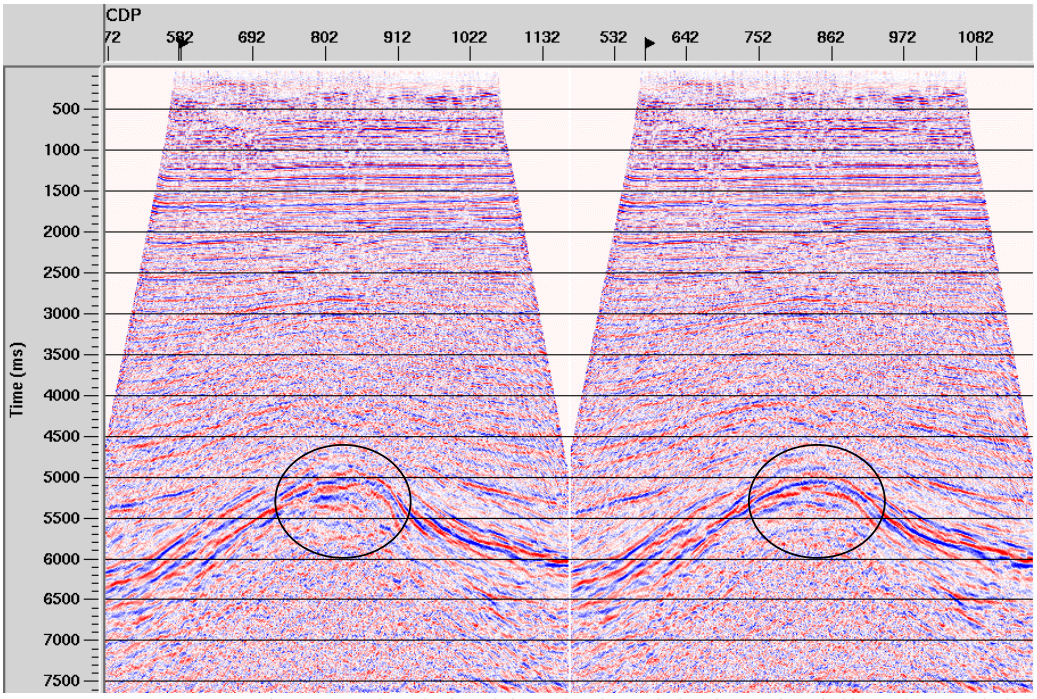


**Figure 5.9:** C-wave brutestacks: left with velocity picked on the full gathers; right: with velocity picked independently on the positive and negative offsets. In the black circles I highlighted the area showing greater improvements.

The next part of the processing sequence is specific to C-waves:

5) Event correlation in P and C-stacks – extraction of vertical depth variant $v_p/v_s$, $\gamma_0$
6) Computation of the effective velocity ratio using velocity information and/or the CCP-scanning technique
7) CCP binning using $\gamma_{eff}$
8) PS-DMO
9) Inverse NMO and new velocity analysis at 40 CCPs interval
10) Stack
11) Migration

Correlating events in the P and C-stack (pseudo zero-offset sections) leads to the arrival times $t_{p0}$ and $t_{c0}$. $t_{p0}$ is the one way P-wave arrival time, while $t_{c0}$ is the composed, P-down/S-up, arrival time. Using equation (5.1) we calculate the one way arrival time for S-waves, $t_{s0}$.

$$t_{c0} = t_{s0} + t_{p0}, \; t_{s0} = t_{c0} - t_{p0}. \tag{5.1}$$

The opposite ratio of the arrival times, $t_{s0}/ t_{p0}$, gives the vertical time (depth) dependent velocity ratio, $\gamma_0$. Figure 5.10 shows the event correlation carried out in the Lomond field. The vertical component DMO stack is on the left, the ACCP brutestack from the inline component is on the right. The arrival times for the inline component have not been changed, the section has just been "squeezed" to roughly ma*tc*h the P-wave one. The reason for that is to avoid any bias in the interpretation. Five events were correlated. At the target, given the geological structure, the correlation is made with a good degree of confidence, but in the shallower part there are uncertainties. This processing step is the principal weakness in the flow; nevertheless it is a necessary one. In Chapter 6 I discuss the possibility of using a well log derived $\gamma_0$ to avoid event correlation

Figure 5.11 shows the values of $\gamma_0$ (average) in P-time: as expected, $\gamma_0$ is higher in the shallow part, where sediments are unconsolidated and S-wave velocity is lower, and decreases with depth; the value of $\gamma_0$ at the reservoir, 2.6 seconds in the P-stack, is around 2.8. The colour scheme follows the velocity one, with warmer colours for higher values. A minimum in the $\gamma_0$ field can be seen in the gas-affected area.

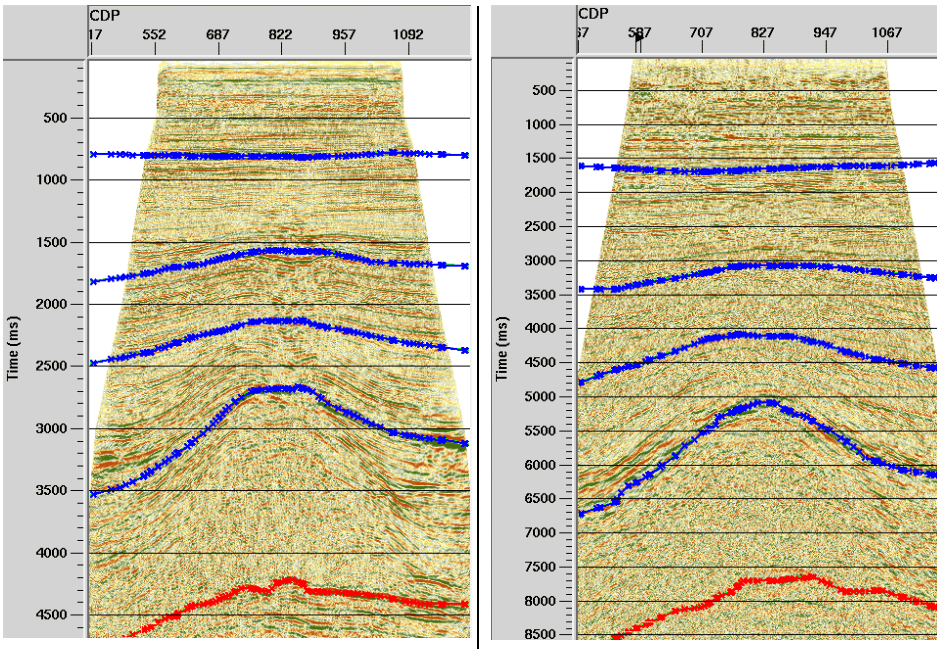


**Figure 5.10**: Event correlation, P-stack on the left and C-stack on the right. Five events were correlated.

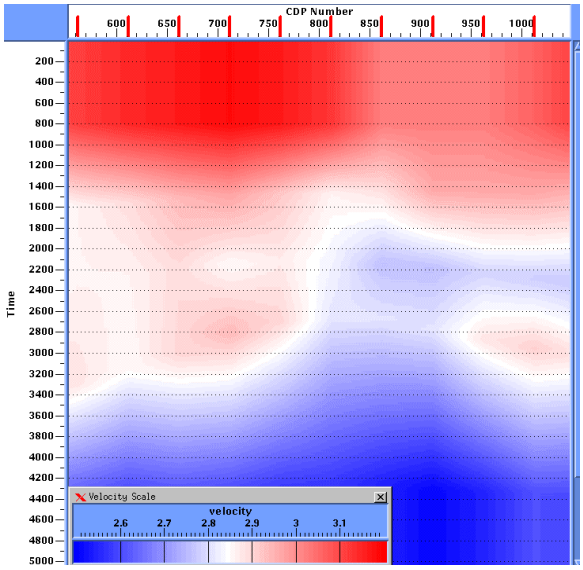


**Figure 5.11**: Average $\gamma_0$ shown in P-time from event correlation. The shallow part has higher values since sediments are unconsolidated and S-velocity is low. A gas-induced minimum can be seen in the central part of the section. The scale shows the values of $\gamma_0$.

This time-dependent $\gamma_0$ can be used to display the C-wave section into P-wave time as shown in Figure 5.12.

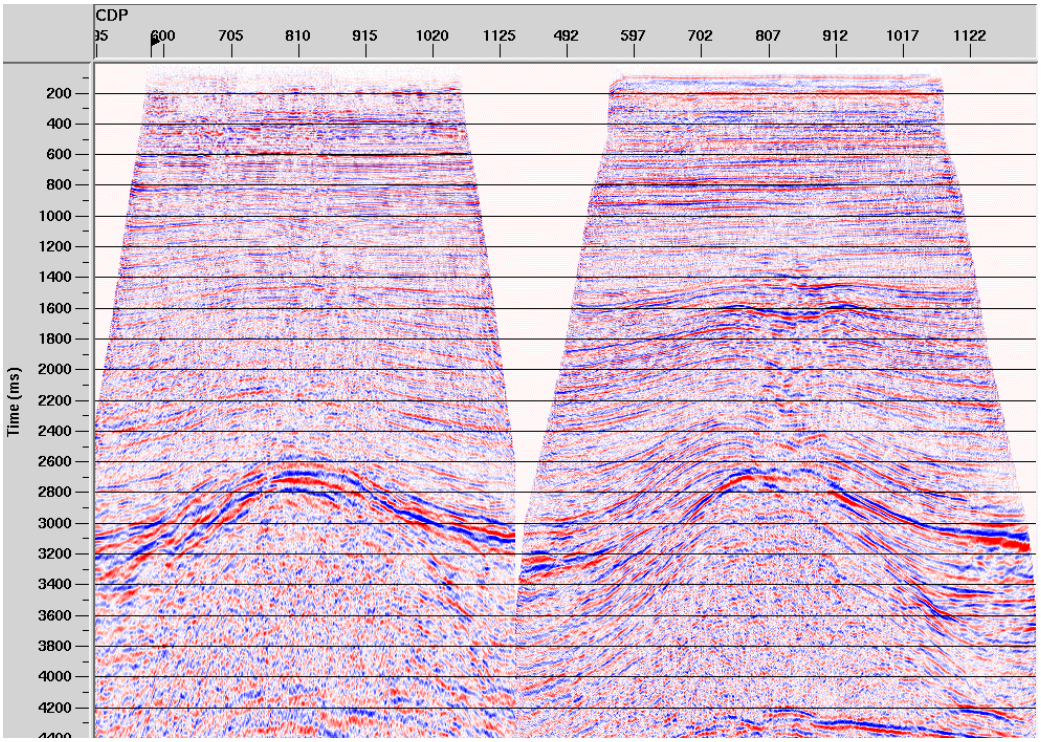


**Figure 5.12**: C-wave section displayed into P-time using the depth variant $\gamma_0$ from event correlation. C-stack on the left and P-stack on the right.

Li et al. (2002) proved that both the CCP position and the C-wave traveltime are not very sensitive to change in the vertical velocity ratio, which is good news since it shows that a raw event correlation does not compromise the accuracy of the entire processing. Figure 5.13 shows their results from an analytical test in a single layer of Dog Creek shale (see Chapter 2), 1000 metres thick, using respectively equation (2.59) and equation (2.56) for CCP position and traveltime computations. It can be seen that for up to 15% variation in $\gamma_0$ the CCP position varies less than 15 metres and the traveltime varies less than 10 milliseconds. In general the near offsets appear to be more sensitive than the far offsets.

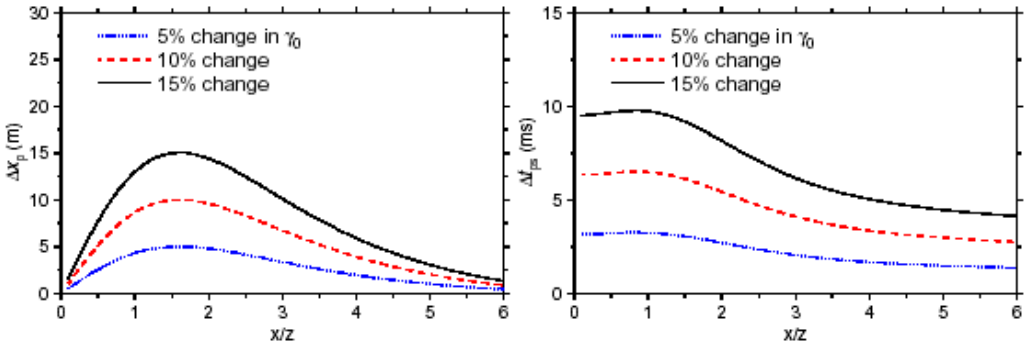


**Figure 5.13**: Left: varieation of the CCP position ($x_c$) with changes in $\gamma_0$, right, vatiation of C-wave traveltime ($t_c$) with changes in $\gamma_0$.

## 5.6. Velocity ratios analysis

This section describes one of the key phases in converted wave processing: the calculation of the effective velocity ratio. Geological complexity, presence of gas and polar anisotropy are all factors that play a role in this task. I discuss here two main methods of calculating $\gamma_{eff}$, one based on velocity information only, equation (2.25), the other based on imaging principles, the CCP-scanning technique (Audebert et al., 1999).

For simplicity of reading I recall here equations (2.24) and (2.25):

$$\gamma_n = \frac{v_{pn}}{v_{sn}}, \tag{2.24}$$

$$\gamma_{eff} = \frac{\gamma_n^{\,2}}{\gamma_0}. \tag{2.25}$$

Equation (2.25) requires $\gamma_0$ and $\gamma_n$. $\gamma_0$ comes from the event correlation shown in the previous section; $\gamma_n$ is more complicated to calculate as it is based on NMO velocities. The NMO C-wave velocity and zero-offset travel time are linked to the P and S-wave NMO velocities and zero-offset travel times as follows (Thomsen, 1999):

$$v_{cn}^{\ 2} t_{c0} = v_{pn}^{\ 2} t_{p0} + v_{sn}^{\ 2} t_{s0} \,. \tag{5.2}$$

Using $\gamma_0$, equation (5.2) can be written as:

$$v_{cn}^{\ 2} = \frac{v_{sn}^{\ 2}}{(1 + 1/\gamma_0)} + \frac{v_{pn}^{\ 2}}{1 + \gamma_0}. \tag{5.3}$$

Manipulating equation (5.3), we can calculate $v_{sn}$ from $\gamma_n$:

$$v_{sn}^{\ 2} = v_{cn}^{\ 2}(1 + \frac{1}{\gamma_0}) - \frac{v_{pn}^{\ 2}}{\gamma_0}. \tag{5.4}$$

Hence we can obtain $\gamma_n$ and $\gamma_{eff}$ from equations (2.24) and (2.25)

Figure 5.14 shows velocity fields for positive and negative offsets, while Figure 5.15 shows the merged velocity field. We can notice high values on the side of the dome structure; the effects of dip are evident in these high apparent velocities, even after PS-DMO. This confidence in assuming that these high velocities are due to dip is justified by looking at the velocities after PSTM (see Figure 7.10 in Chapter 7), where these effects disappear. These high velocity zones leave a clear "imprint" in the $\gamma_n$ and $\gamma_{eff}$ fields. The effects of dip on the C-wave velocity will be analysed in detail in Chapter 7. The gas-effects on the negative offset data can be noticed on the RMS velocities. In the central area, around CCP 800, they are lower than the positive offset velocities.

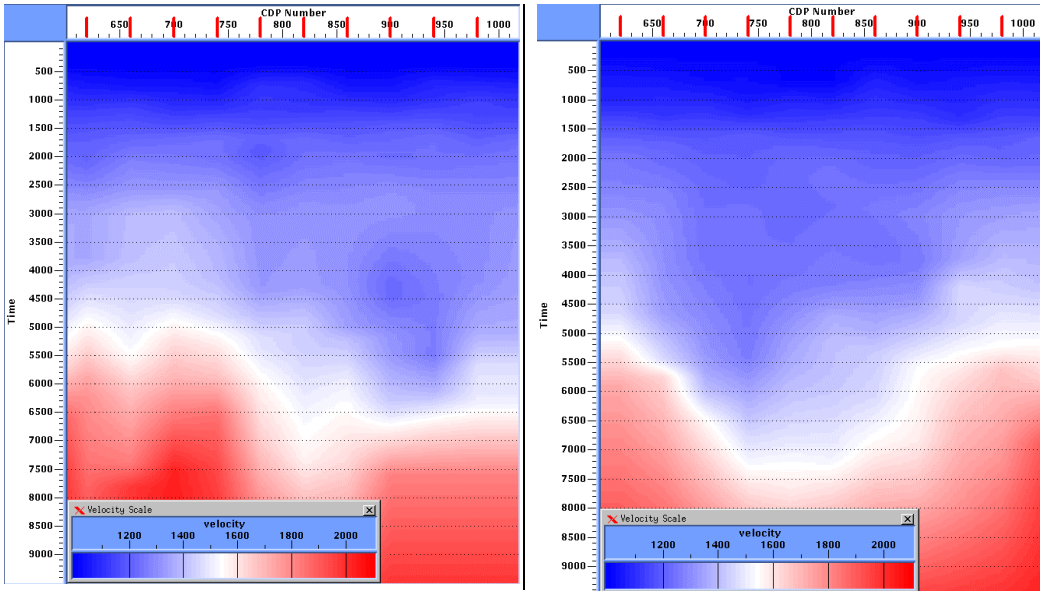


**Figure 5.14**: Left: post-DMO velocity field for the positive offset. Right: velocity field for the negative offset. The areas of steep dips, on the side of the dome structure, show high apparent velocities, even after PS-DMO. Both offsets show relatively low velocity values in the central area.

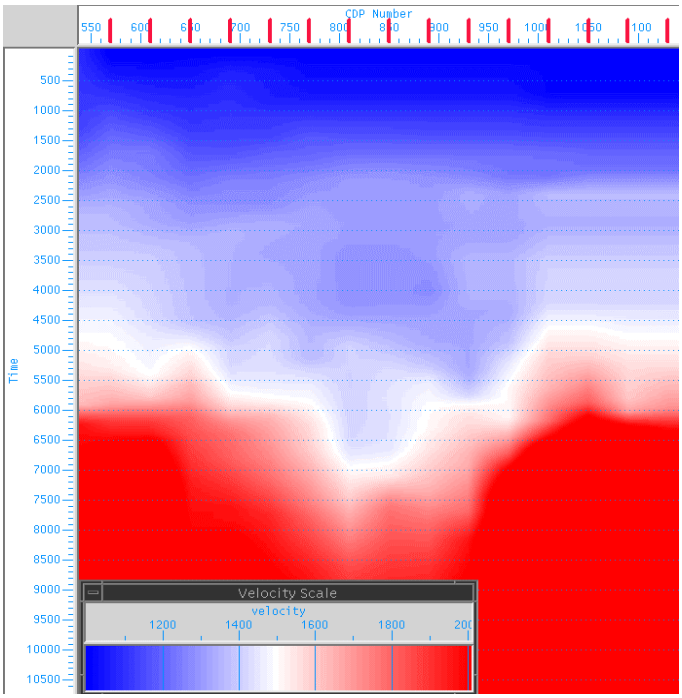


**Figure 5.15**: Merged C-wave Post-DMO velocity field. Again the effects of dip and gas can be easily recognised.

The $\gamma_n$ field is shown in Figure 5.16. The vertical axis is the arrival time in P-time; the colour scale is shown in the top left. The $\gamma_n$ field presents two well-defined areas of minima, with values close to 1.4, on the sides, related to the high C-velocity zones, and higher values in the middle of the field, where dips are minimal. At the reservoir area, 2.4 seconds, $\gamma_n$ is about 1.9. The high P-wave velocity in the salt body produces the high value at the bottom of the picture, in which $\gamma_n$ reaches values of 2.4. The asymmetry in the high velocity zone is due to the correlation of the deepest event (in red in Figure 5.10). On the left of each section the event "disappeared", making the correlation guesswork. The same situation is visible in the $\gamma_{eff}$ diagram.

Short spread stacking velocities are generally higher than the vertical velocities in a VTI medium. In the presence of polar anisotropy, either due to mineral orientation or fine layering (as far as processing is concerned their effects are equivalent and not discernible), $\gamma_n$ is expected to be lower than $\gamma_0$, as $\sigma$ is generally higher than $\delta$ and both $\sigma$ and $\delta$ are usually positive, see equation (2.45) and (2.46) in Chapter 2. The difference between the two ratios found in the Lomond data is quite high: at the reservoir $\gamma_n$ is around 1.9, while $\gamma_0$ is in the order of 2.8. This difference is a good indication of the presence of strong polar anisotropy for the shear waves.

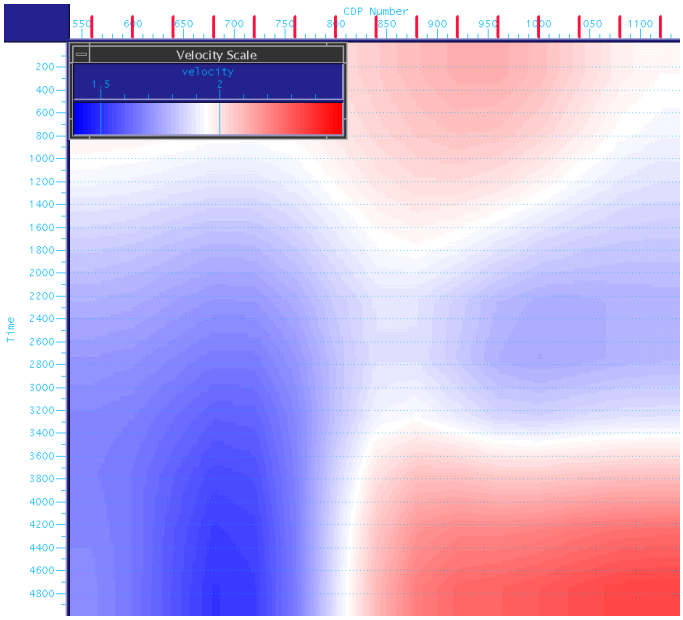


**Figure 5.16**: $\gamma_n$ shown in P-time. The field shows minimum values associated with the area of high apparent velocity due to the presence of dip. At the bottom, high P-velocities in the salt produce an area of high $\gamma_n$ value. The scale shows the values of $\gamma_n$.

Given $\gamma_n$ and $\gamma_0$, the resulting $\gamma_{eff}$ field is shown in Figures 5.17. $\gamma_{eff}$ varies between less than 1 and 1.6, which are values lower than $\gamma_n$ and much lower then $\gamma_0$. Again, the effects of dip produce "signatures", with lower values on the sides and higher values in the middle of the dome structure. Also the effect of the salt is visible. The effect of dip in the computation of $\gamma_{eff}$ is analysed in more detail in Chapter 7.

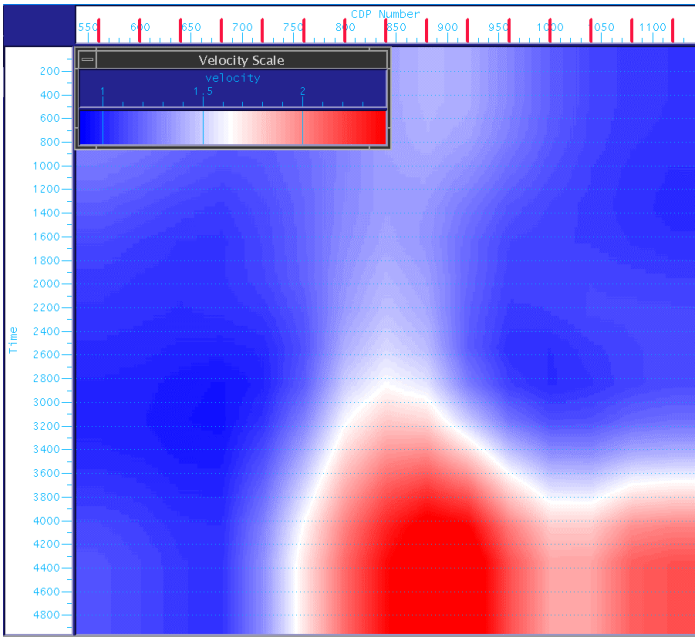


**Figure 5.17**: $\gamma_{eff}$ shown in P-time. The main features are similar to the $\gamma_n$ field, with higher values, about 1.6, in the middle and lower values, less than 1, in the sides of the salt dome. The scale shows the values of $\gamma_{eff}$.

In table 5.1 I show the velocities and the velocity ratios values CDP 740. I picked the RMS P-velocity for the horizon corresponding with the Top Balder. I then picked the RMS C-velocity in what I believe is the same event in the C-wave section. This correlation leads to the value of $\gamma_0$. Using equation (5.4) we can calculate $v_{sn}$, which enables us to estimate $\gamma_n$ (equation (2.24)). Using equation (2.25) we derive $\gamma_{eff}$. I used a program I wrote in C to carry out this task for the entire line.

| picked | picked | $t_{s0} = t_{c0} - t_{p0}$, $t_{s0}/t_{p0}$ | $v_{sn}^2 = v_{cn}^2(1+\frac{1}{\gamma_0}) - \frac{v_{pn}^2}{\gamma_0}$ | $\gamma_n = \frac{v_{pn}}{v_{sn}}$ | $\gamma_{eff} = \frac{\gamma_n^2}{\gamma_0}$ |
|---|---|---|---|---|---|
| $v_{pn}$ | $v_{cn}$ | $\gamma_0$ | $v_{sn}$ | $\gamma_n$ | $\gamma_{eff}$ |
| 2060 | 1420 | 2.8 | 1104.976 | 1.864294 | 1.241283 |

**Table 5.1:** Velocities and velocity ratios for CDP 740.

Figure 5.18 is a diagrammatic representation of the different raypaths along which we calculate the different velocity ratios. $\gamma_0$ is calculated along the vertical direction, shown in dotted lines; $\gamma_n$ is calculated along the dashed lines, which represent the raypath in a homogeneous layer. Finally $\gamma_{eff}$ is calculated along the continuous raypath, which takes into account the layering effects, or extrinsic anisotropy. On the top part of Figure 5.18 I show the calculation for the conversion point position (as a fraction of the total offset) given the values of the velocity ratios in table 5.1. We can see how the CCP position changes for the different ratios (the position for $\gamma_0$ is indicated by a red dot). If we consider 2000 metres offset, the shift from the correct position, given by $\gamma_{eff}$, and the position resulting from using $\gamma_n$ is 200 metres (10%). If we use $\gamma_0$ the shift becomes 380 metres (19%).

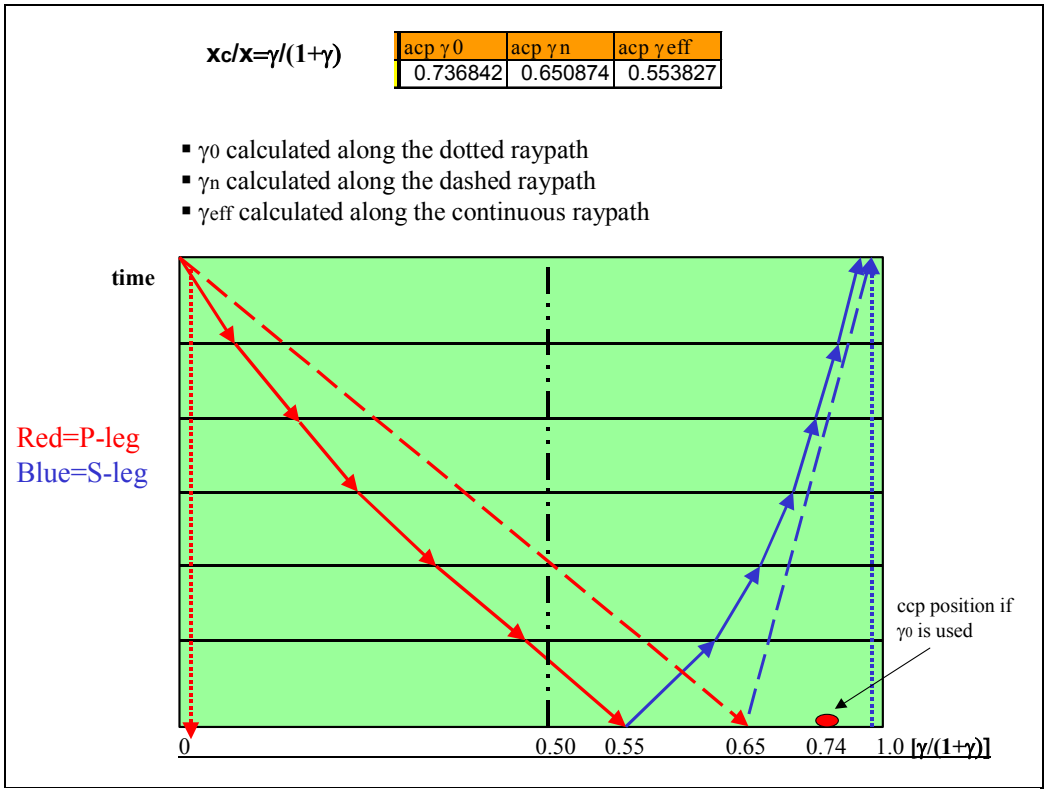


**Figure 5.18:** Diagram showing the raypaths along which we calculate the different velocity ratios. The dotted lines are for $\gamma_0$, the dashed lines for $\gamma_n$, and the continuous lines are for $\gamma_{eff}$. The CCP position is calculated as a fraction of the total offset. The values of the velocity ratios are taken from table 5.1.

## 5.7. CCP-scanning technique

The second method to extract $\gamma_{eff}$ is by using the CCP-scanning technique. This method is based on the fact that if the velocity ratio used during binning is correct, the conversions for the positive and negative offsets come from the same subsurface point. If, instead, a wrong value is applied, the two resulting images will be out of focus and will display a lateral shift in the geological structure; this process is explained in Figure 5.19.

The CCP-scanning technique can be applied in the time domain (Li et al., 2001), binning the positive and negative offsets with different constant values of $\gamma_{eff}$ ($\gamma_{asy}$), looking for the value which gives better image focusing and less (or no) lateral shift.

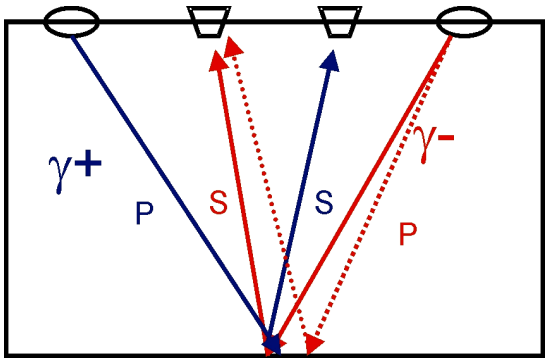


**Figure 5.19**: Scheme of the CCP-scanning technique: if $\gamma_{eff}$ is correct the conversions for the positive and negative offset come from the same sub-surface point, otherwise a lateral shift between the two images appears.

Figure 5.20 shows the results of the CCP-scanning technique applied at the reservoir area of the Lomond data. The values of $\gamma_{asy}$ tested were: 1.00, 1.25, 1.50, 1.75, 2.00 and 2.75. For each quadrant of Figure 5.20 the positive stack is at the top, the negative stack at the bottom. If we focus our attention on the top of the salt dome, the correct value of $\gamma_{asy}$ seems to be close to 1.50. This result is in good agreement with the central part of the $\gamma_{eff}$ field calculated using velocity information. As the value of $\gamma_{asy}$ increases the top of the dome structure shifts to the left, higher ACCP numbers, for the positive offset and to right, lower ACCP numbers, for the negative offset.

The low signal-to-noise ratio and the fact that the negative offset image appears to be disturbed by the presence of gas make the interpretation slightly more difficult. The value of 2.75 is close to the $\gamma_0$ from the event correlation at the reservoir interval but it is definitely a wrong value to use for binning, as the large shift testifies. In difficult areas for velocity analysis, such as those affected by gas clouds or severe dips, the use of the CCP-scanning technique becomes a necessary

step (Li et al., 2001). Its use as the first tool for estimating $\gamma_{eff}$ can reduce the risk of errors and the need for more iteration of velocity analysis, see Chapter 7.

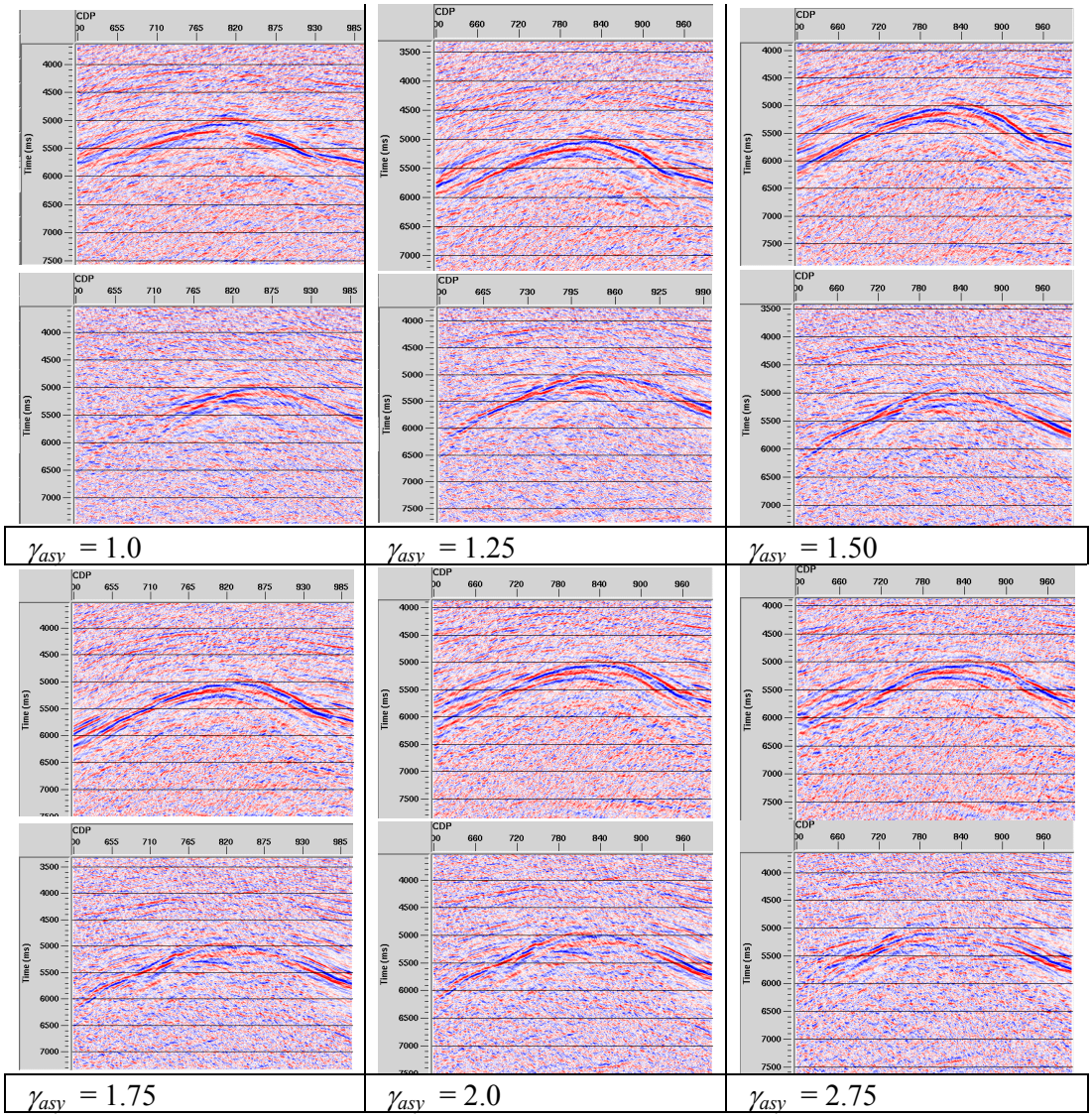


**Figure 5.20:** Positive (top ones) and negative offsets binned with different values of $\gamma_{asy}$. The value that creates the best alignment between the two offset stacks for the top of the salt dome is close to 1.50.

This analysis should also have been carried out for shallower events, but the lack of strong geological features makes the evaluation of any shift very difficult.

Considering also that the results from the CCP-scanning technique agree with the one from equation (2.25) in the areas of no dip, we can safely avoid repeating it in the shallower part of the Lomond data.

## 5.8. C-wave processing, post-DMO

The PS-DMO tool in ProMAX is derived from Harrison (1992) and takes into account the asymmetry of the ray path and the CCP dispersal. It also implements Tessmer and Behle's quartic equation for CCP positioning. The post-DMO sequence follows the one for P-waves, with new velocity analysis, stack and Post Stack Time Migration. Harrison warns that the use of Post-Stack Migration for C-waves is only a good approximation, which holds true if the velocity ratio does not change too much in depth. This requirement is met in the Lomond field, see Figure 5.17.

The left part of Figure 5.21 shows CCP 800 after PS-DMO and CCP binning. The near offset traces in the target area do not show coherent energy. To enhance the signal-to noise ratio in this part we can apply an inner mute, as shown in the right part of Figure 5.21.

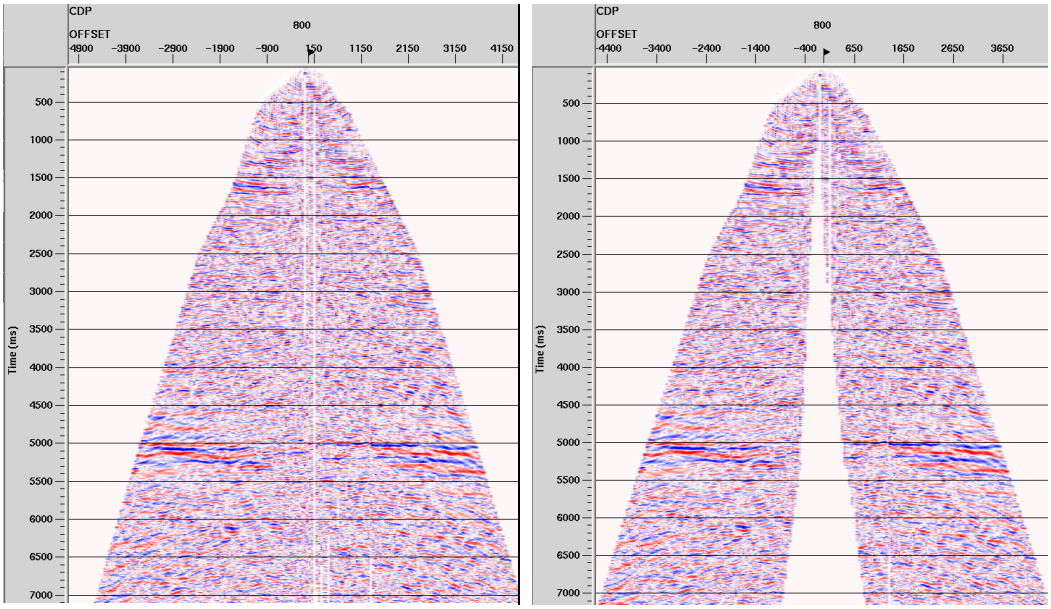


**Figure 5.21**: Left: CCP gather 800 after PS-DMO and second velocity analysis, the near offset data at target level do not show a strong signal. Right: same CCP after internal mute.

The final stack is shown in Figure 5.22. The post-DMO stack is a clear improvement over the pre-DMO one, Figure 5.3. It shows very good signal-to-noise ratio and much higher continuity in the main seismic events. Compared with the P-wave DMO stack, Figure 5.6, we can now distinguish some geological and structural features in the target area, such the fault circled in black.

A further improvement can be achieved if we discard part of the negative offset data. In fact, as shown in Figure 4.3, the negative offset data are more disturbed by the presence of gas. The full offset merging actually reduces the overall quality of the stack compared with the positive offsets only. If we use positive offsets only up to CCP 950 and then we merge positive and negative offsets after this point, we obtain the stack shown in Figure 5.23. The image shows better continuity above all on the crest of the dome structure and in the events just above.

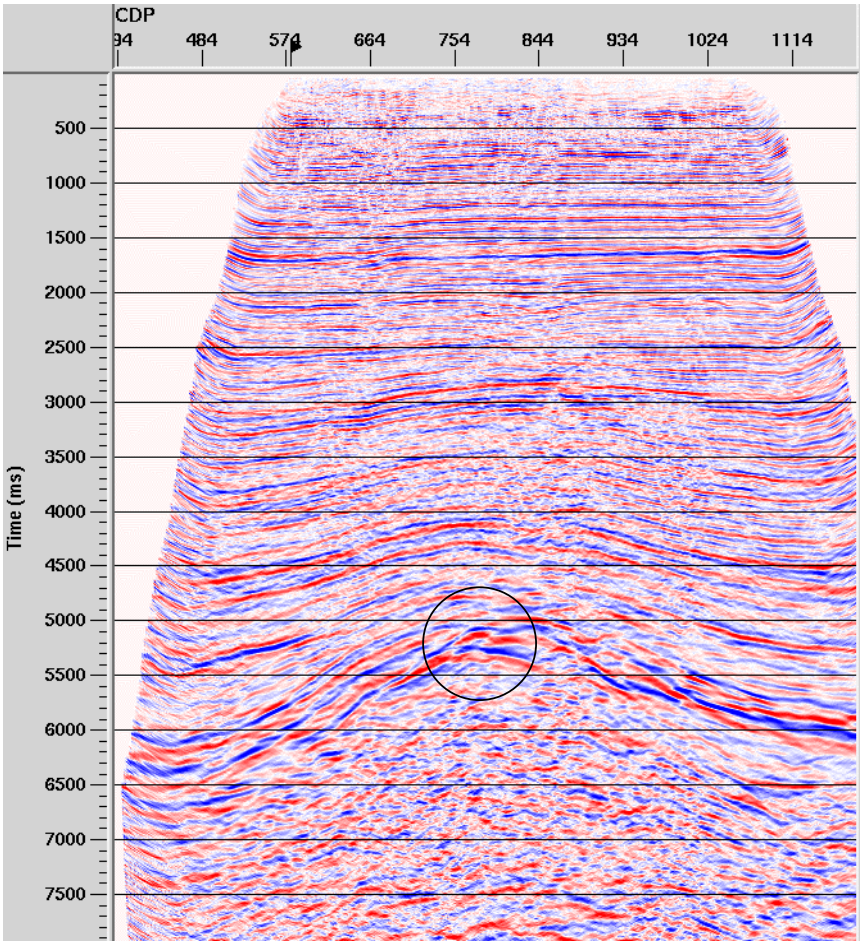


**Figure 5.22**: Final stack using both positive and negative offset data. In the target area we are now able to see geological features, such as the fault inside the black circle.

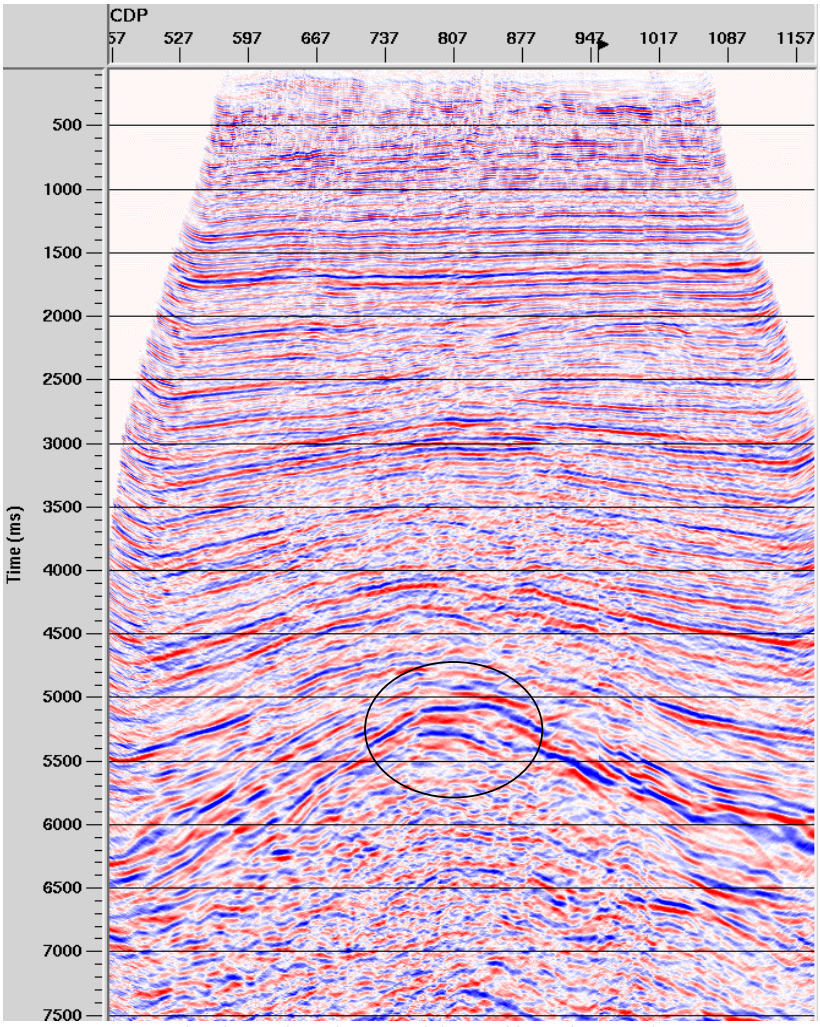


**Figure 5.23**: Final stack using positive offset data only up to CCP 950. Avoiding the disturbance caused by the gas produces a much clearer image in the central area, in the circle. The fault highlighted in Figure 5.21 is now clearer.

The stack in Figure 5.23 is the input to the post-stack migration. The migration velocity is obtained, again, smoothing and reducing the value of the NMO velocity. In the C-wave case the velocity reduction has to be greater. Harrison (1992) shows that in general the migration velocities are on average 6-11% lower than the NMO velocities, and this is in addition to the normal 5-10% adjustment you expect when obtaining migration velocities from NMO ones. This could be due to the higher sensitivity of the S-wave to polar anisotropy. After running a few tests the optimum

migration velocity field found was a smoothed, 90% value, of the NMO velocity field, Figure 5.24.

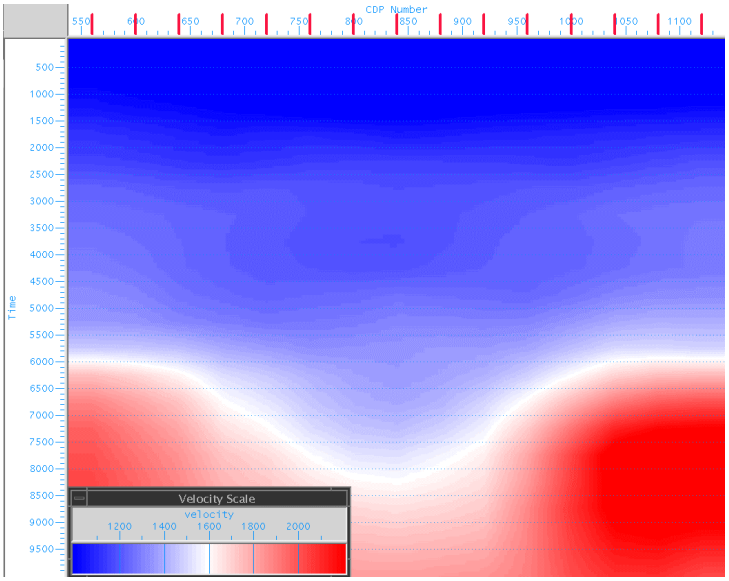


**Figure 5.24**: Migration velocity field, obtained as the 90% of the smoothed RMS velocity. It still features high values on the sides.

The migration algorithm applied is, as for P-waves, a Kirchhoff summation. The final image is shown in Figure 5.25. The result is clearly an improvement over the P-wave migration, Figure 5.7. Continuity and resolution are generally satisfying. This image is now suited for geological interpretation, since uncertainties are strongly reduced. In the target area, now free from gas effects, a horst structure can be easily identified.

The message we can extract from this section is that, even with a relatively simple processing sequence, C-waves lead to better imaging results than P-waves in areas affected by gas, confirming the conclusions reached by Granli et al. (1999).

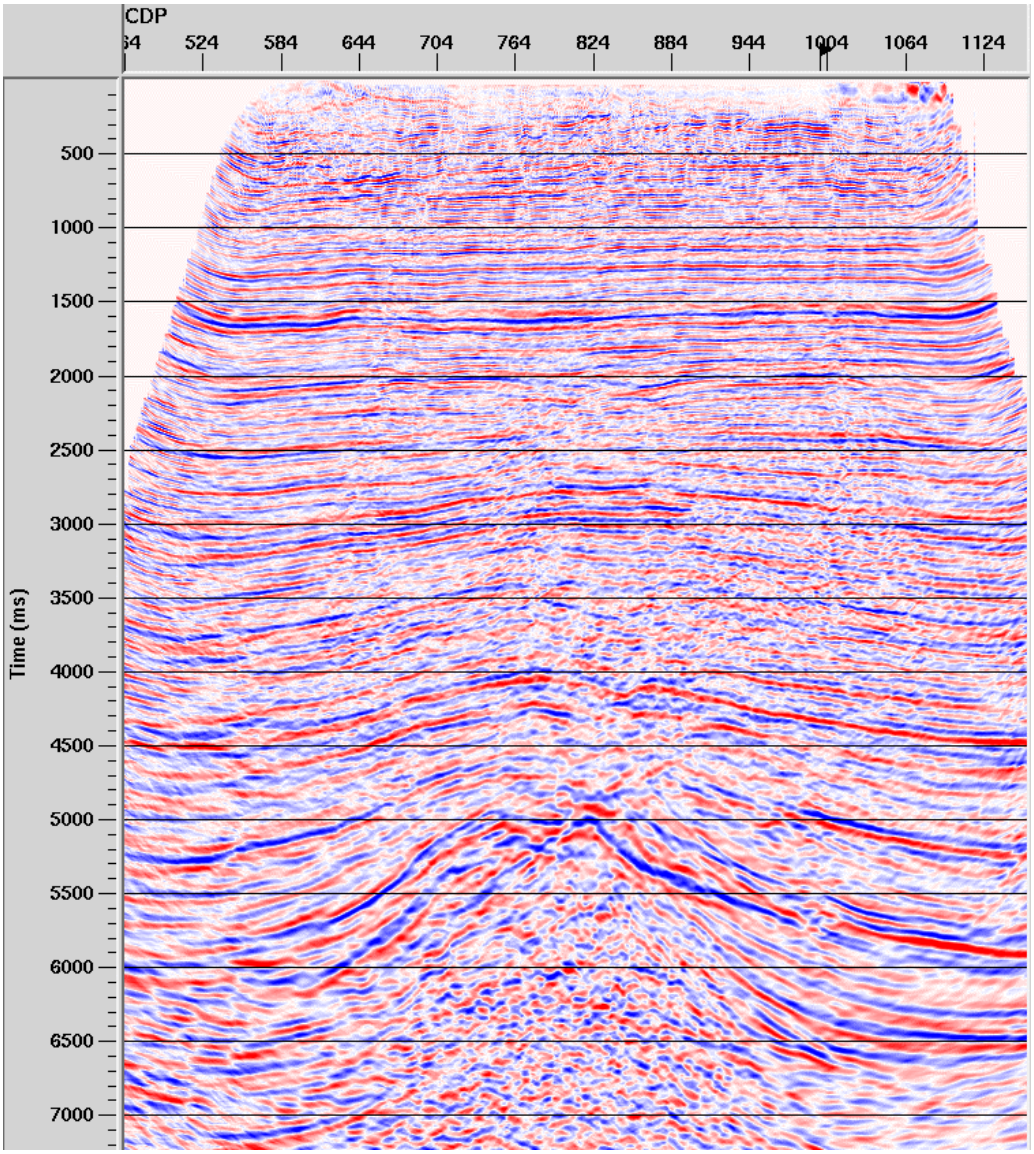


**Figure 5.25**: C-wave migration. The image shows clearly a horst structure at the top of the Lomond reservoir. The overall quality is good.

But, as Granli et al. (1999) warned, this is AN image of the Lomond field and by no mean THE image. Figure 5.26 helps us to understand this point better. It shows the 2D interpretation carried out by geophysicists and geologists at BG Group after receiving the 3D dataset processed by WesternGeco. They also used well information to define the thicknesses of the layers. The small box shows the profile location; the 2D seismic line is very close to this profile. This section is what they

believe to be the better representation of the Lomond field reservoir. If we overly this picture on top of the migration result, Figure 5.27, we see discrepancies in the shape of the horst structure, which seems too narrow in the seismic section, and in the inclination of the main faults as well as in the slope of the right flank in both cases quite a bit lower in the seismic data. So although the main geological structure has been revealed, the image does not seem to tie well with the geological information available. The reasons for this can, hopefully, be narrowed down to:

1. Ignoring the presence of anisotropy, both in DMO and migration;
2. Using the hyperbolic approximation for NMO correction, which leads to the discarding of large quantities of valuable data because of the necessity of using a severe mute, (this point can be partially linked to point 1);
3. Imaging limits of the DMO+Migration sequence.

I address these three points in Chapter 9, where I show the results from the anisotropic Pre Stack Time Migration.

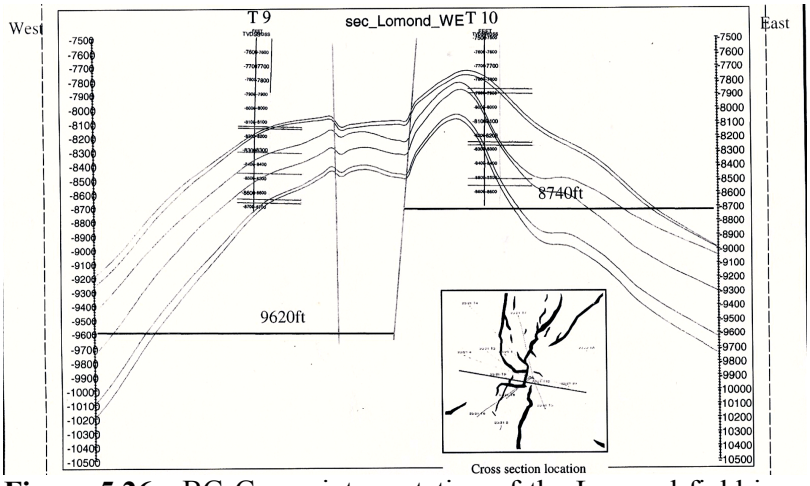


**Figure 5.26:** BG Group interpretation of the Lomond field in proximity of the 2D line, the results of well T9 and T10 helped to define the thickness of the sequence forming the reservoir.

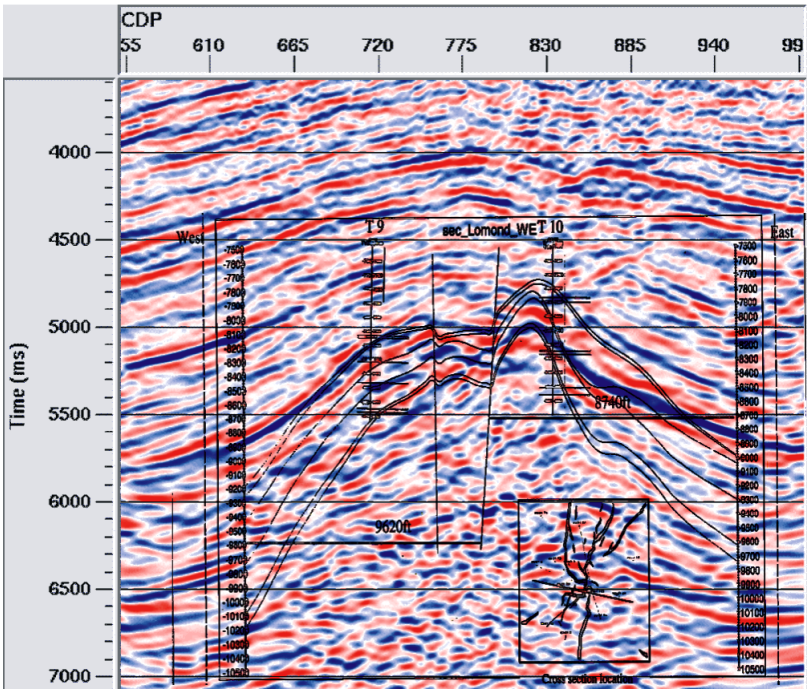


**Figure 5.27:** BG Group interpretation overlaid over the DMO+Migration image. The match is not satisfactory. The top of the horst structure appears too narrow.

## 5.9. The importance of $\gamma_{eff}$

As already mentioned, $\gamma_{eff}$ accounts for the effects of layered induced anisotropy; therefore $\gamma_{eff}$ is the key parameter for C-wave binning. Previous studies (Granli et al., 1999, for example) have ignored the layering effects and used $\gamma_0$ for binning purposes. I show here how this approach degrades the image quality for the Lomond data.

Figure 5.28 shows two Kirchhoff migrated images obtained with the same processing sequence: ACCP binning + hyperbolic NMO + PS-DMO + STACK + Post-STM. The only difference is in the binning: on the left I used $\gamma_0$, on the right $\gamma_{eff}$. The image obtained using $\gamma_0$ is poor; the energy is out of focus, particularly where the structure is complex, as in the crest of the salt dome. It looks like it is over-migrated, although the velocity used was only the 80% of the smoothed RMS

velocity. When $\gamma_{eff}$ is used, the quality of the image greatly improves, with much better focusing of the energy, especially in the central area.

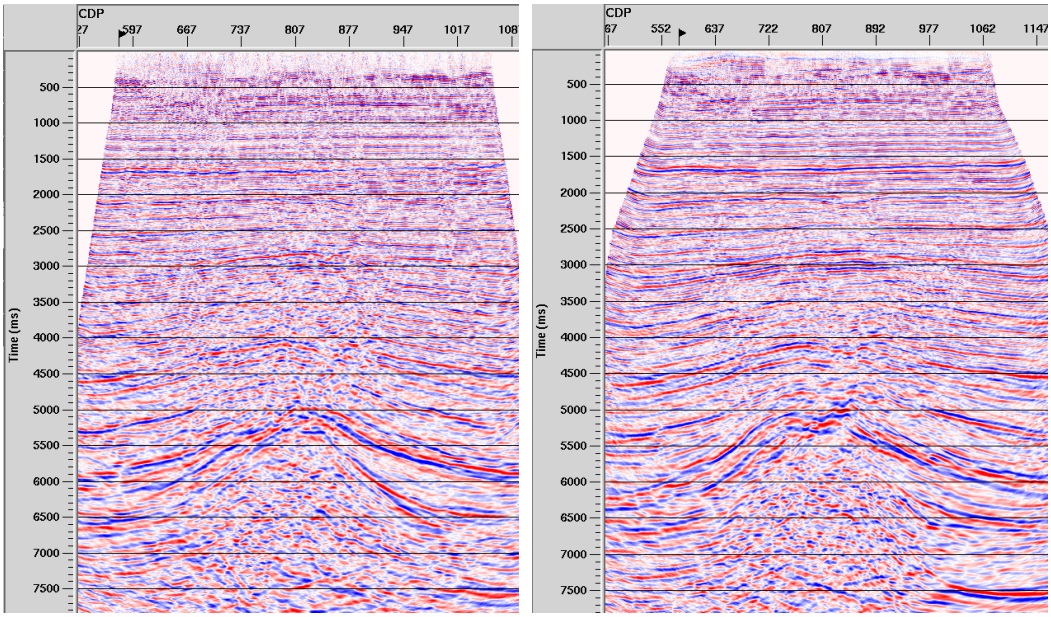


**Figure 5.28**: Left: Post-Stack migration using $\gamma_0$ for binning. Right: Post-Stack migration using $\gamma_{eff}$ for binning. The image quality on the left is quite poor, with energy out of focus. The use of $\gamma_{eff}$ greatly improves imaging.

## 5.10. Conclusions

This chapter showed the initial processing of multicomponent seismic data from the Lomond field. The processing flow applied can be considered a "conventional" flow, although some differences exist in the analysis of the velocity ratios. The sequence is a DMO+PostSTM, both for P and C-waves. For processing simplicity:

- The NMO correction was based on the hyperbolic approximation. Long-offset correction was not applied and so severe mutes were needed to avoid residual moveout,

- Anisotropy was ignored during DMO and Migration.

For the vertical component the results are compromised by the presence of a large gas cloud just above the reservoir area: amplitude dimming and pull-down effects deteriorate the image quality in the key exploration area. The imaging results for the C-waves show clear improvements over the P-wave results. The reservoir area is now free of gas effects and can be more easily interpreted. However discrepancies can be seen between the seismic image and the interpretation of the field performed by BG Group. Limitation of the DMO+PostSTM sequence, valuable data being discarded and the fact that anisotropy was ignored are all factors that may have contributed to this mismatch. In Chapter 9 I will analyse these issues, but here it is worth emphasizing that even with these limitations C-wave imaging in areas affected by gas is superior to P-wave imaging.

C-wave processing highlighted the importance of using the correct velocity ratio; on this subject two main points need to be investigated:

- The possibility of using well log information to avoid the event correlation interpretative step,
- The effects of dip on C-wave velocity, $\gamma_n$ and $\gamma_{eff}$.

These issues will be addressed in the next two chapters.

# Chapter 6: Interpreting vertical velocity ratios from seismic data and well logs

## 6.1. Introduction

As seen in Chapter 5, one of the most difficult steps, and probably the one most prone to error in 4C seismic processing, is the event correlation between P and C-wave stacks. But the need to extract the vertical velocity ratio, $\gamma_0$, in order to obtain $\gamma_{eff,}$ requires this process. There have been suggestions (Leaney et al., 2001) about using well log information to overcome this interpretative step. Shear velocity can now be recorded during well logging thanks to a relatively new acquisition tool, the Dipole Sonic Imager (Schlumberger), which generates both shear and compressional waves. Two of the new wells logged in the Lomond field were acquired with this tool, see Chapter 4.

I present here the results of an integrated analysis of well and seismic data and, in particular, of the vertical velocity ratio obtained from the two datasets. I show how the well log-derived vertical $v_p/v_s$ ratio differs significantly (around 30%) from the value extracted from seismic data and I try to give an explanation, looking at some possible reasons such as the presence of gas, polar anisotropy, frequency-dependent absorption effects and, obviously, event correlation error. Gas does not seem to play a major role in the Lomond Field logs, while polar anisotropy lowers the $v_p/v_s$ ratio in logs by about 15%. Frequency-dependent dispersion is difficult to quantify directly. Studies by Eastwood and Castagna (1986) indicated that in a VTI medium the velocity ratio at log frequencies could be 10 to 15% lower than at

seismic frequencies. This two effects plus some residual errors in event correlation can explain the difference observed in the Lomond data

## 6.2. Interval $\gamma_0$ from seismic

The interval $\gamma_0$ is extracted from seismic data by event correlation. As explained in the previous chapter, this step is a very subjective, since it relies completely on user interpretation and can be easily a source of error. In Figure 6.1 I show again the event correlation carried out for the Lomond data, to highlight that when the geological structure is well defined there is high confidence in the correlation, but in area dominated by horizontal or sub-horizontal layering there is a lot of guesswork involved. After picking the arrival times at zero offset ($t_{p0}$ and $t_{c0}$) we can calculate $t_{s0}$ using equation (5.1). Then the interval velocity ratio is given by (De Angelo et al., 2003):

$$\frac{v_p}{v_s} = 2\left(\frac{\Delta t_c}{\Delta t_p}\right) - 1, \tag{6.1}$$

where $\Delta t_c$ and $\Delta t_p$ are the correlated time intervals for C and P-waves.

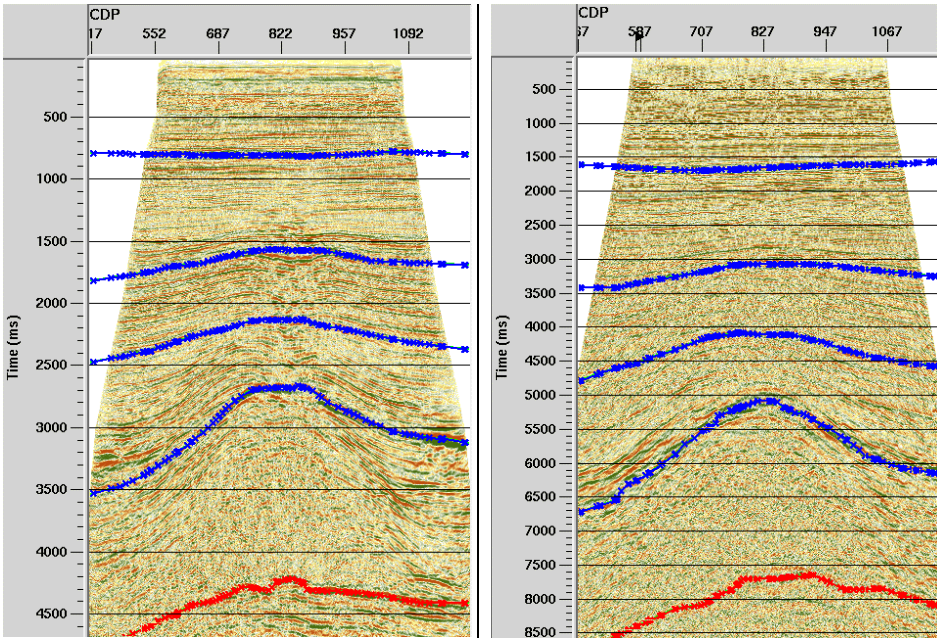


**Figure 6.1**: Event correlation, P-stack on the left and C-stack on the right. Note the uncertainties in interpreting the shallower part of the data.

The resulting interval $\gamma_{0,}$ from the correlation in Figure 6.1, is shown in Figure 6.2. I only display the interval between picked events, without including the interval from time = 0 to the first event.

Differently from the average $\gamma_0$, the interval $\gamma_0$ does not show the classic high values in the shallow part and lower values in the deep part, but tends to be quite constant at values of about 2.8 and then drops to value of around 2 for the last interval correlated. The area of interest is the penultimate layer; this is where the reservoir is located. In this interval $\gamma_0$ is between 2.8 and 2.9.

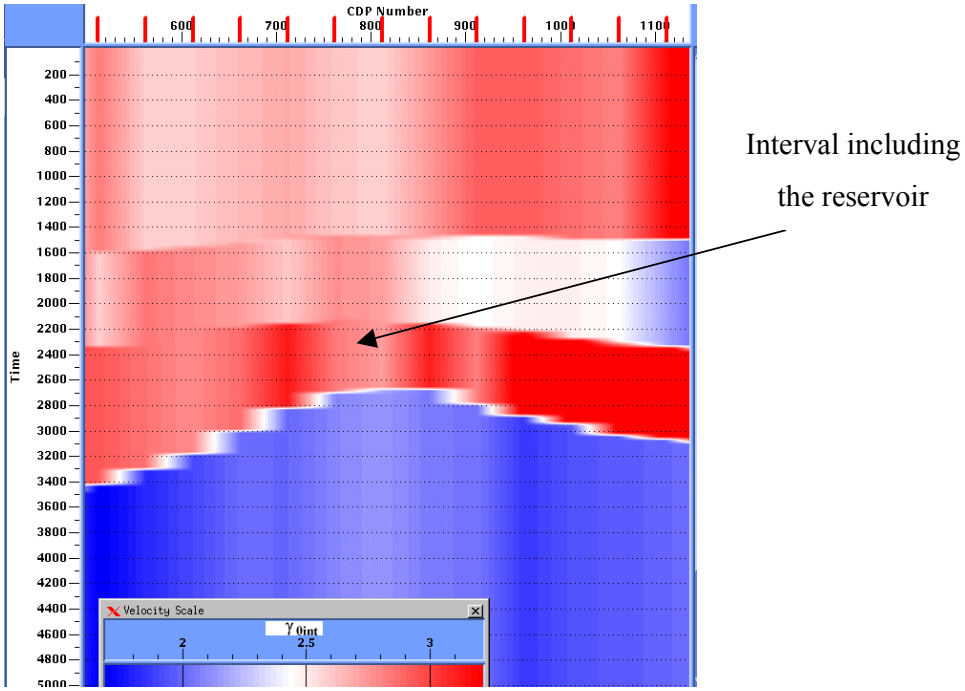


**Figure 6.2**: Interval $\gamma_0$ shown in P-time from event correlation. The interval of main interest, pointed by the arrow, is where the reservoir is located. In this interval the velocity ratio is around 2.8-2.9.

## 6.3. Velocity ratio in wells

Two new wells drilled in the Lomond field have shear logs. Well 23/21-T9 has about 26° of horizontal deviation at the reservoir depth, while well 23/21-T10 is less deviated: about 10°. They were both logged only in the interval between the Top Balder and the Ekofisk formations. The velocity ratio in this interval is similar for both of them, around 1.70 (see Figure 6.3).

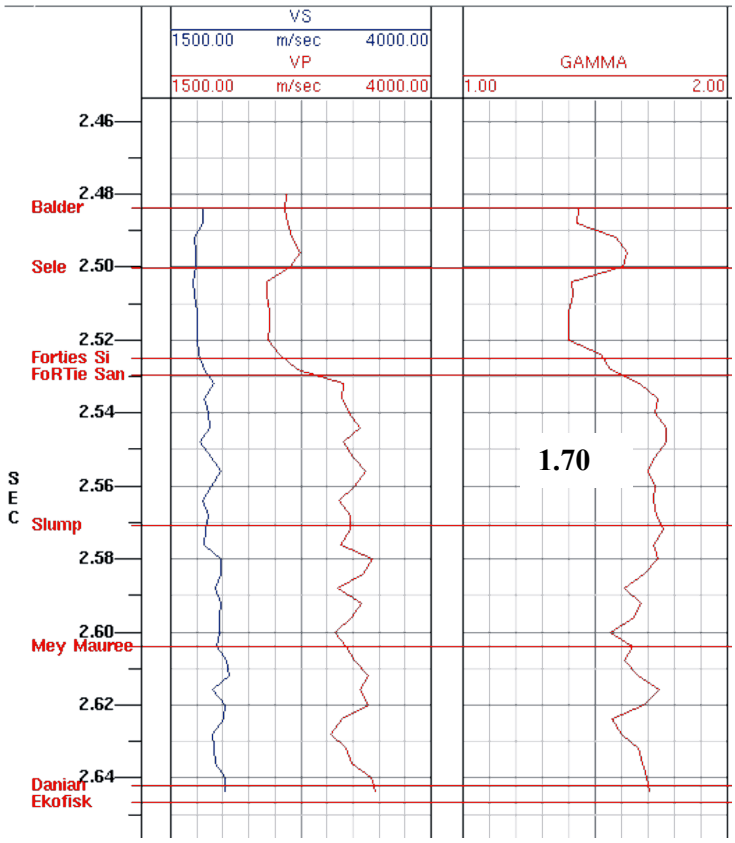


**Figure 6.3**: $v_{p0}$, $v_{s0}$ and $\gamma_0$ from well 23/21-T9. The interval $\gamma_0$ value between the Forties Sandstone and the Ekofisk is about 1.70, which is much lower than the value extracted from seismic data.

This value is considerably lower than $\gamma_0$ in the seismic data, which is around 2.8 in the reservoir area interval, and it is actually closer to the value of $\gamma_n$ or $\gamma_{eff}$ (see Chapter 5). The difference is almost 60%, which seems very high. As the first source of error in this case can be an erroneous event correlation, I decided to carry out a new, more refined, correlation only in the area included in the logs. With the help of some interpretation work by BG Group, I picked the two events shown in blue in Figure 6.4. The new results show a $v_{p0}/v_{s0}$ of around 2.3 in the area close to where well T9 meets the seismic section, Table 6.1.

One consideration should be made at this point: working at this detailed interval $\gamma_0$ is very sensitive to errors in the event correlation. If we had picked the event in red in the C-wave section in Figure 6.4, the $\gamma_0$ values would have been very different, as reported in the second row of Table 1.

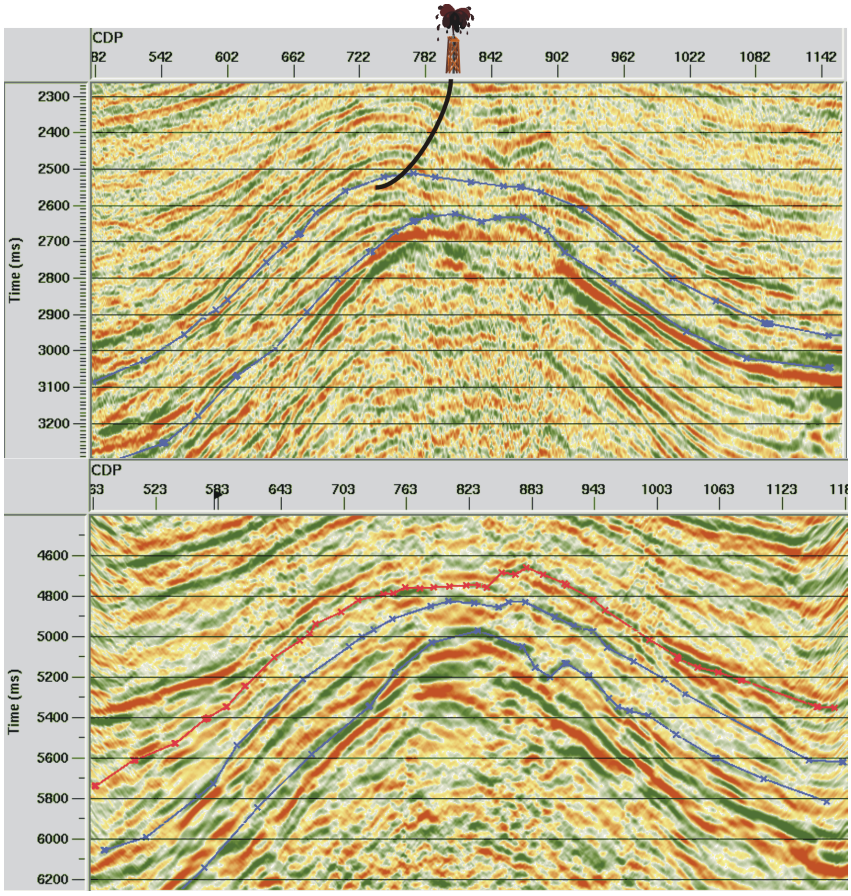


**Figure 6.4**: New event correlation in the reservoir interval. Top: P-stack, bottom: C-stack. The events picked are in blue, while in red I show a possible error in the event choice.

| ACCP | 600 | 680 | 760 | 840 | 900 | 960 | 1020 |
|---|---|---|---|---|---|---|---|
| Layer 1 | 2.38 | 2.31 | 2.24 | 2.01 | 2.31 | 2.39 | 2.47 |
| | | | | | | | |
| Layer 2 | 4.75 | 4.21 | 4.59 | 3.69 | 5.27 | 4.77 | 5.4 |

**Table 6.1:** Interval $\gamma_0$ from new event correlation in the reservoir interval. Layer 1 refers to the correct interpretation, layer 2 to the red pick for the top layer.

In order to verify the validity of the $\gamma_0$ values we can, again, use the CCP-scanning technique (Audebert et al., 1999), as shown in Chapter 5. Using Thomsen (1999), equivalent to equation (2.25), we can calculate $\gamma_{eff}$ for different value of $\gamma_0$:

$$\gamma_{eff} = \left[ (1 + \gamma_0) \left( \frac{v_{cn}^{\,2}}{v_{pn}^{\,2}} \right) - 1 \right]^{-1}. \tag{6.2}$$

$v_{pn}$ and $v_{cn}$ are picked at the reservoir in the area closer to the well, CDP 745, as reported in columns 1 and 2 of table 6.2. For $\gamma_0 = 2.3$, the value coming from the new event correlation, $\gamma_{eff}$ is 1.55; for $\gamma_0 = 2.8$, from the old event correlation, $\gamma_{eff}$ is equal to 1.12. Finally if we use the well-derived velocity ratio, 1.70, the resulting $\gamma_{eff}$ is above 2.8.

| vpn | vcn | γ0 | γeff |
|---|---|---|---|
| 2010 | 1420 | 2.8 | 1.115366 |
| 2010 | 1420 | 2.3 | 1.545551 |
| 2010 | 1420 | 1.7 | 2.877195 |

**Table 6.2:** Given $v_{pn}$ and $v_{cn}$ from velocity analysis in the reservoir area we calculate $\gamma_{eff}$ for different values of $\gamma_0$.

I recall here part of Figure 5.20, about the CCP-scanning technique results for $\gamma_{asy}$ = 1.00, 1.50, and 2.75 ($\gamma_{asy}$ is the depth constant $\gamma_{eff}$). As Figure 6.5 proves, the value of 2.75 produces a large shift in the salt dome structure between the two offsets, and so does the value of 1. Results from the CCP scanning technique validates the choice of $\gamma_0 = 2.3$.

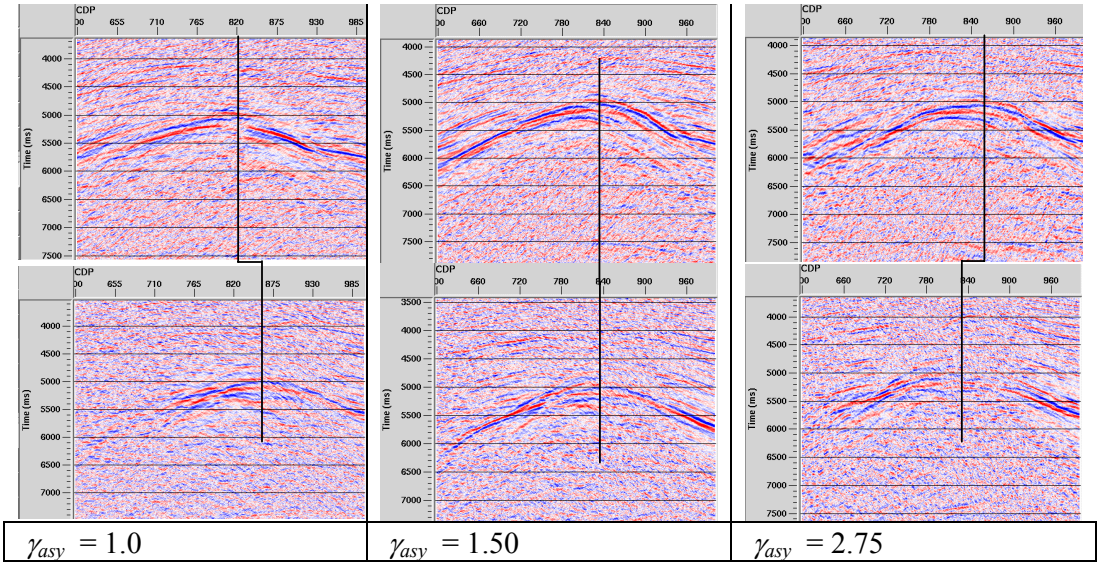


**Figure 6.5:** Positive (top) and negative (bottom) offset stacks binned using $\gamma_{asy}$ = 1.00, 1.50 and 2.75. As shown in Chapter 5 the correct value is close to 1.50, which is the resulting $\gamma_{asy}$ when $\gamma_0$ = 2.3 is used. If $\gamma_0$ = 2.8 and 1.70 are used instead the resulting $\gamma_{asy}$ produces large lateral shifts.

We still need to explain a 30% difference between the values extracted from the well logs and the value extracted from the seismic data. Interestingly, the $t_{c0}/t_{p0}$ ratio ($v_{p0}/v_{c0}$) at the reservoir is around 1.80, which is a value very close to the one found in wells. If the conversion took place at the sea floor rather than at the reflectors we would have pure S-mode in the inline component (after down-propagating the source to the sea floor). This means that the velocity ratio $v_{p0}/v_{c0}$ would be actually $v_{p0}/v_{s0}$, which, as mentioned previously, is close to $\gamma_0$ in well logs. This consideration raises the question: where does the conversion take place?

## 6.4. Where does the conversion take place?

There is evidence that the conversion is actually taking place at the reflectors: shot gathers show the "wobbly" effects of statics in the inline and crossline components but not in the vertical component, which suggests that this is a shear static phenomenon at the receiver. These static effects are due to the very low velocity layer underneath the water bottom, which affects the S-wave traveltime

more than the P-wave one as the latter are faster. Importantly, the static effects disappear in the common receiver domain, which is a collection of traces from the same geographical position at the receiver end. This is a clear indication that only the up-going leg of the raypath is a shear wave and that we are dealing with receiver statics only (Yuan et al., 1998), see Figure 6.6.

Another indication in favour of the conversion at the reflector is the difference seen in the positive and negative offset stacks, Figure 6.7, which are due to the different ray paths through heterogeneities in the positive and negative offsets, as already shown in Chapter 4. The negative offset stack is more disturbed by the presence of gas, which indicates that in the negative shooting the P-wave of the raypath is travelling through the gas, while in the positive shooting only the shear leg encounters the gas. Clearly this phenomenon can happen only if the wave is converted at the reflector.

Finally, if we assume conversion at the sea floor, the S-S ray path is symmetric and we can bin data using the CMP approximation. I ran a test doing the simple isotropic sequence introduced earlier in Chapter 5 (DMO+PostSTM) and binning the data into CMPs. The results in Figure 6.8 show clearly that the energy is out of focus due to the wrong binning. In Figure 6.9 the S-S CMP gather shows strong asymmetry between positive and negative offsets.

In conclusions we can affirm with confidence that the conversion is taking place at the reflector.

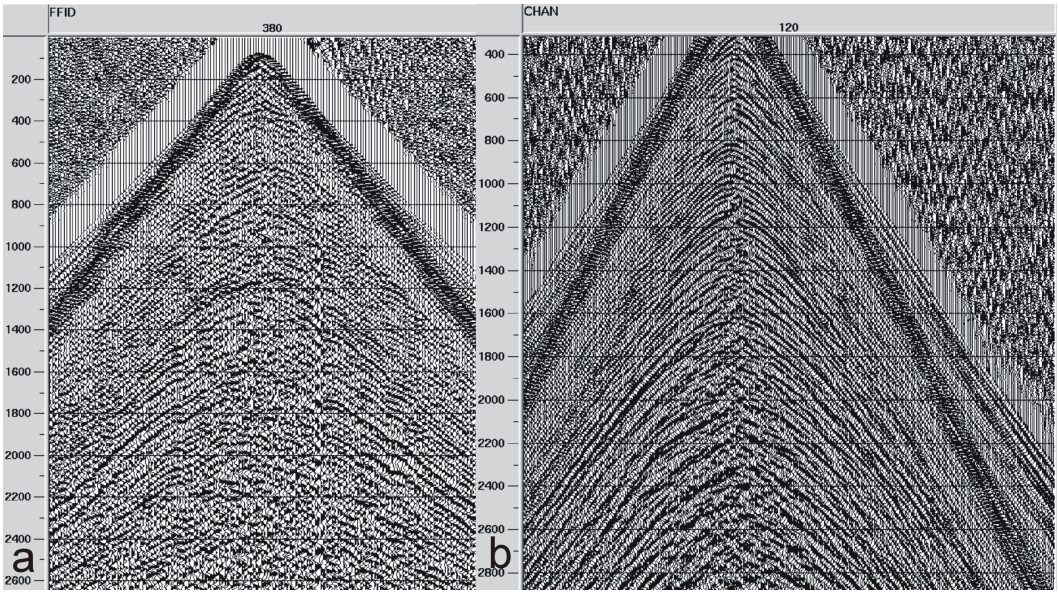


**Figure 6.6:** Shot point gather (a) and receiver gather (b). Static effects are only present in the shot point gather.

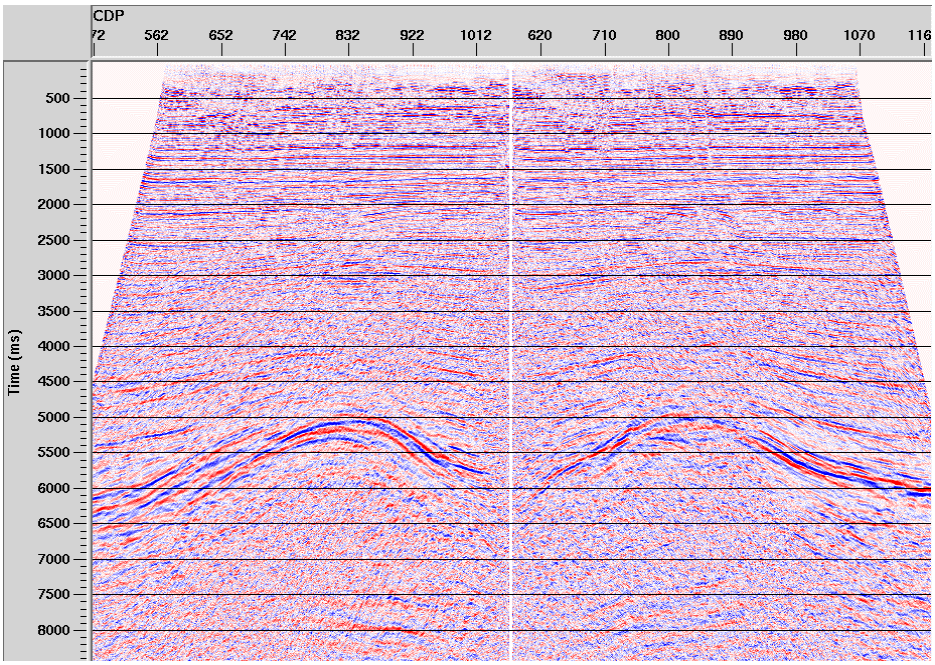


**Figure 6.7**: Positive offset stack, left, and negative offset stack, right The two images show differences due to the different raypath through the gas cloud, the negative offset is more disturbed by the presence of gas.

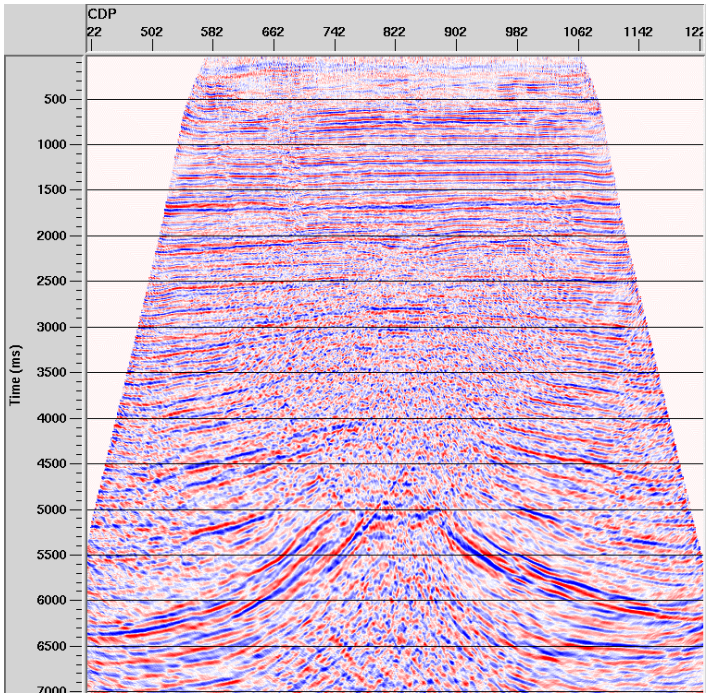


**Figure 6.8**: Converted wave migration after S-S CMP binning. The picture shows out of focus energy.

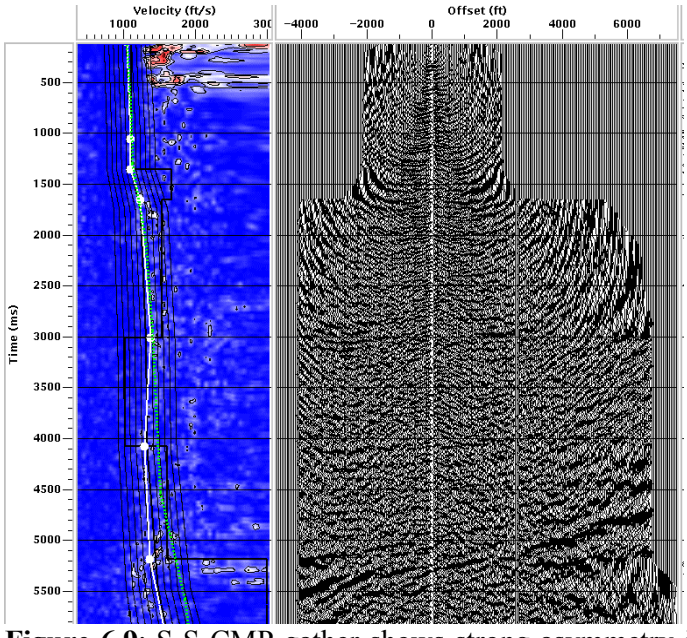


**Figure 6.9**: S-S CMP gather shows strong asymmetry in the dipping reflectors, 5.0 seconds.

## 6.5. Well log analysis

The new interpretation, but more importantly, the results of the CCP-scanning technique, indicate with a good degree of confidence a $v_{p0}/v_{s0}$ value of 2.3 for the seismic data. We have to start questioning now the results given by the well logs. I analysed three possible factors which could lower the velocity ratio in well logs by a 30%: presence of gas, effects of polar anisotropy in deviated wells, and frequency-dependent dispersion.

*Effects of gas*

As for conventional seismic P-waves, sonic logs are also affected by the presence of gas. The velocity ratio decreases as the gas saturation increases. $v_p$ is slowed down whilst $v_s$ is mostly unchanged. Fromyr et al. (2002) show values of $v_p/v_s$ extracted from well logs in the Ty formation, in the Norwegian sector of the North Sea. The Ty formation is a gas-bearing sandstone. When the pores are filled with brine the velocity ratio is constantly about 2.3, but when the gas is the main component of the fluid inclusion $v_p/v_s$ decreases to 1.75, as shown in Figure 6.10.

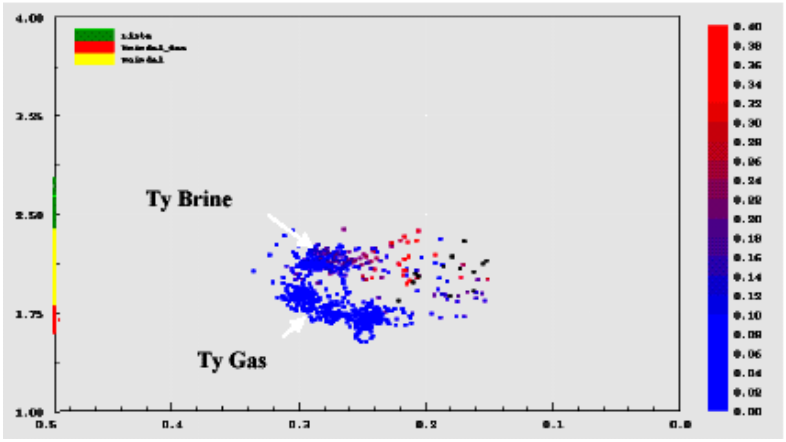


**Figure 6.10**: Well log values taken from the sandstone Ty formation in the Norwegian sector of the North Sea. The x-axis is the Porosity and the color legend is for the volume of shale. from Fromyr et al., (2002).

The difference in velocity ratios due to the presence of gas alone could explain what we have observed in the Lomond field. To check if the presence of gas is the only problem, we use check-shot information, to compare the $v_p$ values from seismic data and well logs. In the Lomond field the wells tie the P seismic section with a good degree of accuracy, as shown in Figure 6.11. The sonic log is corrected using check-shot information and check-shot corrections are small, being of the order of few milliseconds for the integrated sonic log.

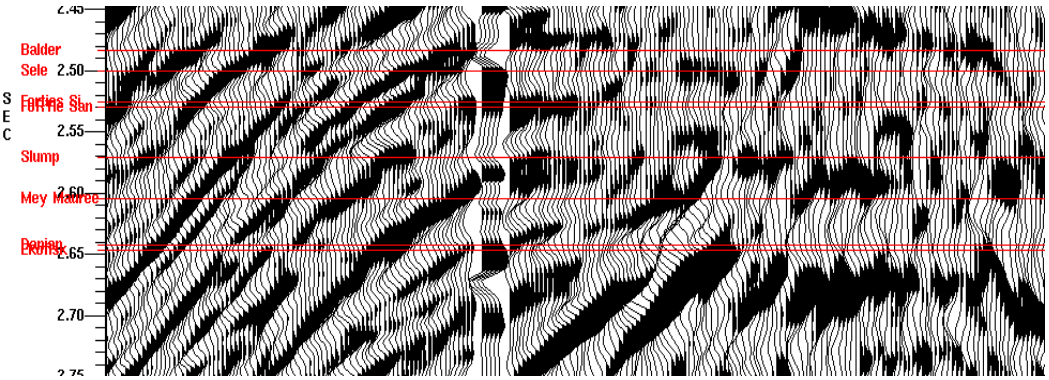


**Figure 6.11**: Well tie between line 381 and well 23/21-T9.

Another clue indicating that gas has a very small effect on the sonic $v_p$ comes from extrapolating the sonic response for 100% of water saturation or 100% of gas saturation. By using the Wyllie time average equation (Wyllie et al., 1956, see Appendix D, courtesy of Richard Martin) corrected for shale, it is possible to calculate porosity from the sonic log. By filling that porosity with either gas or brine, we have calculated pseudo-sonic logs that approximate what the sonic tool (P-wave) would read if all the pores were filled with brine or gas.

Figure 6.12 illustrates the results from well 23/21-T9, showing the new sonic curves along with $v_p/v_s$ ratios calculated from the original sonic curves. In each case the shear wave curve used to calculate the ratio remains the same. On the left the continuous red curve is the original DT, the dotted red curve is the DT for 100% of water saturation and the dashed red curve is the DT for 100% gas saturation. The

green curve is the shear log. On the right the blue curves follow the same scheme. It can be seen that $v_p/v_s$ for a wet reservoir appears very close to the original (and always below 2.0); the difference is mainly because the oil-based mud is affecting the sonic reading. Indeed a broad correlation can be seen between the peaks in the shear wave curve and peaks on the water saturation curve. The water saturation was calculated using porosity (from the density tool), and deep resistivity, thus providing a totally independent measurement from the sonic tool.

These results suggest that in well T9 the sonic $v_p$ is not affected by gas (the volume of which can be seen from the water saturation curve – Swlog), due to the fact that the sonic tool is reading very close to the borehole wall where there is actually very little gas.

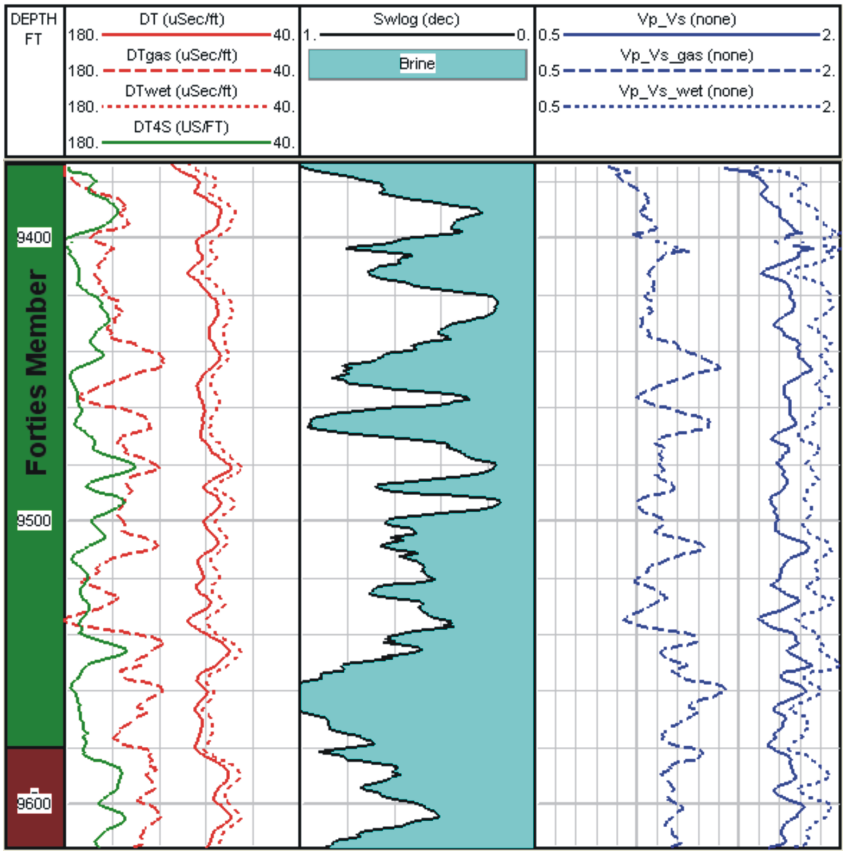


**Figure 6.12**: DT and $v_p/v_s$ calculated for 100% water and gas saturation. The continuous lines are the original curves, the dashed lines are for 100% gas saturation and the dotted lines are for 100% water saturation.

*Effects of polar anisotropy*

Leaney et al. (2000 and 2001) noted that, in deviated wells, the value of $v_s$ is significantly elevated and needs some form of calibration. They explain these high values by the presence of polar anisotropy. We can calculate the effect of the well deviation and the anisotropy on shear waves using (Thomsen, 1986):

$$v_{s(\theta)} = v_{s0}\left(1 + \sigma \sin\theta^2 \cos\theta^2\right). \tag{6.3}$$

Equation (6.3) relates the shear velocity for a propagation with an angle $\theta$, with the vertical shear velocity, the sine and cosine of the angle of propagation and the anisotropic parameter $\sigma$. Well T9 has an average deviation of less then 30$^o$ from the vertical. We can calculate an approximate value of $\sigma$ from the seismic data using this equation:

$$\sigma = \frac{\gamma_0 - \gamma_{eff}}{2\gamma_{eff}}, \tag{6.4}$$

which is valid for a single horizontal layer when $\delta$ is reduced to zero. Considering that generally $\delta$ is very small for most marine sediments (Wang, 2001), this assumption is not too far from the truth. Still it is just an approximation, which gives a qualitative value only.

Figure 6.13 shows the $\sigma$ field. As already seen in Chapter 5, the presence of dips produces a distinct signature: in some areas $\sigma$ reaches values of 1.3, in the central area the value of $\sigma$ is about 0.6. Even considering that this is an approximation, the value of $\sigma$ is very high. Ignoring anisotropy in the Lomond field for converted waves may lead to positioning errors

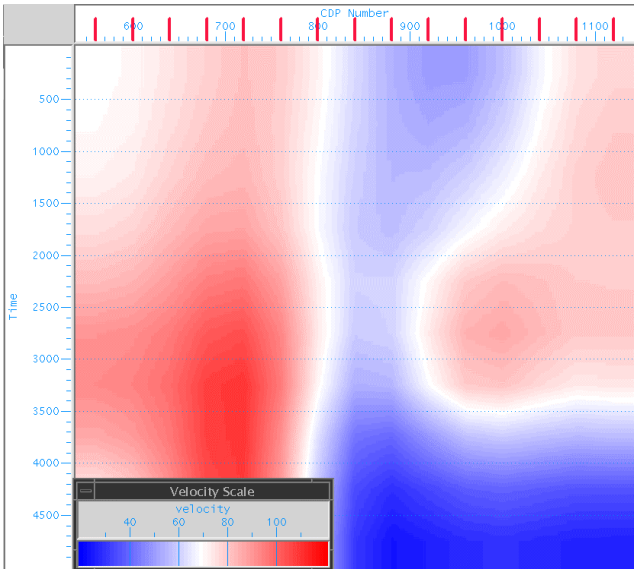


**Figure 6.13**: $\sigma$ in percentage shown in P-time. As shown in the previous Chapter for $\gamma_n$ and $\gamma_{eff}$, the effects of dip are visible. $\sigma$ shows high values on the sides of the structure. The central area, not affected by dip, shows a value of $\sigma = 0.60$.

We take an average value for $\sigma$ of 0.8, and we use equation (6.3). The results show that $v_{s(\theta)}$ is about 15% bigger than $v_{s0}$. The maximum difference between the two is for a 45° deviation and is 20%. This is valid for well 23/21-T9; well T10 is even less deviated (10°), so the effects of anisotropy on it are lower. $v_p$ is also affected by anisotropy in deviated wells, but as S-wave anisotropy is usually higher than P-wave anisotropy, ($\sigma$ generally is higher than $\delta$), the general effect of the presence of polar anisotropy in deviated wells is to lower the value of $v_p/v_s$.

Still this result shows that there must be other factors which make the value of the shear velocity from logs very high, as anisotropy alone cannot account for the observed difference in $v_p/v_s$ ratios.

*Frequency-dependent dispersion*

Moving from sonic frequencies to seismic frequencies may cause changes to $v_p$ and $v_s$, and to their ratio. There are many studies on the subject of frequency dependent-dispersion; for the scope of this work I mention the results of Eastwood and Castagna (1986). They studied the changes in the velocity ratios due to

frequency-dependent dispersion in the presence of gas and polar anisotropy using theoretical models and laboratory experiments, Figure 6.14.

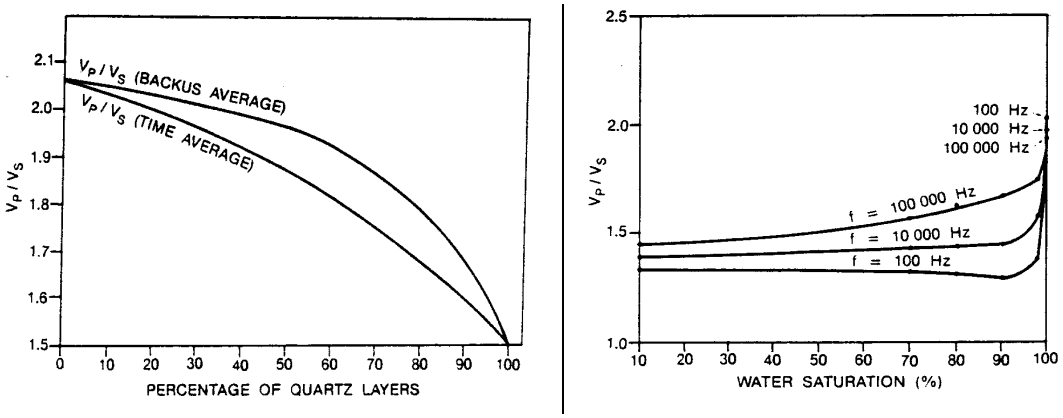


**Figure 6.14**: Left: $v_p/v_s$ computed by the long wavelength approximation (Backus average) and using the time average equation (short wavelet). Right: $v_p/v_s$ versus water saturation, see text for details.

On the left of the figure, the diagram shows the effects of change of the amount of interleaved layers of quartz and clay on $v_p/v_s$. For the long wavelength approximation (Backus average) the curve indicates a much higher increase in the value of the velocity ratio than for the short wavelength equation (time average), with maximum difference for around 30-40% of clay layers. So in the presence of anisotropy $v_p/v_s$ appears higher at lower frequencies than at higher frequencies. The maximum difference in velocity ratio for seismic and well log frequencies should not be more than 15%

On the right of Figure 6.14 the diagram shows the change in $v_p/v_s$ as the water saturation increases (and the gas saturation decreases). The velocity ratio in the presence of gas increases with frequency except for 100% water saturation, when $v_p/v_s$ decreases with frequency. This diagram was obtained from Futterman's equation using experimental data for Masillon sandstone (see Appendix D).

So the presence of gas makes the velocity ratio increase with frequency while anisotropy makes it decrease with frequency. The two effects are in opposite direction. Although in the Lomond field the logs penetrate gas-bearing sandstones, I

have shown the minimal effect that the gas has in the sonic log measurement and so its effects can be discarded.

Quantification of the effects of frequency-dependent dispersion in the Lomond field is difficult. The presence of fractures (with HTI symmetry) leads to orthorhombic symmetry and introduces additional dispersion mechanisms, which may influence $v_p/v_s$ at seismic and sonic frequencies (Mark Chapman, personal communications). However, considering a 15% difference due to anisotropy in deviated wells, a possible 10-15% due to dispersion in anisotropic media and the possibility of some residual errors in the event correlation we may explain the 30% difference in velocity ratios observed in the Lomond Field.

## 6.6. Conclusions

Velocity information from 4C seismic data and well logs shows some discrepancies, the $v_p/v_s$ extracted from the seismic data is around 30% higher. The main reason could be an error in the event correlation, which, as already mentioned in previous chapters, relies on the user interpretation. But using the CCP-scanning technique we have a confirmation that a value of $\gamma_0$ of around 2.3 is correct for seismic processing, so we look at the causes which could lower the $v_p/v_s$ is well logs

Gas shows little or no effect on the $v_p$ measurement, while polar anisotropy in deviated wells lowers the velocity ratio by about 15%. Another cause of discrepancies is the effect of frequency-dependent dispersion, but it is more difficult to quantify with accuracy. In an anisotropic medium the velocity ratio is found to decrease with frequency. These two effects could act together lowering the $v_p/v_s$ ratio from well logs by about 30%. The presence of residual errors in the event correlation cannot be excluded.

It is important to notice that using the raw well log derived velocity ratio as $\gamma_0$ for 4C seismic processing may lead to wrong estimates and should be avoided.

# Chapter 7: Effects of binning velocity ratios on C-wave imaging in the presence of dips

## 7.1. Introduction

In Chapter 5 we have seen the importance of extracting correctly the main parameters needed for converted wave processing. These parameters are $v_{cn}$, $\gamma_0$, $\gamma_n$, and $\gamma_{eff}$. Another parameter, already introduced in Chapter 2, is required to perform anisotropic processing, $\chi_{eff}$. While in the previous chapter we analysed $\gamma_0$, in this Chapter I investigate the behaviour of the remaining parameters.

I mentioned in Chapter 5 that, as a first processing step, C-wave data are binned using a single value of $\gamma$, sorting the data into Asymptotic Common Conversion Points, which are then used for velocity analysis. Here I study the effects of this initial binning value on the C-wave stacking velocity in areas of dipping reflectors. Then I investigate how these changes in the C-wave velocity, due to different binning values, may affect $\gamma_n$ and $\gamma_{eff}$.

The behaviour of the anisotropic parameter $\chi_{eff}$ is finally investigated, since we extract it using residual move out at far offsets, which is also affected by geological complexity.

## 7.2. ACCP binning, and the initial $\gamma$ value, $\gamma_{asy}$

As explained in Chapter 5, the first approximation in C-wave processing is to assume a depth-constant $\gamma_{eff}$. This assumption enables the data to be sorted into ACCP gathers. For convenience we use $\gamma_{asy}$ to denote this initial value of $\gamma_{eff}$. $\gamma_{eff}$ can be estimated from velocity information or using imaging criteria. The two approaches are independent; using both of them has the advantages of not relying directly on the values of the velocity ratios and of being able to check the $\gamma_{eff}$ estimate.

Figure 7.1 is a summary of the workflow for the calculation of $\gamma_{eff}$ (as applied in Chapter 5). The initial guess of $\gamma_{asy}$ allows ACCP binning; ACCP gathers are used in velocity analysis and to produce the C-wave brutestack. P data are then required: event correlation on stacks provides $\gamma_0$ while NMO velocity analysis gives $\gamma_n$. These two parameters are used in equation (2.25) to calculate $\gamma_{eff}$. Alternatively (or in conjunction), we can use positive and negative offset brutestacks with different $\gamma_{asy}$ to estimate $\gamma_{eff}$. This is called the CCP-scanning technique.

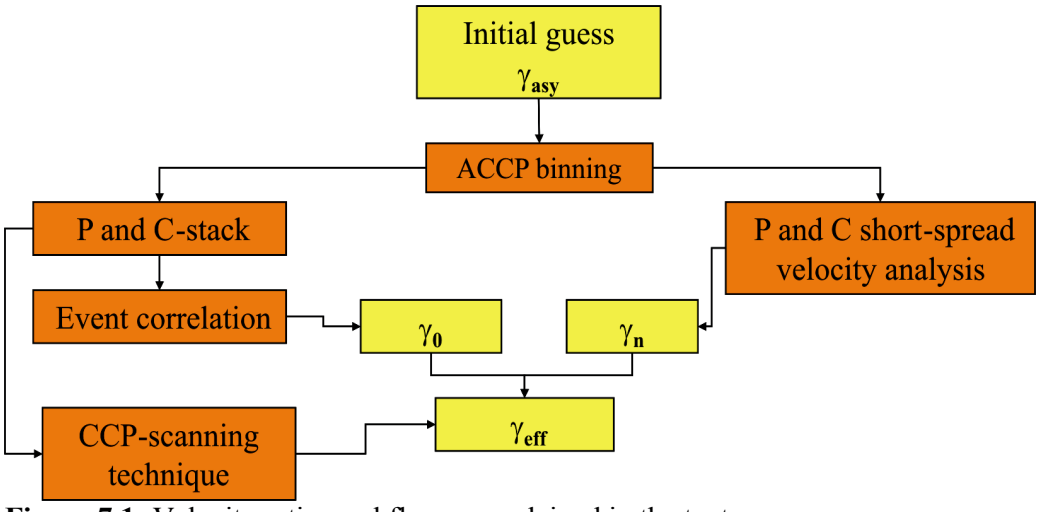


**Figure 7.1:** Velocity ratio workflow as explained in the text.

## 7.3. Previous studies, horizontal layers cases

Dai and Li (2001) investigated the sensitivity of the short-spread C-wave velocity to change in the binning velocity ratio in the Alba field, North Sea. The Alba field structure is mostly composed of horizontal layers and their study showed that the C-wave stacking velocity has little sensitivity to changes in $\gamma_{eff}$. Figure 7.2 summarises their results: clockwise from the top left quadrant we have four velocity spectra obtained using the same values for $v_{cn}$ and varying $\gamma_{eff}$ by a –20%, -10%, +10% and +20% of the estimated correct value. Little difference can be discerned in the position of the picks, but what seems to be changing slightly is the focusing of each peak, which proves the low sensitivity of the velocity to changes in $\gamma_{eff}$.

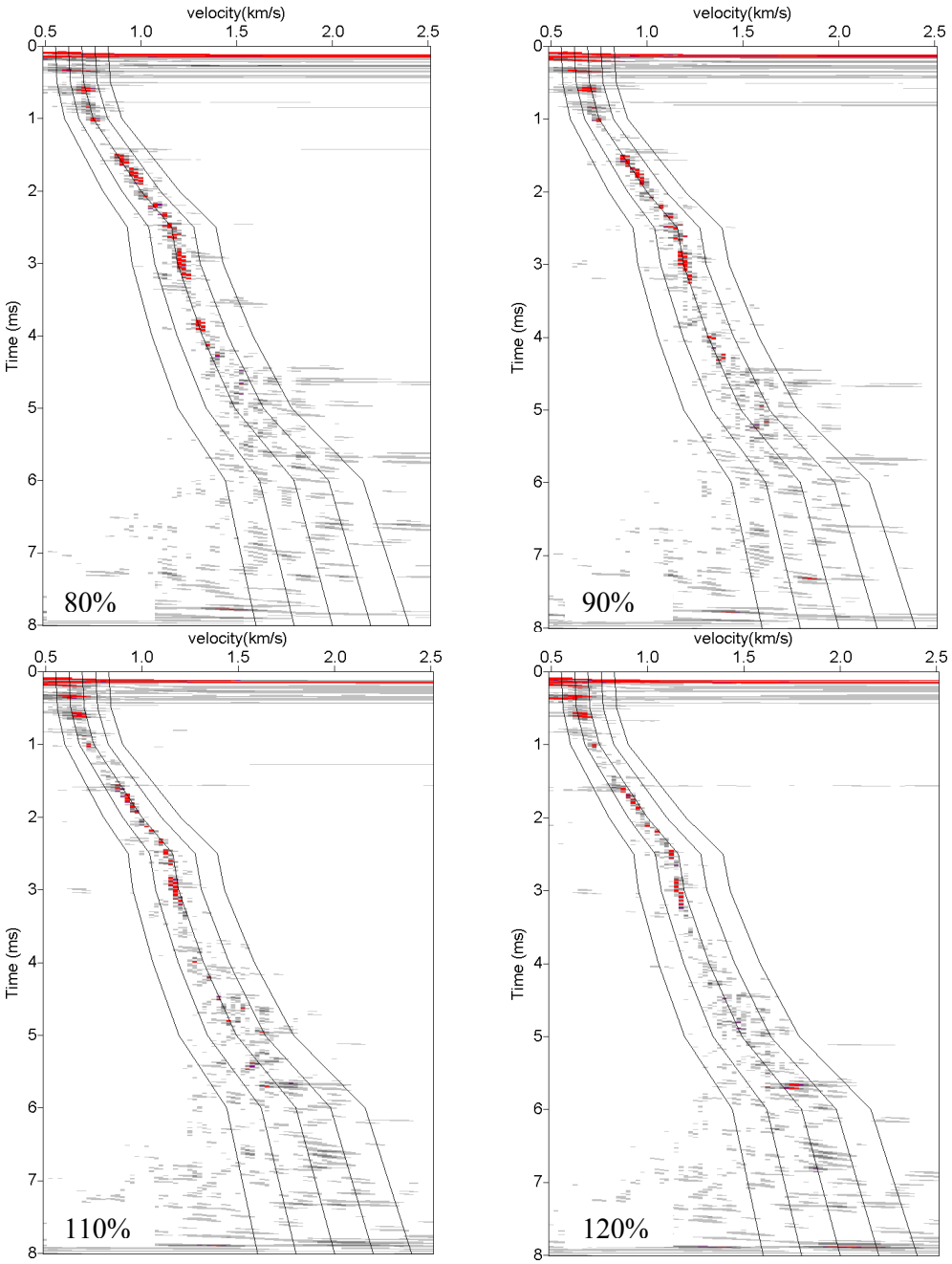


**Figure 7.2**: C-wave velocity spectra from Alba field, same velocity but different $\gamma_{eff}$, 80%, 90%, 110%, 120% of the estimated correct value. There is little or no change in the positions of the picks, marked in red.

These conclusions are intuitive. In a horizontal layered medium there is little lateral velocity variation, therefore a lateral shift in the CCP position will not produce a measurable effect on the velocity value. But the structural geology of the Lomond field is very different from Alba, since dips are relatively large (up to $30^0$), and it is interesting to investigate if, in this setting, changes in the binning velocity ratio affect the calculation of $v_{cn}$.

## 7.4. Effects of $\gamma_{asy}$ on C-wave NMO velocities

To check the sensitivity of the C-wave NMO velocity to $\gamma_{asy}$, I used a different approach from Dai and Li (2001); I picked velocities after binning the data with different values of $\gamma_{asy,}$ separating the positive and negative offsets before picking, because of the presence of diodic velocity effects. Figure 7.3 shows the positive and negative offset stacks for structural reference; the resulting velocity fields for both offsets are shown in Figure 7.4 and 7.5. The $\gamma_{asy}$ used were 1.25, 2.00 and 2.75. For the positive offsets as $\gamma_{asy}$ increases, the seismic line is "squeezed" toward the receivers; the minimum in the velocity field induced by the gas (from ACCP 800) becomes smaller and almost disappears at the high $\gamma_{asy}$. Also the maximum associated with the area of highest dip is reduced as $\gamma_{asy}$ increases. The whole velocity field appears smoother with less lateral difference in velocity. It can be seen that the greatest changes occur in the zone around 5.0 seconds and CCPs 600-750, exactly where the dips are greatest. The presence of dips makes velocities dependent on $\gamma_{asy.}$

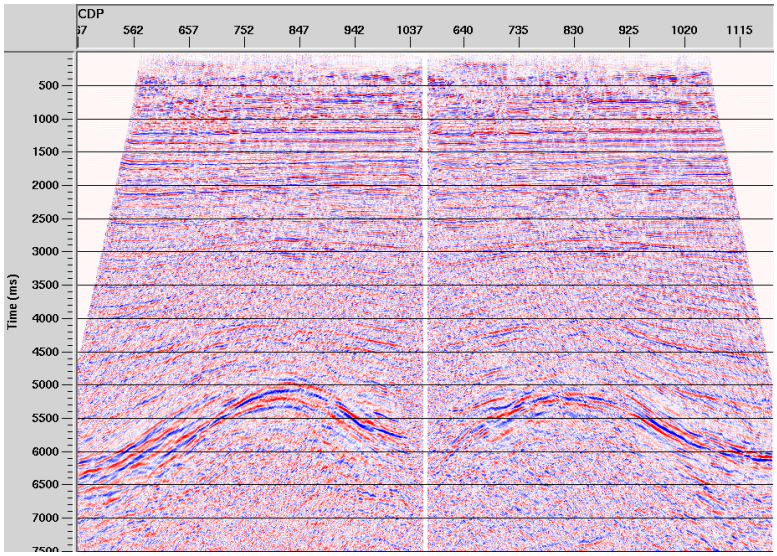


**Figure 7.3**: C-wave positive and negative offset stacks useful for structural reference in the next two figures, $\gamma_{asy}$ used is 2.00.

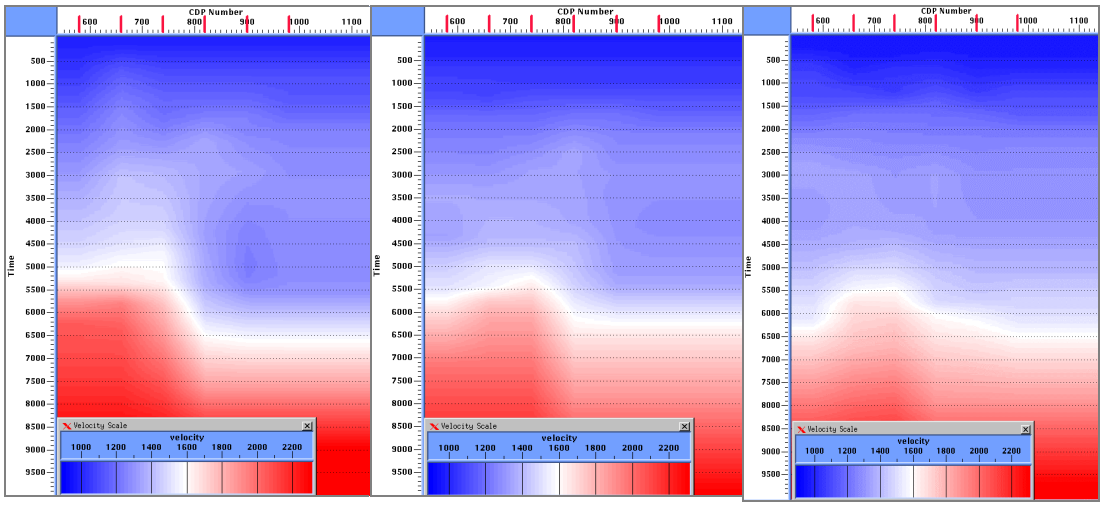


**Figure 7.4**: C-wave positive offset velocity fields for different values of $\gamma_{asy}$. From left to right the binning values are 1.25, 2.00 and 2.75. The area of high velocity, red peak on the left part, moves from left to right as $\gamma_{asy}$ increases.

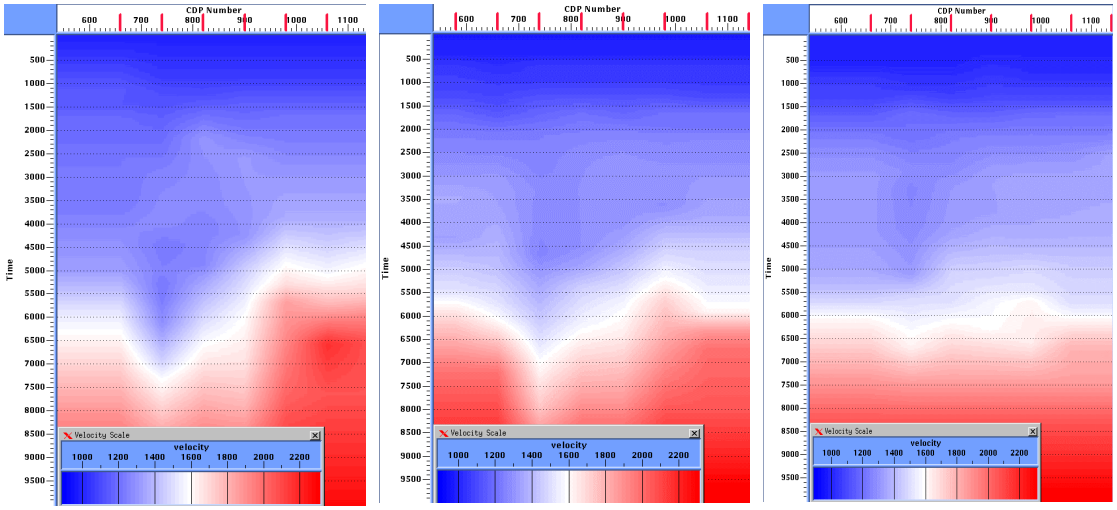


**Figure 7.5**: C-wave negative velocity fields for different values of $\gamma_{asy}$. From left to right the binning values are 1.25, 2.00 and 2.75. As for the positive offset, the area of high velocity moves, this time from right to left, as $\gamma_{asy}$ increases. The minimum in the central part of the velocity field decreases in size as $\gamma_{asy}$ increases.

Analogous results are shown for the negative offsets, Figure 7.5. The negative offsets are strongly affected by the presence of the gas cloud, as the stack testifies. Again the velocity minimum is reduced, but this time it does not disappear as the binning value increases. The velocity field for $\gamma_{asy} = 2.75$ is quite flat. We can also notice in both offsets that, as the salt dome structure shifts as we change values of $\gamma_{asy}$ (see also Figure 5.20 from the CCP-scanning technique in Chapter 5), the position of the area maximum in the velocity field shifts as well

This change of shape in the velocity field is important when we calculate $\gamma_{eff}$ using velocity information, as $v_{cn}$ is used for the calculation of $\gamma_n$. The equation to calculate $\gamma_{eff}$, (2.25), also requires $\gamma_0$ and this, as seen in the previous chapter, is possibly another source of error.

## 7.5. Sensitivity analysis

To gain more insight into the effects of $\gamma_{eff}$ on $v_{cn}$, we calculated the velocity values at $t_{c0}$ = 5.0 seconds (reservoir depth in C-wave time) for the positive offsets, resulting from velocity analysis on ACCP gathers binned with different values of $\gamma_{asy}$: 1.25, 2.00 and 2.75. Given $v_{cn}$ (and $v_{pn}$ from P-wave processing). We then calculated the values of $\gamma_n$ and $\gamma_{eff}$ at the same arrival time, using a constant $\gamma_0$ = 2.80 (obtained from event correlation) and the S-wave NMO velocity.

We quantify changes in $v_{cn}$, $\gamma_n$ and, $\gamma_{eff}$ using their ratios. Figures 7.6 and 7.7 summarise the results. The x-axis is the ACCP number, the y-axis is the ratio. In Figure 7.6 the ratios of values at $\gamma_{asy}$ = 1.25 to values at $\gamma_{asy}$ = 2.0 are shown. In Figure 7.7 the ratios are of values at $\gamma_{asy}$ = 2.0 and $\gamma_{asy}$ = 2.75 The results for the velocity show a maximum velocity change of about 5% for a 37.5% change in $\gamma_{asy}$. For $\gamma_{asy}$ = 1.25 and 2.00 ($\gamma_{asy}$ relative change of 60%), the maximum $v_{cn}$ change increases slightly, up to 7%. The difference is higher on the sides, where we have steep dips, and lower in middle of the 2D line.

$\gamma_n$ and $\gamma_{eff}$ change in the opposite direction to $v_{cn}$. The magnitude of the change increases from $v_{cn}$ to $\gamma_n$ to $\gamma_{eff}$. There is a 23% change in $\gamma_{eff}$ for a 5% change in $v_{cn}$ and there is a 31% change in $\gamma_{eff}$ for a 7% change in $v_{cn}$. For minor variations in $v_{cn}$, less than 2%, the change in $\gamma_{eff}$ is within 10%. These results show how small changes in $v_{cn}$ have a great effect on the calculation of $\gamma_{eff}$. If the resulting value of $\gamma_{eff}$ differs significantly from the $\gamma_{asy}$ used for velocity analysis, new velocity analyses after more appropriate binning are necessary.

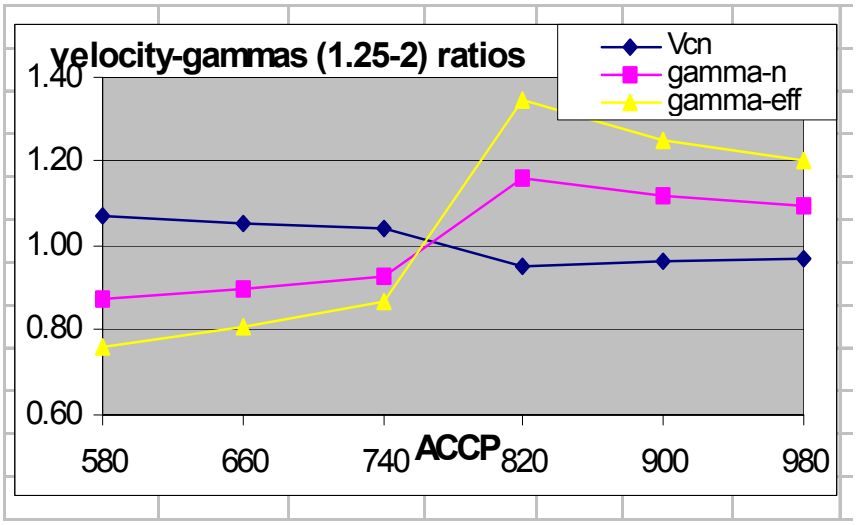


**Figure 7.6**: Relative changes in $v_{cn}$, $\gamma_n$ and $\gamma_{eff}$ for different $\gamma_{asy}$. The blue line is for $v_{cn}(1.25)/v_{cn}(2.00)$, the purple line is for $\gamma_n(1.25)/\gamma_n(2.00)$ and the yellow line is for $\gamma_{eff}(1.25)/\gamma_{eff}(2.00)$.

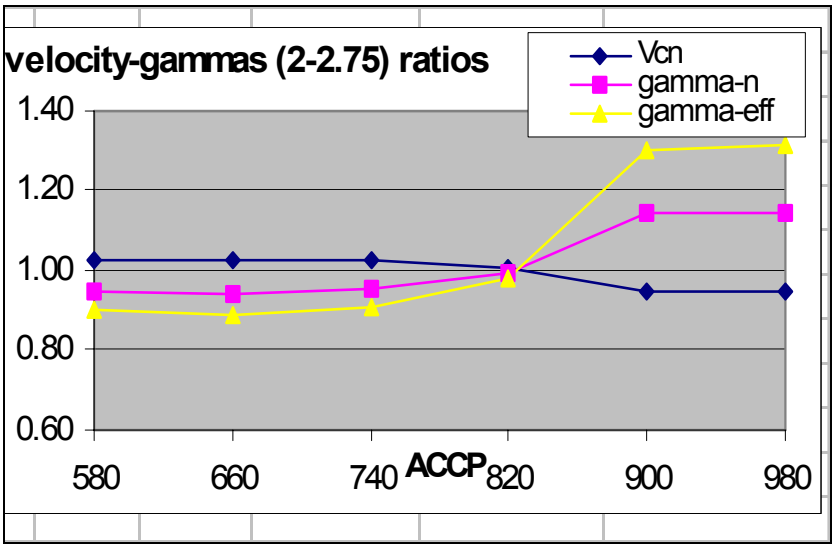


**Figure 7.7**: Relative changes in $v_{cn}$, $\gamma_n$ and $\gamma_{eff}$ for different $\gamma_{asy}$. (a) The blue line is for $v_{cn}(2.00)/v_{cn}(2.75)$, the purple line is for $\gamma_n(2.00)/\gamma_n(2.75)$ and the yellow line is for $\gamma_{eff}(2.00)/\gamma_{eff}(2.75)$.

## 7.6. Estimating $\gamma_{eff}$: DMO and PSTM

Equation (2.25) is based on plane horizontal layers. Before using it we should minimise the effects of dip in the data. We consider separately the effects of DMO and PSTM. Figure 7.9 shows two diagrams for $\gamma_{eff}$, one after DMO, as seen in Figure 5.17 in Chapter 5, and one after PSTM. I changed the colour scale of the DMO results compared with the one shown in Chapter 5 to increase the contrast on the details. The original $\gamma_{asy}$ used for the ACCP binning was 1.60 in both cases. Since the time scale for both $\gamma_{eff}$ diagrams is P-time, for structural reference I show the P-wave stack in Figure 7.8.

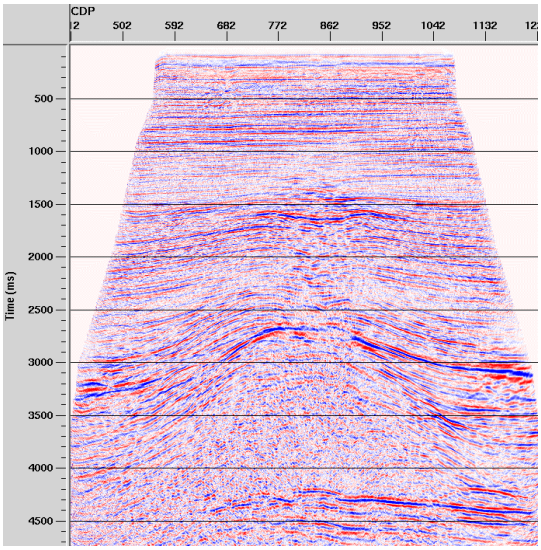


**Figure 7.8**: P-wave stack to be used as a structural reference for the next figure.

After DMO the resulting $\gamma_{eff}$ is too low, even less than 1 on the sides of the structure. This implausible result is caused by the anomalously high C-velocities obtained on both flanks of the salt dome, where the dips are highest. The high values of P-velocities due to the salt are also clear. DMO does not adequately correct for the effects of dip for the converted waves. After PSTM $\gamma_{eff}$ is generally higher and more physically acceptable: on the flanks of the salt dome the value ranges from 1.2 to 1.4,

while on top of the dome it is about 1.6-1.7. The minima caused by the dips are now reduced.

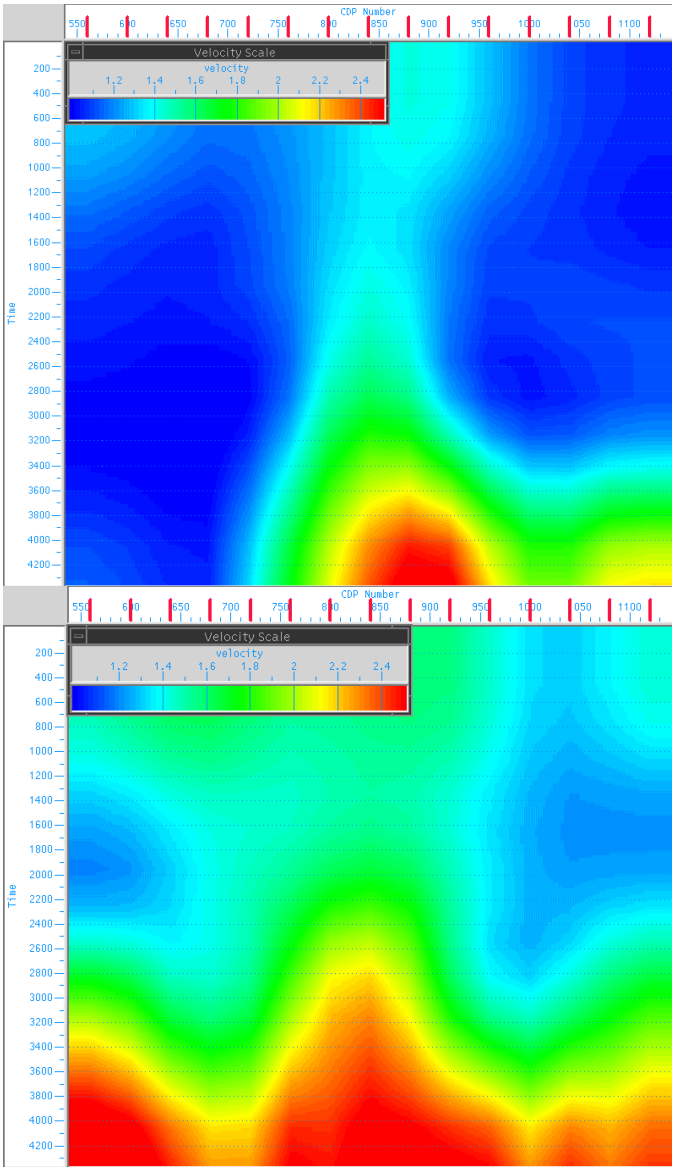


**Figure 7.9**: Top: values of $\gamma_{eff}$ calculated using equation (2.25) after DMO, bottom: the same after PSTM. Even after DMO the effects of the dip are clearly visible in the areas of low $\gamma_{eff}$. After PSTM these effects are reduced. The colour scale is the same.

Figure 7.10 shows the P-wave velocity field after DMO on the top-left part and the C-wave DMO velocity field on the top-right. It is noticeable how the P-velocities follow the structure more closely except for the gas-induced minimum, while the effects of dip dominate the C-velocities. The slow down effect of gas on P-waves plus the erroneously high C-velocity on the flank of the salt dome produce two areas of low values in the $\gamma_n$ (and $\gamma_{eff}$) field. The bottom-left part of Figure 7.10 shows the P-wave PSTM velocity field, which does not show much of a change from the DMO velocity field, proving that the P-wave DMO corrected for the effects of dip. Finally the bottom-right part shows the C-wave PSTM velocity field in which is visible the reduction of the effects of dip. The velocity fields after PSTM appear similar for P-wave and C-waves.

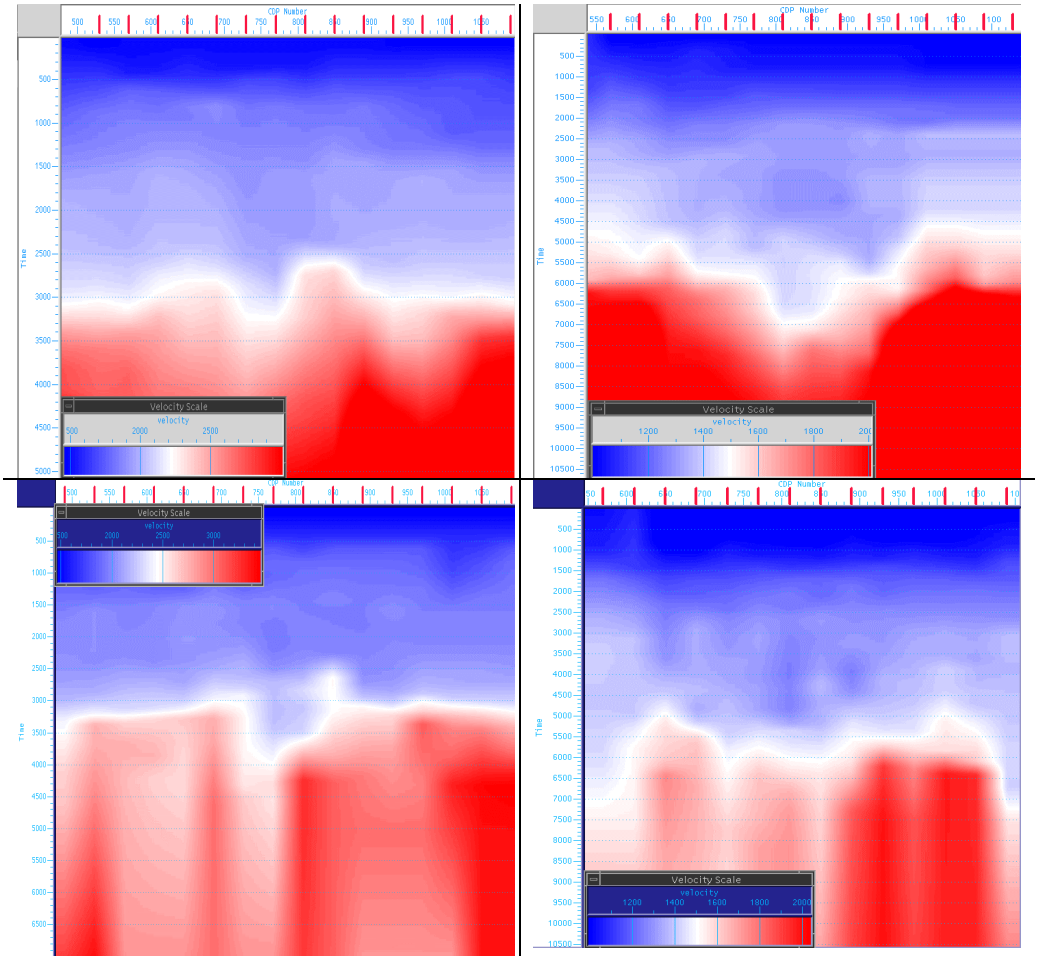

**Figure 7.10**: Top left: P-wave velocity field after DMO, top right: C-wave velocity field after DMO, bottom left: P-wave velocity field after PSTM, bottom right: C-wave velocity field after PSTM. The P velocity field does not show great changes before and after PSTM, while the C-velocity field shows that the effects of dips are strongly reduced after PSTM.

## 7.7. Structural effects on $\chi_{eff}$

In Chapter 2 I introduced the anisotropic parameter for C-waves $\chi_{eff}$ as described by Yuan and Li (2001). $\chi_{eff}$ is used in the three-term traveltime equation (2.56). H. Dai, at the EAP, had developed a new interactive velocity analysis tool based on this equation, called *xva* (Dai, 2003a). Figure 7.11 shows a snapshot of the tool. It has been developed in a Graphic User Interface (GUI) package and works in a

similar way to a conventional velocity analysis tool. But instead of picking only the stacking velocity, here it is also possible to define $\gamma_{eff}$ and $\chi_{eff}$. From left to right of Figure 7.11 we have the velocity spectrum with the velocity curve (in blue), the $\gamma_{eff}$ and the $\chi_{eff}$ curves and the gather display. When changing a pick of one of the three parameters the effects can be immediately visualized on the gather.

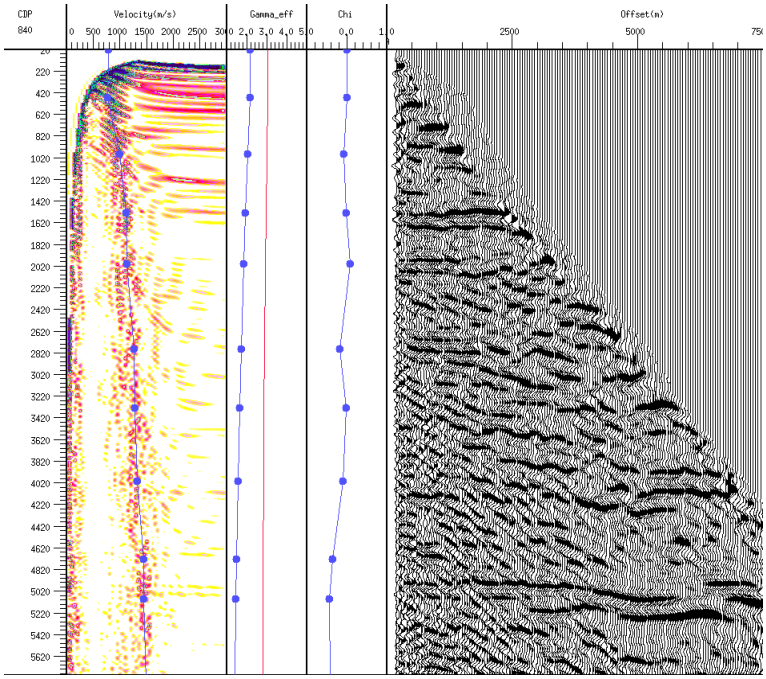


**Figure 7.11:** $v_{cn}$, $\gamma_{eff}$ and $\chi_{eff}$ values obtained from long offset non-hyperbolic moveout. From left to right, the first panel is the velocity spectrum, the second is the $\gamma_{eff}$ panel, the third is the $\chi_{eff}$ panel, and the last is the gather display. We were able to flatten the offset up to 7000 metres. We can notice a phase reversal at far offset**.**

Since all three parameters can be modified in any order, the velocity analysis task can be confusing. I kept the information about $\gamma_{eff}$ from the CCP-scanning technique and equation (2.25), picked the short spread velocities, $v_{cn}$, and finally corrected the residual move-out at the far offset changing the values of $\chi_{eff}$. We can use the velocity tool on ACCP gathers and on Common Image Point (CIP) gathers,

after hyperbolic PSTM and inverse NMO. This tool allows model building in an efficient and reliable way, see Chapter 9.

Figure 7.12 shows the results of $\chi_{eff}$ from the velocity analysis on ACCP gathers: for the positive offsets, top part, we can see a good correlation between geological structure and the value of $\chi_{eff}$ prior to PSTM. High positive $\chi_{eff}$ values are in areas of steep dip. A negative area of $\chi_{eff}$ seems to be associated with the salt dome. The situation is similar for the negative offsets, top part of Figure 7.13, in which, again, lower $\chi_{eff}$ values are associated with the top of the dome, an area with little dips, and the positive values are associated with the areas with steep dips. It is also difficult to know if the presence of gas causes effects on the far-offset traces that can dictate a trend in the value of $\chi_{eff}$. The $\chi_{eff}$ field is very consistent from the positive to the negative offsets. You can notice from Figure 7.12 and 7.13 that, for display purposes, I put the zero in the colour scale on the limit between the green and light blue, so green colours are already positive values.

After PSTM, bottom parts of Figures 7.12 and 7.13, the signature given by the geological structure is harder to see. The general trend for the positive and negative offsets is to show an area of positive values and an area of negative values, but they are reversed in the two offsets. One thing we can notice: the values of $\chi_{eff}$ after PSTM are lower than prior to it. Note that for display purposes I had to change the colour scale compared with the displays prior PSTM. Before PSTM $\chi_{eff}$ ranges from values of –0.60 to values of +1.90, after PSTM $\chi_{eff}$ just reaches values of +1.2 and –0.40. So the up-dip corrections in the trace position applied by the PSTM modified the far-offset residual moveout and reduced what seemed to be anisotropic behaviour.

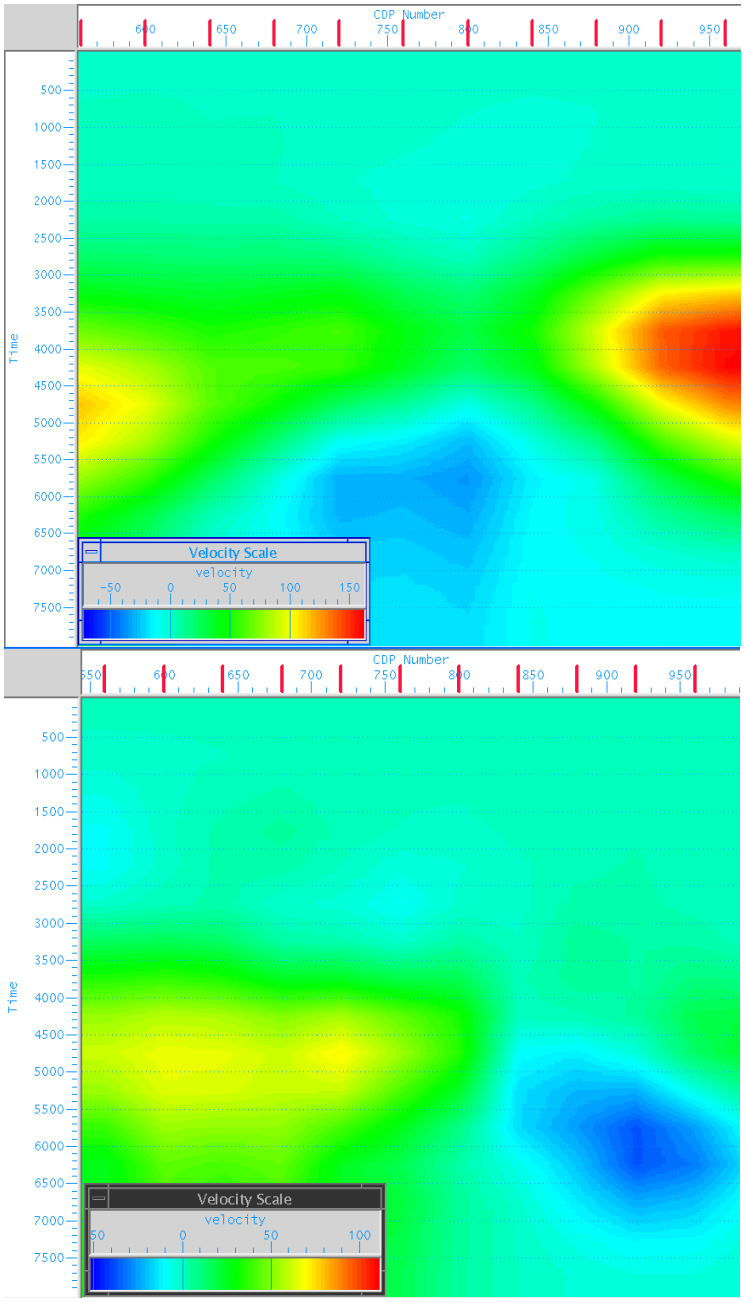


**Figure 7.12:** Top: $\chi_{eff}$ values obtained from long offset non-hyperbolic moveout on ACCP gathers, bottom: $\chi_{eff}$ values obtained from Inverse NMO CIP gathers, both are for the positive offset. Before PSTM $\chi_{eff}$ follows the geological structure, this imprint disappears after PSTM.

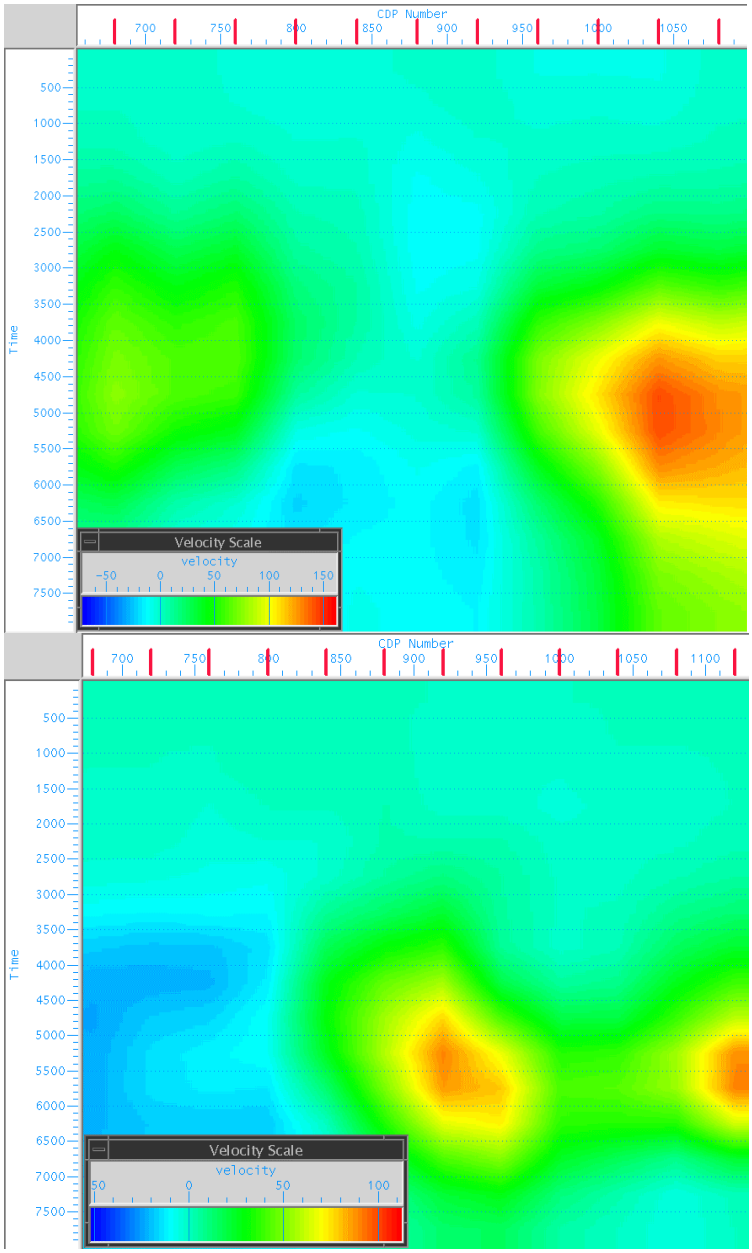


**Figure 7.13:**: Top: $\chi_{eff}$ values obtained from long offset non-hyperbolic moveout on ACCP gathers, bottom: $\chi_{eff}$ values obtained from Inverse NMO CIP gathers, both are for the negative offset. As for the positive offset $\chi_{eff}$ does not show the geological imprint after PSTM.

## 7.8. Discussions and conclusions

Results from velocity analysis in the Lomond Field show that in areas affected by dip $v_{cn}$ is sensitive to changes in $\gamma_{asy}$, the initial value of $\gamma_{eff}$. Then, small errors in the value of $v_{cn}$ are propagated as the square in the re-calculation of $\gamma_{eff}$ and cannot be ignored as they can lead to erroneous values of $\gamma_{eff}$. We have found that the effect of dip can be reduced significantly by running PSTM (results of the C-wave PSTM will be shown in Chapter 9). Some positioning errors could still remain if the original binning value is not correct. The CCP-scanning technique is a robust tool that should also be used in order to improve the estimation of $\gamma_{eff}$ in areas with dips, or where the P-wave velocity information is not reliable. It is advantageous to run it prior to $\gamma_{eff}$ estimation. The values of the anisotropic parameter $\chi_{eff}$ also change after PSTM; before PSTM a direct correlation between the presence of dips and the shape of the $\chi_{eff}$ field is visible. After PSTM $\chi_{eff}$ is generally lower and the imprint of the geological structure is reduced, suggesting that part of the residual moveout attributed to anisotropy prior to PSTM may have been caused by dip.

# Chapter 8: Evidence of anisotropy

## 8.1. Introduction

In this Chapter I present evidence for the presence of polar anisotropy and its effects on seismic data and log measurements. I hope to prove beyond reasonable doubt that the Lomond filed is seismically anisotropic.

Initially I look at the lithology and stratigraphy of this part of the Central North Sea, where shale formations are predominant in the overburden; for example the late Tertiary formations are mainly shaly mudstones. The Rogaland Group, which caps the reservoir, is also composed of finely layered mudstones. This stratigraphy is recognized to be the main source of seismic anisotropic effects.

Physical evidence is obtained by observing the angular dependency of the sonic velocities in well logs, which show higher velocity for higher angle of deviation. Anisotropic affects can be seen in seismic data, especially when compared with well log measurements. From seismic data alone clues are found in the presence of residual moveout in P and C-wave gathers and in the difference between the velocity ratios $\gamma_0$ and $\gamma_n$.

The PSDM image reveals a depth misma*tc*h with the well markers, although the events in the Common Reflection Point (CRP) gathers appear to have the correct velocity applied. Interval velocities from well logs are a few percents lower than those from seismic data. The same can be seen between RMS velocities from check shots and seismic data. It all adds to the conclusion that anisotropy is present in the Lomond field.

## 8.2. Geological evidence for the presence of polar anisotropy

Wang (2001) published results from laboratory experiments, measuring seismic velocities and anisotropic parameters in over 300 samples, from different lithologies and different geographical location such as North Sea, Africa, Gulf Coast and Canada. The lithologies investigated were mainly shales, sands and carbonates. A summary of the results is shown in Table 8.1

| **Shales** | $\varepsilon$ | $\gamma$ | $\delta$ | $\sigma$ | $\eta$ |
|---|---|---|---|---|---|
| Maximum: | 0.512 | 0.553 | 0.242 | 2.016 | 1.049 |
| Minimum: | 0.081 | 0.025 | -0.174 | 0.001 | 0.000 |
| Median: | 0.218 | 0.177 | 0.028 | 0.452 | 0.157 |
| Average: | 0.232 | 0.226 | 0.046 | 0.575 | 0.197 |
| **Sands** | $\varepsilon$ | $\gamma$ | $\delta$ | $\sigma$ | $\eta$ |
| Maximum: | 0.359 | 0.195 | 0.197 | 0.257 | 0.097 |
| Minimum: | -0.007 | -0.003 | -0.074 | -0.073 | -0.019 |
| Median: | 0.057 | 0.035 | 0.038 | 0.008 | 0.003 |
| Average: | 0.069 | 0.037 | 0.046 | 0.040 | 0.015 |
| **Carbonate** | $\varepsilon$ | $\gamma$ | $\delta$ | $\sigma$ | $\eta$ |
| Maximum: | 0.130 | 0.136 | 0.147 | 0.728 | 0.263 |
| Minimum: | -0.016 | -0.049 | -0.164 | -0.265 | -0.062 |
| Median: | 0.007 | 0.004 | -0.022 | 0.092 | 0.024 |
| Average: | 0.017 | 0.014 | -0.016 | 0.124 | 0.040 |

**Table 8.1**: Results from laboratory experiments over around 300 samples, Wang (2001).

Wang concluded that essentially all the shales are highly anisotropic, more so if they are mature and well compacted. Massive sands are intrinsically isotropic, but if they present layering or some percentage of clay they become extrinsically anisotropic. Carbonates as well can be treated as isotropic if they are not layered. The

presence of fractures or cracks in both sandstones and carbonate can cause anisotropic effects.

With these conclusions in mind we look closer at the stratigraphy of the Lomond field area. The left half of Figure 8.1 shows the geological interpretation of well 23/21-T3 made by geologists at BG Group. As this log stops just above the reservoir we complete the shallower information using the logs published in Glennie (1990) for the Central North Sea area, shown in the right part of Figure 8.1. Since horizontal layers mainly compose the shallower structure, this approximation is acceptable. A general geological column for the Central North Sea area is presented in Figure 8.2.

Simplifying, the main lithologies encountered in the logs are, from the bottom, the Upper Cretaceous chalk of the Ekofisk formation, marls and claystones of the Maureen formation and claystones and mudstones of the Lista formation, both Palaeocene. The Lista formation also includes the sandstone body of the May Sandstones, originating in the Andrew Fan. On top of it lies the Sele formation, composed of laminated shales, but again including sandstone bodies from large turbiditic fans, like the Forties Sandstone, which is the reservoir unit of the Lomond field. The Palaeocene sequence ends at the top of the Sele formation, where we find the Balder formation, again mainly composed of laminated clays but also often containing abundant tuffs. These tuffs are responsible for the characteristic seismic response. The Balder and the above units form the reservoir-sealing unit.

The Eocene post-Balder formation is mainly composed of mudstones and siltstones with rare sandstones members. The above Oligocene sediments are very similar to the Eocene sequence (Gatliff et al., 1994).

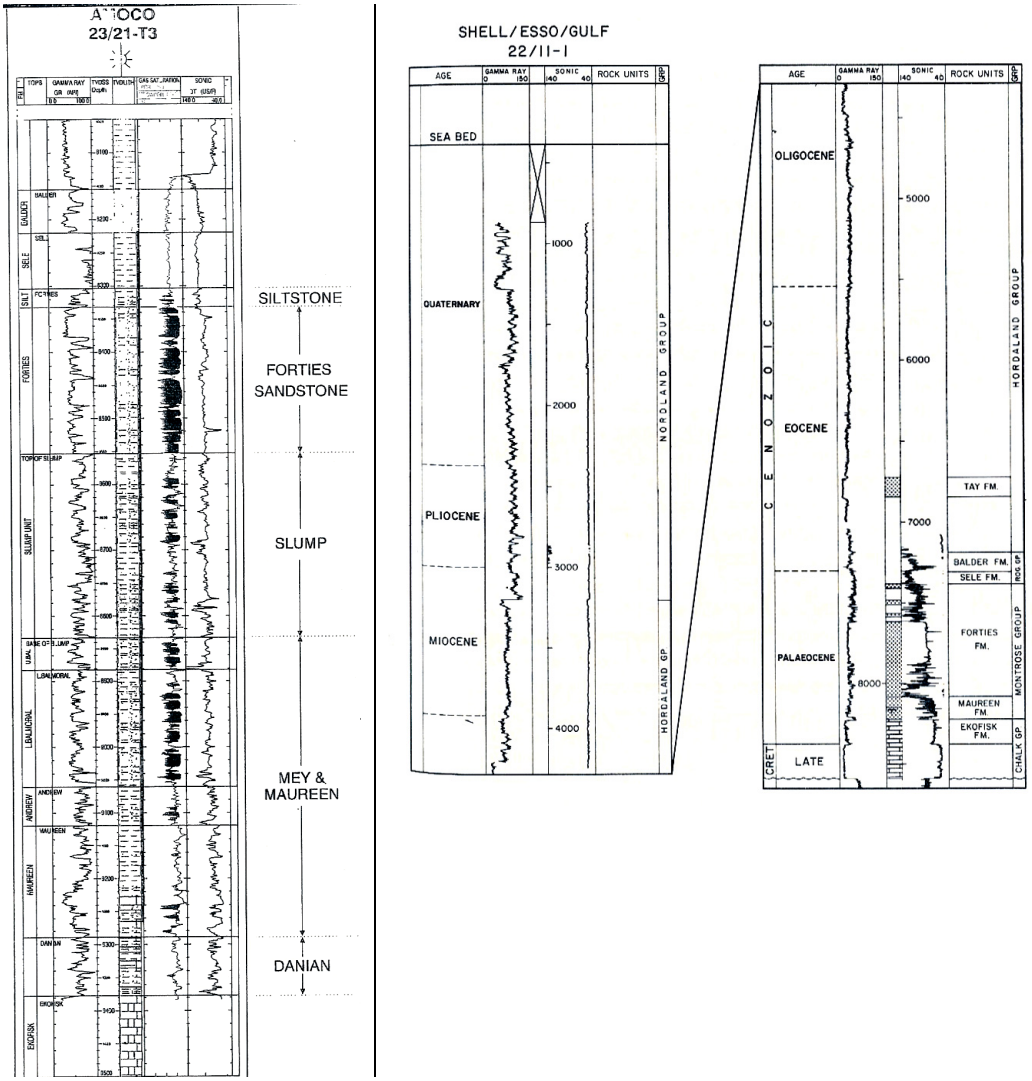


**Figure 8.1**: Left: well 23/21-T3 interpreted by BG Group geologists. Right: information from the shallower part from well 22/11-1 from Glennie (1990).

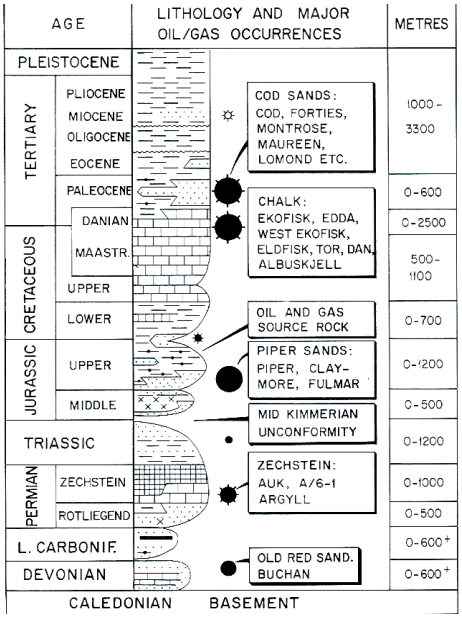


**Figure 8.2**: Geological column for the Central North Sea, from Glennie et al. (1990).

Considering Wang's results and the main lithologies of the overburden, from the Oligocene to the Top-Balder, it is not a surprise to find VTI effects on the seismic data in this area.

Figure 8.3 shows the core logs from the Sleipner Vest field, in the Norwegian sector of the Central North Sea, Block 15/3, taken from the Norwegian Petroleum Directorate archive. This field is around 150 kilometres north of the Lomond field. The core is from the Balder formation, taken at a depth of 2140 metres. The stratigraphy is very similar in the two areas. The core shows a laminated shaly-mud with occasional sandstone horizons and lenses on the centimetre scale. One notable 15-20 centimetres thick sand layer can be observed. The lamination and regular and frequent layering of the mudstones are evident in the picture.

These sediments present the characteristics of a relatively proximal mud that has received occasional sand input, probably from a distal turbiditic depositional environment (Oliver Quinn, personal communication). For this reason, and considering the distance between the two fields, the amount of sand content in the Lomond field could be slightly different.


**Figure 8.3**: Core log picture of a level of the Balder Formation, from the Sleipner Vest field, courtesy of the Norwegian Petroleum Directorate. We can notice the fine lamination in the dark shales and some lighter sands layer. A bigger sand lens can be observed on the top of the rightmost column

## 8.3. Differences between well velocity and angle of deviation

In well logs the dependency of the velocity on the angle of deviation has been noted in anisotropic media (Brandsberg-Dahl and Berkved, 2002). I use a similar approach to verify the presence of polar anisotropy in the Lomond field. Following Thomsen's (1986) approximation for weak anisotropy, the angle dependency of the P-wave velocity can be expressed as:

$$v_{p(\theta)} = v_{p0}\left(1 + \delta sin\theta^{2} cos\theta^{2} + \varepsilon sin\theta^{4}\right) \tag{8.1}$$

As $\delta$ and $\varepsilon$ are usually positive quantities, we expect the velocity to increase as the angle of deviation increases. BG Group had available eleven well logs from the Lomond area and the deviation, as shown in Figure 8.4, changes from near vertical to 45°.

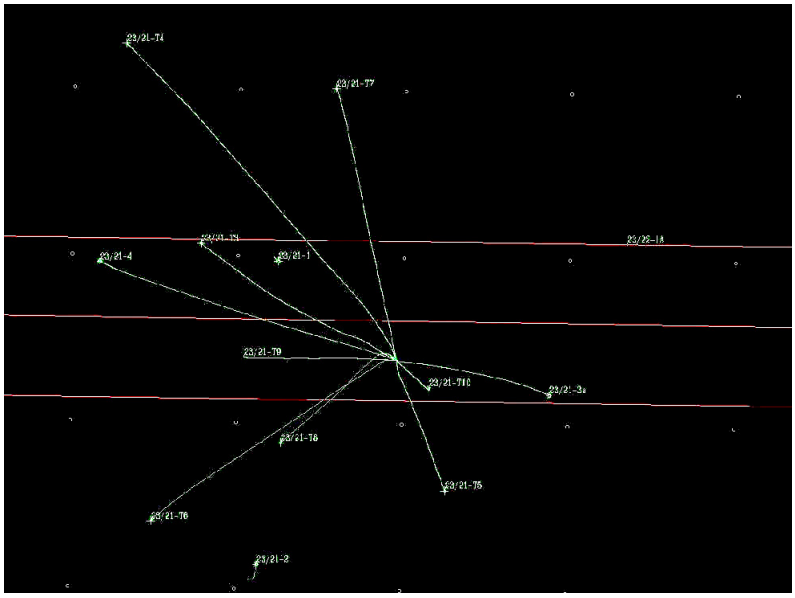


**Figure 8.4**: Well positions in the Lomond Field, in green are indicated the well trajectories. Well log deviation varies from sub-vertical to $45^{0}$.

In Figure 8.5 I show two logs from wells with different angles of deviation, for both pictures the first plot is the transient time, DT, the second is the Gamma Ray, useful to pick the Top Balder event because of the presence of tuffs, which give a characteristic pick in the Gamma Ray curve. I choose to work on the Balder because it is easy to pick on the seismic line as well as on the well logs and, due to its lithology, will probably display anisotropic effects. The well on the left has about 44° of deviation, the one of the right is almost sub-vertical. In the red circle I indicate the peak in the Gamma Ray log associated with the Top-Balder.

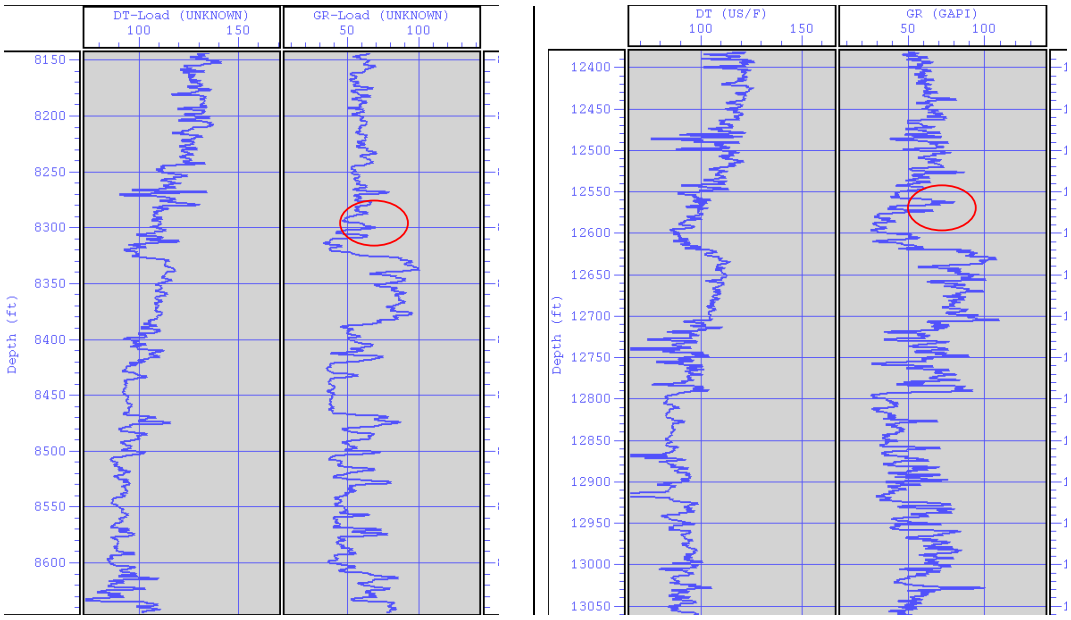


**Figure 8.5**: Well 23/21-1 on the left, almost vertical, and well 23/21-T2, right, with a 45° degrees of deviation.

I plotted the P-velocity against the angle of deviation at the reservoir level to obtain the results shown in the top part of Figure 8.6. A good relation can be seen between angle and velocity; the wells with higher deviation show higher velocity. It could be possible to apply a simple linear regression to fit these points with Thomsen's curve in order to extract estimations of $\delta$ and $\varepsilon$ (Brandsberg-Dahl and Berkved, 2002). Probably though the density of measures is not high enough, plus

there are some considerations to make on these results: since the Balder formation dips, the medium is strictly not a VTI, and the angle of deviation of the well used here, taken from the vertical, probably does not correspond with the angle of the well and the symmetry axis of the medium. Correcting for the effects of dips goes beyond the purpose of this study and requires information about the 3D seismic volume, which are not available to me.

Another consideration is that, because of the dips, the wells encounter the same formation at different depths, so the geological gradient caused by compaction could influence the velocity values. I plotted the velocity as a function of depth to see if the trend observed before is due to the different depths rather than to anisotropy. The results, displayed in the bottom part of Figure 8.6, show little or no correlation between depth and velocity, which is a good validation of the angular dependencies of the sonic velocities.

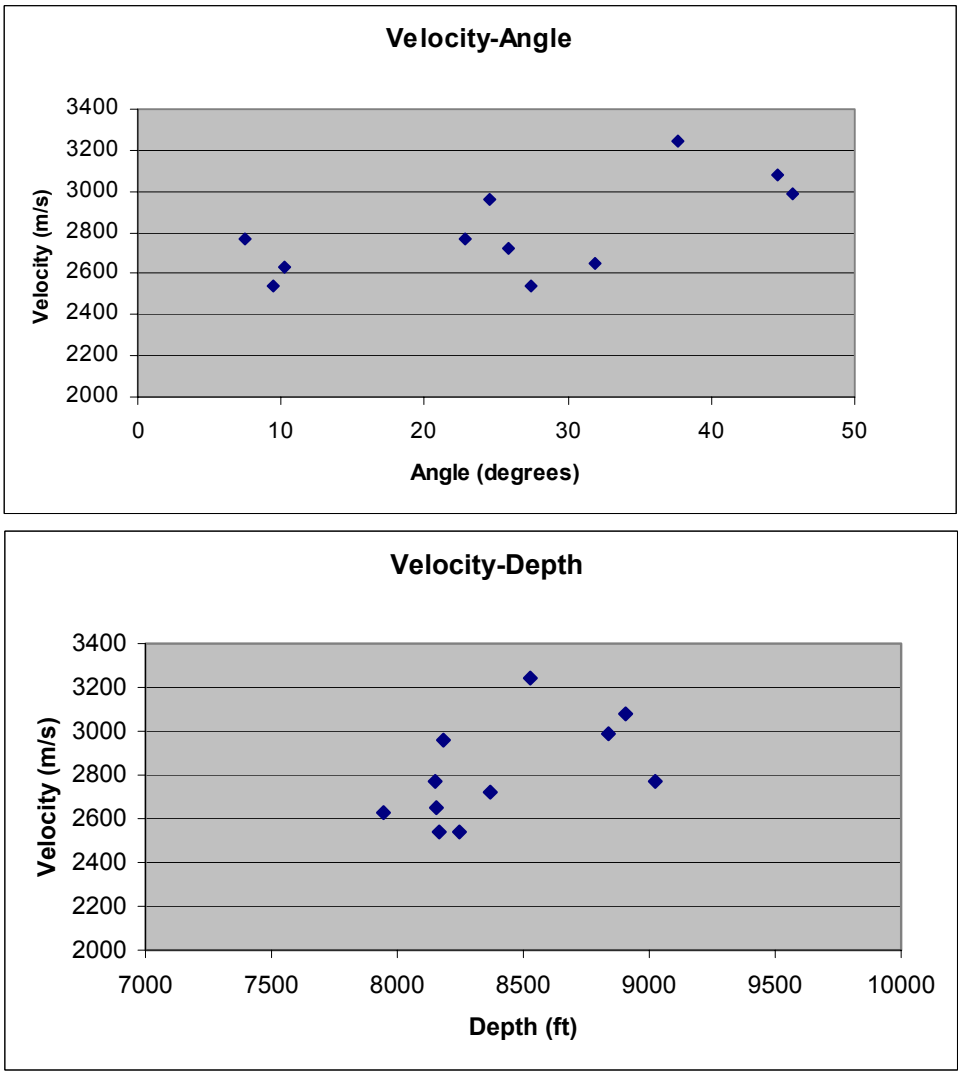


**Figure 8.6**: Top: well velocities plotted against the angle of deviation. Bottom: well velocities plotted against the True Vertical Depth.

This study, although with the limitations mentioned above, is a good independent proof of the presence of seismic anisotropy in the Lomond field.

## 8.4. Non-hyperbolic moveout

Figure 8.7 shows a CMP gather and an ACCP gather displaying residual moveout at far offsets. Polar anisotropy is just one factor contributing to make the moveout non-hyperbolic at far offsets. Observing this behaviour on CDP and ACCP gathers can be considered a necessary but not conclusive proof that the medium is VTI. In fact complex geological structures also induce to similar effects.

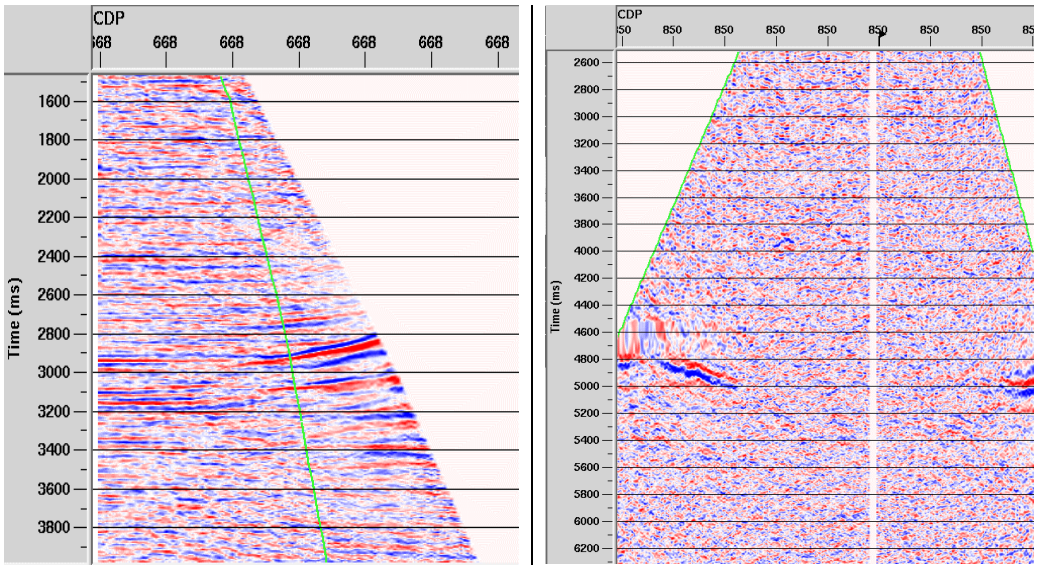


**Figure 8.7:** Left: non-hyperbolic moveout for P-waves. Right: non-hyperbolic moveout for C-waves

## 8.5. Differences between $\gamma_n$ and $\gamma_0$

I have already pointed out in Chapter 5 that differences between $\gamma_n$ and $\gamma_0$ are a strong indicator of the presence of polar anisotropy. In a VTI medium $\gamma_n$ is lower than $\gamma_0$ since generally in marine sediments $\delta$ and $\sigma$ are positive and $\sigma$ is bigger than $\delta$, as shown in Table 8.1. Recalling equations (2.45) and (2.46), relating the vertical P and S velocities with their NMO velocities and the anisotropic parameters $\delta$ and

$\sigma$, we see that both $v_{pn}$ and $v_{sn}$ become bigger than $v_{p0}$ and $v_{s0}$ in anisotropic media. The relative increase in the velocity value is higher for the S-waves though, and this makes the ratio $\gamma_n$ smaller. As mentioned in Chapter 5, Paragraph 5.6, these anisotropic effects can also be due to fine layering of isotropic material. Figure 8.8 is a reminder of the values for the two ratios. The difference between them can be of the order of 70%.

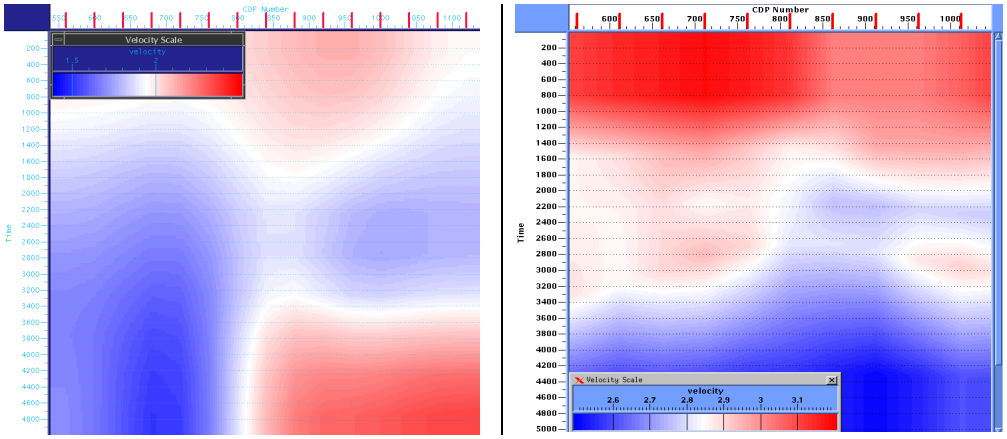


**Figure 8.8**: $\gamma_n$ on the left and $\gamma_0$ on the right, see Chapter 5 for the details. At the reservoir area, 2.4 seconds in P-time, $\gamma_n$ is about 1.9 while $\gamma_0$ is 2.8. This difference is caused by polar anisotropy.

## 8.6. P-wave depth migration

The next few paragraphs involve discussions of mismatches between well quantities and information derived from Pre-Stack Depth Migration (PSDM) processing. Here I give an overview of how I performed it on the vertical component data. The flow is:

- Building the initial velocity model,
    - Starting with the Pre-Stack Time Migrated velocity field (see Figure 8.12 and Appendix E) I converted it to an interval velocity field in depth using the conventional Dix formula. The resulting field is then adjusted to create a more geological-looking model, using interpreted

horizons in the PSTM volume (also converted in depth). Initially the model is kept very smooth. The tool used to do these tasks and the following velocity updates is the ProMAX tool called Interpretative Migration Velocity Analysis.

- Run PSDM,
    - The algorithm used was the Kirchhof depth migration.
- Check results on selected Common Reflection Points (CRP), analogous of the CIPs in time-domain,
    - In a similar way to pre-stack migration in the time domain, see Chapter 9 and Appendix E, residual moveout in CRP gathers indicates that erroneous velocities have been used. In fact, traces within a CRP are all coming exactly from the same reflection point (i.e. no smearing).
- Update the velocity model with a ”top-down layer-stripping” procedure,
    - The velocity field (as well as the interpreted horizons) are modified starting with the shallowest and moving down after flatness is achieved in the layers above. This way we remove the errors from the top-down. The final velocity model is shown in Figure 8.9, selected resulting CIPs are shown in Figure 8.11 and the final depth-migrated image is shown in Figure 8.10.

## 8.7. Differences between seismic interval velocity and well log velocity

Using well log information together with seismic data we can analyse various effects of the presence of seismic anisotropy. In a VTI medium interval velocities from seismic data are generally higher than those from well logs, always assuming $\delta$ and $\varepsilon$ positive.

I take the velocity values from the P-wave PSDM and the final velocity model is shown in Figure 8.9. The red line is the Top Balder horizon. In Table 8.2 I report the values for the velocity from the four well logs closer to the 2D line,

column 4. I also show the values of the interval velocity at the CIP locations where the wells encounter the seismic line, column 3.

As expected, the velocities from the seismic data are always higher than those from the well logs. The difference between the two varies from well to well, from a 2% to a maximum of 11%, columns 5 and 6. For well T10 the seismic interval velocity is slightly affected by the presence of gas.

| Well number | CIP | Int Vp seis | Int Vp wells | Int Vp s-Vp w | Int Vp s/Vp w |
|---|---|---|---|---|---|
| 23/21-4-T2 | 668 | 3134.00 | 3078.79 | 55.21 | 1.02 |
| 23/21-T3 | 746 | 2815.00 | 2650.43 | 164.57 | 1.06 |
| 23/21-T9 | 746 | 2815.00 | 2540.00 | 275.00 | 1.11 |
| 23/21-T10 | 857 | 2706.00 | 2627.59 | 78.41 | 1.03 |

**Table 8.2**: Interval velocities from well logs and seismic data

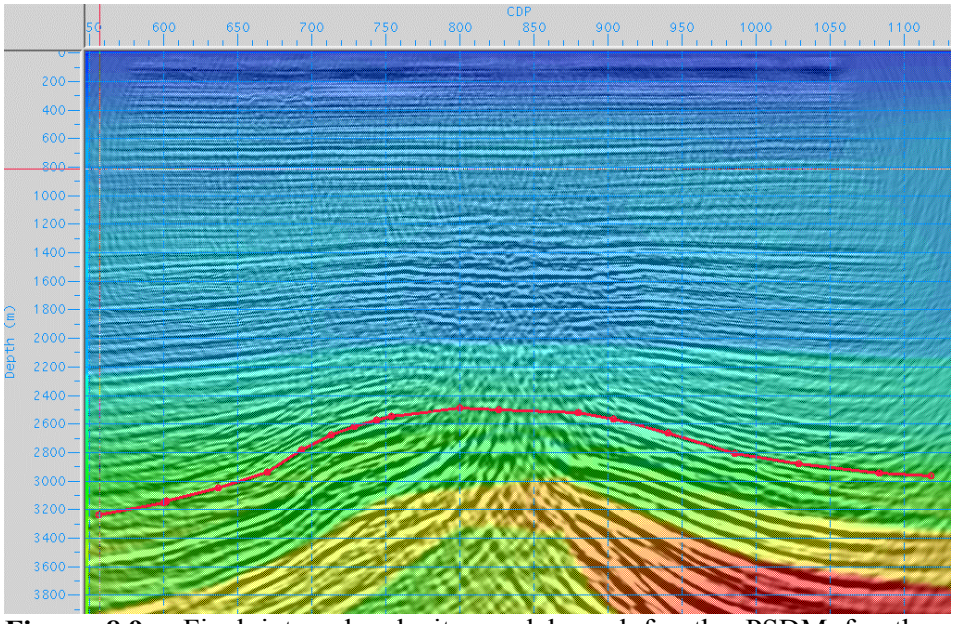


**Figure 8.9**: Final interval velocity model used for the PSDM for the vertical component, the PSDM stack is overlaid on the velocity field. The red line indicates the Top Balder.

## 8.8. Mistie in depth between P-seismic data and well logs

In recent studies the depth mistie between wells and seismic section has been used to extract the anisotropic parameter $\delta$ (Mikhailov and Herkenhoff, 2001, Zhang et al., 2002), as:

$$\delta \approx \frac{Z_{pp} - Z_0}{Z_0} = \frac{\Delta Z_{pp}}{Z_0}. \tag{8.2}$$

The PSDM stack for P-waves in the Lomond field is shown on Figure 8.10. The blue line is, again, the Top Bolder.

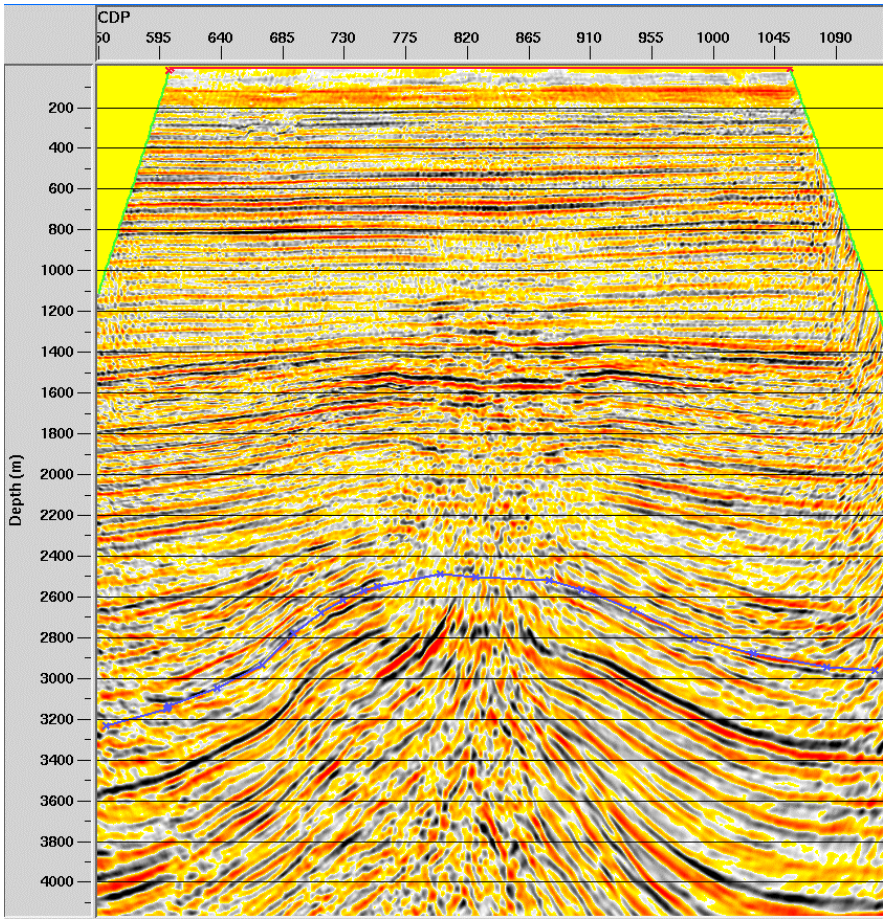


**Figure 8.10**: PSDM result for the vertical component. As for the PSTM, the results outside the gas cloud are good: the dipping flanks are well imaged but, again, the gas obscures the key target. The blue line indicates the Top Balder.

The depth values are reported on Table 8.3. As we can see the Top-Balder appears in the seismic section 134 metres deeper than the well marker in well T9. I have to point out that, as shown in Figure 8.4, the well in question is about 200 metres south of the 2D line and, given the presence of dips, the actual shift could be slightly different. Nevertheless we can attempt to calculate the values of $\delta$ using equation (8.2), so obtaining a result of 0.055.

| |
|---|
| Depth well T9 = 2435 |
| Depth seismic = 2569 |
| Difference = 134 |
| $\delta = 0.055$ |

**Table 8.3**: Depth mismatch between seismic line and well markers

In Figure 8.11 I show a few Common Reflection Points (CRP) around the well area to demonstrate that the depthing error is not due to wrong velocities but to the presence of polar anisotropy, since the events in the CRP appear well corrected.

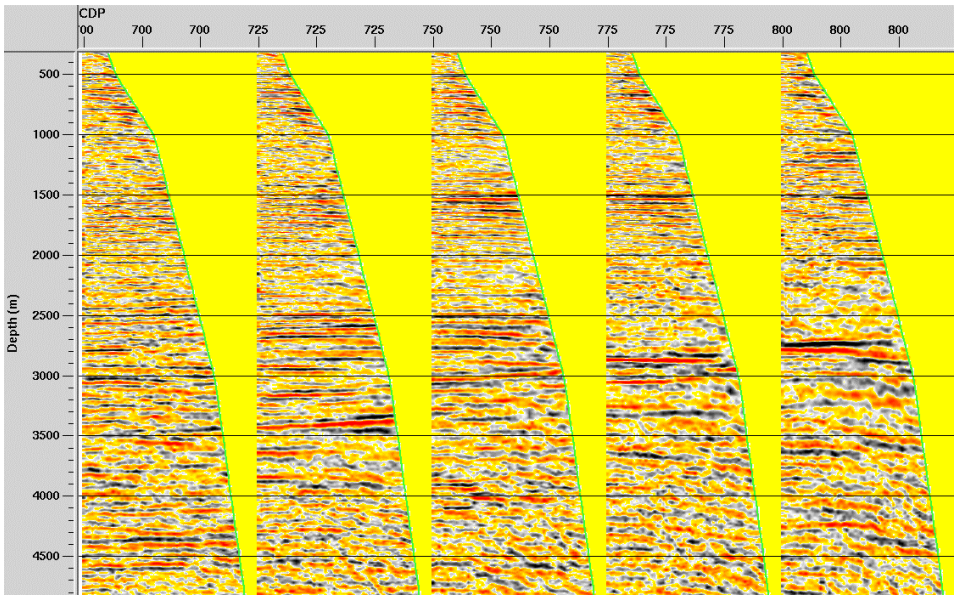


**Figure 8.11**: CRPs after PSDM, the events are well flattened by the velocity field shown in Figure 8.6. Notice the effects of gas on CRP 800.

## 8.9. Differences between check shot velocity and RMS velocity

Check shots were acquired on the four wells closer to 2D the seismic line. We can use this piece of information to verify that the RMS velocities from seismic data are higher than the average velocities given by the check shots, which are for vertical propagation. Figure 8.12 shows the DMO velocity field overlaid on the DMO stack,

the red line indicates the Top-Balder.

The results of this test are shown in Table 8.4. Again the seismic velocities are higher by between 2% and 9%.

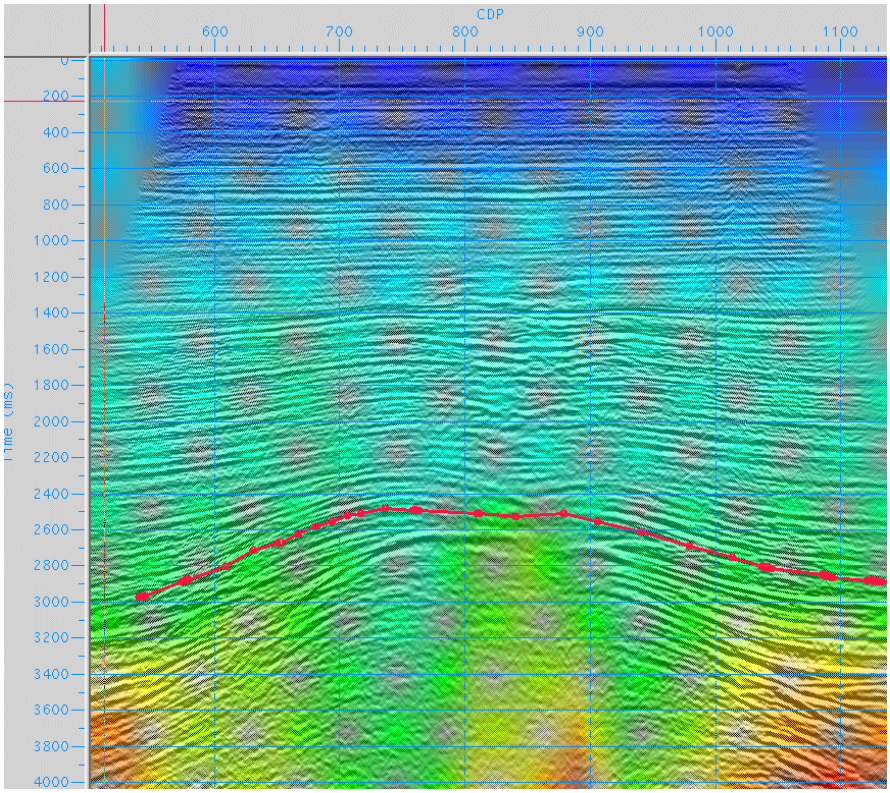


**Figure 8.12**: RMS velocity after DMO overlaid on the DMO stack, the red line is the Top Balder.

| Well number | CDP | RMS Vp seis | RMS CHK Vp | RMS Vp s-Vp c | RMS Vp s/Vp c |
|---|---|---|---|---|---|
| 23/21-4-T2 | 668.00 | 2143.00 | 1971.33 | 171.67 | 1.09 |
| 23/21-T3 | 746.00 | 2000.00 | 1955.90 | 44.10 | 1.02 |
| 23/21-T9 | 746.00 | 2000.00 | 1930.48 | 69.52 | 1.04 |
| 23/21-T10 | 857.00 | 2107.00 | 1999.88 | 107.12 | 1.05 |

**Table 8.4**: RMS velocities from check shots and seismic data.

In summary we can see several indications that the Lomond field is seismically anisotropic. Using both interval and RMS quantities we notice how the values along the vertical direction of propagation are always smaller than the more generally oblique direction represented by the seismic velocities extracted from processing. More indications of the presence of polar anisotropy are given by seismic data alone as well as log data alone.

## 8.10. Conclusions

Shales have always been indicated as the main source of polar anisotropy, due to their laminar structure and the preferential direction of the minerals. Fine layering is also assumed to generate anisotropic effects. Looking at the stratigraphy of the Lomond field, it appears evident where the anisotropy is generated. The Rogaland Group and the above sediments, late Tertiary, consist of large sequences of shaly-mudstones, laminated and with occasional fine layers of sand. Considering also Wang's results on rock samples, it is not really a surprise to find anisotropic behaviour in the Lomond field.

A physical evidence of the presence of polar anisotropy is given by observing a relation between velocity in sonic logs and angular deviation of the wells. The higher velocities are in the wells with higher deviation, in accord with Thomsen's (1986) equation for positive $\varepsilon$ and $\delta$.

The anisotropic effects can be observed in seismic data when looking at the residual moveout at the far offsets and at the difference between the NMO velocity ratio and the vertical velocity ratio. We can also use information from both well logs and seismic data. For example we observe the presence of a mistie in depth between well markers and the PSDM results, even though events in the CRPs after PSDM look well flattened. The differences between interval velocities from well logs and seismic data and between RMS velocities from check shots and seismic data also prove the existence of the same angular dependency observed in the sonic logs. These results leave no doubt of the presence of seismic anisotropy in the Lomond Field.

# Chapter 9: C-wave Anisotropic Imaging

## 9.1. Introduction

In Chapter 5 I presented the imaging results obtained from a simple, isotropic processing sequence. The converted-wave final image was an improvement on the P-wave one, since it was free from gas-related problems. But the image also showed a disappointing tie with the geological interpretation carried out by BG Group using well logs for depth and layer thickness control. Three factors could explain why: limitation of the sequence used (DMO+Migration), presence of polar anisotropy (ignored during processing) and data limited to the near offsets due to the hyperbolic approximation.

In Chapter 8 I proved that anisotropy is present in the Lomond field. Here I move into considering anisotropy in the processing sequence, using also a different flow, more suited to image geologically complex areas. The flow proposed is a Pre-Stack Time Migration, Figure 9.1. This sequence has the advantage of limiting the input of information from P-waves into the C-wave processing; we can define it as a P-wave-independent processing. This approach is robust and simple in its application. The flow requires an initial model building, where we extract the key parameters: $v_{cn}$, $\gamma_{0,}$ $\gamma_{eff}$ and the anisotropic parameter $\chi_{eff}$. The algorithm used is a Kirchhoff Pre-Stack Time Migration developed by Hengchang Dai at the Edinburgh Anisotropy Project. It can treat C-waves as well as P-P and S-S waves and takes into account the effect of polar anisotropy.

We use event correlation to extract $\gamma_0$, information from velocities and the CCP-scanning technique to extract $\gamma_{eff}$, short spread velocity analysis to get $v_{cn}$ and residual long-offset move-out correction to determine the parameter $\chi_{eff}$. These steps have already been explained in Chapters 5, 6 and 7. The migration velocity can be updated during PSTM via velocity analysis on Inverse NMO Common Image Point. $\gamma_{eff}$ and the anisotropy parameter $\chi_{eff}$ can also be updated during PSTM. To update $\gamma_{eff}$ we can use a double scan. This scan searches for the value of $\gamma_{eff}$ producing symmetrical images of dipping events in the CIP positive and negative offsets.

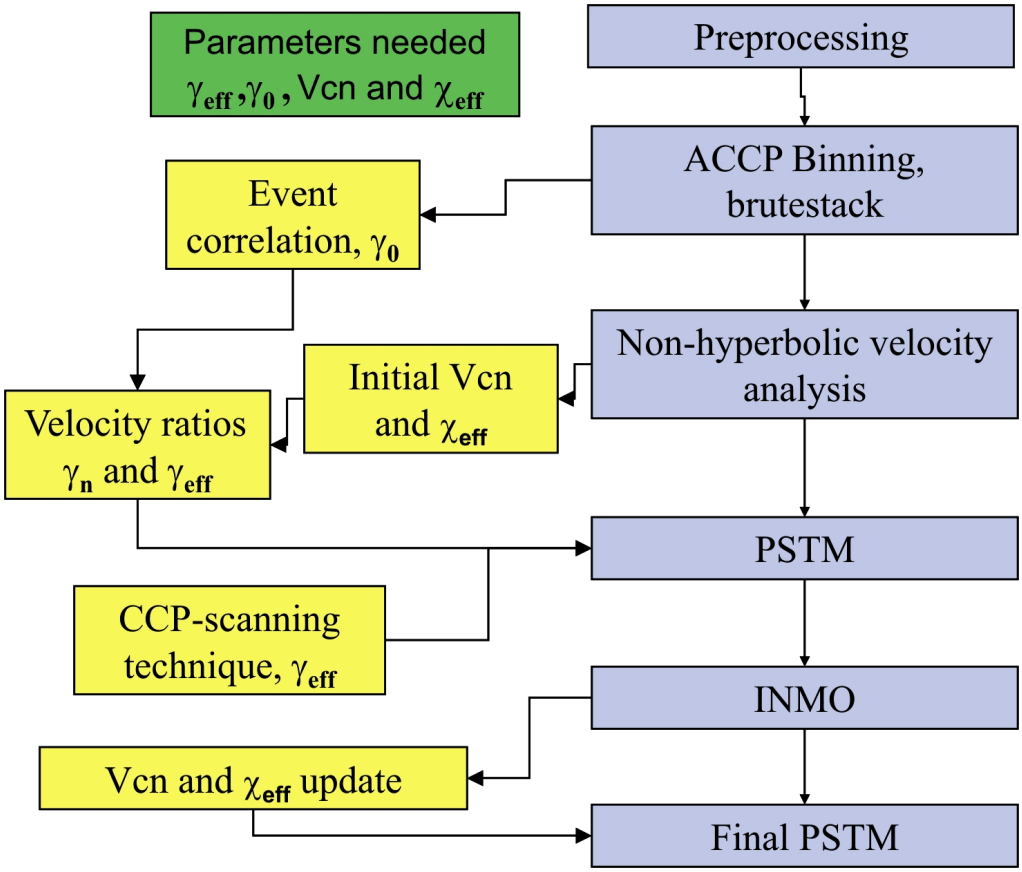


**Figure 9.1**: PSTM processing flow for C-waves, the yellow boxes indicate the model building part of the process, the green box is a reminder of the parameters needed in the PSTM.

## 9.2. Theory: PSTM in a VTI medium

PSTM is known to improve focusing and positioning of structural features in complex areas, for C-waves it has also the merit of compensating for the conversion point dispersal, as it avoids the need for CCP-binning (Li et al., 2001). The PSTM tool proposed here is a Kirchhoff summation that implements Yuan and Li (2001) Double Square Root (DSR) equation in VTI media for traveltime computation.

The choice of the Kirchhoff algorithm is motivated by the fact that in the time domain the Kirchhoff PSTM is fast and requires RMS velocities, available after conventional velocity analysis. The algorithm used here is modified to manage smooth lateral velocity variations, (Dai and Li, 2001). The Kirchhoff PSTM can be applied to mixed modes, P-S or S-P, as well as pure modes, P-P or S-S.

Figure 9.2 shows a schematic picture of the principles of the migration. For a scatter point the PSTM image is achieved by defining the diffraction curve, given by the source and receiver locations and by the traveltime, summing the energy along the curve and relocating the energy to the scatter point position. The scatter point position is determined by the position of the source and the receiver for each trace. The location of the reflector point in the ou*tp*ut trace is defined as the two-way C-travel times for zero-offset (Dai, 2001).

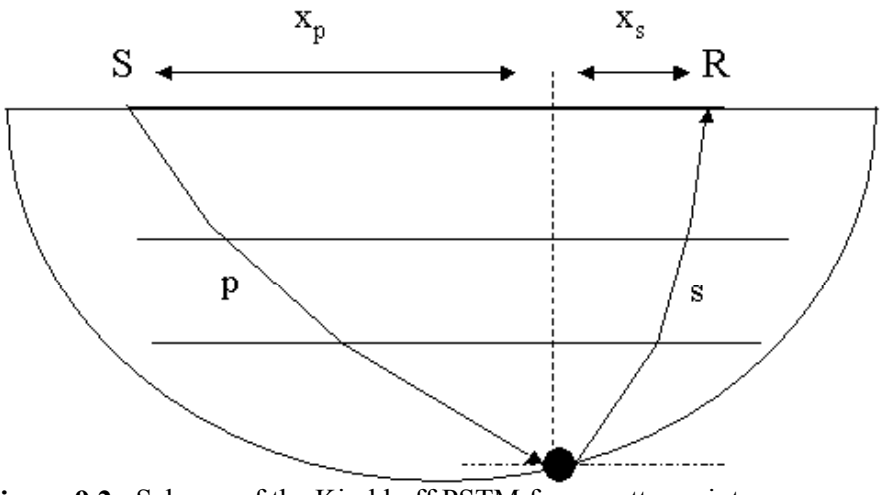


**Figure 9.2**: Scheme of the Kirchhoff PSTM for a scatter point.

The DSR equation for a multi-layered, VTI medium is given by (Yuan and Li, 2001):

$$t_c = \sqrt{t_{p0}^{\,2} + \frac{x_p^{\,2}}{v_{pn}^{\,2}} - 2\eta_{eff}\Delta t_p^{\,2}} + \sqrt{t_{s0}^{\,2} + \frac{x_s^{\,2}}{v_{sn}^{\,2}} - 2\zeta_{eff}\Delta t_s^{\,2}}, \tag{9.1}$$

$$\Delta t_p^{\,2} = \frac{x_p^{\,4}}{v_{pn}^{\,2}\left[t_{p0}^{\,2} v_{pn}^{\,2} + (1+2\eta_{eff})x_p^{\,2}\right]}, \tag{9.2}$$

$$\Delta t_s^{\,2} = \frac{x_s^{\,4}}{v_{sn}^{\,2}\left[t_{c0}^{\,2} v_{sn}^{\,2} + x_p^{\,2}\right]}. \tag{9.3}$$

The anisotropic parameters used here were introduced in Chapter 2.

If we do not want to use information from the P-wave we can express equation (9.1) in terms of $v_{cn}$, $\gamma_0$ and $\gamma_{eff}$, re-writing it as (Dai and Li, 2001):

$$t_c = \frac{t_{c0}}{1+\gamma_0}\sqrt{1 + \frac{x_p^{\,2}(1+\gamma_{eff})}{V_{cn}^{\,2}(1+\gamma_0)\gamma_{eff}}\left(\frac{1+\gamma_0}{t_{c0}}\right)^2 - 2\eta_{eff}\Delta t_p^{\,2}} + \tag{9.4}$$

$$+\frac{t_{c0}\gamma_0}{1+\gamma_0}\sqrt{1 + \frac{x_s^{\,2}(1+\gamma_{eff})}{v_{cn}^{\,2}(1+\gamma_0)\gamma_0}\left(\frac{1+\gamma_0}{t_{c0}}\right)^2 - 2\zeta_{eff}\Delta t_s^{\,2}},$$

$$\Delta t_p^{\,2} = \frac{x_p^{\,4}}{v_{pn}^{\,2}\left[t_{p0}^{\,2} v_{pn}^{\,2} + (1+2\eta_{eff})x_p^{\,2}\right]}, \tag{9.5}$$

$$\Delta t_s^{\,2} = \frac{x_s^{\,4}}{v_{sn}^{\,2}\left[t_{c0}^{\,2} v_{sn}^{\,2} + x_p^{\,2}\right]}. \tag{9.6}$$

Equation (9.4) is defined by five parameters: $v_{cn}$, $\gamma_0$, $\gamma_{eff}$, $\eta_{eff}$ and $\zeta_{eff}$.

$\eta_{eff}$ and $\zeta_{eff}$ are not independent but can be determined by $\chi_{eff}$ using equation (2.55), so equation (9.2) is actually dependent upon four parameters only. These four parameters are the input to the PSTM. Their estimation becomes the most important task of the processing flow.

## 9.3. Model building

We need to define with accuracy the following four parameters prior to the running of the PSTM: $v_{cn}$, $\gamma_0$, $\gamma_{eff}$ and $\chi_{eff}$. The initial part of the model building, concerning $v_{cn}$, $\gamma_0$ and $\gamma_{eff}$, is the same as for the DMO+Migration sequence illustrated in Chapter 5. $v_{cn}$ is extracted by conventional velocity analysis of the near offset data, $\gamma_0$ is estimated by a raw event correlation between the P-wave and the C-wave stacks, $\gamma_{eff}$ can be estimated using velocity information or imaging principles.

To perform anisotropic processing we need to be able to extract the key parameter $\chi_{eff}$. Two different ways of estimating $\chi_{eff}$ are currently used: via the "double scanning" technique" or working on the residual moveout at far offsets, "single scanning". Equation (2.56) can be used for the double scanning given the values of $v_{pn}$, $\gamma_0$ and $\gamma_{eff}$ as input. The double scanning technique, as described in Li and Yuan (2001), searches for the values of $v_{cn}$ and $\chi_{eff}$. Operationally a single event per double scan is selected in CCP or ACCP gathers. This method has given good results in several documented cases, Alba, Valhall and Guillemot (Dai and Li, 2001, Dai and Li, 2003 and Yuan et al., 2001).

Two example of the double scanning results in the Lomond field are shown in Figure 9.3. The event scanned is the top of the dome structure. On the left we see the results for ACCP 760: the double scanning produce a strong peak for $v_{cn}$ = 1524 m/s and $\chi_{eff}$ = 0.021. On the right I show the results for ACCP 840, where the scan produces a double pick: pick one is for $v_{cn}$ = 1371 m/s and $\chi_{eff}$ = -0.30, pick two is for $v_{cn}$ = 1433 m/s and $\chi_{eff}$ = -0.75. This ambiguity could be due to low signal to noise ratio, to the depth of the event, or to the presence of a phase reversal at far offsets.

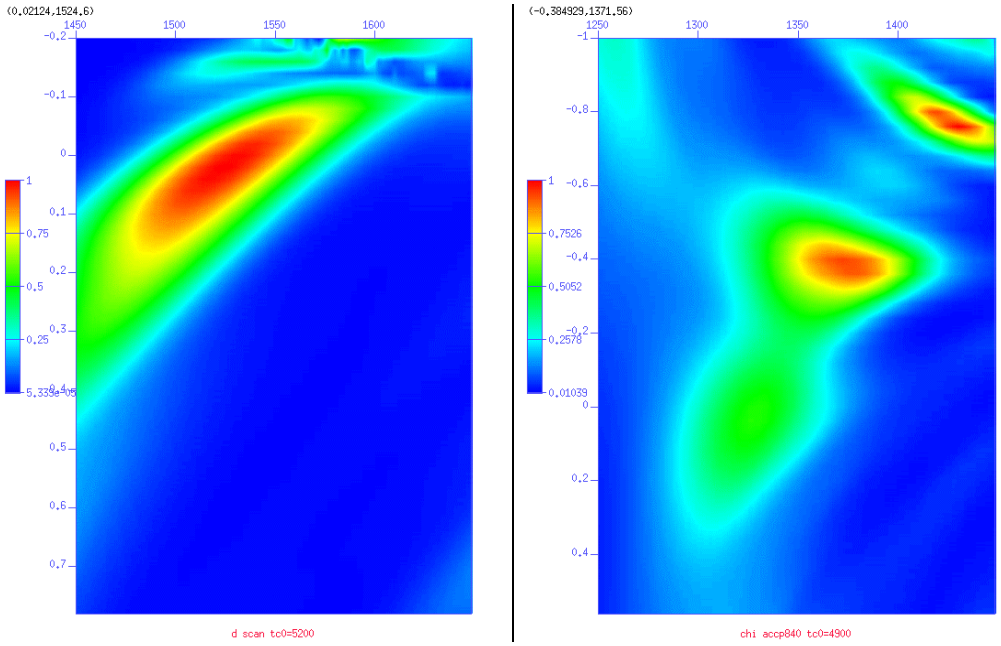


**Figure 9.3:** $v_{cn}$ and $\chi_{eff}$ values obtained from the double scanning technique, left is for ACCP 760, right for ACCP 840. The event scanned is the top of the anticline, $t_{c0}$ around 5.0 seconds.

The double scanning technique can be tedious to apply to an entire dataset, as it is an event-by-event procedure. The second approach, working on the residual moveout for the far-offset data using a single scan is more practical from a processing point of view. In this case I used Dai's tool for anisotropic velocity analysis, presented in Chapter 7, which allows the picking of $v_{cn}$, $\gamma_{eff}$, and $\chi_{eff}$ in one step. For the Lomond field processing I kept the $\gamma_{eff}$ derived from previous analysis and I worked only on $v_{cn}$ and $\chi_{eff}$.

The validity of this new tool can be appreciated when confronting the results of the anisotropic NMO correction using the values of $v_{cn}$ and $\chi_{eff}$ given by the double scanning technique and by the velocity analysis tool. Figure 9.4 shows the anisotropic NMO correction applied to ACCP 760: on the left I used the double scanning technique output, on the right the results from the velocity analysis. Only the event at $t_{c0}$ = 5.0 seconds is NMO corrected. On the left a small residual moveout can be still be seen, while the event in the gather on the right is almost perfectly flat.

Similarly in Figure 9.5 we have the results from ACCP 840. In this case I used both picks resulting from the double scanning technique. Pick two gives obviously wrong results, middle picture, while pick one is quite good, left picture, although a small residual moveout at the very far offset can be seen. Again the values giving the optimum flattening of the gather at far offsets are the ones coming from the velocity analysis tool. The $\chi_{eff}$ fields derived from the anisotropic velocity analysis are shown in Chapter 7.

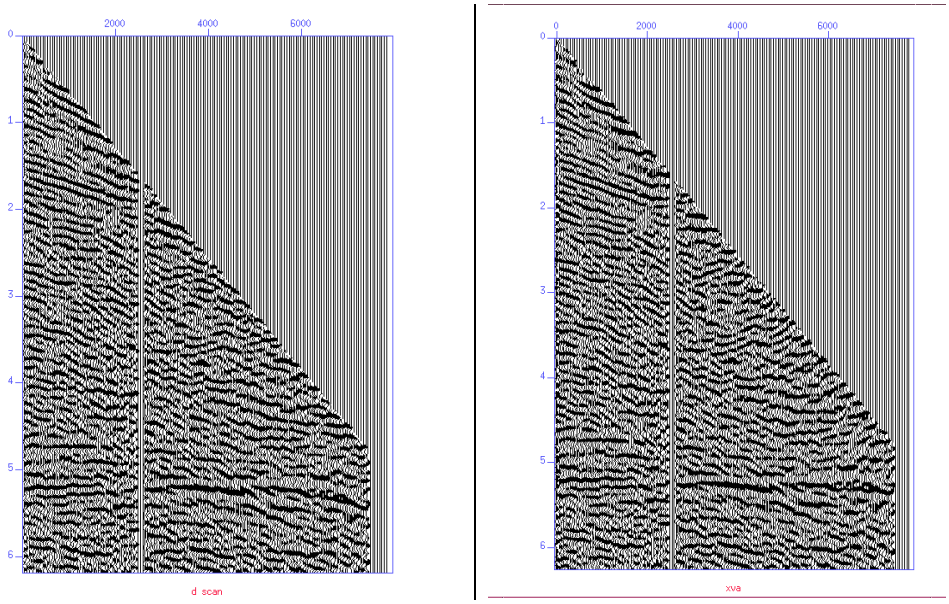


**Figure 9.4:** Anisotropic NMO correction for ACCP 760, using parameters from double scan, left and from velocity analysis, right. Only the event at $t_{c0}$ = 5.0 seconds is NMO corrected. The parameters giving the optimum correction are the ones from the velocity analysis.

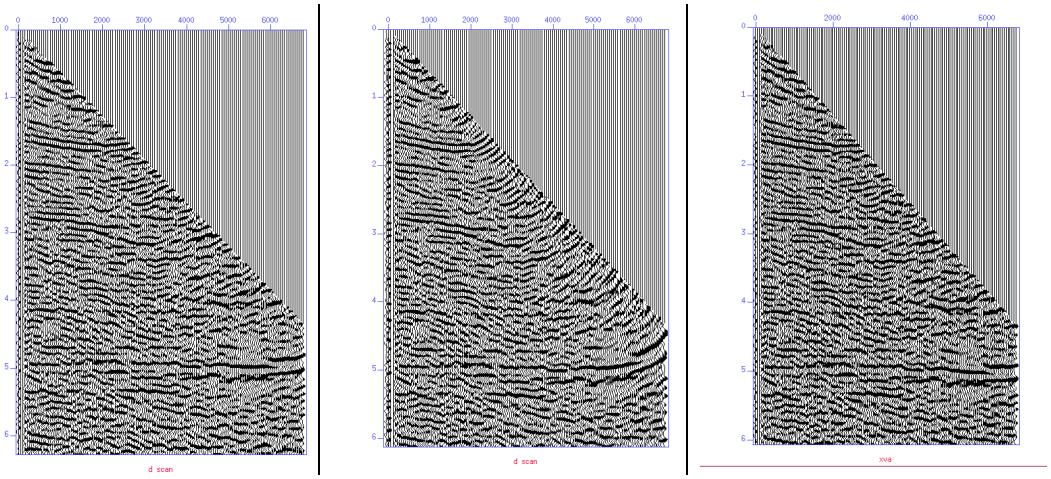

**Figure 9.5:** Anisotropic NMO correction for ACCP 840: anisotropic parameters from the first pick in the double scan, left, second pick, middle and from the velocity analysis, right. Only the event at $t_{c0}$ = 5.0 seconds is NMO corrected. Again, the parameters best correcting the event are the ones from the velocity analysis.

## 9.4. Processing: Anisotropic PSTM

In this section I show the results of the PSTM processing flow, comparing them to the best image obtained by the more "conventional" flow based on DMO+ Migration. The initial RMS velocity and $\chi_{eff}$ used in the PSTM come from the long-offset velocity analysis on ACCP gathers. $v_{cn}$, $\gamma_{eff}$ and $\chi_{eff}$ can all be updated during PSTM. We do that applying reverse NMO to selected Common Image Points (CIP) after PSTM, obtaining Inverse NMO(INMO)-CIPs suited for velocity analysis. Applying the inverse NMO to the CIPs removes the effects of the non-hyperbolic component of the velocity (Dai, 2003b). Dai and Li (2003) show that the velocity picked on the Inverse NMO CIPs tends to converge to the correct value of the migration velocity after few iterations. Often one pass of velocity updating is adequate, but in more difficult areas more iterations may be needed.

With this procedure we optimise the velocity in the correct migrated position. I believe this iterative approach is to prefer to the option of Residual Moveout (RMO) correction used often in the industry. The RMO follows the full iteration flow up to inverse NMO. Then residual moveout is calculated to maximize the

stacking response as in conventional velocity analysis. This way, although the image will be sharp and well focused, the lateral positioning of the CIPs has not been updated. Sometimes more than one migration is carried out before the final RMO. However, in our case, after each iteration of velocity analysis, we re-migrated the data to their updated lateral position.

Figure 9.6 shows this procedure: clockwise from the top left quadrant we have ACCP 880 after NMO (positive offsets), CIP 880 after the first PSTM run, the same CIP after inverse NMO, (INMO-CIP gather), and CIP 880 after the second run of PSTM. The sharpness of the image at around $t_{c0}$= 5.0 seconds is greatly improved. This CIP does not need a further velocity update.

In Figure 9.7 I show the initial PSTM result and the second PSTM result for another CIP, CIP 960. This part of the 2D line is interesting: it is where dips are high and where there is a strong velocity difference between the events around 6.0 seconds and the one at 6.5 seconds. Picking the right velocity for each event causes a stre*tc*h in the middle and far offset. Probably the RMS velocity difference is also due to different dips of the events. After the first run of PSTM the difference is attenuated and we are able to reduce the stre*tc*h applying the correct migration velocity. A third run of velocity update is necessary here as well as some updating in the $\chi_{eff}$ value.

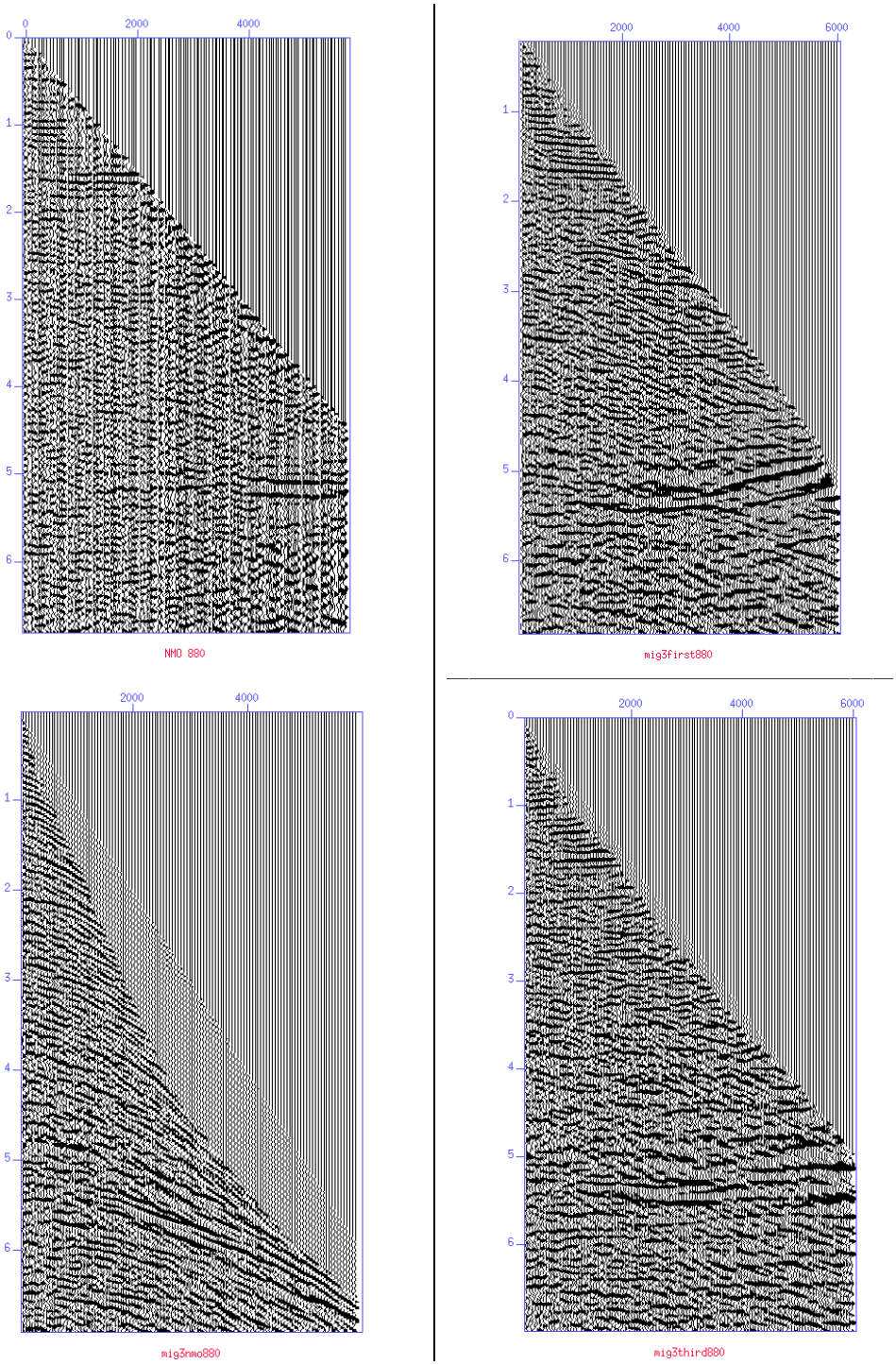


**Figure 9.6:** Top left: ACCP 880 after anisotropic NMO, top right: CIP 880 from PSTM first run, bottom left: INMO-CIP 840, bottom left: CIP 880 after PSTM second run. A single pass of velocity update is enough to properly correct this CIP.

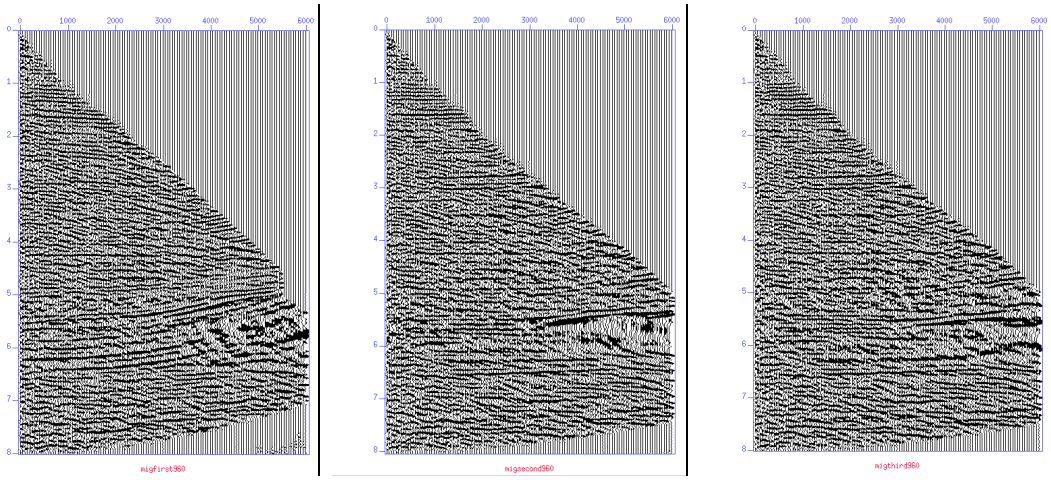

**Figure 9.7:** Another example of velocity update during PSTM. Some CIPs may require more than one update. Left: CIP 960 from PSTM first run middle: CIP 960 after PSTM second run and on the right: CIP 960 after PSTM third run. In this case a second pass of velocity updated is required to adequately correct this CIP.

In the migrated domain we have also the possibility to verify the validity of our estimate of $\gamma_{eff}$ by controlling the asymmetry of dipping events in the positive and negative offsets. The principle is illustrated in Figure 9.8. a, b and c are three events in a CIP gather; a is horizontal, while b and c have different degrees of dips, increasing from b to c. In Figure 9.8 (a) $\gamma_{eff}$ is correct and the migration velocity is not. We notice the usual residual moveout for the three events. On the right, (b), the migration velocity is correct while $\gamma_{eff}$ is not. What we see now is an asymmetry in the two offsets, proportional to the amount of dip.

I mentioned this phenomenon in Chapter 5 and 6. In fact we can observe it in CCP gathers. But the advantage of working on CIPs is that we estimate it in the correct subsurface location and not in the pre-migrated one. Model updating optimises the parameters in their correct migrated position.

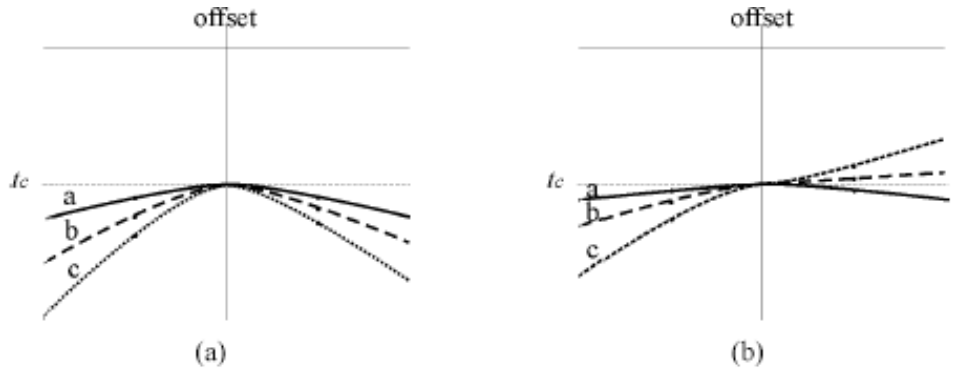


**Figure 9.8:** Errors in the migrated velocity (a) and in $\gamma_{eff}$ (b) for a CIP (from Dai and Li, 2003).

The effects of $\gamma_{eff}$ on real data are illustrated in Figure 9.9. From the top row I display CIP 900 with the correct $\gamma_{eff}$ applied, 1.80, with a low $\gamma_{eff}$, 1.10, and with a high $\gamma_{eff}$, 3.00. The asymmetry in the main event when the wrong $\gamma_{eff}$ is used is evident.

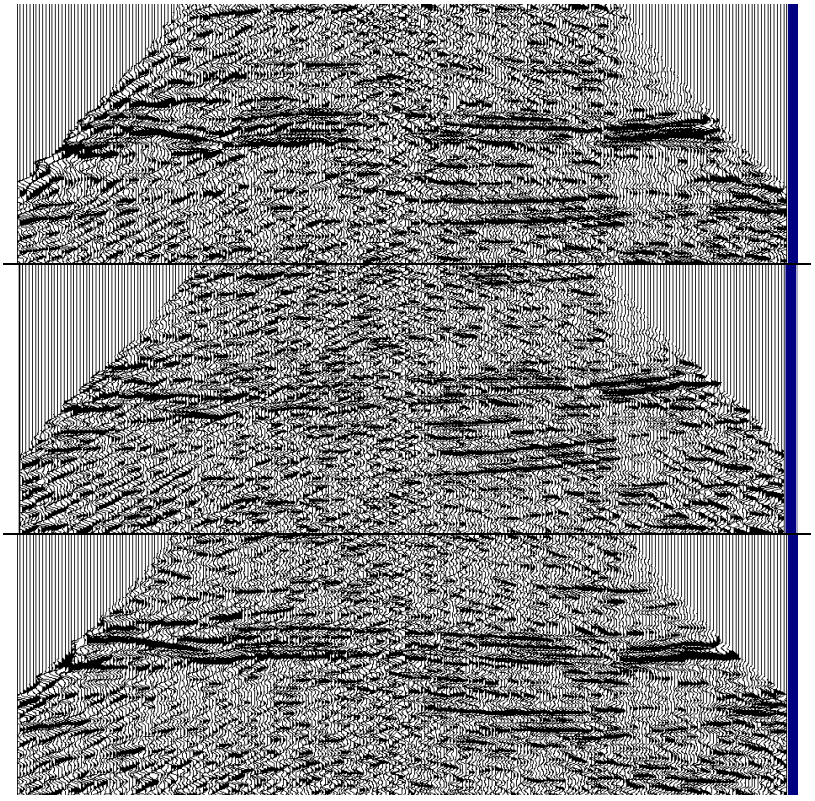

**Figure 9.9:** Effects of $\gamma_{eff}$ in a CIP gather. The CIP on the top row is migrated with the correct $\gamma_{eff}$, while the one in the middle is migrated with a low value of $\gamma_{eff}$. Finally the CIP in the bottom row is the PSTM ou*t*put when a high $\gamma_{eff}$ is used.

This effect can be exploited to correctly estimate $\gamma_{eff}$ for PSTM. To do so I created a double-scan similar to the one presented by Boelle and Ricarte (2003). It scans for the migration velocity, $v_{cmig}$, and for $\gamma_{eff}$. It migrates selected CIPs with a selected velocity interval and a selected $\gamma_{eff}$ interval, and then stacks them.

Figure 9.10 shows the results of the double scanning for CIP 920, chosen because is in the dipping part of the section. I set the velocity interval at 100 m/s and the $\gamma_{eff}$ at 0.25. As the arrows on top of the figure show, velocity is constant in a single column and increases from left to right for each column. $\gamma_{eff}$ increases for each trace in a single column. I limited the scan to the near offset data in order to reduce the effects of anisotropy. Figure 9.10 is a close up of the reservoir area. The interesting thing to notice is that the scan is able to focus $\gamma_{eff}$ but not the migration

velocity, probably due to the fact that the scan was limited to near offset traces only. In fact, the stronger peaks in the three central columns (yellow circle) are all for values of $\gamma_{eff}$ equal to 1.75-2.00 but for velocity equal to 1300, 1400 and 1500 m/s. I tested the scan with longer values of offsets but the quality of the $\gamma_{eff}$ focusing decreased. Here I conclude that, although the scan does not seem to be able to provide the optimum migration velocity, it can still be used to obtain a quick estimate of $\gamma_{eff}$ for PSTM.

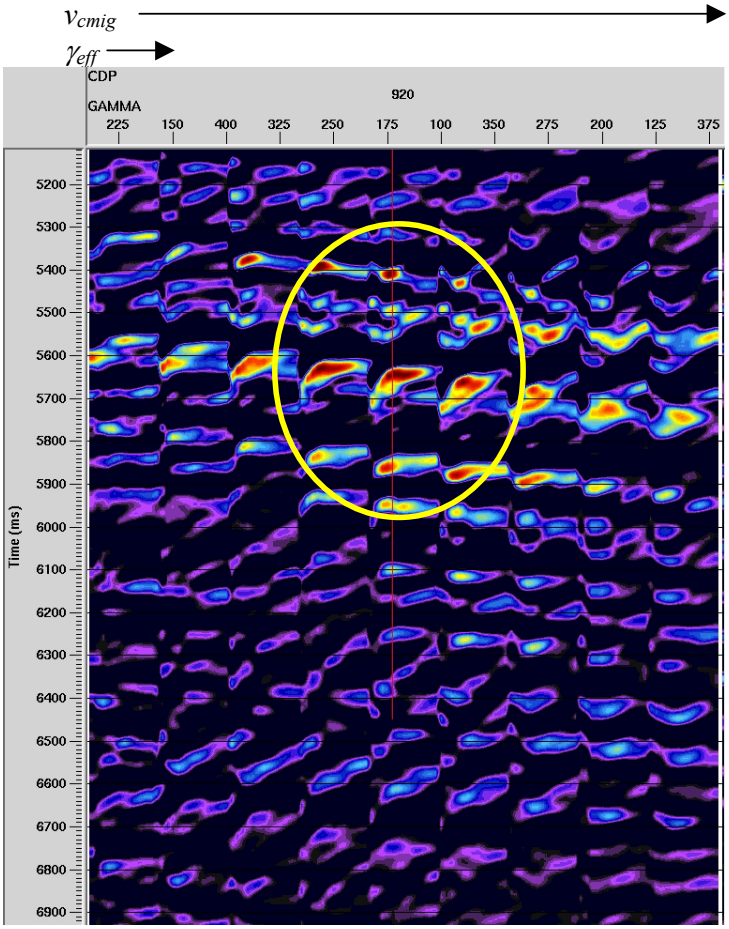


**Figure 9.10:** Double scan results for CIP920. The peaks in the yellow circle are well focused for $\gamma_{eff}$ = 1.75-2.00 but not so for the migration velocity.

Figure 9.11 shows the final PSTM result. The quality of this image at the target is excellent, there is very good continuity of the events in the reservoir area and the dipping flanks of the structure are properly imaged. The horst structure is now well defined. As the negative offset is badly affected by the presence of gas, it was merged only from CCP 950 onward.

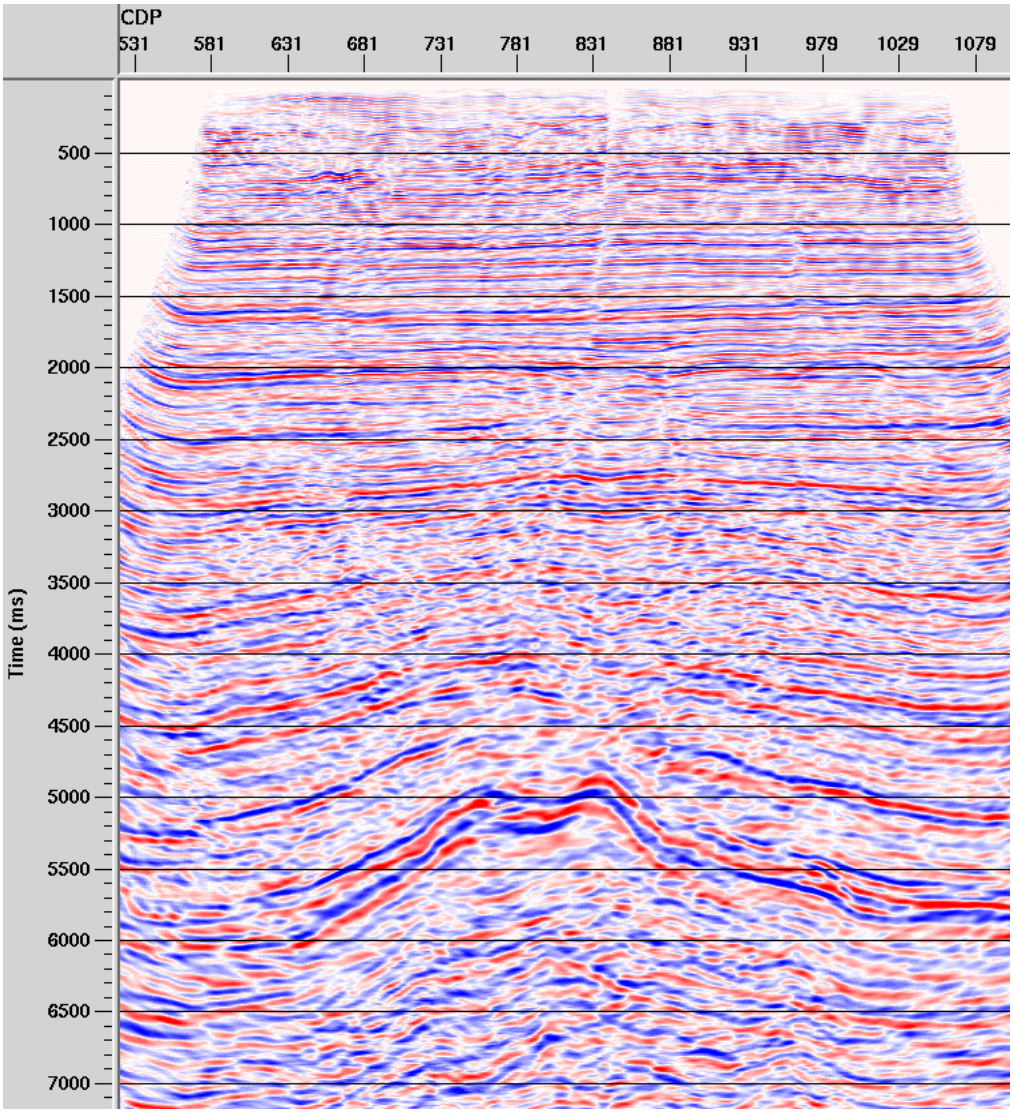


**Figure 9.11**: Final result obtained with the anisotropic PSTM. The quality of the image in the reservoir area is very good, the horst structure forming the reservoir is now easy to interpret.

Overall it is a good improvement on the result obtained with the DMO+Migration sequence at the reservoir. Figure 9.12 shows blow-ups of the target zone from the two processing sequences, on the top there is the DMO+Migration image, the bottom shows the PSTM image. We can appreciate how, after PSTM, the horst structure is more continuous and easier to interpret. On the shallower part, however, the events show better continuity in the DMO+Migration image. This is due to the fact that in this part of the data there is not a lot of coherent energy contained in the far-offset traces (see gathers in Figures 9.6 and 9.7) and the use of the full offset range introduces some noise, which deteriorates the continuity of the events. This phenomenon is discussed further in paragraph 9.5. In this interval a time-variant mute could probably improve the results.

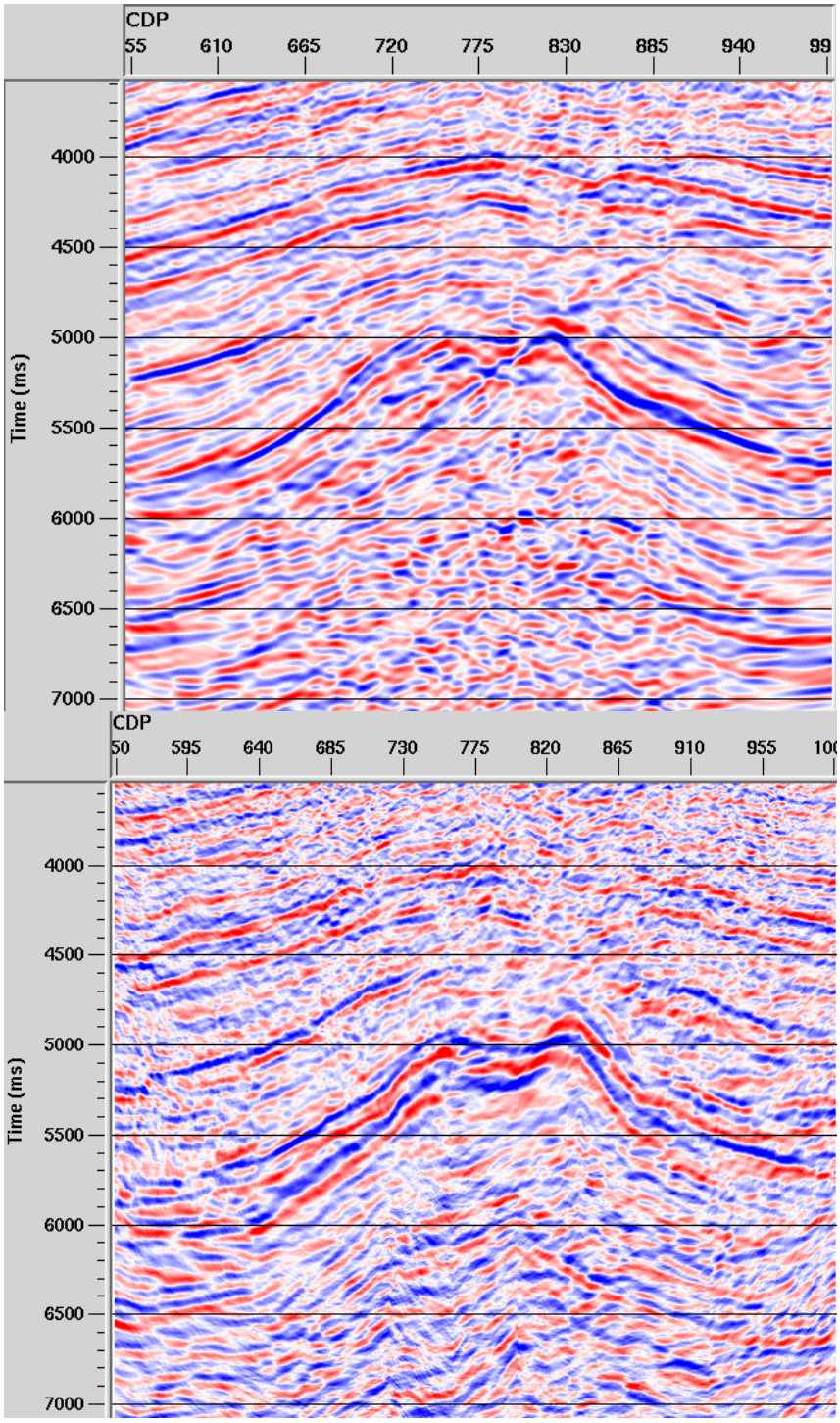


**Figure 9.12**: Blow-ups of the target area for the DMO+Migration sequence, top, and the PSTM sequence, bottom. The improvement in the target area in the PSTM image is evident.

We can also compare the PSTM image with a 2D line extracted over the same area from the 3D volume processed by the contractor, Figure 9.13. Again, the image quality after PSTM is higher. WesternGeco 3D processing sequence is a DMO+Migration, the presence of polar anisotropy is ignored and the maximum offset is limited to 3000 metres.

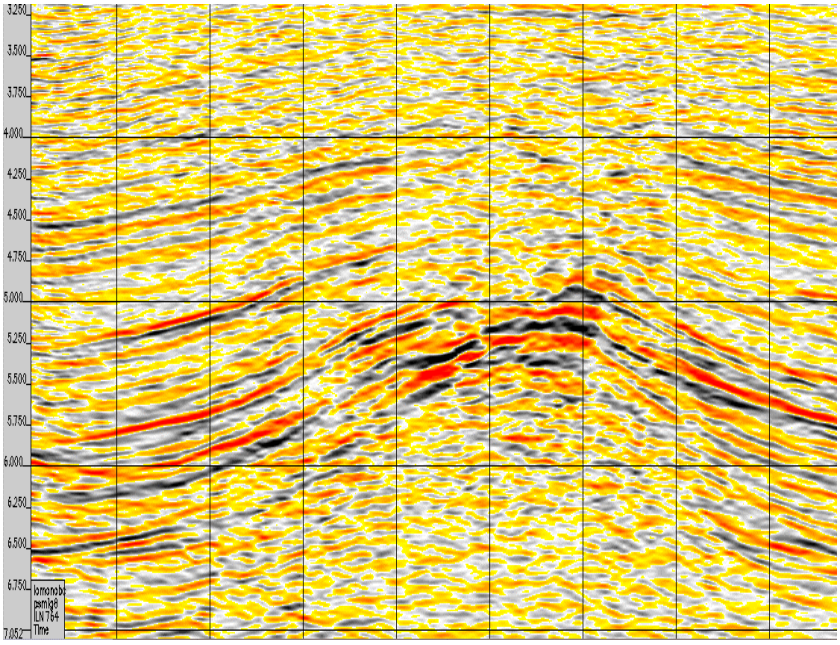

**Figure 9.13**: Lomond 3D line extracted at the 2D line location, courtesy of BG. The horst structure at the top of the reservoir is not clear in this image.

It is important to see if the PSTM result can improve the tie with the BG Group interpretation. The top part of Figure 9.14 shows the interpretation, as seen in Chapter 5. The bottom part of Figure 9.14 shows the interpretation overlain on the PSTM image. The tie between the two is extremely convincing. To fully appreciate the improvement in the event positioning I also reproduce here Figure 5.26 in Chapter 5, re-named Figure 9.15. We can notice, above all, the different position of the two normal faults, in particular the one on the left. If interpretation were carried out on the DMO+Migration image the left fault would be positioned as the dashed

line in Figure 9.15. This positioning appears implausible in a horst/graben structure, as interpreted by BG.

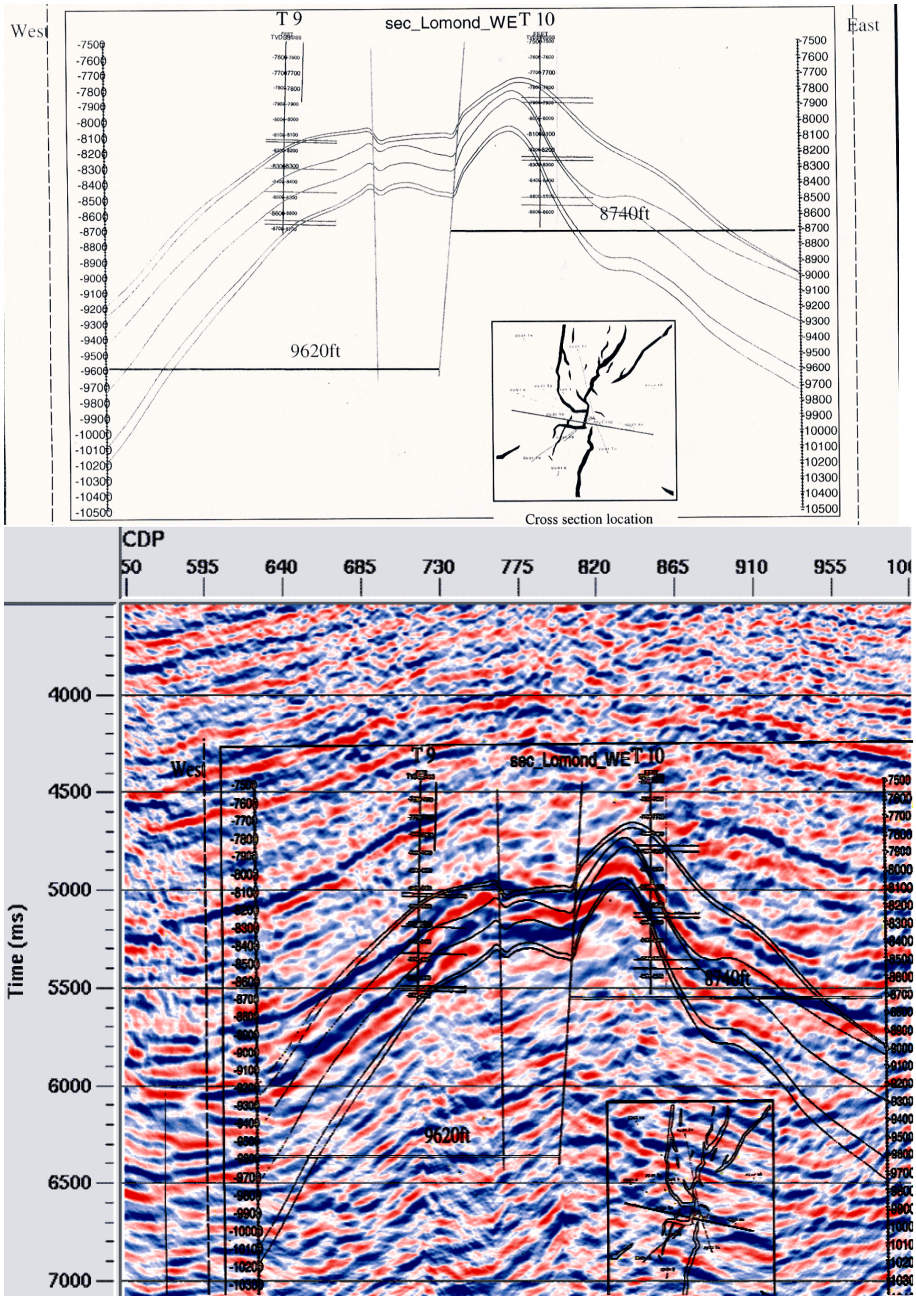


**Figure 9.14**: Top, BG Group interpretation of the Lomond field in proximity of the 2D line. Bottom, BG Group interpretation overlaid on the PSTM image, the match between the two is considerable.

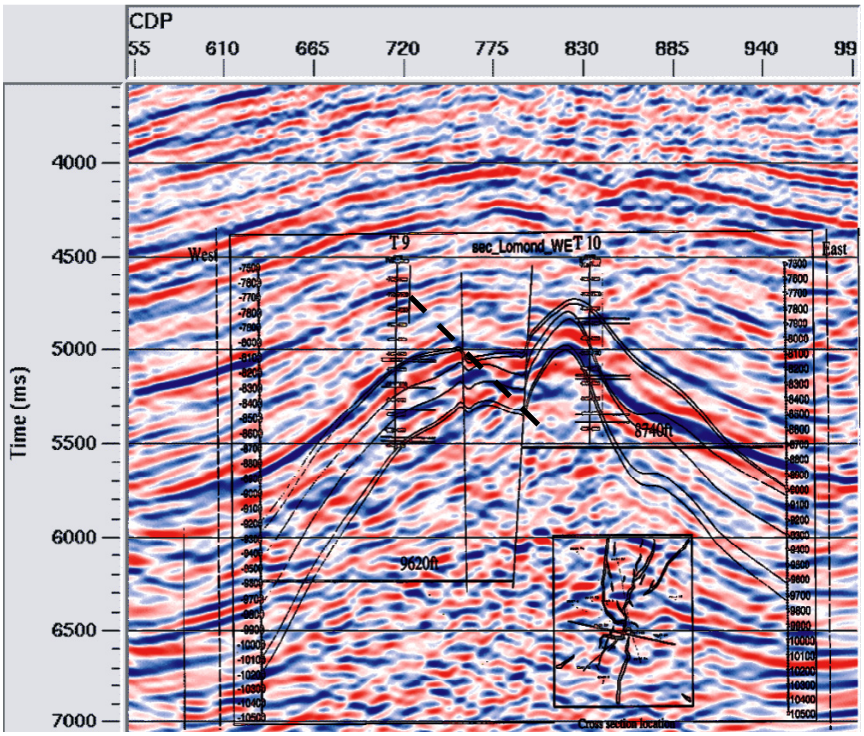


**Figure 9.15:** BG Group interpretation overlaid over the DMO+Migration image. Note the erroneous positioning of the fault in the left flank of the structure (dashed line).

## 9.5. The importance of the far offset data

The anisotropic PSTM provided the best image so far. The reasons for this are the improved lateral positioning of the events, lack of CCP smearing and the possibility of using the full offset range. To appreciate the third point better we can see what happens if we run an isotropic PSTM with short offset data only, up to 3500 metres, and with the long offset data included. These tests were run without velocity iterations, therefore the derived images are inferior to the images derived with iterations (e.g. top and bottom part of Figure 9.12). Nevertheless they demonstrate the effects of limiting the offset. Figure 9.16 summarises the results: at the top we have the isotropic PSTM image for the short offset, at the bottom the isotropic PSTM

for the full offset. Using the long offset data with the isotropic approximation produces far offset stretch and introduces lower frequencies in the stacked data; these effects are evident in the image. Nevertheless the continuity of the main event is greater than on the short offset image. Also we can notice that the events above 5.0 seconds are weaker and disturbed by noise on the full offset image. This is the same effect we noticed in the previous paragraph when comparing the anisotropic PSTM image with the DMO+Migration image.

From these results it appears that the far-offset data are required to produce a better image of the target, while shallower events are clearer when using the short-offsets only, due to the lack of coherent energy at far-offset traces. Even when compared with the full-offset anisotropic PSTM image, this part of the image shows better continuity when the offset is limited to 3000 metres.

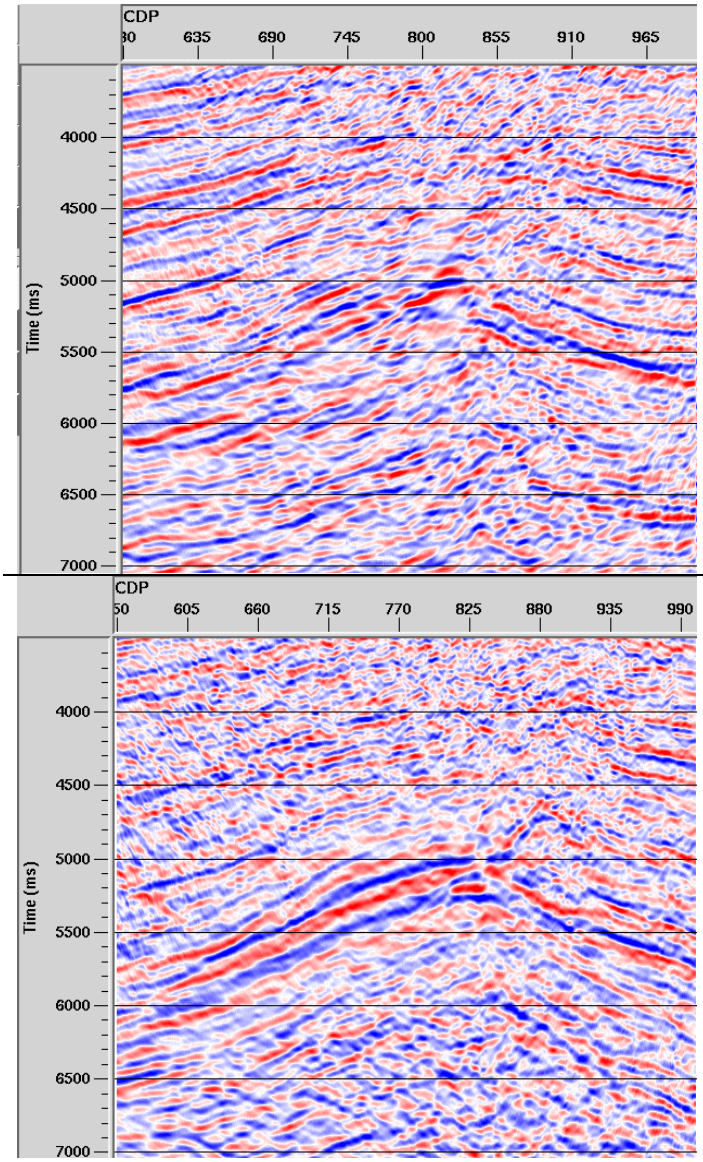


**Figure 9.16**: Top: isotropic PSTM with offset limited to 3500 metres. Bottom: isotropic PSTM using the full offset range. The short offset isotropic PSTM shows better continuity in the events above the reservoir, the isotropic PSTM with full offset has better continuity in the reservoir area, although at the expenses of the introduction of lower frequency.

## 9.6. DMO+Migration flow, anisotropic NMO

In this section I include long offset data in the DMO+Migration sequence, applying anisotropic, non-hyperbolic NMO pre- and post-PS-DMO. The NMO-corrected ACCP gathers are shown at the top of Figure 9.17, while at the bottom we have the same gathers with hyperbolic NMO correction. Note the improvements in the far offset traces, which is particularly important, since in the target area most of the energy is concentrated in this part of the spread.

Figure 9.18 shows the ACCP stacks with and without the anisotropic long offset correction. In the hyperbolic stack, right, the offset was limited to 3500 metres. In the anisotropic ACCP stack, left, the main reflector in the target area shows better continuity and sharpness. On the top of the structure, circled in the figure, we can now see a fault in the full offset section. It is also interesting the different appearance of the event at around 5.7 seconds and ACCP 1010, second black circle. The events above the target look instead worse when full offset is used, see black circles at around 4.0 seconds. This confirms the observations made in the previous paragraph: the energy in this region is concentrated in the near offsets, so that the use of the full offset is mainly introducing noise, which deteriorates the continuity of the events.

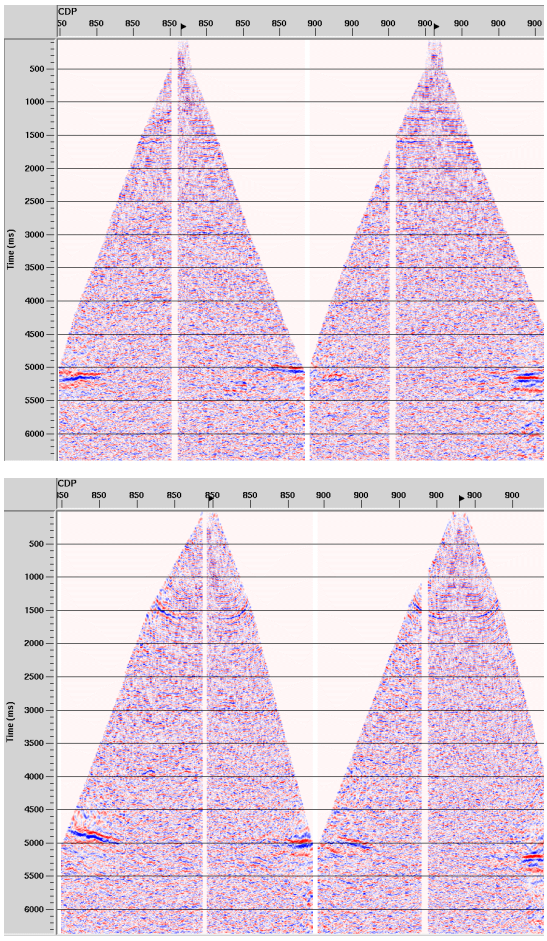


**Figure 9.17**: NMO corrected ACCP gathers, top: using the three-term anisotropic equations, bottom: using the hyperbolic approximation. Note the improvement for the event at 5.0 seconds.

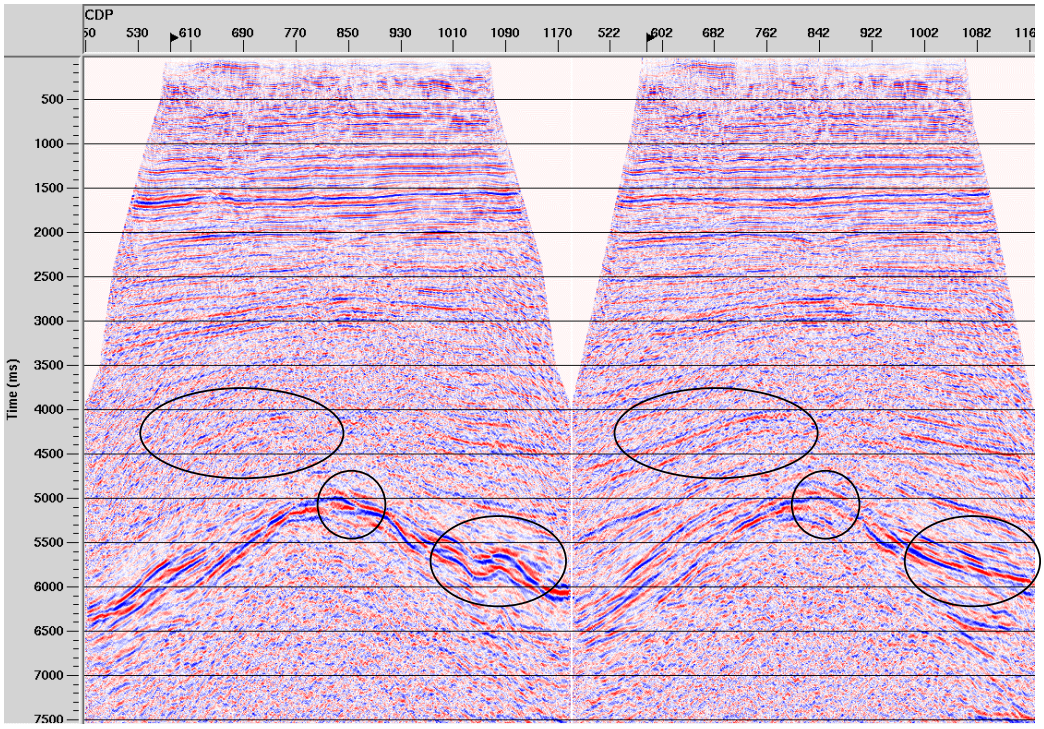


**Figure 9.18**: ACCP stacks, left, full offset after anisotropic NMO correction. Right, short offset after hyperbolic NMO correction. The two black circles at around 5 seconds indicate two interesting differences in the main reflector. The black circles at around 4 seconds shows that in that region the use of far-offsets data introduces noise and deteriorates the continuity of the events.

The post PS-DMO/NMO corrected gathers are shown in Figure 9.19. The main events looked well corrected, but I circled a feature in the positive offset of CCP 800, which is present also in the neighbouring CCPs, not displayed in Figure 9.19 (CCPs displayed here are at 50 CCPs interval). This energy stacks up to create a strong event in the stacked section, Figure 9.20. This event does not seem somehow "real" and at this moment in time I can only speculate the reason for its presence: since the PS-DMO module in ProMAX does not include anisotropy, the process might have displaced and mis-positioned some of the energy in the far offset traces, where the CCP smearing is naturally higher.

Needless to say this feature creates problem during the Post Stack Migration, even lowering the velocity to 80% of the smoothed stacking velocity the resulting

image is particularly poor, with effects similar to over-migration, Figure 9.21.

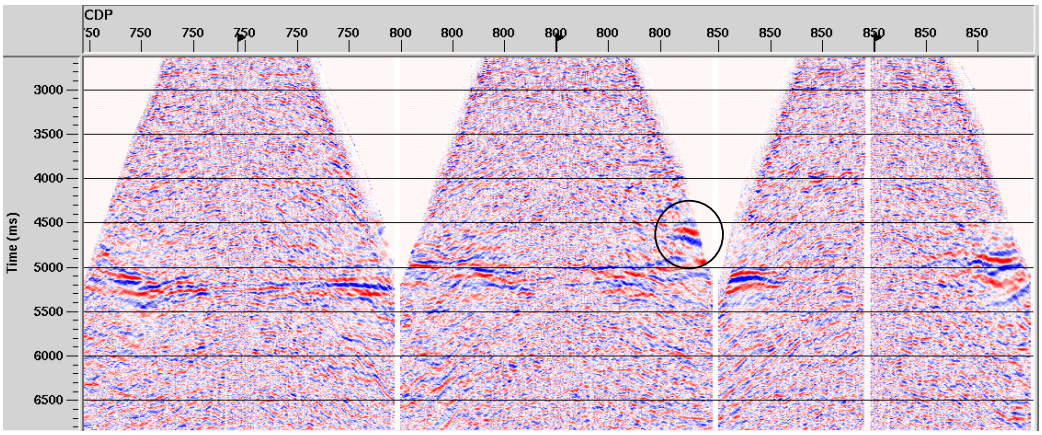


**Figure 9.19**: NMO corrected CCP gather after PS-DMO and new anisotropic velocity analysis. The main events are well corrected. In black I circled some energy moved into an anomalous position.

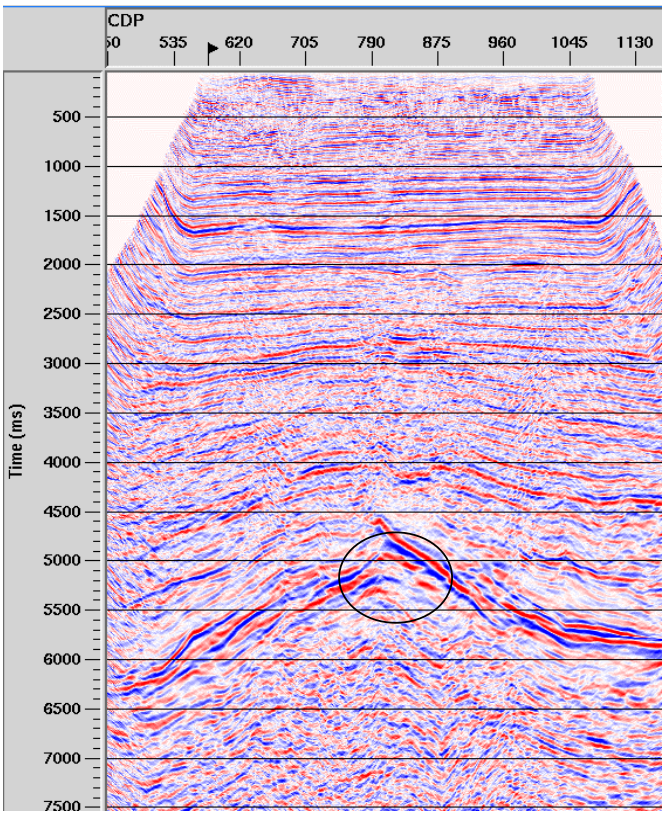


**Figure 9.20**: PS-DMO stack using long offset data. The quality of the stack is not great, and in the centre of the section a strong event appears, circled in black. Whether this event is real is questionable.

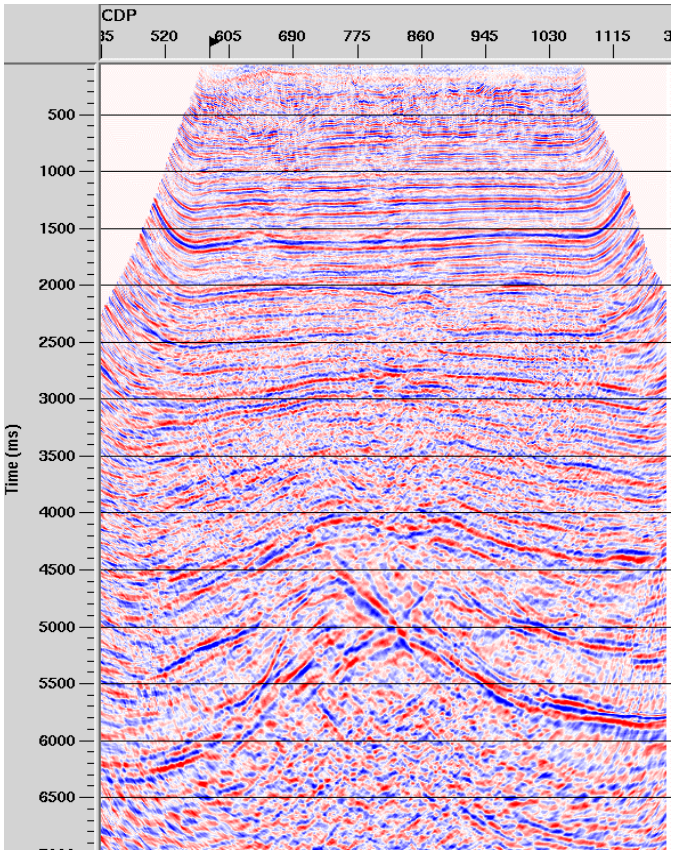


**Figure 9.21**: Final migration using long offset data. The presence of the strong event shown in the DMO stack degraded the overall quality of the image.

So, although the ACCP stack with long offset correction looked like an improvement at the target area compared to the short offset one, the PS-DMO seems not to be able to handle long offset data with dips in an anisotropic medium. The best results for the DMO-Migration sequence are definitely obtained limiting the offset range to x/z up to 0.7.

The sequence of anisotropic NMO + (isotropic) PS-DMO+ Post Stack Migration does not produce a reliable image. For a proper comparison with the full anisotropic PSTM I should have used an anisotropic PS-DMO, but to my knowledge such a tool has not been developed yet. Indeed even for P-wave processing there has been only limited effort to include anisotropy in DMO. Alkalifah (1996) proposed to use explicit ray-tracing to calculate the DMO operator in a VTI medium but his algorithm had high sensitivity to the anisotropic parameter $\eta$, which is difficult to

extract with accuracy from velocity analysis (Traub and Li, 2002). Given the power of today's computers, the full PSTM has largely become the tool chosen for developing anisotropic codes. In C-wave this is even more sensible, since we avoid CCP binning.

Here I conclude that in complex areas the best imaging tool for C-waves is the PSTM, as it allows us to properly handle the presence of dips, anisotropy and long offset data.

## 9.7. Conclusions

In this Chapter I showed the results from an anisotropic PSTM flow applied to the Lomond field data. This processing sequence was chosen considering both the structural complexity of the area and the presence of polar anisotropy, as seen in the previous chapter. This workflow requires a careful model building; $v_{cn}$, $\gamma_0$, $\gamma_{eff}$ and $\chi_{eff}$ are the parameters needed. The model building procedure was already shown in the previous chapters. Importantly, we can perform model updating in the time-migrated domain, which allows to optimise the parameters in their true migrated position.

The final image obtained at the target is excellent; comparing it to the result from the DMO+Migration sequence highlights the improvements in the positioning and continuity of the main events at the reservoir target. This image ties with high degree of accuracy the interpretation carried out by BG Group, which is probably the proof of the reliability of the processing results.

The methodology presented is robust and relatively simple to apply, although more time consuming when compared with the isotropic DMO+Migration sequence, since we have to extract four parameters instead of two ($v_{cn}$ and $\gamma_{eff}$). The PSTM sequence has also the advantage of relying less on P-wave information.

Testing isotropic PSTM with short and long offset data led to the conclusion that in the Lomond target area the far offset traces are needed to produce good imaging. A question then rises: can we include long offset data into the

DMO+Migration sequence? The answer is negative: the PS-DMO does not seem to handle correctly the energy at far offset traces, even if the input is properly NMO corrected at far offsets. The PS-DMO stack shows an artefact, which degrades the migrated image. This can be due to the fact that the PS-DMO uses an isotropic algorithm, or to the limitation of the algorithm itself.

The results indicate that the PSTM flow is the most suitable tool in imaging anisotropic media with complex geological structure.

# Chapter 10: Discussions and the road ahead

## 10.1. Ph.D. conclusions

This work is focused on improving the practice of converted wave processing in anisotropic media in the time domain. The results presented here come from a 2D 4C dataset acquired over the Lomond Field, in the Central North Sea. This area shows clear indications of the presence of polar anisotropy, which needs to be included in the processing sequence. I accounted for the anisotropy effects using a flow based on anisotropic PSTM. This flow requires a complex model building procedure. I demonstrated that ignoring the presence of anisotropy leads to poor results in the imaging process.

Basic C-wave processing is dependent upon two parameters: the hyperbolic C-wave stacking velocity, $v_{cn,}$ and the effective velocity ratio, $\gamma_{eff}$. $\gamma_{eff}$ determines the CCP position in a layered medium. When velocity information, vertical and NMO velocity ratios, are used to calculate $\gamma_{eff}$, we have to consider error propagation. Results of a sensitivity analysis show that, in areas affected by dip, stacking velocities are sensitive to changes in the initial binning $v_p/v_s$ ratio. These small velocity errors, due to apparent velocities in dipping areas, propagate as the square in the re-calculation of the depth-variant velocity ratio and must be taken into account. If the resulting value of $\gamma_{eff}$ differs significantly from the initial velocity ratio used for velocity analysis, new velocity analyses after more appropriate binning are necessary. The CCP-scanning technique, which is based on imaging criteria, may be tedious to

apply, but gives more reliable results in zones of complex geology, since it is velocity-independent.

The vertical velocity ratio, $\gamma_0$, is extracted from event correlation on P- and C-wave stacks. It can also be estimated from well logs when shear logs are acquired. In the Lomond Field the seismic derived $\gamma_0$ was about 30% higher than that calculated from well logs. Even though event correlation is an interpretative step, therefore subject to possible errors, I validated the seismic-derived $v_p/v_s$ using the CCP-scanning technique. The lower value in well logs may be due to the presence of gas, the effects of polar anisotropy in deviated wells and the effects of frequency-dependent dispersion. In the Lomond field wells, gas had little effect on the sonic log, while the presence of anisotropy lowered the value of the $v_p/v_s$ by about 15%. Frequency-dependent dispersion could have had a similar effect but it was difficult to quantify. Residual errors in the event correlation could also be partially responsible for the measured difference. Importantly, I proved that using the well-log derived $\gamma_0$ led to an erroneous value of $\gamma_{eff}$. In fact, the best image was obtained using the seismic-derived vertical velocity ratio. Using the raw well-log derived velocity ratio as main input in C-wave processing should be avoided.

I presented an integrated analysis to confirm the presence of polar anisotropy in the Lomond field. The geology of this area is dominated by an overburden mainly composed of shales and mudstones, often laminated, with sandstone bodies from turbiditic events present. This lithology is recognised to be the main source of seismic anisotropy. I performed a PSDM on the P-P data. The final image revealed a depth mismatch with the well markers. The event in the CRP looked well-flattened, proving that the correct velocity was used and that the mismatch was probably due to the presence of anisotropy. Effects of anisotropy may also be observed in well logs, which show angular dependency of sonic velocity, with higher velocity for higher angles of deviation. Similar angular dependency of the velocity was observed comparing interval and average velocities from well logs and check shots (vertical propagation) and from seismic data (non-vertical propagation). These observations led to the conclusion that the Lomond field is seismically anisotropic.

To account for the presence of anisotropy during processing I used the parameter $\chi_{eff}$, the effective parameter representing converted-wave anisotropy. $\chi_{eff}$ is a combination of P- and S-wave anisotropy. This parameter can be estimated from

converted wave seismic data alone via a double-scan or a single scan. The single scan proved to be more reliable in the Lomond data. The imaging was performed using a sequence based on anisotropic PSTM. This flow requires careful model building, since it is dependent upon four parameters: $v_{cn}$, $\gamma_0$, $\gamma_{eff}$ and $\chi_{eff}$. This model can be updated in the time-migrated domain. I compared $\gamma_{eff}$ and $\chi_{eff}$ before and after the updating to show how the presence of dip had a strong effect in their calculation. $\chi_{eff}$ before PTSM showed a direct correlation with the geological structure. This correlation disappeared after PSTM, proving that part of the residual moveout attributed to anisotropy was caused by dip. Similarly, $\gamma_{eff}$ calculated after PSTM did not show the areas of minima present before PSTM in the dipping parts of the region. This analysis confirmed the importance of optimising the parameters in the time-migrated domain.

The anisotropic PSTM image at the target was of good quality. It ma*tc*hed with a high degree of accuracy the geological interpretation performed by BG Group, which is a good proof of the quality of the processing. PSTM tests showed that accounting for the presence of anisotropy allowed the use of the full range of offsets, which was important to produce the correct image. Due to a lack of coherent energy at far-offset traces in the area above the reservoir, some noise was introduced in this interval.

Comparing this result with the image obtained with a "conventional", isotropic sequence based on DMO and post-stack migration highlighted the differences in the lateral positioning of the events in the reservoir area. The DMO+migration image suffered from failing to account for the presence of anisotropy and from the limitation of the processing flow. Nevertheless it was an improvement compared to the P-wave image, confirming that, even with a simple, isotropic sequence, C-waves produce better results in gas-affected areas. A test using full-offset data after non-hyperbolic NMO as input for the isotropic PS-DMO did not produce a satisfactory image. These results led to the conclusion that the anisotropic PSTM is the better imaging tool in complex and anisotropic areas, when working in the time domain.

## 10.2. The road ahead

C-wave imaging has moved forward over the years, the PSTM results showed here are proofs of that. Still more needs to be done. The VTI assumption has limits. If we consider the Lomond Field, we know that there are dips up to 30%. This can lead to a more complex anisotropic geometry, Tilted Transverse Isotropy (TTI), which is more difficult to parameterise for processing purposes.

I believe the full potential of multicomponent technology is in the possibility of unifying P and S-wave information, to move into a joint interpretation, which can lead to lithology and fluid information. This way multicomponent seismic data can become one of the most valuable tools for reservoir characterization. The challenge is to find a methodology to correlate the two volumes with a high degree of accuracy. At the moment the correlation is still based on human interpretation and therefore prone to error, above all when the geological structure is mainly horizontal.

Understandably, it is the desire of every interpreter to be able to tie the P and C-wave sections in depth. But multicomponent joint P and C-wave PSDM, although applied in cases, is not widespread. The problem is not the algorithm, but in the difficulty of producing correct velocity and anisotropy models. Most approaches assume correct P-wave velocity and scan the C-wave data to define the S-wave velocity (Zhang, 2001, Mikhailov and Herkenhoff, 2001). These procedures rely on an initial event correlation and are difficult to implement in areas with no clear geological reference or in the presence of gas clouds. Anisotropy is often determined by depth misma*tc*h between the wells and the seismic data (see Chapter 8); these results are then only valid around the well area. Other approaches (Kendall et al., 2001, and Jing et al., 2002) scan the data for different values of $\varepsilon$ and $\delta$, but they are very time consuming and not always successful. More work needs to be done to include anisotropy in PSDM in a way which is, at the same time, accurate and practical to use.

# References

Aki, K. and Richards, P.J., 1980, Quantitative Seismology: Theory and Methods, University Science Books.

Alkhalifah, T. A. and Larner, K., 1994, Migration error in transversely isotropic media: Geophysics, 59, 1405-1418.

Alkhalifah, T. A. and Tsvankin, I., 1995, Velocity analysis for transversely isotropic media: Geophysics, 60, 1550-1566.

Alkhalifah, T. A., 1996, Transformation to zero offset in transversely isotropic media, Geophysics, 61, 947-963.

Audebert, F., Granger, P.Y., and Herrenshmidt, A., 1999, CCP-Scan technique: True common conversion point sorting and converted-wave velocity analysis solved by PP and PS pre-stack depth migration: 69th Internat. Mtg. Soc. Expl. Geophys., Expanded Abstract. 1186-1189.

Bagaini, C., Bale, R., Brunelliere, J., Caprioli, P. and Ronen S., 2000, High fidelity seabed data processing, 70th Mtg. Soc. Expl. Geophys., Expanded Abstract. 1209-1212.

Ball, V., and Corrigan, D., 1996, Dual sensor summation of noisy ocean-bottom cable data, 66th Internat. Mtg. Soc. Expl. Geophys., Expanded Abstract, (28-31).

Barr, F. J. and Sanders, J. I., 1986, Attenuation of water-clumn reverberation using pressure and velocity detectors in a water-bottom cable, 59th Internat. Mtg. Soc. Expl. Geophys., Expanded Abstract, (653-656).

Berg, E., 1997, 4C-2D or 3D sea bed seismic methodology, proceedings of IIR Forum on Acquisition, Processing and Interpretation of Marine Seismic Data, (1274-1282).

Boelle, J. L. and Ricarte, P., 2003, Deep target Pre Stack Time Migration and Migration Velocity Analysis using converted PS data, 73th Internat. Mtg. Soc. Expl. Geophys., Expanded Abstracts.

Brandsberg-Dahl, S. and Berkved, O.I., 2002, Anisotropy P-wave velocity derived from deviated wells at the Valhall Field, 64th Mtg.: Eur. Assn. of Expl. Geophys., Expanded Abstract, P135.

Caldwell, J., Christie, P., Engelmark, F., McHugo, S., Ozdemir, H., Kristiansen, P., and MacLeod, M., 1999, Shear waves shine brightly, Schlumberger Oilfield Review.

Chen, H., and Castagna, J. P., 2000, Anisotropic effects on full and partial stacks, Geophysics, 65, 1028-1031.

Cordier, J.P., 1985, Velocities in reflection seismology, D.Reidel Publishing Company.

Crampin, S., 1985, Evaluation of anisotropy by shear wave splitting, Geophysics, 50, 142-152.

Dai H., and Li, X.-Y., 2001, Anisotropic migration and model building for Alba 4C data., 71st Internat. Mtg. Soc. Expl. Geophys., Expanded Abstract, 795-798.

Dai H., and Li, X.-Y., 2003, Migration velocity analysis of C-wave using INMO-CIP gathers of PKTM: a case study from the Gulf of Mexico, 65th Mtg EAGE Conference, Exoanded Abstract, in press.

Dai H., Li, X.-Y., and Mueller, M., 2000, Compensating for the effect of gas clouds by prestack migration: A case study from Valhall, 70th Internat. Mtg. Soc. Expl. Geophys., Expanded Abstract. 1047-1050

Dai, H., 2003a, Interactive estimation of anisotropic parameters and velocities from PS converted waves, 73th Internat. Mtg. Soc. Expl. Geophys., Expanded Abstract (1577-1580)

Dai, H., 2003b, Sensitivity analysis of migration velocities for P-S converted wave (C-wave) imaging, 64th Mtg.:Eur. Assn. of Expl. Geophys., session: P008

De Angelo, M. V., Backus, Milo, Hardage, B. A., Murray, Paul, and Knapp, Steve, 2003, Depth registration of P-wave and C-wave seismic data for shallow marine sediment characterization, Gulf of Mexico: The Leading Edge, v. 22, no. 2, 96–105.

Dellinger, J.; Clarke, R.; Gutowski, P., 2001, Horizontal vector infidelity correction by general linear transform, 71st Mtg. Soc. Expl. Geophys., Expanded Abstract. 865-868

Eastwood, R. L. and Castagna, J. P., 1986, Interpretation of *Vp*/*Vs* ratios from sonic logs, in Domenico, S. N., Ed., Shear-wave exploration: Soc. of Expl. Geophys., 139-153.

Esmersoy C., Koster K., Williams M., Boyd A. and Kane M., 1990, Shear Wave Logging with Dipoles, Schlumberger Oilfield Review 2, N4, 9-12

Fromyr, E., Randazzo, S., Duffaut, K. and Amundsen, L., 2002, Imaging and characterization with PP and PS – A feasibility study from the North Sea, 72nd Mtg. Soc. Expl. Geophys., Expanded Abstract.

Futterman, W. I., 1962, Dispersive body waves, J. Geophys. Res., 67, 5279-5291.

Gaiser, J. E., 1998, Compensating OBC data variation in geophone coupling, 68th Mtg. Soc. Expl. Geophys., Expanded Abstract. 1429-1432.

Garotta, R., 2000, Shear waves from acquisition to interpretation, SEG Distinguished Instructor short course, Distinguished instructor series, N. 3

Garotta, R., Granger, P.-Y., and Dariu, H., 2002, Combined interpretation of PP and PS data provides direct access to elastic rock properties, The Leading Edge, Vol.21, N.6

Garotta, R., Granger, P.-Y., Audebert, F., 2003, About Gamma ratios and their combinations, 65th Mtg.: Eur. Assn. of Expl. Geophys., Expanded Abstract, MC 1.

Gatliff, R. W., Richards, P. C., Graham, C. C., McCormac, M., Smith, N. J. P., Long, D., Cameron, T. D. J., Evans, D., Stevenson, A. G., Bulat, J. and Ri*tc*hie, J. D., 1994, The geology of the central North Sea, British Geological Survey, United Kindom Offshore Report, London HMSO, (64-74)

Geco-Prakla, 1998, Multi-component 3D seismic survey final report, not published.

Glennie, K. W., 1990, Introduction to the petroleum geology of the North Sea, Blackwell Science, Third edition, (273-291).

Granli, J. R., Arntsen, B., Sollid, A., and Hilde, E., 1999, Imaging through gas-filled sediments using marine shear wave data, Geophysics, 64, 668-677.

Gray, S.H., Etgen, J., Dellinger, J., and Whitmore, D., 2001, Seismic migration problems and solutions, Geophysics, 66, 1622-1640.

Gruping. T., 1998, Introduction to formation evaluation, Course notes for MSc in Petroleum Geology, Aberdeen University.

Hanssen P., Li X.-Y., and Ziolkowski A., 2000, Converted waves for sub-basalt imaging?, 70th Internat. Mtg. Soc. Expl. Geophys., Expanded Abstracts, session: MC 2.3.

Harrison, M., 1992, Processing of P-SV surface-seismic data: anisotropy analysis, dip-moveout, and migration, Ph.D. dissertation, University of Calgary.

Hodgson, N. A., Farnsworrth, J., Fraser, A. J., 1992, Salt related tectonics, sedimentation and hydrocarbon plays in the Central Graben, North Sea, UKCS, Hardman R.F.P, Exploration Britain: Geological insights for the next decade, Geological Society Special Pubbl., No. 67, 31-63.

Hoffe, B. H., Cary, P. W., Lines, L. R., 1999, A simple and robust method for combining dual-sensor OBC data? CREWES Research Report, Volume 11.

Hubral, P., and Krey, T., 1980, Interval velocities from seismic time measurements, SEG, Tulsa.

Jing, C., Shatilo, A. and Willen, D., 2002, Converted-wave migration velocities from common-receiver image focusing analysis, 72nd Internat. Mtg. Soc. Expl. Geophys., Expanded Abstract, (994-997)

Kendall, R. R., Gray, S., Miao, X., 2001, Anisotropic prestack depth migration for multicomponent data – methodology and examples, 63rd EAGE Meeting, Expanded Abstract, L-30.

Kendall, R.R., Gray, S.H. and Murphy, G.E., 1998, Subsalt imaging using prestack depth migration of converted waves, 68th Mtg. Soc. Expl. Geophys., Expanded Abstract. 2052-2055.

Kristiansen, P., Fowler, P., Mobley, E., 2003, Anisotropic Kirchhoff prestack time migration for enhanced multicomponent imaging, 73rd Mtg. Soc. Expl. Geophys., Expanded Abstract, 961-964

Leaney, S., Bale, R., Wheeler, M., and *Tc*herkashnev, S., 2001, Borehole-integrates anisotropic processing of converted modes, The Leading Edge, Vol. 20, N. 9.

Leaney, S., Wheeler, M., *Tc*herkashnev, S., Probert, T., and Law, A., 2000, Borehole-calibrated anisotropic processing of converted modes - a sub-chalk imaging study, 70th Internat. Mtg. Soc. Expl. Geophys., Expanded Abstract, MC2.6

Levin, F.K.,1971, Apparent velocity from dip interface reflections, Geophysics, 36, 510-516

Li, G., Ziolkowski, A., Taylor, D., and Hall, G., 2002, An approach to determine subsurface structure using P-P and P-SV reflections, 64th Eur. Assn. of Expl. Geophys., Expanded Abstract, P006.

Li, X.-Y., and Yuan, J., 1999, Geophone orientation and coupling in sea-floor data, Geophysical Prospecting, 47, 995-1013.

Li, X.-Y., and Yuan, J., 1999a, Converted-wave moveout and parameter estimation for tranverse isotropy, 61st Mtg.: Eur. Assn. of Expl. Geophys.. Expanded Abstract, 32-35

Li, X.-Y., and Yuan, J., 1999b, Anisotropic velocity analysis for 4C seismic data, a case study, 69th Internat. Mtg. Soc. Expl. Geophys., Expanded Abstract. 732-735.

Li, X.-Y., and Yuan, J., 2001, Converted-wave imaging in inhomogeneous, anisotropic media: Part I – Parameter estimation, 63rd Eur. Assn. of Expl. Geophys., Expanded Abstract, I, P109.

Li, X-Y., Dai, H., Mueller, M.C., and Barkved, O.I., 2001, Compensating for the effects of gas clouds on C-wave imaging: A case study from Valhall, The Leading Edge, Vol. 20, N. 9.

Li, X-Y., Yuan, J. and Bagaini, C., 2000, Lomond data analysis: geophone coupling and converted-wave imaging, EAP, Annual Report, 7,185-212.

Loinger, E., Gaiser, J.E., Lucini, A., Pestoni, M. and Walters, R.M., 2002, 3D/4C Emilio, Azimuth processing for anisotropy analysis, 64th Eur. Assn. of Expl. Geophys., Expanded Abstract, F023.

MacLeod, M., Hanson, R., Hadley, M. Reyholds, K., Lumley, D., MacHugo, S., and Probert, T., 1999, The Alba Field OBC seismic survey, 69th Internat. Mtg. Soc. Expl. Geophys., Expanded Abstracts, 725-727.

Mancini, F., Li., X.-Y., Ziolkowki, A., and Pointer, T., 2002, Interpreting velocity ratios from 4C seismic data and well logs in the presence of gas and anisotropy, 72nd Mtg.: Soc. Expl. Geophys. Expanded Abstract, 1002-1005.

Mikhailov, O., and Herkenhoff, F., 2001, Robust estimation of anisotropy parameters from correlation of PP and PS images and wells, 63rd Eur. Assn. of Expl. Geophys., Expanded Abstract, P113.

Nedlin, G., 1986, Special features of P-S arrivals, Geophysics, Vol.51, (347-352)

Pope, D., Kimmedal, J. And Hansen, J., 2000, Using 3D 4C Seismic to drill beneath the Lomond gas cloud, 62nd Mtg.:Eur. Assn. of Expl. Geophys., Expanded abstract, L01.

Reid, F.; MacBeth, C., 2000, Tests of vector fidelity in permanently installed multicomponent sensors, 70th Internat. Mtg. Soc. Expl. Geophys., Expanded Abstracts, 1213-1216

Robein, E., 2003,Velocities, Time-imaging and Depth imaging in Reflection Seismics. Principles and Methods, Chapter 4, EAGE Publications.

Soubaras, R., 1996, Ocean-bottom hydrophone and geophone processing, 66th Internat. Mtg. Soc. Expl. Geophys., Expanded Abstract, (24-27).

Tessmer, G., and Behle, A., 1988, "Common conversion point data-stacking technique for converted waves, Geophysical prospecting, 36, 671-688.

Thomsen, L., 1986, Weak elastic anisotropy, Geophysics, 51, 1954-1956.

Thomsen, L., 1999, Converted-Wave reflection seismology over inhomogeneous, anisotropic media, Geophysics, 64, 678-690.

Thomsen, L., Barkved, O. I., Haggard, B., Kimmedal, J. H, Rosland, B., 1997, Converted-wave imaging of Valhall reservoir, 59th Mtg.: Eur. Assn. of Expl. Geophys., Expanded Abstract, B048

Traub, B. M., Li, X.-Y., 2002, Sensitivity of Anisotropic Parameter Estimation from 4C Data - Modelling and Case Studies, 64th Mtg.: Eur. Assn. Geosci. Eng., F018

Tsvankin, I., and Thomsen, L., 1994, Nonhyperbolic reflection moveout in anisotropic media: Geophysics, 59, 1290-1304.

Tsvankin, I., and Thomsen, L., 1995, Inversion of reflection traveltimes for transverse isotropy: Geophysics, 60, 1095-1107.

Van der Baan, M., Kerrane, T., Kendall, J.-M., Taylor, N., 2003, Imaging sub-basalt structures using locally converted waves, First Break, Volume 21, N.6.

Van Dok, R. and Gaiser J., 2001, Stratigraphic description of the Morrow formation using mode-converted shear waves: Interpretation tools and techniques for three land surveys, The Leading Edge, Vol. 20, N. 9.

Veltri, L.M., Angerer, E., Gaiser, J.E., Grandi, A. and Lynn, H., 2002, Emilio Field – Anisotropy analysis from PP and PS data, 64th Mtg.: Eur. Assn. of Expl. Geophys., Expanded Abstract, F046.

Wang, Z., 2001), Seismic anisotropy in sedimentary rocks. 71th Internat. Mtg. Soc. Expl. Geophys., Expanded Abstract, RP2, 1740-1743

Winterstein, D., F., 1990, Velocity anisotropy terminology for geophysicists, Geophysics, 55, 1070-1088.

Wyllie, M. J. R., Gregory, A. R. and Gardener, L. W., 1956, Elastic wave velocities in heterogeneous and porous media. Geophysics, **21** (1); 41-70.

Yilmaz, O., 2000, Seismic data analysis, Soc. of Expl. Geophys.

Yuan J., and Li, X.-Y., 2001, PS-wave conversion-point equations for layered anisotropic media, 63rd Mtg.: Eur. Assn. of Expl. Geophys., Session: P112.

Yuan J., Li, X.Y., and Zhu, X., 2002, C-wave anisotropic parameter estimation from conversion point, 64th Mtg.: Eur. Assn. of Expl. Geophys., session: P253

Yuan J., Li, X.-Y., and Ziolkowski, A., 2001, Converted-wave moveout analysis in layered anisotropic media – A case, 63rd Mtg.: Eur. Assn. of Expl. Geophys., Expanded Abstract, L-27

Yuan, J., and Li X.-Y., 1998, A new approach for converted wave moveout in transversely isotropic media, 68th Internat. Mtg. Soc. Expl. Geophys., Expanded Abstract. 1495-1498.

Yuan, J., Li X.-Y, Ziolkowski, A., and Strijbos, F., 1998 Processing 4-C sea-floor seismic data: A case example from the North Sea, 68th Internat. Mtg. Soc. Expl. Geophys., Expanded Abstract. 714-717.

Zhang, Y., 1992, Stacking P-SV Converted Wave Data with Raypath Velocity, 62nd Internat. Mtg. Soc. Expl. Geophys., Expanded Abstract, 1214-1217

Zhang, Y., Pham, D. and Lou, M., 2002, Velocity Update via Joint Velocity Inversion for Anisotropic Depth Migration, 72nd Internat. Mtg. Soc. Expl. Geophys., Expanded Abstract, (141-144).

Ziolkowski, A., Underhill, J. and Johnston, R., 1998, Wavelet, well ties, and the search for subtle stratigraphic trap, Geophysics, 63, 297-313.

# Appendix A: Preprocessing

## A.1. Preprocessing sequence, details

The preprocessing sequence applied to the Lomond field data is:

- Geometry application
- Gain recovery

  Amplitude multiplied by a factor $T^2$ (T is time),
- Signature deconvolution

The goal of signature deconvolution is to produce a shorter wavelet (the shortest possible within the bandwidth of the data) than the original wavelet (Ziolkowki et al, 1998). This short wavelet is to be preserved unchanged during the following processing steps, above all deconvolution, so that we have a good control over it between wells. As the source signature was not recorded during acquisition the approach tried here was to model it using the PGS software Nucleus. I modelled the WesternGeco's source array and from it I calculated the far field signature at any point in the water (Figure A1 and A2).

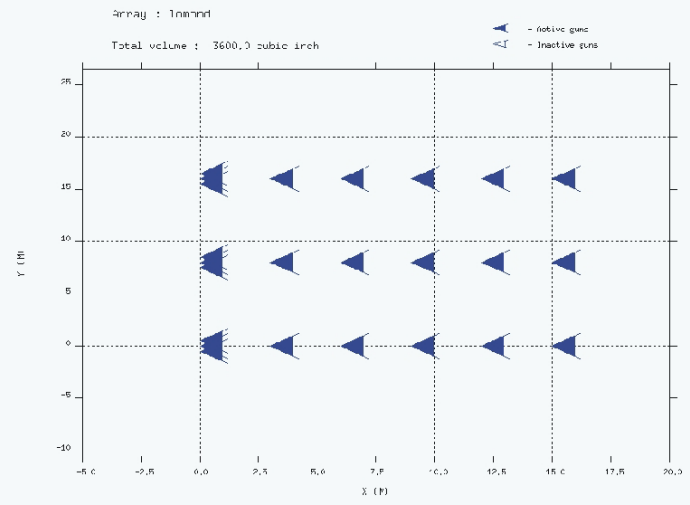


**Figure A1:** WesternGeco's gun array.

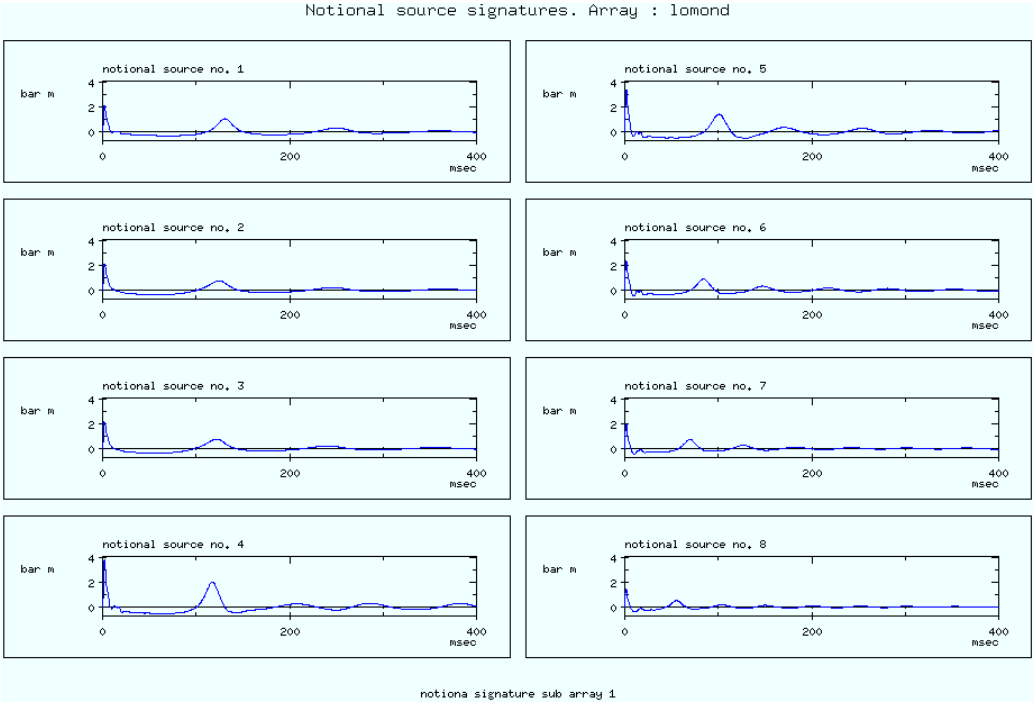


**Figure A2**: Notional signature from 8 different guns (sub-array 1) calculated from the source array in Figure A1.

The result is a very long wavelet (Figure A3).

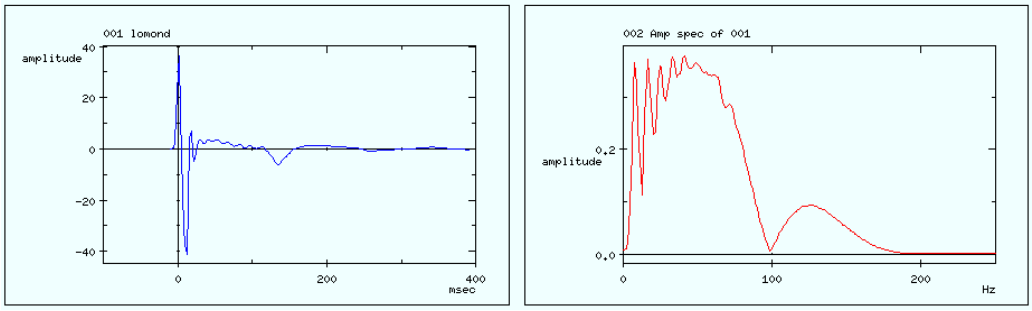


**Figure A3**: Lomond far-field wavelet and its amplitude spectrum.

Following Ziolkowki et al. (1998), I compressed it to a minimum-phase wavelet in the available bandwidth. This process is illustrated in Figure A4: from left to right we have (1) the original wavelet, (2) its amplitude spectrum, (3) a desired short wavelet created from (1), and (4) amplitude spectrum of (3). A Wiener filter (5) was designed to shape (1) into (3), so that convolving (1) with the filter (5) we obtain the resulting short wavelet (6). (7) is its spectrum. (6) and (7) look very much like (3) and (4) which proves the good performance of the Wiener filter.

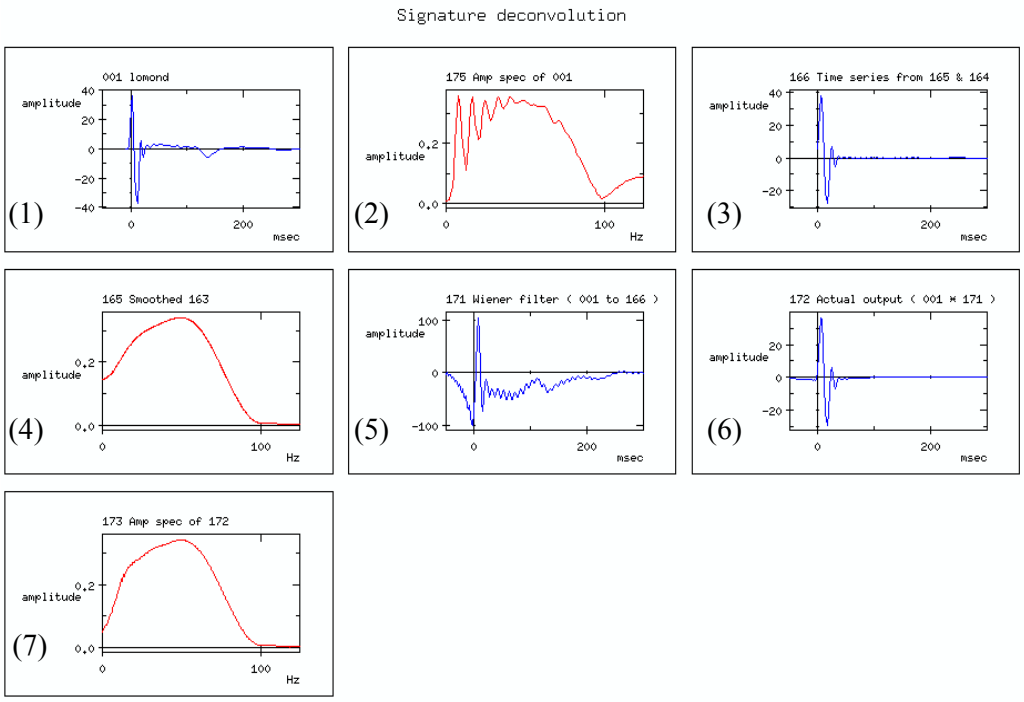


**Figure A4**: Signature deconvolution process, see text for details.

The desired wavelet (3) was produced using the following steps:

1) Band Pass filter 8Hz/18dB-125Hz/72dB,
2) Spectrum smoothing,
3) Minimum phase equivalent of the ou*tp*ut of (2),
4) Predictive deconvolution with a 36 ms gap,
5) Spectrum smoothing.

The same process was applied to produce a short wavelet for converted waves with the only difference of considering the overall lower frequency content of the data, Figure A5.

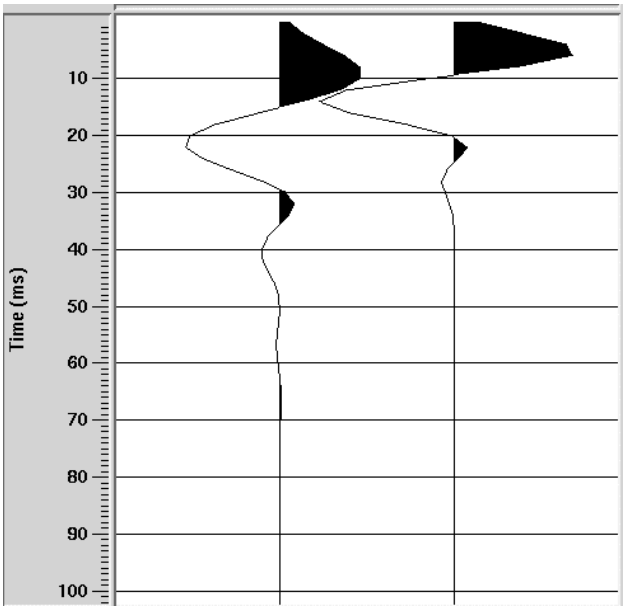


**Figure A5**: C-wave wavelet, left, and P-wave wavelet, right.

- Random Noise and Spikes editing,

The data contained noise and some spikes, which can cause unwanted artifacts during processing, above all when DMO and Migration are applied. I initially used the tool available in ProMAX called "Spike and Noise Bursts Edit". The main parameters to set for each option are the calculating windows in time, space (number of traces) and threshold. After testing different combinations, I used the tool in cascade, repeating it three times: the first to tackle spikes, applying a threshold value of 3. Then twice for noise editing, first editing low frequency (threshold of 5) followed by high frequency editing, again with a threshold of 5. I also used another tool, which is more powerful but less "safe" as it tends to remove useful signal as well as noise. It is called "spike to median ratio editor", the parameters to choose are the method for amplitude calculation, amplitude threshold and temporal and spatial windows. I chose to use the sum of the squares for the calculation with a threshold of 5. Figure A6 shows the effects of the noise removal sequence for the P-wave data.

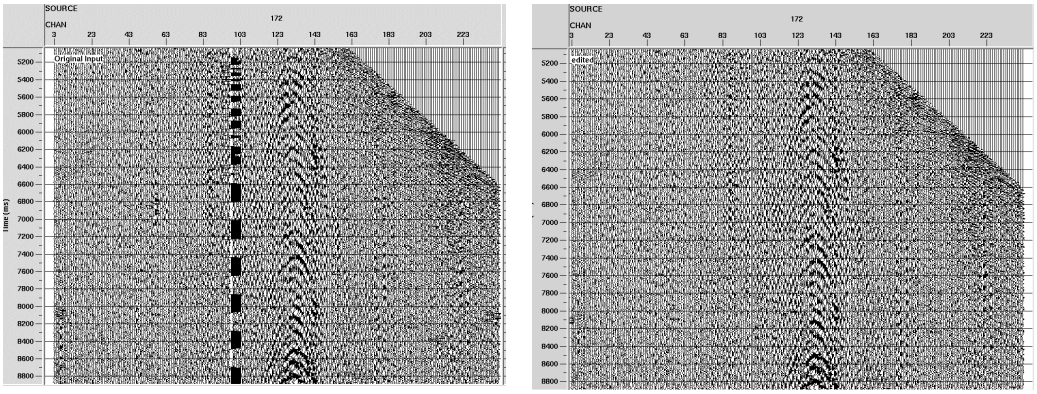

**Figure A6**: A P-wave shot point gather before and after random noise and spikes removal.

- Linear noise removal, F-K filter

Some parts of the data were also affected by some linear noise introduced by another vessel acquiring data nearby. To remove it I applied an F-K filter. The F-K (frequency-wavenumber) transform is a double Fourier's transform which move the data from the t-x domain into the F-K domain. Events with different apparent horizontal velocity tend to stack in different areas in this domain; we can then define a polygon and "cut out" the areas dominated by the noise. Figure A7 shows on the left the data cut out by the FK-filter, while on the right we have the data passed-in by the FK filter. These results are for a P-wave shot point.

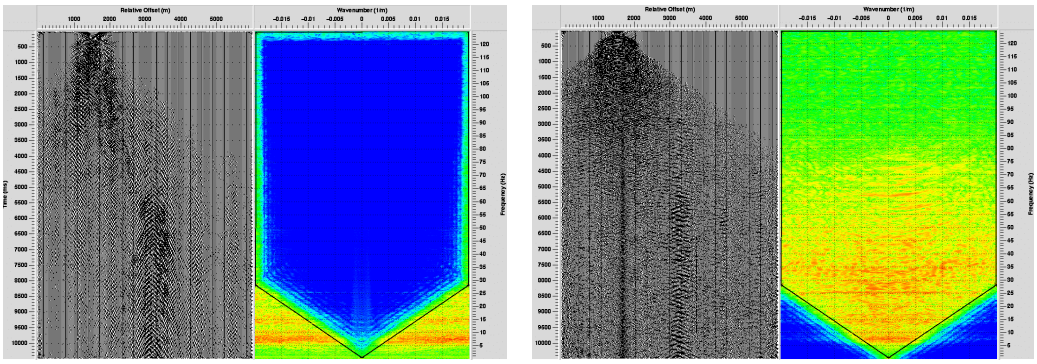

**Figure A7**: A P-wave shot-point gather during F-K filter analysis, the data filtered out are shown on the left, while on the right the ou*tp*ut data after F-K filter are shown.

- Deconvolution

As the seismogram is a convolution of the earth response and the wavelet (plus some noise), deconvolving the wavelet with the seismogram should give the earth response sequence. In reality we do not know the wavelet, as often, as in our case, it is not measured during acquisition. Still deconvolution is always applied in the seismic processing, it improves signal resolution, whitening the amplitude spectrum and it is a powerful anti-multiple. But it also changes the wavelet shape on a trace-by-trace basis, which is a problem when stratigraphic interpretation is made and well tying is attempted, Ziolkowki et al. (1998). Signature deconvolution plus a gapped deconvolution with a gap larger than the wavelet keep the wavelet unchanged during deconvolution. The gap used was 48 milliseconds with a 200 milliseconds operator length for P-waves and 64 milliseconds gap and 300 milliseconds for C-waves, since the wavelet is longer. The deconvolution results for a P-wave shot point are shown in Figure A8.

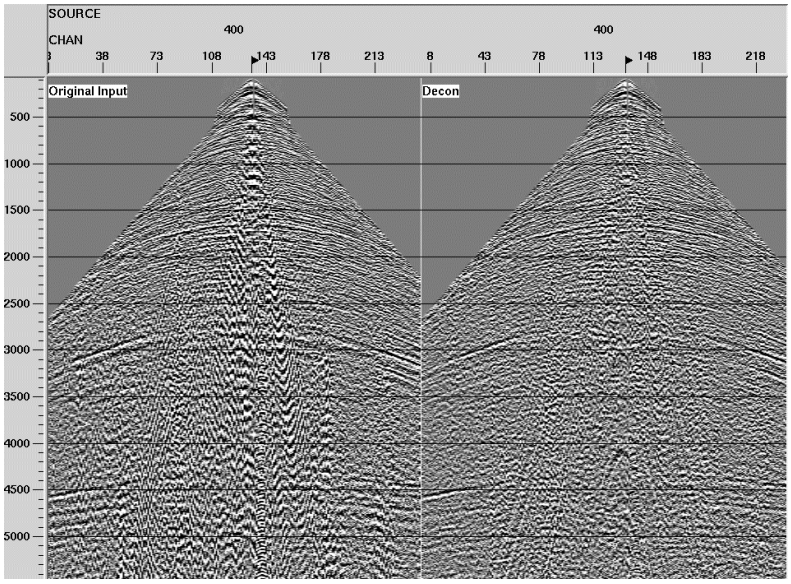


**Figure A8**: A P-wave shot point before and after deconvolution. The ou*tp*ut data looks sharper and with less “ringing”.

Figure A9 shows the P-wave stack before and after preprocessing. There are noticeable improvements in the sharpness of the events thanks to the reduction of the lower frequencies, mainly due to the wavelet shaping.

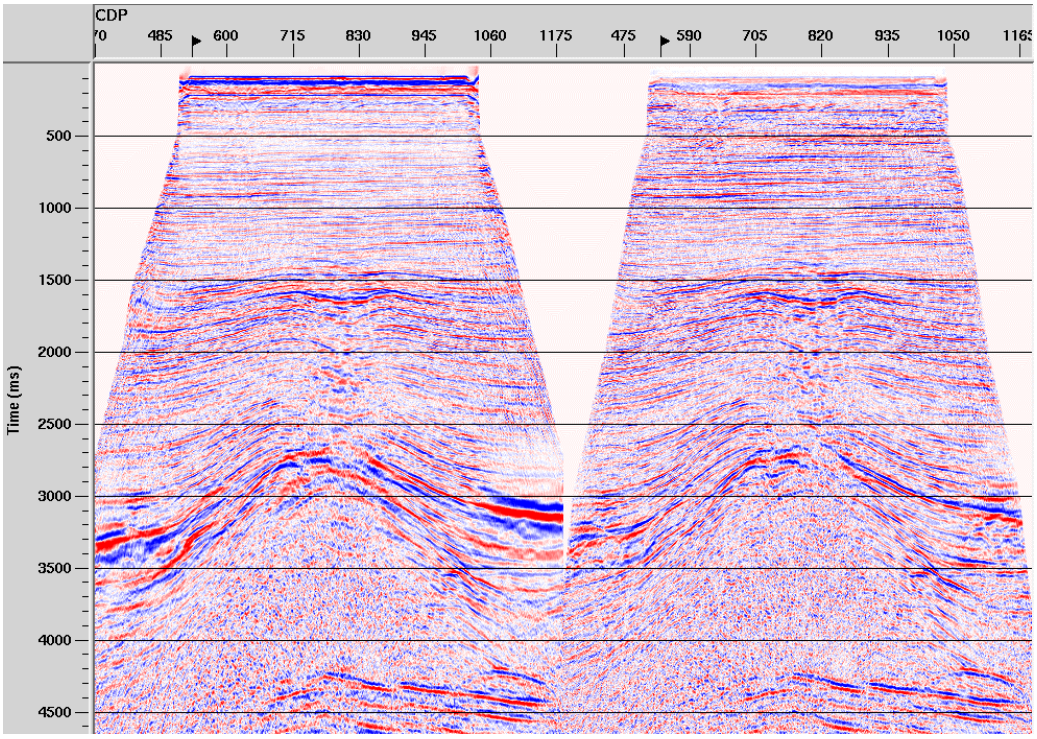


**Figure A 9**: P-wave stack before and after preprocessing. Notice the sharper image and higher frequency content.

### C-wave receiver statics

In the preprocessing step we have to include the shear static correction for C-waves. Shear statics are due to low velocity layers just underneath the sea floor, which affect only the S-leg of their raypath. There are different methodologies to correct for them; I chose to use a manual pick. After sorting the data into receiver gathers and stacking the first 1000 meters of offset I picked two shallow, horizontal events, then averaged the two picks, smoothed the resulting values over a 60 traces (receivers) window and subtracted this values from the average ones. This assumes

that the smooth values are the static–free arrival time. Figure A10 shows the receiver stack before and after the static correction. The total values of the correction ranges between +/- 35 milliseconds, Figure A11. The final result of the preprocessing for C-waves is displayed in Figure A12. The continuity of the main events in the ou*tp*ut section is greatly improved compared to the raw stack.

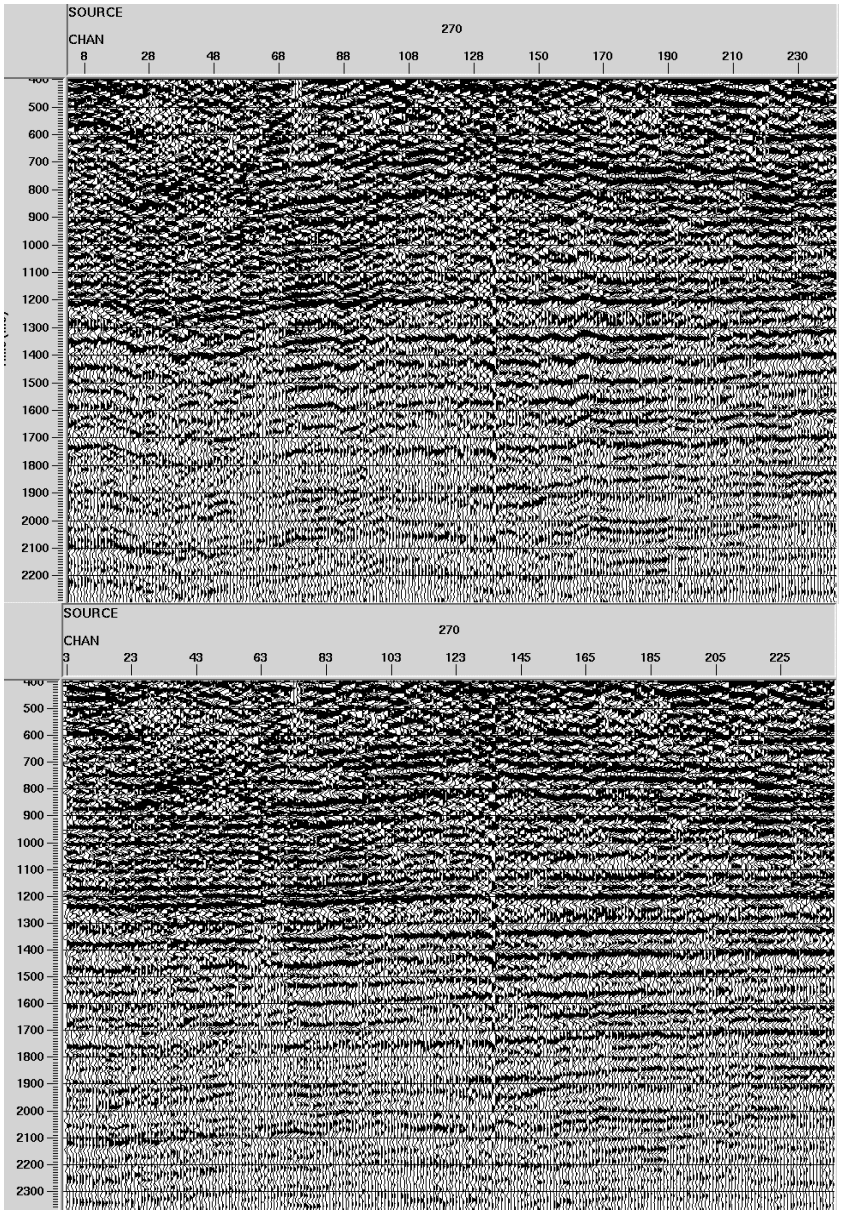


**Figure A10**: C-wave receiver stacks, before and after static correction. The static correction successfully removed the "wobbly" effects shown in the input data.

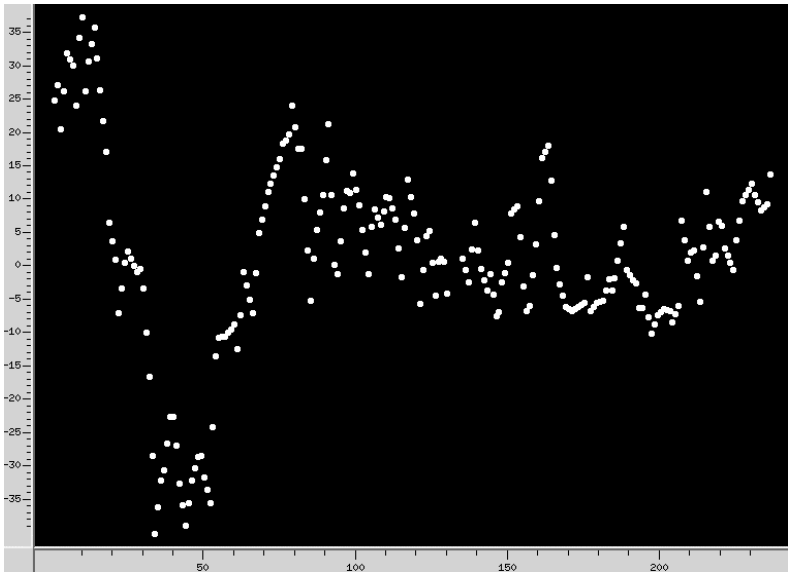

**Figure A11**: The statics calculated from the receiver stack. The values range between +/- 35 milliseconds

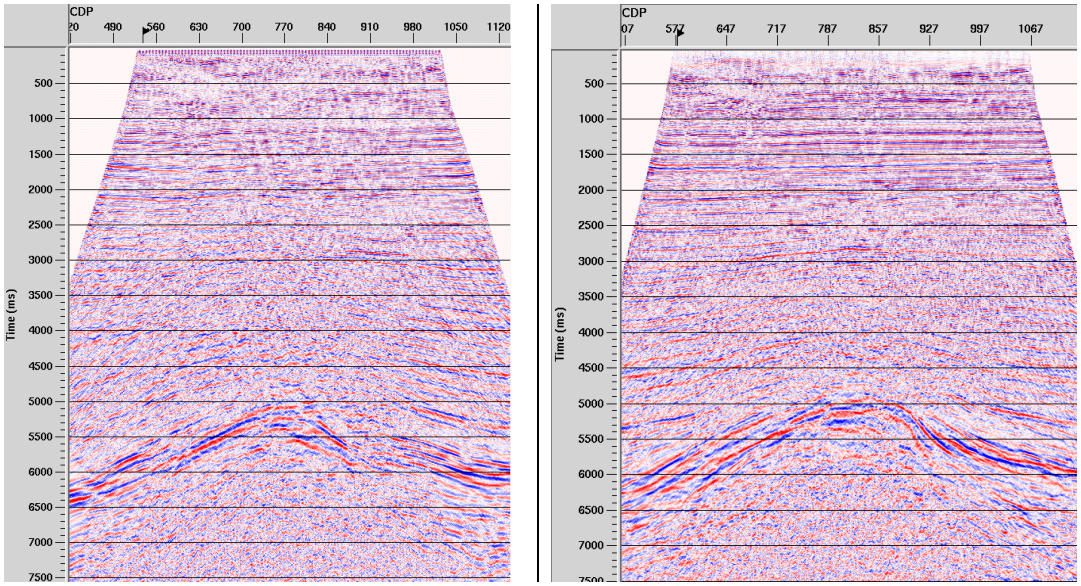


**Figure A12**: C-wave stack before and after preprocessing. The continuity of the main event is greatly improved,

# Appendix B: ProMAX preprocessing flow

In this Appendix I reproduce the ProMAX flow used for preprocessing of both P-and C-waves.

## B.1. ProMAX flows for P-wave and C-wave preprocessing

**Flow fabio/z-381/z-preproc**

Disk Data Input

Filter Application

Resample/Desample

True Amplitude Recovery

Trace Muting

Spike & Noise Burst Edit

Spike & Noise Burst Edit

Spike & Noise Burst Edit

Spike to Median Ratio Editor

Spiking/Predictive Decon

F-K Filter

Disk Data Output

**Disk Data Input**

| | |
|---|---|
| Read data from other lines/surveys? | *No* |
| Select dataset | *z-comp* |
| Propagate input file history | *Yes* |
| Trace read option | *Get All* |
| Read the data multiple times? | *No* |
| Process trace headers only? | *No* |

| | |
|---|---|
| Override input data's sample interval? | *No* |

**Filter Application**

| | |
|---|---|
| Application option | *Convolution* |
| Re-apply trace mute after filter? | *No* |
| Average multiple filters? | *Yes* |
| Time on input filter representing time zero | *620.0* |
| SELECT filter dataset | *wiener-scaled* |

**Resample/Desample**

| | |
|---|---|
| Ou*tp*ut sample rate | *4.0* |
| Apply Anti-Alias filter? | *Yes* |
| Use a high-fidelity Anti-Alias filter? | *Yes* |
| Use a zero phase Anti-Alias filter? | *No* |
| Remove minimum-phase filter time delay? | *Yes* |
| Re-apply trace mute after resample? | *No* |

**True Amplitude Recovery**

| | |
|---|---|
| Apply spherical divergence corrections? | *No* |
| Apply inelastic attenuation corrections? | *No* |
| Apply dB/sec corrections? | *No* |
| Apply time raised to a power corrections? | *Yes* |
| Time-Power constant | *2.0* |
| APPLY function to data or REMOVE effect of amplitude corrections? | *Apply* |
| Maximum application TIME | *0.0* |

**Trace Muting**

| | |
|---|---|
| Re-apply previous mutes | *No* |
| Mute time reference | *Time 0* |
| TYPE of mute | *Top* |
| Starting ramp | *30.0* |
| EXTRAPOLATE mute times? | *Yes* |
| Get mute file from the DATABASE? | *Yes* |
| SELECT mute parameter file | *z-fbmute2* |

**Spike & Noise Burst Edit**

| | |
|---|---|
| Do you wish to automatically edit spikes? | *Yes* |
| Spike detection threshold value | *3.0* |
| Operator length | *200.0* |
| Do you wish to automatically edit noise bursts? | *No* |

**Spike & Noise Burst Edit**

| | |
|---|---|
| Do you wish to automatically edit spikes? | *No* |
| Do you wish to automatically edit noise bursts? | *Yes* |
| Frequency of noise bursts relative to data | *LOWER* |
| Threshold to trip noise edit | *5.0* |
| Minimum noise block length | *50.0* |
| Percentage to expand noise blocks | *50.0* |
| Do you wish to infill edited zones? | *Yes* |

**Spike & Noise Burst Edit**

| | |
|---|---|
| Do you wish to automatically edit spikes? | *No* |
| Do you wish to automatically edit noise bursts? | *Yes* |
| Frequency of noise bursts relative to data | *HIGHER* |
| Threshold to trip noise edit | *5.0* |
| Minimum noise block length | *50.0* |
| Percentage to expand noise blocks | *50.0* |
| Do you wish to infill edited zones? | *Yes* |

**Spike to Median Ratio Editor**

| | |
|---|---|
| Operation MODE | *Both* |
| Method for gate amplitude calculation | *Sum of the squares* |
| Window length in milliseconds | *500.0* |
| Perform median filter based on | *Recording channel number* |
| Median length in traces of primary sort | *29* |
| Number of bins | *240* |
| Center of first bin. | *1.0* |
| Increment between bins. | *1.0* |
| Amplitude ratio threshold | *5.0* |
| Diagnostic Printout Level | *1* |

**Spiking/Predictive Decon**

| | |
|---|---|
| TYPE of deconvolution | *Minimum phase predictive* |
| Decon operator length s | *240* |
| Operator prediction distance s | *48* |
| Is prediction distance water relative? | *No* |
| Apply prediction filter correction? | *No* |
| Apply user specified taper? | *No* |
| Operator 'white noise' level s | *0.1* |
| Window rejection factor | *2.0* |
| Time gate reference | *Time 0* |
| Get decon gates from the DATABASE? | *Yes* |
| SELECT decon gate parameter file | *decon* |
| Ou*tp*ut traces or filters | *Normal decon output* |
| Apply a bandpass filter after decon? | *No* |
| Re-apply trace mute after decon? | *Yes* |

**F-K Filter**

| | |
|---|---|
| Type of F-K filter | *Arbitrary Polygon* |
| Distance between input traces | *25.0* |
| Panel width in traces | *240* |
| Test the filter impulse response? | *No* |
| Percent flat for time ramping | *100.0* |
| Percent flat for offset ramping | *100.0* |
| Get polygon mute file from the database? | *Yes* |
| Select mute parameter file | *fk* |
| Mode of F-K filter operation | *ACCEPT* |
| Percent flat for F-K filter windowing | *100.0* |
| Time length of F-K filter ms | *500.0* |
| Spatial extent of F-K filter traces | *48* |
| Re-apply T-X trace mute after filter? | *Yes* |
| Percentage of K-space to keep around K=0 | *5.0* |

**Disk Data Ou*tp*ut**

| | |
|---|---|
| Ou*tp*ut Dataset Filename | *z-preproc* |
| New, or Existing, File? | *New* |
| Record length to ou*tp*ut | *0.0* |

| | |
|---|---|
| Trace sample format | *16 bit* |
| Skip primary disk storage? | *No* |

**ProMAX Flow fabio/x-381/x-preproc**
Disk Data Input
Trace Kill/Reverse
Trace Muting
True Amplitude Recovery
IF
Phase Rotation
ENDIF
Spike & Noise Burst Edit
Spike & Noise Burst Edit
Spike & Noise Burst Edit
Filter Application
Spiking/Predictive Decon
F-K Filter
Disk Data Output

**Disk Data Input**

| | |
|---|---|
| Read data from other lines/surveys? | *Yes* |
| Select dataset | *fabio x-new 00055134* |
| Trace read option | *Sort* |
| Interactive Data Access? | *No* |
| Select primary trace header entry | *Live source number usr-defined* |
| Select secondary trace header entry | *Signed source-receiver offset* |
| Select tertiary trace header entry | *No trace header entry selected* |
| Sort order list for dataset | *300:*/* |
| Presort in memory or on disk? | *Memory* |
| Read the data multiple times? | *No* |
| Process trace headers only? | *No* |
| Override input data's sample interval? | *No* |

**Trace Kill/Reverse**

| | |
|---|---|
| Trace editing MODE | Kill |
| Get edits from the DATABASE? | *No* |
| Trace selection MODE | *Kill/Reverse traces in select list* |
| PRIMARY edit list header word | *Recording channel number* |

| | |
|---|---|
| SPECIFY traces to be edited | *133-136* |

**Trace Muting**

| | |
|---|---|
| Re-apply previous mutes | *No* |
| Mute time reference | *Time 0* |
| TYPE of mute | *Top* |
| Starting ramp | *30.0* |
| EXTRAPOLATE mute times? | *Yes* |
| Get mute file from the DATABASE? | *Yes* |
| SELECT mute parameter file | *x-fbmute* |

**True Amplitude Recovery**

| | |
|---|---|
| Apply spherical divergence corrections? | *No* |
| Apply inelastic attenuation corrections? | *No* |
| Apply dB/sec corrections? | *No* |
| Apply time raised to a power corrections? | *Yes* |
| Time-Power constant | *2.0* |
| APPLY function to data or REMOVE effect of amplitude corrections? | *Apply* |
| Maximum application TIME | *0.0* |

**IF**

| | |
|---|---|
| Trace selection MODE | *Include* |
| SELECT Primary trace header word | *Signed source-receiver offset* |
| SPECIFY trace list | *-12000-0* |

**Phase Rotation**

| | |
|---|---|
| Phase rotation angle | *-180.0* |
| Re-apply trace mute after phase rotation? | *No* |

**ENDIF**

**Spike & Noise Burst Edit**

| | |
|---|---|
| Do you wish to automatically edit spikes? | *Yes* |
| Spike detection threshold value | *3.0* |

| | |
|---|---|
| Operator length | *200.0* |
| Do you wish to automatically edit noise bursts? | *No* |

**Spike & Noise Burst Edit**

| | |
|---|---|
| Do you wish to automatically edit spikes? | *No* |
| Do you wish to automatically edit noise bursts? | *Yes* |
| Frequency of noise bursts relative to data | *LOWER* |
| Threshold to trip noise edit | *3.0* |
| Minimum noise block length | *30.0* |
| Percentage to expand noise blocks | *50.0* |
| Do you wish to infill edited zones? | *Yes* |

**Spike & Noise Burst Edit**

| | |
|---|---|
| Do you wish to automatically edit spikes? | *No* |
| Do you wish to automatically edit noise bursts? | *Yes* |
| Frequency of noise bursts relative to data | *HIGHER* |
| Threshold to trip noise edit | *4.0* |
| Minimum noise block length | *30.0* |
| Percentage to expand noise blocks | *50.0* |
| Do you wish to infill edited zones? | *Yes* |

**Filter Application**

| | |
|---|---|
| Application option | *Convolution* |
| Re-apply trace mute after filter? | *Yes* |
| Average multiple filters? | *Yes* |
| Time on input filter representing time zero | *200.0* |
| SELECT filter dataset | *wiener-PS@-scaled-resam4* |

**Spiking/Predictive Decon**

| | |
|---|---|
| TYPE of deconvolution | *Minimum phase predictive* |
| Decon operator length s | *300* |
| Operator prediction distance s | *96* |
| Is prediction distance water relative? | *No* |
| Apply prediction filter correction? | *No* |
| Apply user specified taper? | *No* |

| | |
|---|---|
| Operator 'white noise' level s | *0.1* |
| Window rejection factor | *2.0* |
| Time gate reference | *Time 0* |
| Get decon gates from the DATABASE? | *Yes* |
| SELECT decon gate parameter file | *x-decon* |
| Ou*tp*ut traces or filters | *Normal decon output* |
| Apply a bandpass filter after decon? | *No* |
| Re-apply trace mute after decon? | *Yes* |

**F-K Filter**

| | |
|---|---|
| Type of F-K filter | *Arbitrary Polygon* |
| Distance between input traces | *25.0* |
| Panel width in traces | *240* |
| Test the filter impulse response? | *No* |
| Percent flat for time ramping | *100.0* |
| Percent flat for offset ramping | *100.0* |
| Get polygon mute file from the database? | *Yes* |
| Select mute parameter file | *fk-x* |
| Mode of F-K filter operation | *ACCEPT* |
| Percent flat for F-K filter windowing | *100.0* |
| Time length of F-K filter ms | *500.0* |
| Spatial extent of F-K filter traces | *48* |
| Re-apply T-X trace mute after filter? | *Yes* |
| Percentage of K-space to keep around K=0 | *5.0* |

**Disk Data Ou*tp*ut**

| | |
|---|---|
| Ou*tp*ut Dataset Filename | *x-prep-sig-sta* |
| New, or Existing, File? | *New* |
| Record length to ou*tp*ut | *0.0* |
| Trace sample format | *16 bit* |
| Skip primary disk storage? | *No* |

# Appendix C: Theory of PZ summation

In Chapter 5 I mentioned the possibility of summing the hydrophone and the vertical component responses. The reason for doing so is the possibility of removing multiples. Figure C1 shows three of the most common first order multiples which affect marine-acquired seismic data: (a) the receiver side multiple (ghost), (b) the source side multiple (peg-leg) and (c) the interbed. Ghosts and peg–legs are commonly referred to water-column reverberation.

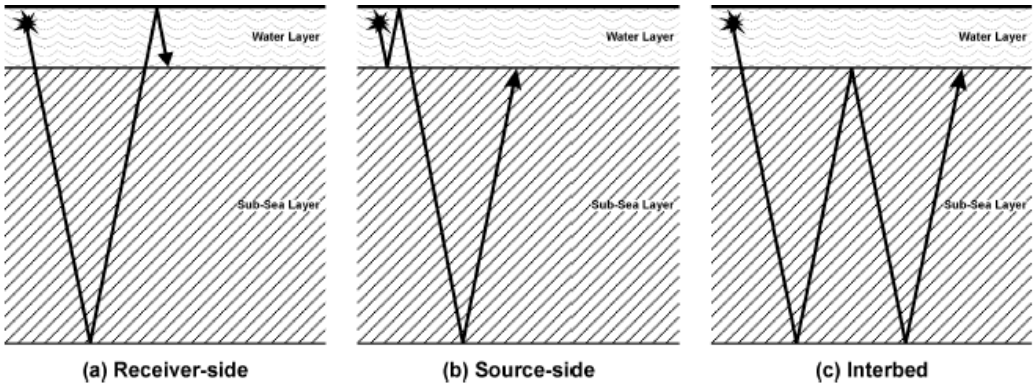


**Figure C1**: Most common first order multiples, from Hoffe et al. (1999)

The problem of water-column reverberation can be greater in OBC acquisition than in traditional streamer acquisition. The reason is that the receivers are at a greater depth, i.e. a greater distance from the water surface. This translates into having receiver ghosts at a much lower frequency. The frequency of the ghost no*tc*hes is in fact dependent on the receivers depth: [$f=k(v/2\Delta z)$], where $k$ is an integer, $v$ is the water velocity and $\Delta z$ is the receivers depth. This lower frequency makes difficult to eliminate the ghosts using a deconvolution operator (Soubaras, 1996).

Ghost effects can instead be removed by summation of the hydrophone and the vertical geophone records (PZ summation) (Barr and Sanders, 1986, Soubaras, 1996). This technique exploits the fact that the response of the hydrophone and the vertical component are opposite in sign. The hydrophone measures a total pressure fields and it is not directional while the vertical component records a velocity and is directional. If we call H the pressure recorded at the hydrophone and G the vertical velocity recorded at the geophone we can see that their response at the receivers is (Ball et al., 1996):

$$H = \frac{(1-z)}{(1+rz)} A, \qquad \text{C.1}$$

$$G = \frac{(1+z)}{1+rz} A. \qquad \text{C.2}$$

$r$ is the water-bottom reflection coefficient, $z$ is the two way propagation of sound in the water layer and $A$ is the subsurface response.

To remove the ghost effect, Barr and Sanders (1989) proposed to add the two responses as follow:

$$\frac{(1-r)}{2} H + \frac{(1+r)}{2} G . \qquad \text{C.3}$$

Here the value of $r$ is needed. Barr and Sanders (1986) used an empirical estimation of it, 0.32, derived for a sandy water bottom with a velocity contrast of 1.13. Ball and Corrigan (1996) proposed to calculate $r$ using a more complicated function, which has the property of being unbiased by the effects of source side reverberation.

In practice, prior to summation, the amplitude and phase, if needed, have to be carefully ma*tc*hed; usually the geophone is scaled to ma*tc*h the hydrophone.

# Appendix D: Petrophysics

In Chapter 6 I discussed the P-velocity value from sonic logs for different fluid contents. Here I show the detail of that process. I also present the equations used to calculate the effects of frequency-dependent dispersion.

## D.1. Derivation of sonic log values for 100% brine or gas saturation

*Sonic*

The Wyllie time average equation is the following:

$$\Delta t = \phi \Delta t_{fl} + (1-\phi)\Delta t_{mat}, \tag{D.1}$$

where:

$\Delta t =$ Sonic reading,

$\Delta t_{fl} =$ Travel time in fluid,

$\Delta t_{mat} =$ Travel time in matrix,

$\phi =$ Porosity.

This equation can incorporate a shale correction;

$$\Delta t = \phi\ \Delta t_{fl} + V_{sh}(\Delta t_{sh}) + (1 - V_{sh} - \phi\ )\Delta t_{mat}, \tag{D.2}$$

where:

$\Delta t =$ Sonic reading,

$\Delta t_{fl} =$ Travel time in invaded zone fluid (mud filtrate, residual water and gas),

$\Delta t_{mat} =$ Travel time in matrix,

$\phi$ = Porosity,

$Vsh$ = Shale volume from gamma ray,

$\Delta t_{sh}$ = Shale sonic transit time.

The introduction of the shale parameter, $V_{sh}$, means that we have calculated a shale-corrected porosity. If we used effective porosity calculated from the density log all we would be effectively doing is re-scaling the density log in sonic units. Shale-corrected porosity must be calculated from the sonic log. In order to do this the above Wyllie time average equation was used to find the average sonic values for fluid and matrix. A cross-plot was taken of sonic values against core porosities corrected to reservoir conditions (equation used: Porosity corrected = measured porosity*0.938 from Amoco, 1996 report) – for all wells in Lomond that have core. Values were only plotted if shale content was less then 10% (in order to get a clean matrix point). A linear regression line (the most common type where we take an average y for specific x) yields a matrix point of 55.92. This is very close to expected value of 55.1 for quartz. The fluid point of 236.88 appears reasonable given that oil is 238, and the fluid is mostly oil based mud with some gas and residual water.

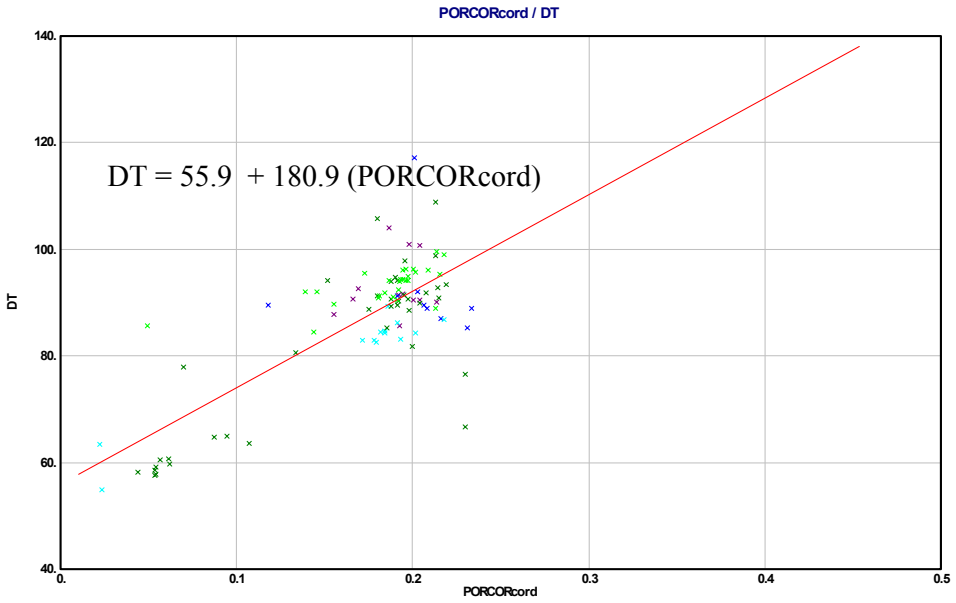


**Figure D1:** Linear regression line to extract the matrix point.

Using the transit times for matrix and fluid, porosity was calculated using the equation above re-arranged:

$$\phi = \frac{\Delta t - \Delta t_{mat} + Vsh(\Delta t_{mat} - \Delta t_{sh})}{\Delta t_{fl} - \Delta t_{mat}}. \quad \text{(D.3)}$$

A value of 90usec/ft for shale was used. This was found by inspection of logs in pure shale horizons. As a QC porosity from the sonic was plotted along side effective porosity from the density log. They both showed a similar trend.

Now by taking values for every parameter apart from $\Delta$t, we can calculate the sonic transit time for a given fluid content:

$$\Delta t = \phi\ (\Delta t_{fl} - \Delta t_{mat}) + \Delta t_{mat} - Vsh(\Delta t_{mat} - \Delta t_{sh}). \quad \text{(D.4)}$$

We can also QC that our shale correction is correct by re-calculating the sonic curve using a fluid value of 238usec/ft. The new line fell directly on the old line as expected.

*Water*

We will assume a reservoir temperature of 260$^{o}$F (Amoco 1996 report). Water resistivity varies across the field (e.g. well 23/21-T3 0.02ohmm at 260$^{o}$F, well 23/21-T8 0.015ohmm at 260$^{o}$F, source: Amoco 1996 report). These values translate into a range of salinity values from 125,000ppm to 250,000ppm. If we are to 'fill our reservoir with all water' it does not matter what we choose as long as we are consistent. A salinity of 200,000ppm was chosen. Constants assumed were;

$\Delta t_{fl} = 180.5$usec/ft (Gruping, 1998 – for 200,000ppm and 15psi we assume that temperature and pressure would have little effect on this value)

$\Delta t_{mat} = 50.53$usec/ft,

$\Delta t_{sh} = 90$usec/ft.

*Gas*

Constants assumed were;

$\Delta t_{fl} = 626$usec/ft for methane at 15psi (Gruping, 1998),

$\Delta t_{mat} = 50.53$usec/ft,

$\Delta t_{sh} = 90$usec/ft.

No available conversion to reservoir conditions was available for the transit time of gas. Therefore this is only a rough approximation.

## D.2. Backus average and Time equation

For a any layered medium described by $V_{pi}$, $V_{si}$ and $\rho_i$, as the P-velocity, S-velocity and density for the layer *i*, the time average velocity for both P and S-waves is described as:

$$V_t = \left[ \frac{1}{D} \left( \sum_{i=1}^{n} \frac{d_i}{V_i} \right) \right]^{-1}, \tag{D.5}$$

where $d_i$ is the thickness of the layer *u* and D is the total thickness of the medium.

Backus described the effective modulus ($M_b$) for both P and S-waves as:

$$M_b = \left[ \frac{1}{D} \left( \sum_{i=1}^{n} \frac{d_i}{M_i} \right) \right]^{-1}, \tag{D.6}$$

where $M_i$ is the modulus of each layer *i*. Then for long wavelengths and vertical propagation the velocity for both P and S-waves is described as:

$$V_b = \sqrt{\frac{M_b}{\rho}} = \left( \frac{\rho}{D} \sum_{i=1}^{n} \frac{d_i}{\rho_i V_i} \right)^{-1/2}, \tag{D.7}$$

in which $\rho$ is the bulk density:

$$\rho = \frac{1}{D} \sum_{i=1}^{n} d_i \rho_i . \tag{D.8}$$

## D.3. Futterman's equation

Futterman (1962) assumed linearly dependent coefficient and invoked the principle of causality to derive dispersion relations. He described the velocity and the quality factor as a function of frequency, V(F) and Q(F), as:

$$V(F) = V_0\left[1 - \frac{1}{\pi Q_0} ln\left(\gamma F/F_0\right)\right]^{-1}, \tag{D.9}$$

$$Q(F) = Q_0\left[1 - \frac{1}{\pi Q_0} ln\left(\gamma F/F_0\right)\right], \tag{D.10}$$

with:

$F_0$ = low frequency cut-off (reference frequency). For frequencies lower than $F_0$ Q tends to infinity,

$V_0$ = reference velocity (Futterman, 1962),

$Q_0$ = reduced quality factor (Futterman, 1962),

ln $\gamma$= Euler's constant = 0.5772156649.

Equation (D.9) and (D.10) are valid for $F/F_0$ higher than 6.

The ratio of the P and S-wave velocity as a function of frequency was given by:

$$\frac{V_p}{V_s}(F) = \frac{V_{p0}}{V_{s0}} \frac{\left[1 - \frac{1}{\pi Q_{s0}} ln\left(\gamma F/F_0\right)\right]}{\left[1 - \frac{1}{\pi Q_{p0}} ln\left(\gamma F/F_0\right)\right]} = \frac{V_{p0} Q_s Q_{p0}}{V_{s0} Q_p Q_{s0}}. \tag{D.11}$$

$Q_{p0}/Q_{s0}$ controls the direction of $V_p/V_s$ dispersion, if $Q_{p0}/Q_{s0}$ is greater than 1 the velocity ratio decrease with frequency, if $Q_{p0}/Q_{s0}$ is less than 1 then $V_p/V_s$ increases with frequency. Experimental data suggest that $Q_{p0}/Q_{s0}$ is greater than 1 only on for 100% water saturation.

# Appendix E: P-P PSTM

## E.1. P-wave PSTM

For completion of the discussion in 3.3, I present here the results of the PSTM flow for P-waves. The PSTM processing flow for P-waves is quite simple, after the first velocity analysis we have:

- First run of PSTM using RMS velocity
- Remove NMO and new velocity analysis
- Final PSTM and Stack

In fact this sequence is not dissimilar to the PSTM flow for C-waves shown in Chapter 9. The only difference is that here we are only working to optimise the migration velocities, since we ignore anisotropy and no other parameter is involved.

The resulting gathers after the second run of PSTM are shown in Figure E1. CDP 851 is on the left: the events are flat, but the effects of gas are visible at around 2.4 seconds. CDP 901, on the right, since it is outside the gas-affected zone, shows good continuity and well-flattened events. The velocity field used in the PSTM is shown in Figure E2.

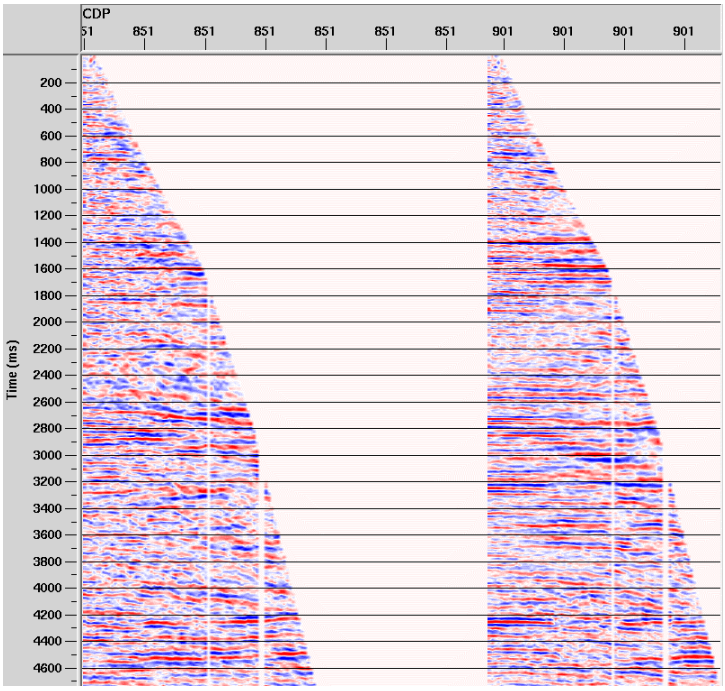


**Figure E1**: CDPs after the second run of PSTM. The CDP on the left is inside the gas-affected area; we can see the disturbance at about 2.4 seconds.

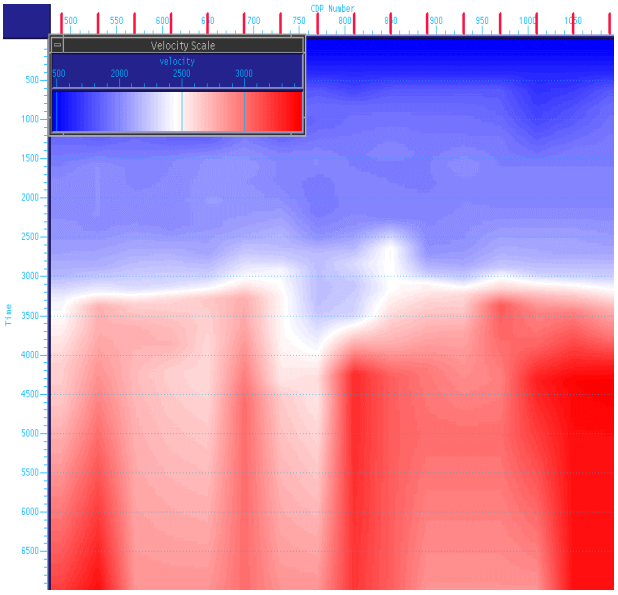


**Figure E2:** Migration velocity field after updating. The field is smooth, but the effect of the gas produces an area of minimum in the central part of the field.

Figure E3 shows the PSTM stack. The image is not too dissimilar from the one resulting from the DMO+PostSTM but few differences can be appreciated. In Figure E4 we can see a zoom in of the target area for the two images, on the left there is the PSTM result, on the right the DMO+PostSTM one. The maximum offset is the same for the two sequences. Two black arrows point to some of the areas with differences. Generally the PSTM image shows higher energy in the dipping events, more noticeable on the left flank of the dome structure. One of the main differences is the good continuity in the sub-salt event in the PSTM section. So, even if not by much, the PSTM image is to be preferred to the DMO+Post*P*STM result.

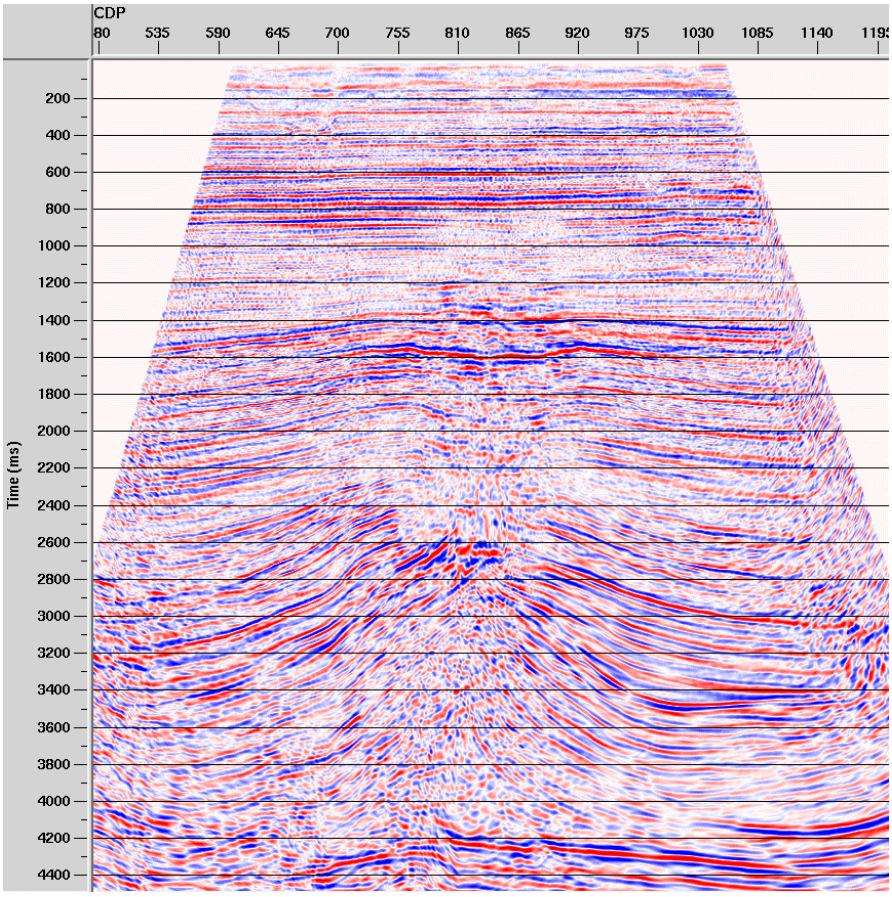


**Figure E3**: Final PSTM stack. The flanks of the structure are well imaged; there is good continuity in areas of steep dips. The sub-salt event appears more continuous than in the DMO+Post Mig image.

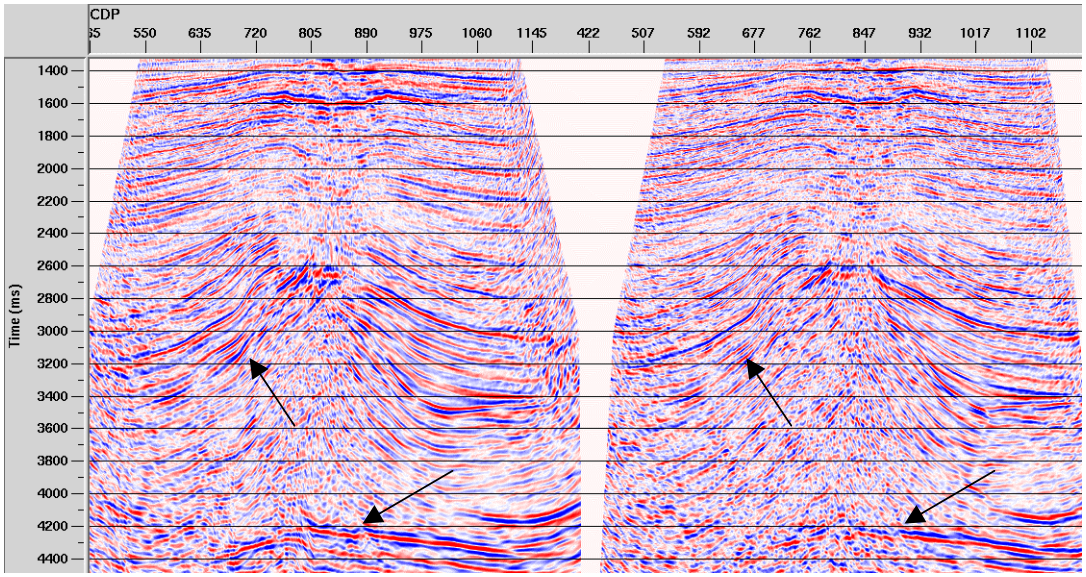


**Figure E4**: PSTM image on the left, DMO+PostSTM image on the right (as in Figure 3.3). The main differences are in the sub salt event and on the left flank of the dome structure

# Appendix F: Published material

- Mancini, F., Li., X.-Y., Ziolkowski, A., and Pointer, T., 2002, Interpreting velocity ratios from 4C seismic data and well logs in the presence of gas and anisotropy, 72nd Mtg.: Soc. Expl. Geophys. Expanded Abstract.

- Mancini, F., Li., X.-Y., Ziolkowski, A., and Pointer, T., 2003, Effects of binning velocity ration on C-wave imaging in the presence of dips, 65th Mtg EAGE Conference, Expanded Abstract.

- Mancini, F., Li., X.-Y., Ziolkowski, A., Dai, H., and Pointer, T., 2004, C-wave anisotropic imaging using PSTM: a case example from the North Sea, 66th Mtg EAGE Conference, Expanded Abstract.

# Interpreting velocity ratios from 4C seismic data and well logs in the presence of gas and anisotropy

*Fabio Mancini*, The University of Edinburgh; Xiang-Yang Li, British Geological Survey;*
*Anton Ziolkowski, The University of Edinburgh; Tim Pointer, BG Group.*

**Summary**

In processing multicomponent seismic data the velocity ratio $v_p/v_s$ is a parameter of great importance. Converted wave binning relies upon it and the use of an incorrect value may lead to poor imaging results. Seismic anisotropy and subsurface heterogeneities, such as gas clouds, cause changes in the velocity ratio. This paper performs an integrated analysis of well and seismic data to understand the meaning of the different velocity ratios and the way they are influenced by the presence of anisotropy and/or gas.

**Introduction**

Interest in multicomponent seismic data is growing year after year. The advantages of having shear wave information and a better image in the presence of gas clouds make this technology an important tool for reservoir characterisation. The main processing problems are well known: binning converted waves (CCP positioning) and the effects of anisotropy and gas on seismic velocities. The binning problem is precisely linked to the velocity ratio $v_p/v_s$. This ratio determines the common converted point trajectory in depth. In this paper we analyse different velocity ratios in the Lomond field, North Sea. The Lomond field is a gas/condensate field and its structure is a salt induced anticline heavily faulted on top. Gas leaks through these faults producing a large gas cloud which causes distortions and bright spots in the imaging when P waves are used. For this reason using converted waves, which are much less affected by the presence of gas, was considered. Geco Prakla acquired a 3D 4C seismic data over the Lomond field. Three 2D lines were also acquired, with inline shooting. Compressional and shear logs are also available.

**Velocity Ratios**

In order to achieve good imaging for converted waves different velocity ratios are required. With $v_{cn}$, $v_{pn}$ and $v_{sn}$ we indicate the short spread stacking velocity for C-waves, P-waves and S-waves respectively, $v_{c0}$, $v_{p0}$ and $v_{s0}$ are the vertical velocities again for the 3 wave-types, $\gamma_n$ is the stacking velocity ratio, $\gamma_0$ is the vertical velocity ratio and $\gamma_{eff}$ is the effective velocity ratio. The main relationships are (Thomsen, 1999):

$$v_{cn}^2 t_{c0} = v_{pn}^2 t_{p0} + v_{sn}^2 t_{s0} \tag{1}$$

$$\gamma_0 = \frac{v_{po}}{v_{s0}} = \frac{t_{s0}}{t_{p0}}, \gamma_n = \frac{v_{pn}}{v_{sn}}, \gamma_{eff} = \frac{\gamma_n^2}{\gamma_0} \tag{2}$$

**Gamma zero, $\gamma_0$**

The conventional flow for joint processing of multicomponent seismic data requires processing P-waves as a starting point followed by a sequence for C-waves which more or less is: asymptotic binning (ACCP); isotropic velocity analysis; stacking and event correlation in the two stacked volumes. The values of $\gamma_0$ (average and interval) are given using the arrival time ratio, equation (2). Figure 1 and 2 show results: $\gamma_0$ decreases with depth; the value at the reservoir, 2.6 seconds, is around 2.8-2.9.

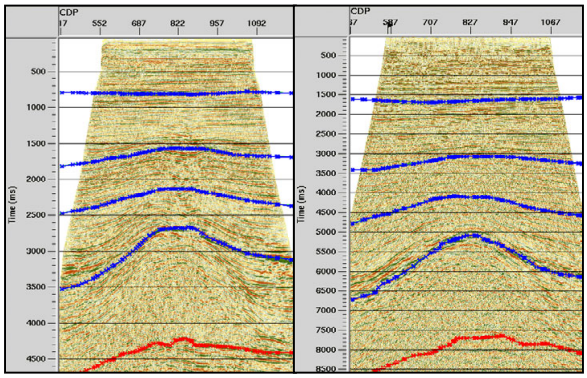


**Figure 1**: *Event correlation, P-stack on the left and C-stack on the right, The pull-down effect of the gas in the P section has been considered. The ACCP was carried out with a $\gamma_0$ value of 2.75. 5 events were correlated*

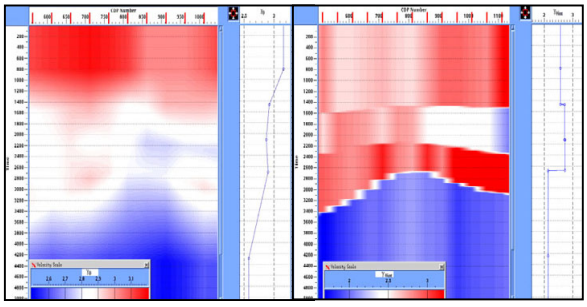

**Figure 2**: *Average $\gamma_0$ (left) and interval $\gamma_0$ (right) from event correlation shown in P time, the profile shows ACCP 810*

**Gamma nmo, $\gamma_n$**

Short spread stacking velocities are generally higher than vertical velocities in the presence of polar anisotropy (VTI). A VTI medium can be described using Thomsen's (1986) parameters ε and δ. It is also convenient to use the parameter σ described as:

$$\sigma = \gamma_0^2(\varepsilon - \delta) \tag{3}$$

This leads to:

$$v_{pn} = v_{po}\sqrt{1+2\delta}, v_{sn} = v_{s0}\sqrt{1+2\sigma} \tag{4}$$

If we assume δ = 0:

$$\sigma \approx \frac{\gamma_0 - \gamma_{eff}}{2\gamma_{eff}} \tag{5}$$

In the presence of VTI $\gamma_n$ is expected to be lower than $\gamma_o$ as σ is generally very high. Figure 3 shows $\gamma_n$ estimated for the Lomond field using the C-wave velocity from the positive offset.

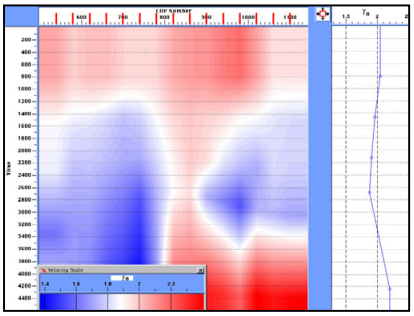

**Figure 3**: *$\gamma_n$ shown in P time, the profile shows ACCP 820*

The difference between the two ratios is quite high. At the reservoir $\gamma_n$ is below 1.8 while $\gamma_o$ is in the order of 2.9. It is important to notice the effect of the gas on $\gamma_n$, the decrease of P velocity in the gas cloud creates two well defined areas of minimum in the ratio. The higher values around CCP 860 are due to a gas-induced minimum in the C-wave velocity, where the P-leg of the ray path travels through the gas.

**Gamma effective, $\gamma_{eff}$, and sigma, σ**

We can now evaluate the value of $\gamma_{eff}$ and σ from equation (5) assuming δ=0, Figure 4. Considering that generally δ is very small for most marine sediments this assumption is not too far from the truth. Again, the effects of the gas are noticeable: in some areas it makes σ reach values of 1.2. But even ignoring these effects the value of σ is very high, between 0.5 and 0.8. Ignoring anisotropy in the Lomond field for converted waves will lead to positioning errors.

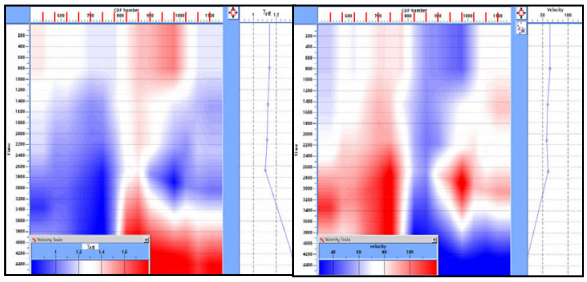

**Figure 4**: *Left: $\gamma_{eff}$, right: σ in percentage, both shown in P time. The profiles show ACCP 820*

$\gamma_{eff}$ varies between 1 and 1.4, which are values much lower then $\gamma_o$. Due to the presence of gas this result may be not completely reliable. For a QC we use an approximation to the CCP-scan technique, (Audabert et al., 1999). Figure 5 shows the positive and negative offset stacks, the two sections are slightly shifted.

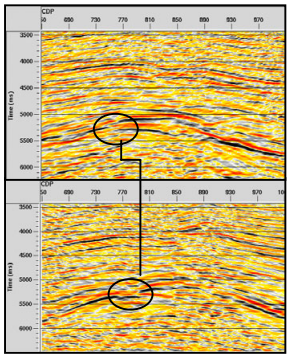

**Figure 5**: *Positive (top) e negative (bottom) offset stacks. The horizontal shift at the fault is around 20 CCP, 250 meters.*

$\gamma_{eff}$ is the key parameter for C-wave binning. The use of $\gamma_0$ will degrade the quality of the imaging. Figure 6 shows two sections obtained using $\gamma_{eff}$ and $\gamma_0$. The processing sequence is the same for both: ACCP + isotropic NMO + DMO + STACK + PostSTM. It can clearly be seen that the use of $\gamma_0$ for binning causes a very poor image quality, particularly when the structure is complex, as in the crest of the salt dome.

**Velocity ratio in wells**

Two new wells drilled in the Lomond field have shear logs. The velocity ratio is similar for both of them, around 1.70,

Figure 7. This value is considerably lower then the $\gamma_o$ in the seismic data, it is actually closer to the value of $\gamma_n$ or $\gamma_{eff}$. Interestingly the $t_{c0}/t_{p0}$ ratio at the reservoir is around 1.80. This could suggest that the conversion takes place at the sea-floor rather then at the reflectors so that the inline component contains S-S waves rather than P-S waves.

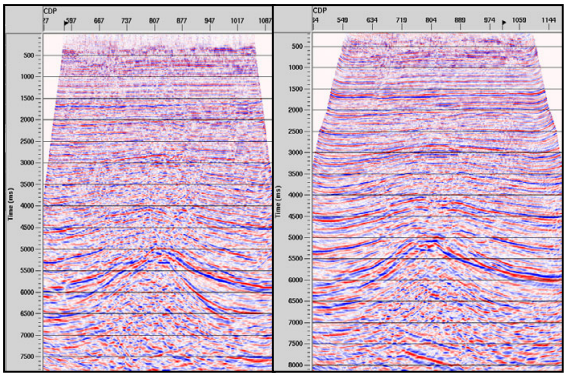

**Figure 6**: *C-wave migration using $\gamma_0$ (left) and $\gamma_{eff}$ (right)*

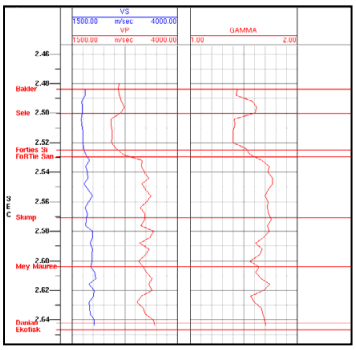

**Figure 7**: *$v_{p0}$, $v_{s0}$ and $\gamma$from well 23/21-T9.*

**Where does the conversion take place?**

There is evidence that indicates that the conversion is taking place at the reflectors: shot gathers show the "wobbly" effects of statics in the inline and crossline component but not in the vertical component, which suggests that is a shear static phenomenon. Plus these effects disappear in the receiver domain indicating that they are receiver statics due to the up going S wave as P wave statics are very low (Yuan et al., 1998). Other indications are: strong diodic velocities (Thomsen, 1999), which are due to the different ray paths through heterogeneities in the positive and negative offsets and they happen only if the wave is converted at the reflector, as shown in Figure 7. The value of $\gamma_o$ from event correlation clearly depends on the user interpretation. In the Lomond field the salt dome structure helps the interpreter in the task, but in the shallower part interpretation is more difficult. If we assume $\gamma_o$ to be acceptable, we have to start questioning the validity of the logs. It is interesting to notice that in Tommaliten Alpha field, which is also a gas field, (Granli et al., 1999) the well logs values for the Balder and Ekofisk formations are similar to the one found in the Lomond field, while $\gamma_o$ from event correlation show higher values, around 2.60.

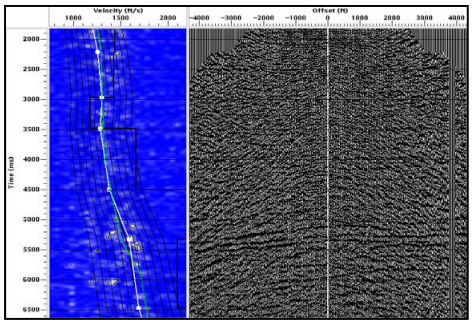

**Figure 8**: *Diodic velocity effects in positive and negative offsets. Same events are corrected with different velocities in the positive and negative offsets. Events in the positive offset require higher velocity.*

The Lomond field does not seem to be an isolated case. Several studies from the North Sea (Valhall, Tommaliten Alpha, Guillemot) show $\gamma_0$ values from event correlation of around 2.5, which is now considered a sort of average for marine sediments.

**Well tie**

We start with analysing $v_p$ values from seismic data and well logs. In the Lomond field the wells tie the P seismic section with a good degree of accuracy. This proves that the sonic and the seismic $v_p$ are comparable and that $\delta$ is indeed small. Sonic $v_p$ can also be checked using check shots: the corrected times of the integrated log are in the order of few milliseconds. Clearly, the cause for the difference in velocity ratios has to be searched in the value of $v_s$ in sonic logs.

**Effects of gas**

As for seismic velocities, sonic logs are affected by the presence of gas. The velocity ratio decreases as the gas saturation increases. $v_p$ is slowed down while $v_s$ is mostly unchanged as S-waves do not travel through fluids. The decrease in $v_p/v_s$ plotted against the P slowness (transit time) is being used as a lithology and gas detector (Schlumberger Oilfield Bulletin, 2000). Values of $v_p/v_s$

from well measurements for gas bearing sandstones in the North Sea are often below 2.0.

**Effects of polar anisotropy**

Leaney et al., 2000, write that in deviated wells the value of $v_s$ is significantly elevated due to polar anisotropy and it needs some form of calibration. We can calculate the effect of the well deviation and the anisotropy on shear waves using (Thomsen, 1986):

$$v_{s(\theta)} = v_{s0}\left(1 + \sigma \sin^2\theta \cos^2\theta\right) \quad (6)$$

Well T9 has an average deviation of less then 30° from the vertical (but locally the deviation can be higher). Using $\sigma$ from seismic data (0.8) we get a difference between $v_{s0}$ and $v_{s(\theta)}$ of about 15%. The maximum difference is for a 45° deviation and is 20%, while, if we assume $\delta$=0 ($v_{pn}$=$v_{p0}$), the difference between $v_{s0}$ (seismic) and $v_{s(\theta)}$ (well log) is around 60%. In summary these results show that there must be other factors which make the value of the shear velocity from logs very high as anisotropy alone can not account for such a large difference in $v_p/v_s$ ratios.

**Other factors**

Eastwood and Castagna, 1986, studied the effects of frequency-dependent dispersion in presence of gas and polar anisotropy using theoretical models and laboratory experiments. They found that anisotropy makes the $v_p/v_s$ decrease with frequency while in the presence of gas $v_p/v_s$ should instead increase with frequency. For 100% water saturation the ratio, again, decreases with frequency. However they found that the maximum difference in velocity ratio for seismic and well log frequencies shouldn't be more then 15%. In the Lomond field the logs are through gas bearing sandstones, which should contrast the decrease of the ratio due to the presence of VTI.

**Conclusions**

Velocity analysis from a 4C dataset over the Lomond field shows the importance of carefully considering the effects of polar anisotropy and subsurface heterogeneities such as gas clouds on the velocity ratios. $\gamma_{eff}$ is the key parameter for binning C-wave data, if $\gamma_0$ is used the result is a poor quality image. Gas can make $\gamma_{eff}$ measures unreliable, some focusing analysis may be needed. Gas and polar anisotropy create serious difficulties when well logs are used to help seismic processing. Effects of frequency dependent dispersion and VTI in deviated wells added together do not seem to be enough to explain the difference between well and seismic velocity ratios found in the Lomond field. Using well log derived velocity ratio as $\gamma_0$ for seismic data may lead to wrong estimates and should be carefully considered.

**References**

Audebert, F., Granger, P.Y., and Herrenshmidt, A., 1999, CCP-Scan technique: True common conversion point sorting and converted-wave velocity analysis solved by PP and PS pre-stack depth migration: 69th Internat. Mtg. Soc. Expl. Geophys., Expanded Abstract. 1186-1189.

Eastwood, R. L. and Castagna, J. P., 1986, Interpretation of Vp/Vs ratios from sonic logs, in Domenico, S. N., Ed., Shear-wave exploration: Soc. of Expl. Geophys., 139-153.

Granli, J.R., Arntsen, B., Sollid, A. and Hilde, E., 1999, Imaging through gas-filled sediments using marine shear wave data, Geophysics, 64, 668-677.

Leaney, S., Wheeler, M., Tcherkashnev, S., Probert, T., and Law, A., 2000, Borehole-calibrated anisotropic processing of converted modes - a sub-chalk imaging study, 70th Internat. Mtg. Soc. Expl. Geophys., Abstract, MC2.6

Li, X-Y., Dai, H., Mueller, M.C., and Barkved, O.I., 2001, Compensating for the effects of gas clouds on C-wave imaging: A case study from Valhall, The Leading Edge, Vol. 20, N. 9.

Schlumberger, DSI Dipole sonic imager, 2000, Schlumberger Oilfield Bulletin.

Thomsen, L., 1986, Weak elastic anisotropy, Geophysics, 59, 304-313.

Thomsen, L., 1999, Converted-Wave reflection seismology over inhomogeneous, anisotropic media, Geophysics, 64, 678-690.

**Acknowledgements**

Fabio Mancini has a Natural Environment Research Council Industrial CASE studentship. We would like to thank BG Group for providing the data, for the permission to show them and for additional sponsorship

# D-09 EFFECTS OF BINNING VELOCITY RATIOS ON C-WAVE IMAGING IN THE PRESENCE OF DIPS

FABIO MANCINI [2,1], XIANG-YANG LI [1], ANTON ZIOLKOWSKI [2] and TIM POINTER [3]

[1]*British Geological Survey*

[2]*Department of Geology and Geophysics, University of Edinburgh, West Mains Road, Edinburgh EH9 3JW, UK*

[3]*BG Group*

**Abstract**

C-wave processing usually requires iterations involving velocity analysis and binning. As a first step the data are binned using a single value of $\gamma$ (Vp/Vs) before any P-wave independent velocity analysis, therefore sorting the data into Asymptotic Common Conversion Points. We analyse the effects of this initial binning value of $\gamma$ on C-wave imaging in areas of dipping reflectors. The data are from a 2D 4C line acquired over the Lomond field, in the North Sea. The results show that the C-wave NMO velocities in the presence of dips are sensitive to changes in the value of the binning velocity ratio. C-wave imaging relies on accurate knowledge of the effective velocity ratio $\gamma_{eff.}$ This parameter is determined by a combination of the vertical and the NMO velocity ratios. Errors in the C-wave NMO velocity lead to wrong estimates of $\gamma_{eff}$. Running a pre-stack time migration prior to the calculation of $\gamma_{eff}$ reduces velocity errors due to the presence of dips. We can further improve the accuracy of $\gamma_{eff}$ by using the CCP-scanning technique.

**ACCP binning, initial $\gamma$ value, $\gamma_{asy}$**

As the up-going leg of the C-wave raypath (S-wave) is slower than the down-going leg (P-wave), Snell's law requires that it is reflected at a more acute angle to the normal to the interface. This means that the conversion point is generally shifted towards the receiver so that the Common Mid Point (CMP) assumption is no longer valid even for plane horizontal layers. The Common Conversion Point (CCP) position is defined not only by the acquisition geometry but also by the velocity ratio between P and S-waves ($\gamma_{eff.}$). $\gamma_{eff}$ changes with depth and may change laterally. As a first approximation we can keep it constant, binning the data into Asymptotic CCP (ACCP) gathers. For convenience we use $\gamma_{asy}$ to denote this initial value of $\gamma_{eff.}$ From Thomsen (1999), we have:

$$x_c = \frac{\gamma_{asy} x}{1+\gamma_{asy}}; \qquad (1) \qquad\qquad \gamma_{eff} = \frac{\gamma_n{}^2}{\gamma_0}, \qquad (2)$$

where $\gamma_0$ is the vertical velocity ratio extracted as the ratio of the arrival times on the zero-offset sections (P-wave and C-wave stacks) and $\gamma_n$ is the NMO velocity ratio ($v_{pn}/v_{sn}$). Equation (1) relates the CCP position ($x_c$) to the CMP position ($x$). The parameter $\gamma_{eff}$ takes into account the effects of layering induced polar anisotropy. $\gamma_{eff}$ can be also estimated by applying the CCP-scanning technique (Audebert at al, 1999). This technique is robust in the presence of strong geological structures and has the advantage of not relying directly on the values of the velocity ratios, but is based on imaging concepts, so it can be used independently of the results of equation (2).

**Effects of $\gamma_{asy}$ on C-wave NMO velocities**

The initial C-wave velocity analysis is run on ACCP gathers. To check the sensitivity of the C-wave NMO velocity ($v_{cn}$) to $\gamma_{asy}$, we picked velocities after binning the data with different values of $\gamma_{asy}$. We separated the positive and negative offsets before picking, because diodic velocity effects are present in the Lomond Field (Mancini et al., 2002). The resulting velocity fields for the positive offsets are shown in Figure 1. On the left-hand side the C-wave positive offset stacks is shown for reference. The $\gamma_{asy}$ used were 1.25, 2.00 and 2.75. As $\gamma_{asy}$ increases, the seismic line is "squeezed"

toward the receivers, the minimum in the velocity field induced by the gas (from ACCP 800) becomes smaller, the whole velocity field appears smoother, and the lateral difference in velocity decreases. It can be seen that the greatest changes occur in the zone around 5000 ms and CCPs 600-750. This is where the dips are greatest. The presence of dips makes velocities dependent on $\gamma_{eff}$. Where dips are negligible velocities are not sensitive to changes in $\gamma_{eff}$, Dai and Li (2002).

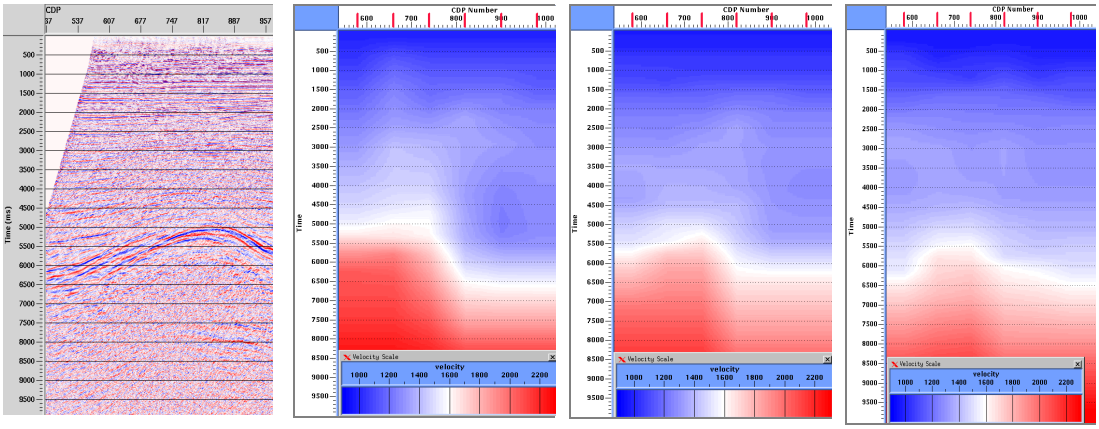

**Figure 1:** C-wave positive offset stack and velocity fields for different values of $\gamma_{asy}$. From left to right the binning values are 1.25, 2.00, 2.75.

This change of shape in the velocity field is important when we calculate $\gamma_{eff}$ using equation (2), as $v_{cn}$ is used for the calculation of $\gamma_n$. Equation (2) also requires $\gamma_0$. To extract $\gamma_0$ we have to correlate the events from the same reflector on the stacked P and C-sections, which gives the vertical arrival times for P and C-waves, tp0 and tc0. This step is always subjective and could be a big source of errors. Well log information could supply $\gamma_0$ at a well location when a dipole shear log is acquired, but the results have to be carefully considered as shear logs in deviated wells are often unreliable (Leaney et al., 2000; Mancini et al., 2002).

**Sensitivity analysis**

To gain more insight into the effects of $\gamma_{eff}$ on $v_{cn}$, we calculated the velocity values at tc = 5000 ms (reservoir depth in C-wave time) for the positive offsets, resulting from velocity analysis on ACCP gathers binned with different values of $\gamma_{asy}$: 1.25, 2.00 and 2.75. Given $v_{cn}$ (and $v_{pn}$ form P-wave processing) we then calculated the values of $\gamma_n$ and $\gamma_{eff}$ at the same arrival time, using a constant $\gamma_0$ = 2.80 (obtained from event correlation) and the S-wave NMO velocity, calculated as follows

$$v_{sn}^2 = v_{cn}^2 (1 + 1/\gamma_0) - \frac{v_{pn}^2}{\gamma_0}. \qquad (3)$$

We quantify changes in $v_{cn}$, $\gamma_n$ and, $\gamma_{eff}$ using their ratios. Figure 2 summarises the results. The x-axis is the ACCP number, the y-axis is the ratio. The results for the velocity show a maximum velocity change of about 5% for a 37.5% change in $\gamma_{asy}$. For $\gamma_{asy}$ = 1.25 and 2.00, ($\gamma_{asy}$ relative change of 60%), the maximum $v_{cn}$ change increases slightly, up to 7%. The difference is higher on the sides, where we have steep dips, and lower in middle of the 2D line.

$\gamma_n$ and $\gamma_{eff}$ change in the opposite direction to $v_{cn}$. The magnitude of the change increases from $v_{cn}$ to $\gamma_n$ to $\gamma_{eff}$. There is a 23% change in $\gamma_{eff}$ for a 5% change in $v_{cn}$ and there is a 31% change in $\gamma_{eff}$ for a 7% change in $v_{cn}$. For minor variations in $v_{cn}$, less than 2%, the change in $\gamma_{eff}$ is within 10%. We can also notice that, as the salt dome structure shifts from left to right for higher values of $\gamma_{asy}$ (confront Figure 1), the position of the area of minimum change shifts as well. These results show how small changes in $v_{cn}$ have a great effect on the calculation of $\gamma_{eff}$. If the resulting value of $\gamma_{eff}$ differs significantly from the $\gamma_{asy}$ used for velocity analysis, new velocity analyses after more appropriate binnings are necessary.

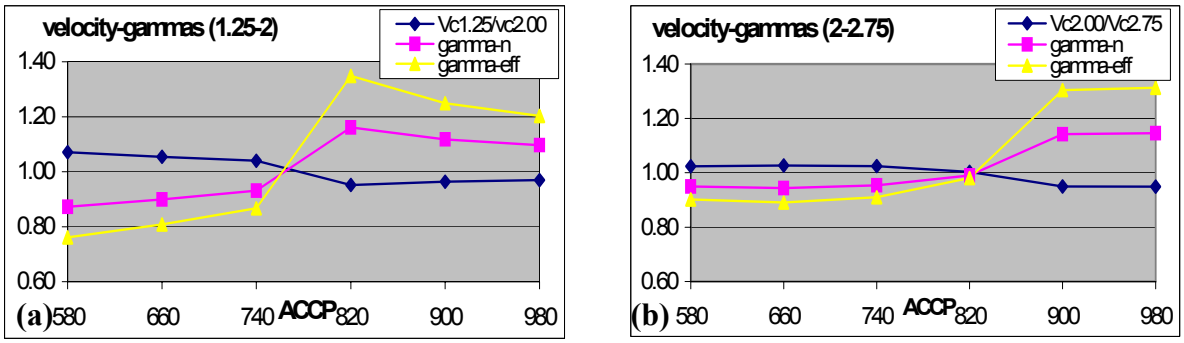


**Figure 2:** Relative changes in $v_{cn}$, $\gamma_n$ and $\gamma_{eff}$ for different $\gamma_{asy}$. (a) The blue line is for $v_{cn}$ (1.25)/ $v_{cn}$ (2.00), the purple line is for $\gamma_n$ (1.25)/ $\gamma_n$ (2.00) and the yellow line is for $\gamma_{eff}$ (1.25)/ $\gamma_{eff}$ (2.00). (b) Same colours as in (a) for $v_{cn}$ (2.00)/ $v_{cn}$ (2.75), $\gamma_n$ (2.00)/ $\gamma_n$ (2.75) and $\gamma_{eff}$ (2.00)/ $\gamma_{eff}$ (2.75).

## Estimating $\gamma_{eff}$: DMO vs. PSTM

Equation (2) is based on plane horizontal layers. Before using equation (2) we should minimise the effects of dip in the data. We consider separately the effects of DMO and pre-stack time migration (PSTM). Figure 3 shows two diagrams for $\gamma_{eff}$, one after DMO, and one after PSTM. The original $\gamma_{asy}$ used for the ACCP binning was 1.50 in both cases. On the left-hand side the P-wave stack is shown for structural reference. Both $\gamma_{eff}$ diagrams are shown in P-time. After DMO the resulting $\gamma_{eff}$ is too low, even less than 1 on the sides of the structure. This implausible result is caused by the anomalously high C-velocities obtained on both flanks of the salt dome, where the dips are highest. The high values of P-velocities due to the salt are also clear. DMO does not adequately correct for the effects of dip for the converted waves. After PSTM $\gamma_{eff}$ is generally higher and more physically acceptable: on the flanks of the salt dome the value ranges from 1.2 to 1.4, while on top of the dome it ranges from 1.6 to 1.8. The minima caused by the dips are now reduced.

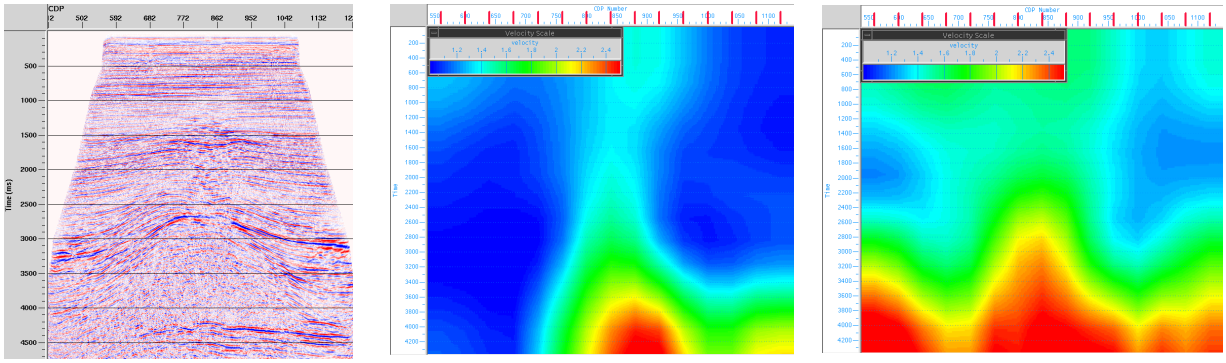

**Figure 3:** Left: P-wave stack, middle: values of $\gamma_{eff}$ calculated using equation (2) after DMO, right: the same after PSTM. Even after DMO the effects of the dips are clearly visible in the areas of low $\gamma_{eff}$. After PSTM these effects are reduced. The colour scale is the same

## CCP-scanning technique

The CCP-scanning technique can be used as an independent tool to extract $\gamma_{eff}$. We apply it in the time domain (Li et al, 2001), binning the positive and negative offsets with different values of $\gamma_{asy}$, looking for the value which gives better image focusing and less (or no) lateral shift in the geological structure. We used values of $\gamma_{asy}$ = 1.25, 1.50, 1.75, 2.00, Figure 4. As $\gamma_{asy}$ increases, the salt dome shifts toward the right (higher ACCP numbers) for the positive offset image and towards the left for the negative one. The negative offset image appears to be disturbed by the presence of gas and this makes the interpretation slightly more difficult. The correct value of $\gamma_{asy}$ seems to be between 1.50 and 1.75, which agrees which the value of $\gamma_{eff}$ given by equation (2) after PSTM.

In difficult areas for velocity analysis, such as those affected by gas clouds or severe dips, the use of the CCP-scanning technique becomes a necessary step (Li et al., 2001). Its use as the first tool for estimating $\gamma_{eff}$ can reduce the risk of errors and the need for more iterations.

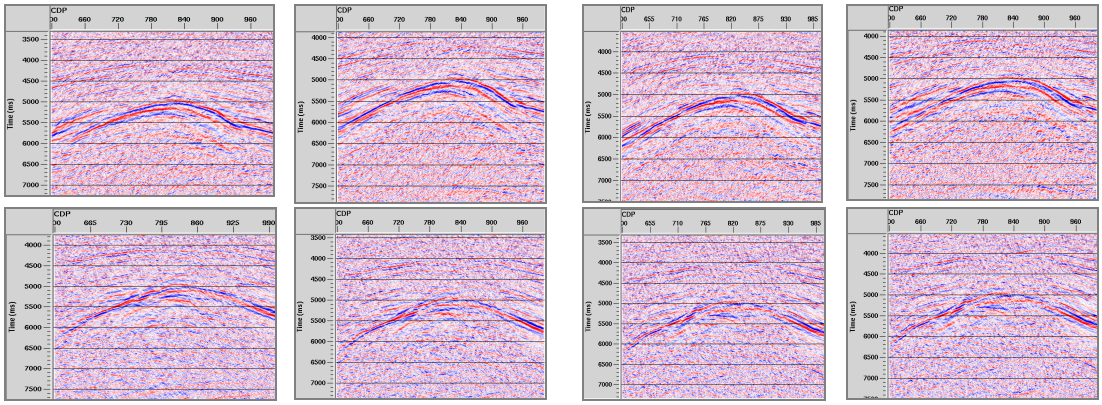

**Figure 4:** Positive (top ones) and negative offsets binned with different values of $\gamma_{asy}$, from left to right: 1.25, 1.5, 1.75, 2.0. The value that creates the best structural alignment for two offsets is between 1.5 and 1.75.

## Discussions and conclusions

In areas affected by dip $v_{cn}$ is sensitive to changes in $\gamma_{asy}$, the initial value of $\gamma_{eff}$. Then, small errors in the value of $v_{cn}$ are propagated as the square in the calculation of the next estimate of $\gamma_{eff}$ and cannot be ignored as they can lead to unrealistic values of $\gamma_{eff}$. We have found that the effect of dip can be reduced significantly by running PSTM on ACCP gathers. It is advantageous to run it prior $\gamma_{eff}$ estimation. Some positioning errors could still remain if the original binning value is not correct. The CCP-scanning technique is a robust tool that should also be used in order to improve the estimation of $\gamma_{eff}$.


## Acknowledgements

Fabio Mancini has a Natural Environment Research Council Industrial CASE Studentship. We thank BG Group for providing the data, for the permission to show them and for additional sponsorship.


## References


Audebert, F., Granger, P.Y., and Herrenshmidt, A., 1999, CCP-Scan technique: True common conversion point sorting and converted-wave velocity analysis solved by PP and PS pre-stack depth migration: 69th Internat. Mtg. Soc. Expl. Geophys., Expanded Abstract. 1186-1189.

Dai, H., and Li, X.-Y., 2002, Sensitivity analysis of migration velocities for P-S converted wave (C-wave) imaging, 64th Mtg.:Eur. Assn. of Expl. Geophys., Session: P008

Leaney, S., Wheeler, M., Tcherkashnev, S., Probert, T., and Law, A., 2000, Borehole-calibrated anisotropic processing of converted modes - a sub-chalk imaging study, 70th Internat. Mtg. Soc. Expl. Geophys., Session: MC2.6.

Mancini, F., Li., X.-Y., Ziolkowki, A., and Pointer, T., 2002, Interpreting velocity ratios from 4C seismic data and well logs in the presence of gas and anisotropy, submitted to the 72nd Mtg.: Soc. Expl. Geophys. Session: MC2.1.

Li, X-Y., Dai, H., Mueller, M.C., and Barkved, O.I., 2001, Compensating for the effects of gas clouds on C-wave imaging: A case study from Valhall, The Leading Edge, Vol. 20, 1022-1028.

Thomsen, L., 1999, Converted-Wave reflection seismology over inhomogeneous, anisotropic media, Geophysics, 64, 678-690.

# E038 C-wave anisotropic imaging using PSTM: a case example from the North Sea

Fabio Mancini [1], Xiang-Yang Li [2], Anton Ziolkowski [3], Hengchang Dai [2] and Tim Pointer [4]

[1] *Total E&P UK, 33 Cavendish Sq., London W1G 0PW, UK*

[2] *British Geological Survey, Murchison House, West Mains Road, Edinburgh EH9 3LA, UK*

[3] *Department of Geology and Geophysics, University of Edinburgh, West Mains Road, Edinburgh EH9 3JW, UK*

[4] *BG Group, 100 Thames Valley Park Drive, Reading, Berkshire, RG6 1PT, UK*

## Abstract

In this paper we present the results from an anisotropic C-wave Pre Stack Time Migration (PSTM) of a 2D line acquired over the Lomond Field, North Sea. The key processing steps are model building prior to PSTM and model updating during PSTM. Four parameters are required to define the model: C-wave short-spread velocity, $v_{cn}$, the vertical and the effective velocity ratios, $\gamma_0$ and $\gamma_{eff}$, and the anisotropic parameter $\chi_{eff}$. C-wave velocity and $\chi_{eff}$ can be updated using inverse NMO on Common Image Points (CIPs) obtained from PSTM. The final results are very good. Comparing them with results from a more "conventional" isotropic PS-DMO plus Post Stack Migration demonstrates great improvement in the image quality.

## Introduction

The Lomond Field, in the Central North Sea, is an excellent area to test C-wave processing tools: it has a complex structure, dominated by a salt-induced anticline fractured on top, large gas effects, due to the escape of gas from the fractured reservoir, and it has a strongly anisotropic (VTI) overburden of laminated shales.

We present here the results of an anisotropic PSTM processing sequence applied to the inline component from a 2D 4C line acquired over the Lomond Field. We apply a Kirchhof PSTM based on a Double Square Root equation (DSR) (Dai and Li, 2003). The DSR is fully defined by four parameters: the C-wave short-spread velocity, two velocity ratios and one anisotropic parameter. These parameters can be extracted by non-hyperbolic processing of C-waves. Their correct definition, that is, the model building, is the crucial step of the processing sequence. This model can then be updated during PSTM; more on this procedure can be found in Dai and Li (2003). The PSTM approach has a double advantage over the more "conventional" PS-DMO plus Post Stack Migration sequence: it does not require CCP binning and only needs limited information from P-waves.

## Parameterization

We define here the four parameters required for the PSTM: $v_{cn}$, $\gamma_0$, $\gamma_{eff}$ and $\chi_{eff}$. $v_{cn}$ is the C-wave short-spread velocity, $\gamma_0$ is the vertical velocity ratio, $\gamma_{eff}$ is the effective velocity ratio, which takes into account the effects of layering, and $\chi_{eff}$ is the C-wave anisotropic parameter (Li and Yuan, 2001). Equations (1) (2) and (3) (Thomsen, 1999) explain the link between the different velocity ratios. $v_{pn}$ and $v_{sn}$ are the P and S short-spread velocities while $v_{p0}$ and $v_{s0}$ are the P and S vertical velocities. The expression for $\chi_{eff}$ is shown in equation (4):

$$\gamma_{eff} = \frac{\gamma_n^{\,2}}{\gamma_0} \qquad (1)$$

$$\gamma_n = \frac{v_{pn}}{v_{sn}} \qquad (2)$$

$$\gamma_0 = \frac{v_{p0}}{v_{s0}} \qquad (3)$$

$$\chi_{eff} = \eta_{eff}\gamma_0\gamma_{eff}^{\,2} - \zeta_{eff} \qquad (4)$$

with $\eta_{eff}$ and $\zeta_{eff}$ given by:

$$\eta_{eff} = \frac{1}{8t_{p0}V_{pn}^{\,4}}\left(\sum V_{pni}^{\,4}(1+8\eta_i)\Delta t_{p0i} - t_{p0}V_{pn}^{\,4}\right) \qquad (5)$$

$$\zeta_{eff} = \frac{1}{8t_{s0}V_{sn}^{\,4}}\left(t_{s0}V_{sn}^{\,4} - \sum V_{sni}^{\,4}(1+8\zeta_i)\Delta t_{s0i}\right) \qquad (6)$$

## Model Building

### $\gamma_0$

A raw $\gamma_0$ is estimated from event correlation between the P and C stacked sections (pseudo-zero offset) using the ratio of the arrival times, $t_{s0}/t_{p0}$. The event picking in the Lomond field is shown in Figure 1b. $\gamma_0$, as expected, is higher in the shallow part, where sediments are unconsolidated, and decreases with depth. At the reservoir ($t_{p0}$=2.2 s.) $\gamma_0$ is about 2.8 (Figure 1c). The effects of the gas cloud are noticeable on the $\gamma_0$ profile.

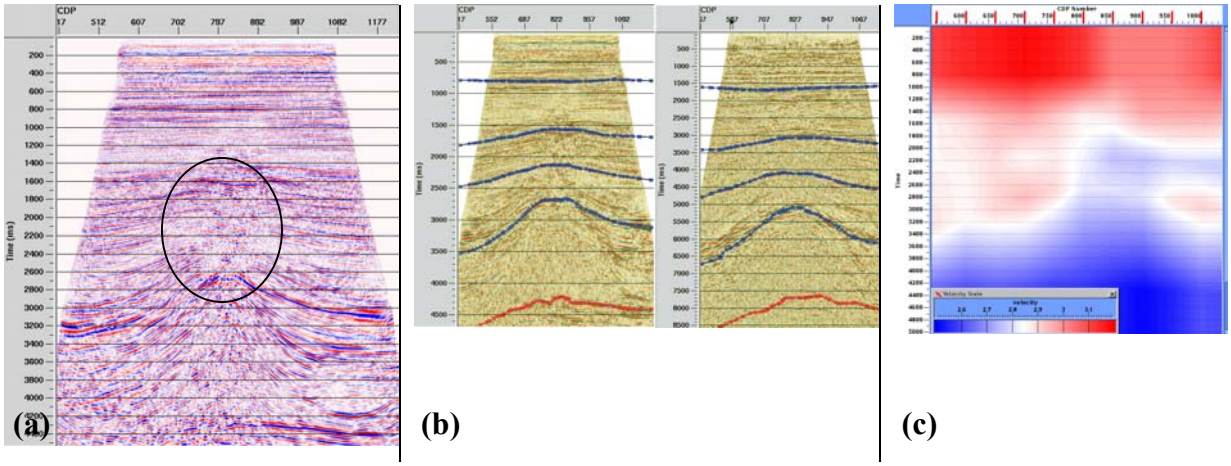


Figure 1: (a): P-wave stack. The area affected by the gas is circled in black; we can notice amplitude dimming and pull-down effects. (b): event correlation, P-stack on the left and C-stack on the right. Five events were correlated. (c): average $\gamma_0$ in P-time. At the target ($t_{p0}$=2.2 s.) $\gamma_0$ is about 2.8.

### $v_{cn}$ and $\gamma_{eff}$

$v_{cn}$ is obtained by short-spread velocity analysis on Asymptotic Common Conversion Point (ACCP) gathers. Given $v_{pn}$ (from P-wave processing) and $v_{cn}$ we can calculate $\gamma_n$ and $\gamma_{eff}$ using equation (2) and (1). The results are shown in Figure 2. From left to right we have $v_{pn}$, $v_{cn}$ and $\gamma_{eff}$. Due to high apparent C-velocity introduced by the presence of dips (Figure 2b) the $\gamma_{eff}$ field shows very low values, even below 1 in the areas affected by strong dip. In the middle of the section $\gamma_{eff}$ is about 1.5-1.6. $\gamma_{eff}$ can also be determined using a velocity independent procedure, based on imaging principles: the CCP-scanning technique (Audebert et al., 1999). With this technique we search for the value of $\gamma_{eff}$ giving the least lateral shift between the positive and negative offset stacks. Figure 3 shows the results of the CCP-scanning technique applied at the reservoir area of the Lomond data, the values of $\gamma_{eff}$ used are: 1.25, 1.50, 1.75 and 2.00. For each quadrant of Figure 3 the positive stack is at the top, the negative stack at the bottom. If we focus our attention on the top of the salt dome, the correct value of $\gamma_{eff}$ is about 1.50. This result is in good agreement with the central part of the $\gamma_{eff}$ field calculated using velocity information.

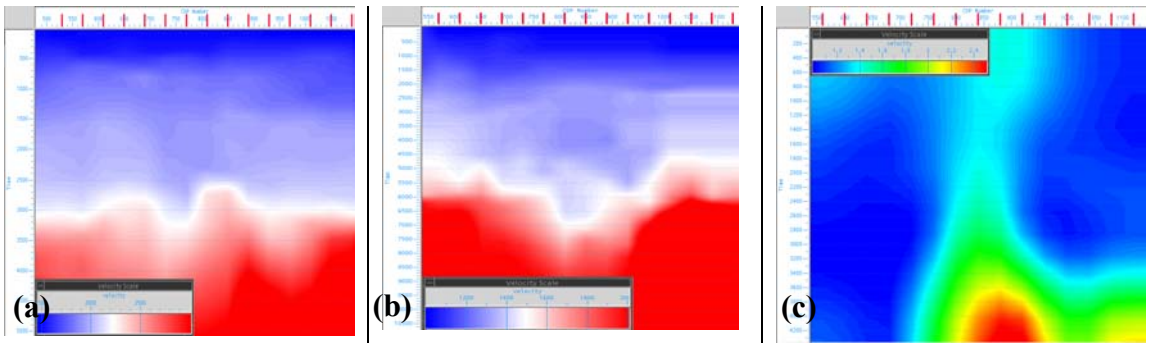


Figure 2: (a): P-wave DMO velocity field, (b): C-wave DMO velocity field and (c): $\gamma_{eff}$ in PP time.

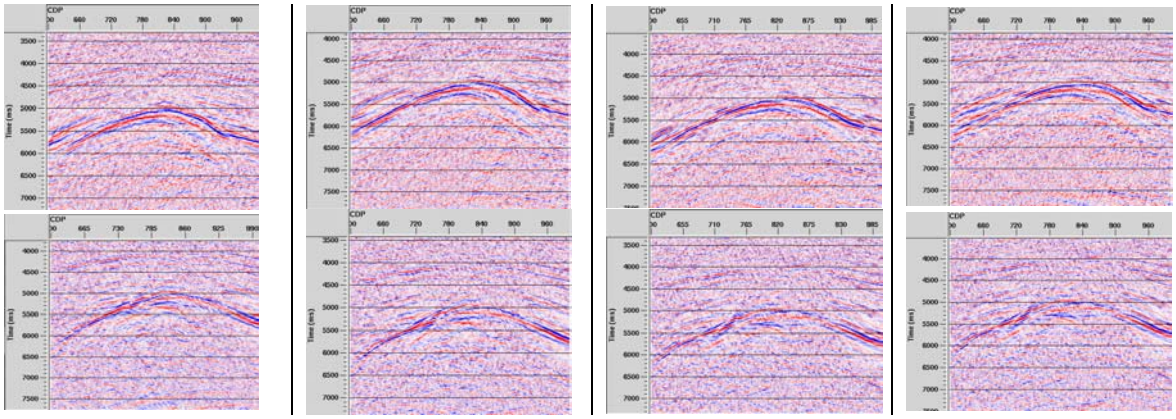

Figure 3: Positive (top) and negative (bottom) offset stacks, binned with different values of $\gamma_{eff}$, from left to right: 1.25, 1.50, 1.75 and 2.0. The best structural alignment is obtained with $\gamma_{eff}$ = 1.50.

**$\chi_{eff}$**

$\chi_{eff}$ is calculated from residual long offset moveout correction on ACCP gathers, using the three-term equation presented by Li and Yuan (2001). The $\chi_{eff}$ fields for the positive and negative offsets are shown in Figure 4. We can notice that $\chi_{eff}$ has quite high values (up to 1.60) and that it tends to follow the geological structure. This consideration leads us to believe that the presence of dips has effects on the calculation of $\chi_{eff}$ (Mancini et al., 2003).

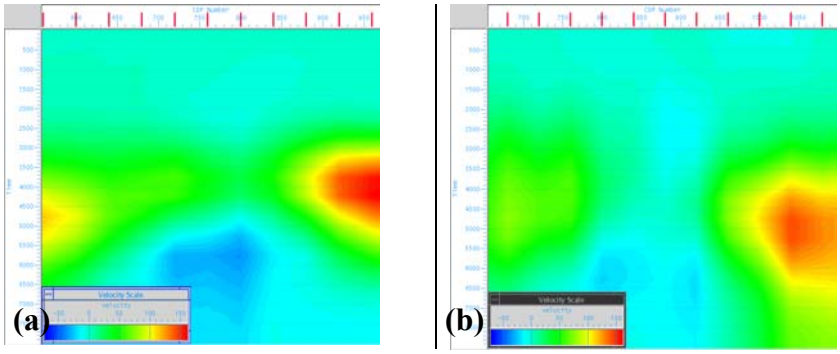


Figure 4: $\chi_{eff}$ values obtained from long offset non-hyperbolic moveout on ACCP gathers. In (a) there are the values from the positive offsets, in (b) the values are for the negative offsets.

## PSTM in practice

After the initial model building on ACCP gathers, $v_{cn}$ and $\chi_{eff}$ can be updated during PSTM. The procedure is explained in Dai and Li (2003): a reverse NMO is applied to selected Common Image Points (CIPs) after PSTM, obtaining inverse NMO(INMO)-CIPs. Applying the inverse NMO to the CIPs removes the effects of the non-hyperbolic component of the velocity. Dai and Li (2003) show that the velocity picked on the Inverse NMO CIPs tends to converge to the correct value of the migration velocity after few iterations. Often one pass of velocity updating is adequate, but in more difficult areas more iterations may be needed. Figure 5 is an example of this procedure: from left to right we have ACCP 880 after non-hyperbolic NMO, CIP 880 after the first PSTM run, the INMO-CIP gather and CIP 880 after the second run of PSTM. The sharpness of the image at around $t_{c0}$= 5.0 s. is greatly improved. This CIP does not need further velocity update.

The full PSTM image is shown in Figure 6a. The image quality is very good, with great definition of the horst structure forming the top of the Lomond Field. In Figures 6b and 6c we show the detail of the reservoir area for the PSTM flow and for a more "conventional" isotropic PS-DMO + Post Stack Migration sequence. This sequence is limited to the near offsets, with hyperbolic velocity analysis before and after PS-DMO (Mancini et al., 2002). At the target the improvements in the overall continuity and, in particular, in the lateral positioning of the faults defining the horst after PSTM are noticeable. Above the reservoir the use of the full offset range introduces some noise, which deteriorates the continuity of the events. In this part of the data a time-variant mute can probably improve the results.

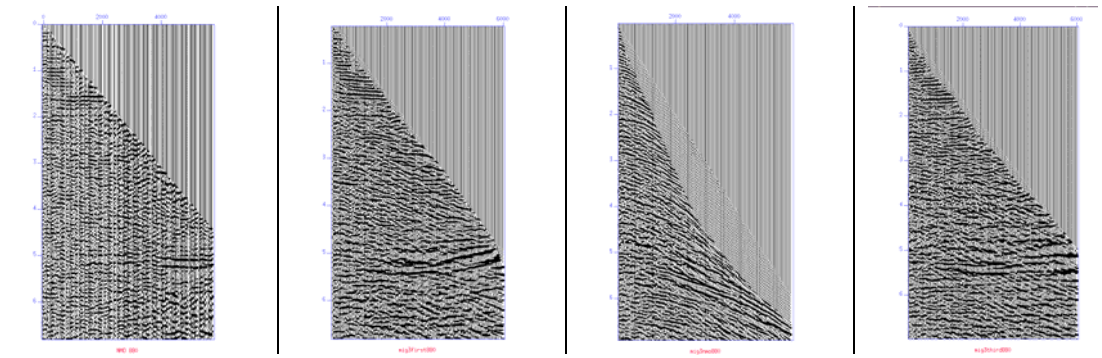

Figure 5: From left to right: ACCP 880 after anisotropic NMO, CIP 880 from PSTM first run, INMO-CIP 880, CIP 880 after PSTM second run.

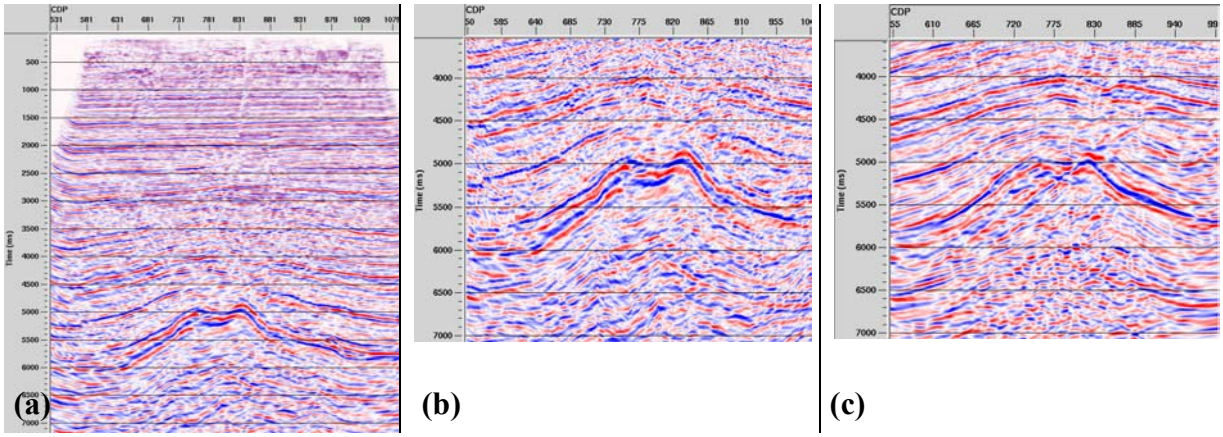


Figure 6: (a): C-wave PSTM; (b): zoom-in of the target area (after PSTM); (c): zoom-in of the target area after PS-DMO+Migration

## Conclusions

We have shown here the results from an anisotropic C-wave PSTM sequence applied on a 2D line acquired over the Lomond Field. Prior to PSTM we need to extract four key parameters required in the process. $\gamma_0$ is given by a raw event correlation, $\gamma_{eff}$ can be obtained from velocity information and/or using the CCP-scanning technique, $v_{cn}$ and $\chi_{eff}$ are extracted during long-offset velocity analysis on ACCP gathers. These parameters can be updated during PSTM. The final image is a great improvement compared with the results from the more "conventional" PS-DMO + Migration flow.

## Acknowledgements

This work was carried out while Fabio Mancini was a student at the University of Edinburgh and at the Edinburgh Anisotropy Project (EAP). We thank the Natural Environment Research Council for the studentship. We also thank BG Group for providing the data, for the permission to show them and for additional sponsorship.

## Reference

Audebert, F., Granger, P.Y., and Herrenschmidt, A., 1999, CCP-Scan technique: True common conversion point sorting and converted-wave velocity analysis solved by PP and PS pre-stack depth migration: 69th Internat. Mtg. Soc. Expl. Geophys., Expanded Abstract. 1186-1189.

Dai H., and Li, X.-Y., 2003, Migration velocity analysis of C-wave using INMO-CIP gathers of PKTM: a case study from the Gulf of Mexico, 65th Mtg EAGE Conference, Expanded Abstract.

Li, X.-Y., and Yuan, J., 2001, Converted-wave imaging in inhomogeneous, anisotropic media: Part I – Parameter estimation, 63rd EAGE Conference, Expanded Abstract, I, P109.

Mancini, F., Li., X.-Y., Ziolkowski, A., and Pointer, T., 2002, Interpreting velocity ratios from 4C seismic data and well logs in the presence of gas and anisotropy, 72nd Mtg.: Soc. Expl. Geophys. Expanded Abstract, 1002-1005.

Mancini, F., Li., X.-Y., Ziolkowski, A., and Pointer, T., 2003, Effects of binning velocity ration on C-wave imaging in the presence of dips, 65th Mtg EAGE Conference, Expanded Abstract.

Thomsen, L., 1999, Converted-Wave reflection seismology over inhomogeneous, anisotropic media, Geophysics, 64, 678-690.